ORIENTATIONAL ORDERING OF HYDROGEN MOLECULES ADSORBED ON GRAPHITE

by

PHILIP ROMAN KUBIK

B.Sc., University of British Columbia, 1974
M.Sc., University of British Columbia, 1977

A THESIS SUBMITTED IN PARTIAL FULFILLMENT OF

THE REQUIREMENTS FOR THE DEGREE OF

DOCTOR OF PHILOSOPHY

in

THE FACULTY OF GRADUATE STUDIES

DEPARTMENT OF PHYSICS

We accept this thesis as conforming

to the required standard

THE UNIVERSITY OF BRITISH COLUMBIA

May, 1984

In presenting this thesis in partial fulfilment of the requirements for an advanced degree at the University of British Columbia, I agree that the Library shall make it freely available for reference and study. I further agree that permission for extensive copying of this thesis for scholarly purposes may be granted by the head of my department or by his or her representatives. It is understood that copying or publication of this thesis for financial gain shall not be allowed without my written permission.

Department of Physics

The University of British Columbia
1956 Main Mall
Vancouver, Canada
V6T 1Y3

Date July 16, 1984

ABSTRACT

NMR has been employed to measure the orientational behaviour of sub-monolayers of H_2 and D_2 adsorbed on graphite from .3 K to 12 K. For the temperature and coverages used, the hydrogen forms a lattice commensurate with that of the graphite ($\sqrt{3}$ x $\sqrt{3}$ structure) and can be modelled by a hexagonal lattice of interacting quantum quadrupoles. Each molecule also experiences a crystal field arising from Van der Waals interactions with the substrate and with the other hydrogen molecules. For such a system, mean field theory predicts a variety of orientationally ordered phases, depending on the relative strength of the crystal field and the molecular field, which are always in opposition. A key question to be answered by experiment was whether the strong fluctuations associated with quantum effects and the two dimensional nature of the system would in fact allow a finite transition temperature.

We have observed that for 90% ortho-H_2 (J=1), the splitting of the high temperature NMR doublet increases rapidly with decreasing temperature near .6 K and additional structure appears. In addition, the .3 K spectrum agrees well with the expected T=0 spectrum for the orientationally ordered pinwheel phase of mean field theory. Consequently, the rapid increase in the splitting is interpreted as an orientational ordering transition.

In contrast to the results for H_2, the NMR spectrum of 90% para-D_2 (J=1) shows no rapid changes, evolving smoothly from a doublet to a very broad and weak structure. There is no evidence of orientational ordering, at least down to .3 K. The different behaviour of H_2 and D_2 is particularly puzzling in light of the fact that the bulk solids both order orientationally into the same structure at similar temperatures.

From the temperature dependence of the splitting of the high temperature NMR doublets, we have extracted the values of the crystal fields and effective quadrupole coupling constants of H_2 and D_2. The quadrupole coupling constant of D_2 is somewhat less than the rigid lattice value as one would expect in the presence of translational zero point motion. However, that of H_2 is much too small for this mechanism to be responsible.

TABLE OF CONTENTS

Page

LIST OF TABLES

LIST OF FIGURES

Page

ACKNOWLEDGEMENTS

This project was proposed by my supervisor Walter Hardy and his insight into the numerous tribulations that have arisen has been invaluable, not only for dealing with the problem at hand, but also for furthering my own ability to deal with subsequent mysteries. Since the hydrogen samples used in these experiments deteriorate with time, it was sometimes necessary to make measurements day and night for periods of up to three weeks. I am indebted to Hans Glättli, Erwin Batalla, and Walter for their assistance in collecting data at very irregular hours during those periods. Other members of the Microwave Spectroscopy group, in particular Michael Morrow and Bryan Statt, have also provided valuable help. Assistance with the preparation and analysis of my enriched hydrogen samples has been given by two summer students, Stephen Morris and Louis Taillefer. I also acknowledge the generosity of Charlie Schwerdtfeger in allowing me to use his magnet for a period much longer than either of us anticipated.

The mean field theory and high temperature expansions that John Berlinsky and Brooks Harris developed were vital to the development of my understanding of the orientational behaviour of adsorbed hydrogen. They both collaborated closely with me and provided much stimulation.

Assistance has been cheerfully provided to me by

virtually every member of the departmental technical staff so all of them have earned my gratitude. However, particular mention should be made of the prompt assistance given to me by Bill Walker and Rolf Weissbach when a piece of equipment required repair.

Finally, I wish to thank the National Research Council and the Killam Foundation for postgraduate fellowships.

CHAPTER I

INTRODUCTION

1.1 Techniques Available for the Study of Physisorbed Hydrogen

Although there have been numerous studies of hydrogen chemisorbed on various surfaces, particularly metals, physisorbed molecular hydrogen[1] has received relatively little attention. Physisorption studies have concentrated on the inert gases. In many of these studies the basal plane of graphite has been used as a substrate because graphite is available in forms with both a high specific surface area and a high proportion of uniform basal planar adsorbing surfaces.

Hydrogen should be a good probe of gas-surface interactions and two-dimensional (2D) phases because the microscopic interactions of hydrogen molecules are very well known. However there are several stumbling blocks to the study of physisorbed hydrogen. Sub-monolayers of hydrogen on graphite do not solidfy until the temperature is reduced to 20K or less (Nielsen et al, 1977). This severely restricts the use of many modern surface analysis techniques such as low energy electron diffraction (LEED), Auger electron spectroscopy, and field emission microscopy, the apparati for which are normally designed for operation at higher temperatures. Also, hydrogen, being a very light molecule, scatters electrons and X-rays very weakly so there are large background signals from the substrate. In addition to surface methods there are several bulk techniques

that can be adapted to surface studies provided that the substrate has a large area. However, they suffer from low signal to noise (S:N) ratios. Neutron diffraction from H_2 is inhibited by the fact that scattering from para-H_2 (p-H_2), the equilibrium species at low temperature, is almost entirely incoherent. The situation is more favourable for D_2 which scatters primarily coherently. Specific heat measurements have been used extensively and effectively to study the 2D phases of helium. In the case of hydrogen, however, such measurements would be complicated by the presence of heating arising from conversion.[2] The technique of nuclear magnetic resonance (NMR), which has been valuable for the study of adsorbed ^3He, would also be expected to be useful for the study of adsorbed hydrogen. P-D_2 and o-H_2 both have total nuclear spin I=1. o-D_2 has I=0 and 2 and p-H_2 has I=0. The first three species all give an NMR signal; o-H_2 is a particularly good subject for NMR because it has a large nuclear magnetic moment. However, as we shall see later, the NMR spectra of adsorbed hydrogen are considerably broader than those of ^3He so the S:N ratios are not as good.

Many of the theoretical techniques used in statistical mechanics could be applied to adsorbed hydrogen but there would be complications due to the quantum nature of hydrogen molecules. This renders difficult the application of Monte Carlo and renormalization group (RG) methods which have been used extensively for other adsorbed systems. Mean field theory has

been used quite successfully to study the orientational behaviour of hydrogen molecules adsorbed on graphite (Harris and Berlinsky, 1979).

1.2 Previous Work

The earliest measurements on H_2 adsorbed on graphite were adsorption isotherms (Constabaris et al, 1961). Since then there have been other pressure measurements (Dericbourg, 1976; Daunt et al., 1981) but all of this work has been primarily concerned with multilayer adsorption. For several inert gases, most notably Kr, adsorbed on graphite, the adsorption isotherms show structure arising from 2D phases in the sub-monolayer region (Thomy and Duval, 1969). Similar behaviour has not been observed for H_2.

Inelastic neutron scattering (Stockmeyer et al, 1978) and molecular beam scattering (Mattera et al, 1980) have been employed to measure the energy levels of adsorbed hydrogen molecules. From the molecular beam work it has been possible to derive a laterally averaged molecule-surface interaction potential. A binding energy of 483 K for H_2 on graphite has also been obtained.

Specific heat (Bretz and Chung, 1974), elastic neutron scattering (Nielsen et al, 1977) and LEED (Seguin and Suzanne, 1982) have been used to attempt to study the 2D translational phases. Peaks in the specific heat were observed between 8 K and 16 K for three coverages of less than half a monolayer. For the two lowest coverages (.0112 and .0277 molecules/$\AA^2$), the

specific heat increased as T^2 between 1K and 4K and then exponentially with 1/T up to the peak. An incommensurate 2D Debye solid would be expected to give T^2 behaviour at low temperatures. Nevertheless this interpretation was rejected on the basis of the size of the proportionality constant between the temperature of the specific heat peak (the melting temperature in this picture) and the square of the Debye temperature. The proportionality constant did not agree with the prediction of the Kosterlitz-Thouless theory of dislocation mediated melting. The validity of the theory for this system is not established, however, and other theories give different proportionality constants. The specific heat will increase exponentially with 1/T if one has two phase coexistence on the surface or if there is a registered solid. Using the former interpretation, the specific heat peaks were taken to represent a 2D liquid to 2D vapour transition.

Subsequently, a translational phase diagram of coverage ρ versus temperature T for H_2 and D_2 on graphite (Fig. 1) was obtained by elastic neutron scattering. Nearly all of the measurements were made using o-D_2 but those p-H_2 data that were obtained did not suggest that the phase diagram for H_2 was different from that of D_2.

In the low temperature and low coverage region, scattering peaks corresponding to a $\sqrt{3}$ x $\sqrt{3}$ registered solid were observed. In this structure (Fig. 2), a hydrogen molecule is located at the centre of every third carbon ring. This structure has also

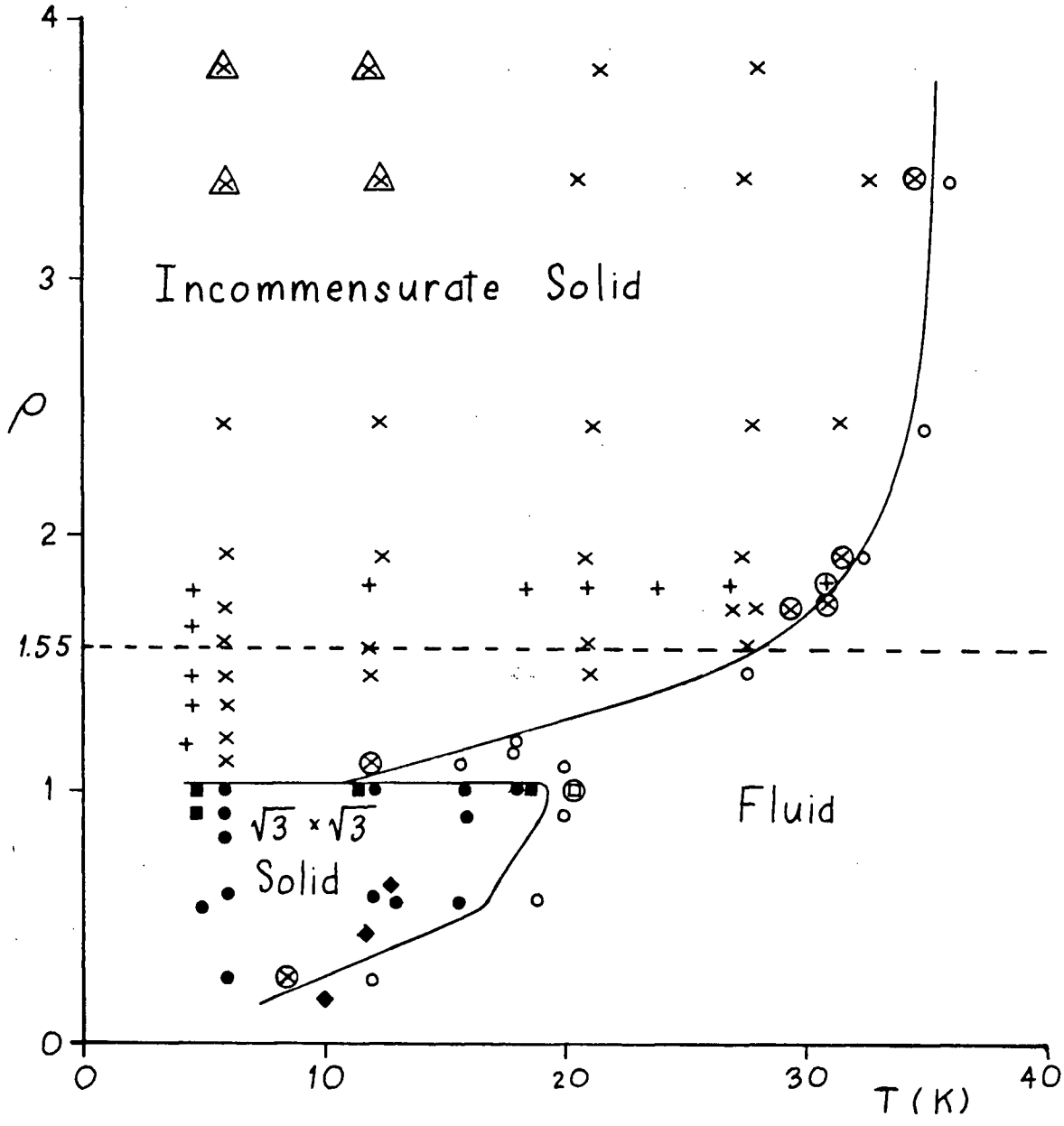

Fig. 1 Translational phase diagram for H_2 and D_2 adsorbed on Grafoil, plotted as coverage ρ versus T. The coverage is normalized to full coverage by the $\sqrt{3}x\sqrt{3}$ solid. Phase boundaries were deduced by Nielsen et al (1977) from neutron scattering data. The specific heat peaks observed by Bretz and Chung (1974) are also shown. The dashed line indicates monolayer coverage.

		p-H_2	o-D_2
Specific heat peak		◆	
$\sqrt{3}x\sqrt{3}$ solid		■	●
Incommensurate solid	neutron	+	×
Fluid	scattering	□	○
Deformed scattering peaks			△

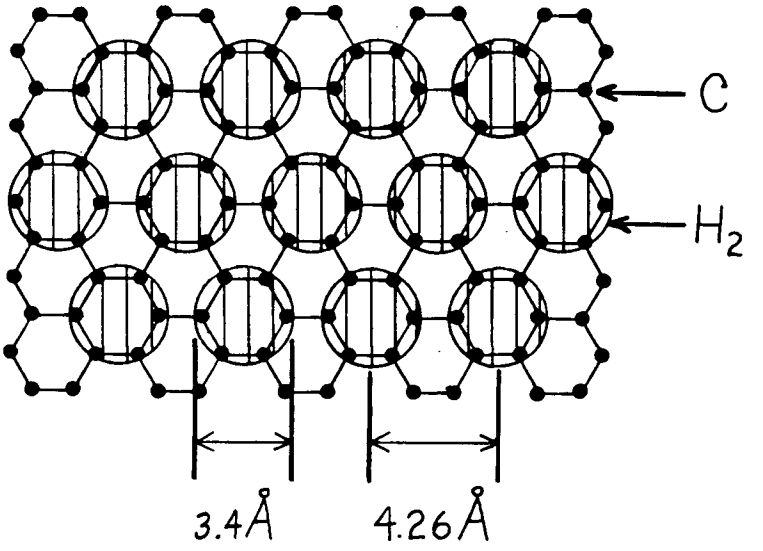

Fig. 2 The $\sqrt{3}x\sqrt{3}$ registered phase of H_2 adsorbed on the graphite basal plane. The diameter of the H_2 molecules is equal to the minimum of the H_2-H_2 potential. The H_2 molecules are nearly spherical.

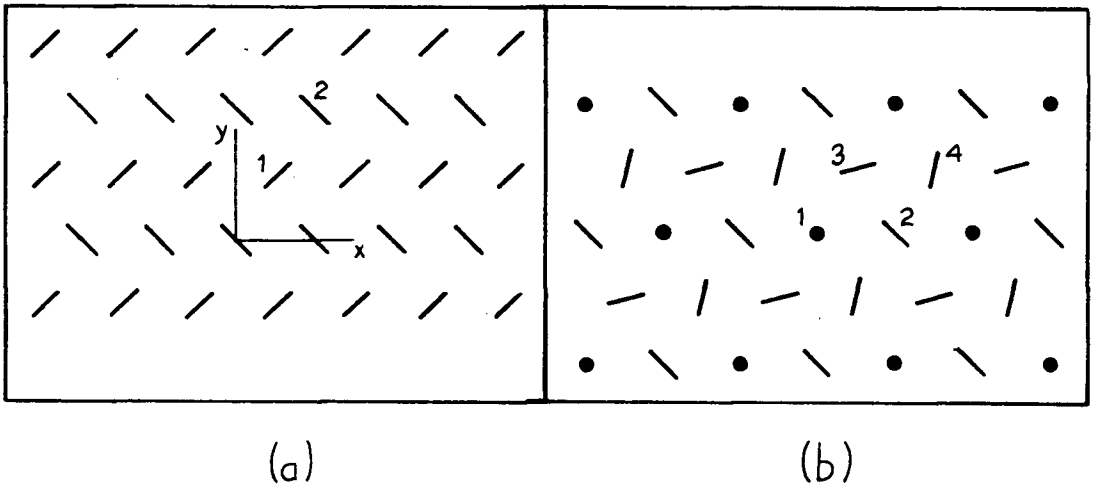

Fig. 3 Orientationally ordered states. (a) Herringbone: the molecular axes are parallel to the surface for both sublattices. (b) Pinwheel: the molecular axes of sublattices 2, 3, and 4 are parallel to the surface but those of sublattice 1 are perpendicular.

been observed for ^3He, ^4He, N_2, Kr, and CH_4 adsorbed on graphite. Note that in Fig. 1 ρ is normalized to complete coverage by the $\sqrt{3} \times \sqrt{3}$ solid (.0637 Å^{-2}).

As T was increased the $\sqrt{3} \times \sqrt{3}$ peaks disappeared over a 3K temperature interval indicating a transition to a fluid phase. Note that the specific heat peaks for the two lowest coverages used by Bretz and Chung (ρ =.18 and .44) coincide approximately with the neutron scattering phase boundary but that the peak for ρ =.64 is at a lower temperature. The two low coverage specific heat peaks apparently indicate melting rather than boiling.

At coverages greater than ρ=1 and at low temperatures an incommensurate, triangular solid was observed by neutron scattering.

The $\sqrt{3} \times \sqrt{3}$ structure has also been seen in LEED measurements of H_2 on graphite at 10K (Seguin and Suzanne, 1982). Unfortunately, in this technique, the pressure of the 3D vapour rather than the coverage is measured; the relationship between the two in the sub-monolayer regime is not known.

NMR has been used to measure the longitudinal and transverse relaxation times T_1 and T_2 of o-H_2 adsorbed on graphitized carbon black (Spheron 6)[3] in the temperature range $12\ K \leq T \leq 28\ K$ (Riehl and Fisher, 1973). This substrate has a high specific area of basal plane surfaces which are fairly homogeneous (steps in the Kr isotherms can be seen) and flat but lack any preferred orientation. Coverages ranged up to .3 monolayers (ρ =.52). T_1 and T_2 both increased linearly with ρ as

expected for a 2D gas, in which relaxation occurs through modulation of the intramolecular spin - spin interactions by collisions, in the short correlation time limit. This interpretation is consistent with the phase boundary of Fig. 1 except perhaps for the highest coverages and lowest temperatures: here the high excitation frequency of 30 MHz may have led to RF heating.

For molecular reorientation, the short correlation time limit is expressed by

$$\omega_o \tau_c << 1 \qquad (I-1)$$

where ω_o is the resonance frequency and τ_c, the correlation time, is the time between collisions. If longitudinal and transverse relaxation occur by the same mechanism, then in this limit $T_1 = T_2$ in 3D. Riehl and Fisher assumed implicitly that this would also apply to a 2D gas. Since they found T_2 to be considerably less than T_1, they felt that there must be an additional mechanism for transverse relaxation. They were able to identify a possible mechanism by assuming a model in which hindered rotational states of the molecules were coupled to the translational states. More recent theoretical work (Cowan, 1980) has shown that in 2D both T_1 and T_2 depend strongly on the angle between the applied static magnetic field H_o and the substrate and that for a powder substrate, the effective T_2 would be considerably shorter than T_1 even in the motional narrowing limit $\omega_o \tau_c << 1$. Consequently the conclusions of Riehl and Fisher have been undermined.

1.3 Scope of this Thesis

This thesis describes a study of the orientational behaviour of J=1 H_2 and D_2 molecules adsorbed on graphite using the technique of NMR. The measurements span the temperature range of .3K to 12K at a coverage of ρ =.85. Therefore, according to Fig. 1, the hydrogen should be in the $\sqrt{3}$ x $\sqrt{3}$ solid phase.

In this phase, the hydrogen can be modelled by a hexagonal lattice of interacting quantum quadrupoles. Each molecule also experiences a crystal field arising from Van der Waals interactions with neighbouring molecules and with the substrate. Harris and Berlinsky (1979) have used mean field theory (MFT) to study such a system and have predicted the existence of a variety of orientationally ordered phases which depend on the relative strength of the crystal field and the molecular field and on the temperature. Subsequently a Monte Carlo calculation (O'Shea and Klein, 1979) for the analogous system of classical quadrupoles predicted the existence of two of the phases which are shown in Fig. 3. If the crystal field were zero, they found ordering into the pinwheel phase. If it were large enough to force all of the molecular axes to lie in a plane parallel to the surface, ordering into the herringbone phase was seen.[4]

A system closely analogous to physisorbed H_2 is physisorbed N_2, which also forms a $\sqrt{3}$ x $\sqrt{3}$ registered lattice on graphite (Kjems et al, 1976); the major difference is that the N_2 molecules can be treated as classical rotors because of

their large moment of inertia. Adsorbed N_2 molecules have been observed to undergo an orientational ordering transition into the herringbone phase at 28 K. Techniques used to study this transition were specific heat (Chung and Dash, 1977; Migone et al, 1983), neutron scattering (Eckert et al, 1979), LEED (Diehl et al, 1982), and NMR (Sullivan and Vassiere, 1983).

One of the goals of the present work was to answer the question of whether orientational ordering of J=1 molecules will occur as predicted by MFT and the classical Monte Carlo calculations or whether it would be suppressed by either 2D fluctuations or quantum fluctuations. It has been shown that long range positional order cannot exist for T>0 in a 1D or 2D lattice on a smooth substrate.[5] For a 3D lattice the mean square displacement $\langle |\vec{u}(\vec{R})|^2 \rangle$ of a molecule with an equilibrium position $\vec{R}$ remains finite as $R \to \infty$. For a 2D lattice $\langle |\vec{u}|^2 \rangle$ increases as log R and in 1D as R; in both cases it diverges for an infinite lattice. These arguments apply to such diverse systems as superconductors, superfluids, and magnetic spins. Although long range positional order is precluded in a 2D lattice, it can still have long range directional order. If $\vec{R}$ is an equilibrium lattice vector and $\vec{r}=\vec{R}+\vec{u}(\vec{R})$, define $\theta(\vec{R})$ to be the angle between $\vec{r}$ and an arbitrary axis. On a triangular lattice directional order can be measured by $\langle \exp i6[\theta(\vec{R})-\theta(0)] \rangle$. It remains finite $R \to \infty$. Much of the recent effort in the study of the translational phase transitions of inert gases adsorbed on graphite has been directed towards the discovery of

hexatic phases which have short range positional order but power law decay of the directional order. A phase of this type, which is clearly a consequence of a melting process rather than substrate interactions, has been seen for Xe on graphite (Rosenbaum et al, 1983).

A triangular lattice of quadrupoles is an example of a system exhibiting frustration, a key concept in the behaviour of glassy systems. A system is frustrated if it is impossible for every pair of neighbouring molecules to achieve their lowest energy configuration. For a pair of quadrupoles this is a T configuration. A square lattice of quadrupoles with nearest neighbour interactions only is not frustrated as shown in Fig. 4(a). It is impossible for all nearest neighbours on a triangular lattice to be mutually perpendicular so there is frustration [Fig.4(b)]. Frustration is reduced when the system is diluted. For hydrogen there will always be some dilution because conversion produces J=0 molecules which have spherical wave functions. These have no EQQ interactions so they act like vacancies. If there is no frustration, then the system is stable against small amounts of random dilution [Fig. 4(c)]. In the presence of frustration, random dilution will cause local reorientation of molecules but reorientation of large numbers of molecules will be blocked by energy barriers at low temperatures. The system may not be able to achieve the lowest energy configuration, becoming stuck in a metastable state (a glass), which depends upon the thermal history. Low (J=1) concentration

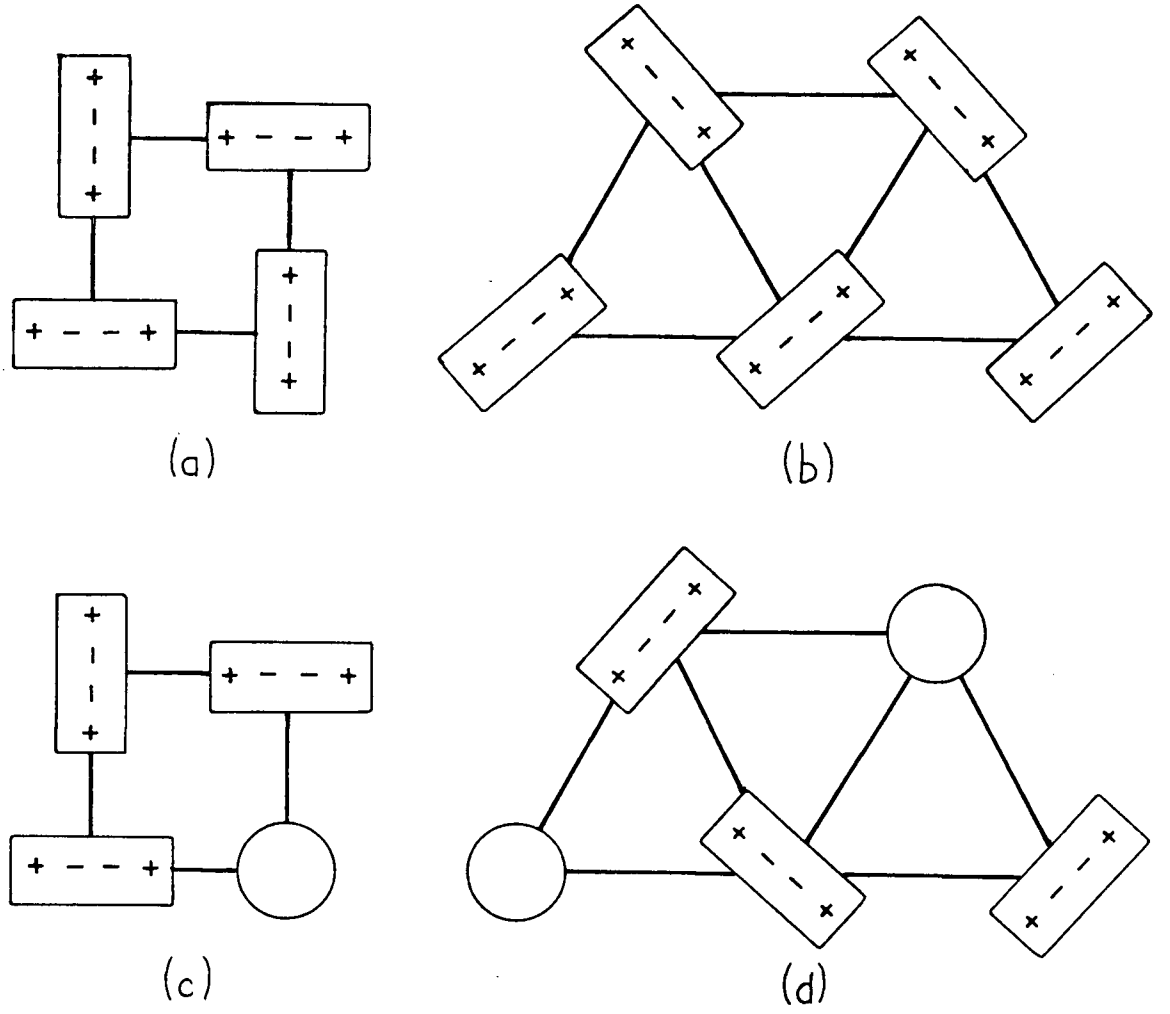

Fig. 4 The effect of vacancies on lattices of quadrupoles with and without frustration: (a) square lattice (not frustrated), (b) triangular lattice (frustrated), (c) square lattice with vacancies, and (d) triangular lattice with vacancies.

absorbed hydrogen is a likely candidate for the formation of a quadrupolar glass. Such a state would be characterized by freezing of the molecules into random orientations. This has in fact been proposed for bulk H_2 when the J=1 concentration falls below .55 (Sullivan, 1976) but is still a subject of controversy (Estève et al, 1982; Washburn et al, 1982).

Early measurements of the NMR spectra of H_2 and D_2 in the orientationally disordered state (the pararotational state) are described in Kubik and Hardy (1978). The results for the crystal field V_c and quadrupolar coupling constant Γ were

H_2 $\quad |V_c| = .56$ K $\quad \Gamma \simeq 0$

D_2 $\quad |V_c| = 2.4$K $\quad \Gamma = .5$ K

With these values the MFT of Harris and Berlinsky (1979) (described in Chapter III) predicts that pure p-D_2 (J=1) should undergo a second order phase transition near 3K into either the pinwheel or herringbone phase depending upon the sign of V_c. It was not possible to predict an orientational ordering temperature for o-H_2 (J=1) without a more accurate value of Γ. Although MFT can be expected to be quite good at predicting the symmetry of the ordered states, it is likely to predict transition temperatures that are too high because it ignores fluctuations. In fact in the early work no ordering was seen down to 1.2K.

O'Shea and Klein (1979) also made an estimate of the ordering temperature from their classical Monte Carlo calculations. They renormalized Γ in order to take into account quantum effects by comparing the experimental bulk hydrogen ordering temperature

with 3D classical Monte Carlo results. They then applied the same renormalization to their 2D Monte Carlo calculations to get a transition temperature of 1.0-1.5K depending upon the strength of the interaction with the substrate.

Encouraged, we constructed an 8.5 MHz continuous wave NMR spectrometer (described in Chapter VII) in order to extend our measurements down to .3K. Considerable effort was expended to attain adequate S:N ratios. Particularly troublesome was coherent interference induced by modulation of the magnetic field. It was found (Chapter VIII) that 90% J=1 H_2 undergoes a rapid orientational ordering transition into the pinwheel phase at .6K. NMR spectra of H_2 each required at least two hours of signal averaging so we did not determine whether or not the transition was first order. In contrast, the D_2 NMR spectrum underwent a smooth evolution down to .3K, becoming very broad and weak (Chapter IX). This behaviour is very puzzling and is not understood. Analysis of the D_2 spectra was severely hampered by poor S:N ratios: 5-20 h of signal averaging was used for the low temperature spectra. Some suggestions for improving the S:N ratios are contained in Chapter X. We were able to deduce values of V_c and Γ from the high temperature spectra. The D_2 spectra were analyzed in terms of MFT and the results agreed well with the values obtained earlier using the ^{4}He cryostat. For H_2 we were able to employ a high temperature expansion of the order parameters. It reduces to MFT if only terms up to first order in Γ/T are retained. Expanding as far as $(\Gamma/T)^3$, we

obtained values of $|V_c|$ and Γ similar to those found earlier but we were also able to ascertain that V_c was positive. Finally, NMR intensity measurements showed that conversion obeyed a first order rate equation, presumably being catalyzed by the Grafoil. These results are presented in Chapter V.

As well as describing the results of our experiments, this thesis was intended to serve as an operations manual for the NMR spectrometer and ^{3}He cryostat. Consequently it contains a considerable amount of detail concerning the operation of the system. For this reason the following sections could be omitted on a first reading: 5.1-5.3, 5.5, 6.1-6.4, 7.4, and 7.5. In addition, sections 3.3 and 3.4 contain details of the theory not essential to an understanding of the results. Section 10.1 contains a concise summary of the results. The reader may wish to peruse it after reading Chapters I and II in order to get a preview of the results.

Notes to Chapter I

1. Throughout this thesis "hydrogen" refers to H_2 and D_2.

2. The rotational angular momentum J of a hydrogen molecule may be either even (para-H_2 and ortho-D_2) or odd (ortho-H_2 and para-D_2). The J=0 and J=1 states are separated by 171 K (86 K) for H_2 (D_2) so that at low temperatures one would expect only the J=0 state to be occupied. However odd J to even J transitions (conversion) are very slow so in general one is working with a non-equilibrium mixture of J=0 and J=1 molecules.

3. Manufactured by Cabot Carbon Co. It is more heterogeneous than the Grafoil substrate (Union Carbide Corp.) used in the present work.

4. Throughout this thesis the "orientation of the molecular axes" will be referred to. However, according to quantum mechanics the axis of a molecule in a particular rotational state is not fixed in space: rather its orientational distribution is described by the molecular wave function. For J=0 molecules the wave functions are spherical. For J=1 molecules the wave functins are ellipsoidal. In that case the "orientation of the molecular axes" should be taken to mean the orientation of the symmetry axis of the wave function.

5. This result does not apply to registered phases. A good discussion of this subject is contained in section 7.3 of Dash (1975).

CHAPTER II

ORIENTATIONAL PROPERTIES OF HYDROGEN

2.1 Orientational Interactions

Even in the bulk solid or on the surface of graphite, hydrogen molecules can be modelled very well by free rotors. The free rotor energies E are given by

$$E = BJ\,(J+1) \qquad \text{(II-1)}$$

where B = 85.35 K (43.04 K) for H_2 (D_2) (Silvera, 1980). The difference in the values of B arises from the different moments of inertia. Since the J=1 state of H_2 (D_2) is 171 K (86.1 K) above the J=0 state, one would expect only the latter to have any significant population at liquid helium temperatures. However for homonuclear molecules conversion between odd and even J states may be very slow. For example, ^1H nuclei are fermions so the H_2 wave function must be antisymmetric with respect to their interchange. Rotational states with even parity must be combined with nuclear spin states with I=0, which have odd parity. Odd rotational states must have I=1. Similar arguments apply to D_2 except that deuterons are bosons so the rotational and nuclear spin states have the same parity. The states with the greatest spin degeneracy are labelled ortho; the others are para. These results are summarized in Table I. The factor g_J is the degeneracy of the nuclear spin states.

For homonuclear molecules, conversion requires a simul-

taneous change of parity of the spin and orbital states. On the surface of Grafoil conversion is quite slow: our measurements (Chapter V) give a rate of .40%/h for pure o-H_2 and .07 %/h for pure D_2 on one of our substrates. This has allowed us to study samples containing up to 97% J=1 molecules.

Table I: States of Hydrogen

Molecule	J	I	g_J
p-H_2	even	0	1
o-H_2	odd	1	3
o-D_2	even	0,2	6
p-D_2	odd	1	3

Provided that J is a good quantum number, the most general form of the interaction between two hydrogen molecules with orientations $\vec{\omega}_1'$ and $\vec{\omega}_2'$ with respect to the intermolecular axis $\vec{R}_{12}$ is a sum over J_1 and J_2 of terms of the form

$$V_{J_1J_2} = 4\pi\, \varepsilon_{J_1J_2}(R_{12}) \sum_m a_m\, Y_{J_1}^m(\vec{\omega}_1')\, Y_{J_2}^{m*}(\vec{\omega}_2') \qquad \text{(II-2)}$$

where Y_J^m is a spherical harmonic with the phase convention of Rose (1957). Only even values of J_1 and J_2 are required because each molecule has inversion symmetry. Transforming to an arbitrary reference frame $V_{J_1J_2}$ becomes

$$V_{J_1J_2} = 4\pi\, \varepsilon_{J_1J_2}(R_{12}) \sum_{m,n} a_{mn}\, Y_{J_1}^m(\vec{\omega}_1)\, Y_{J_2}^n(\vec{\omega}_2)\, Y_{J_1+J_2}^{m+n*}(\vec{\Omega}_{12}) \qquad \text{(II-3)}$$

where $\vec{\omega}_1$, $\vec{\omega}_2$, and $\vec{\Omega}_{12}$ are the orientations of the two molecules and the internuclear axis.

To the extent that J is a good quantum number, then for each pair of J=1 molecules, only matrix elements of V_{J1J2} with J_1 and J_2 equal to 0 or 2 will be non-zero. Many body interactions will be ignored. The anisotropic part of the Hamiltonian is then

$$H = \sum_i H_c^i + \sum_{i<j} H_{EQQ}^{ij} \qquad \text{(II-4a)}$$

$$= \sum_i (8\pi/5) \sum_m Y_2^m(\vec{\omega}_i) \sum_j B(R_{ij}) Y_2^{m*}(\vec{\Omega}_{ij})$$

$$+ \sum_{i<j} \sum_{m,n} \zeta_{m,n}(R_{ij}) Y_2^m(\vec{\omega}_i) Y_2^n(\vec{\omega}_j) Y_4^{m+n*}(\vec{\Omega}_{ij}) \qquad \text{(II-4b)}$$

The one body term is known as the crystal field term; it arises from Van der Waals interactions between the hydrogen molecules. Now consider a system of adsorbed, J=1 hydrogen molecules in the $\sqrt{3}$ x $\sqrt{3}$ phase. If we take the z axis to be normal to surface, then when the crystal field interactions of a molecule are summed over all of its neighbours only the m=0 term will survive because the z axis is a six-fold axis of symmetry. There will also be a contribution to the crystal field V_c from the interaction of the molecule with the surface. The anisotropic Hamiltonian can be rewritten as

$$H = -(2/3)(5\pi)^{1/2} V_c \sum_i Y_2^o(\vec{\omega}_i)$$

$$+ \sum_{m,n} \sum_{i<j} \zeta_{m,n}(R_{ij}) Y_2^m(\vec{\omega}_i) Y_2^n(\vec{\omega}_j) Y_4^{m+n*}(\vec{\Omega}_{ij}) \qquad \text{(II-5a)}$$

The hydrogen contribution to V_c is

$$V_c^H = -(3/5)(16\pi/5)^{1/2} \sum_j B(R_{ij}) Y_2^o(\vec{\Omega}_{ij}) \qquad \text{(II-5b)}$$

The main contribution to the two body term is from the electrostatic quadrupole-quadrupole (EQQ) interaction (Silvera, 1980; Van Kranendonk, 1983).

It is useful to rewrite (II-5a) in terms of the second rank spherical tensor operators $T_2^m(J)$ defined by

$$T_2^{\,o} = (5/16\pi)^{1/2}(3J_z^{\,2}-2) \qquad \text{(II-6a)}$$

$$T_2^{\pm 1} = \mp(15/32\pi)^{1/2}(J_{\pm}J_z+J_zJ_{\pm}) \qquad \text{(II-6b)}$$

$$T_2^{\pm 2} = (15/32\pi)^{1/2}J_{\pm}^{\,2} \qquad \text{(II-6c)}$$

It is a consequence of the Wigner-Eckart theorem (Rose, 1957) and our choice of normalization that within the J=1 manifold the matrix elements of the spherical harmonics and spherical tensors are equal. The Hamiltonian for the J=1 system (II-5a) is then

$$H=(1/3)(16\pi/5)^{1/2}V_c\sum_i T_2^{\,o}(\vec{J}_i) + \frac{4}{25}\sum_{i<j}\sum_{m,n}\zeta_{m,n}(R_{ij})T_2^{\,m}(\vec{J}_i) \times T_2^{\,n}(\vec{J}_j)\quad Y_4^{\,m+n*}(\vec{\Omega}_{ij}) \qquad \text{(II-7)}$$

If one considers only nearest neighbour interactions and a rigid lattice, then the coefficient ζ_{mn} is

$$\zeta_{mn}(R_{ij}) = (20\pi/9)(70\pi)^{1/2}\,\Gamma_o C(224;mn) \qquad \text{(II-8)}$$

where C(224; mn) is a Clebsch-Gordon coefficient and Γ_o is the nearest neighbour quadrupole coupling constant. For a pair of molecules separated by a distance R_o, each with quadrupole moment eQ, Γ_o is given by

$$\Gamma_o = \frac{6e^2Q^2}{25R_o^{\,5}} \qquad \text{(II-9)}$$

For the $\sqrt{3}$ x $\sqrt{3}$ structure on graphite, R_o = 4.26 Å so Γ_o = .528 K (.510 K) for H_2 (D_2).

In the bulk solid the coupling constant deduced from experiment has been found to be smaller than Γ_o by a factor of .87 for both H_2 and D_2 (Silvera, 1980). Originally it was felt that the reduction was due to zero point motion of the molecular centres and could be accounted for by averaging $Y_4^o(\vec{\Omega}_{ij})/R_{ij}^5$ weighted by the pair distribution function: Harris (1970a) showed that the averaging process changes the magnitude of the effective EQQ interaction but not its form. The pair distribution function can be obtained from the ground state wave function of the phonons. Γ is renormalized downwards because short range correlations needed to minimize hard core repulsion cause the pair distribution function to fall off more rapidly for small separations than for large. The main difficulty in the calculation is that the phonon wave function is not known very well. More recent calculations (Goldman, 1979) indicate that zero point motion alone is insufficient to account for the reduction of Γ; it is also necessary to take into account Van der Waals contributions to the two body term of (II-7). For the 2D system zero point motion is likely to be even greater than in 3D, leading to greater renormalization.

2.2 Hydrogen Molecules on a Surface

The remainder of this chapter will be restricted to a consideration of the pararotational (disordered) state. In that

state each molecule is in a site of six-fold symmetry. For J=1 molecules the Wigner-Eckart theorem implies that this is equivalent to axial symmetry. The Hamiltonian of (II-7) will cause the J=1 state to be split by an energy Δ into an $m_J=0$ and doubly degenerate $m_J=\pm 1$ states. The $m_J=0$ state has a prolate spheroidal wave function with its z axis normal to the substrate; the $m_J=\pm 1$ states have oblate spheroidal wave functions. Naively one can think of these as molecules standing up or lying down on the surface. The system can be described by an orientational order parameter σ defined by

$$\sigma=(5\pi)^{1/2}\langle Y_2^o(\vec{\omega}_i)\rangle=-(4\pi/5)^{1/2}\langle T_2^o(\vec{J}_i)\rangle =-(1/2)\langle 3J_{iz}^2-2\rangle \quad \text{(II-10)}$$

The brackets < > indicate a thermal average. An equivalent expression for σ can be obtained in terms of the fractional population p_o of the $m_J=0$ state

$$\sigma= (3/2)(p_o-1/3) \quad \text{(II-11)}$$

As $T\to\infty$, all three m_J states become equally populated so $\sigma\to 0$. At T=0, $\sigma=1$ or $-1/2$ depending upon whether the ground state has $m_J=0$ or $m_J=\pm 1$. A plot of $|\sigma|$ versus T^{-1} is shown in Fig. 5. In the high temperature limit it is easy to obtain an expression for σ since the EQQ interactions are averaged out by molecular reorientation. Neglecting the second term in (II-7), the energies of the m_J states are

$$E_o= (V_c/3)\langle Y_1^o|3J_z^2-2|Y_1^o\rangle$$

$$=-(2/3)V_c \quad \text{(II-12a)}$$

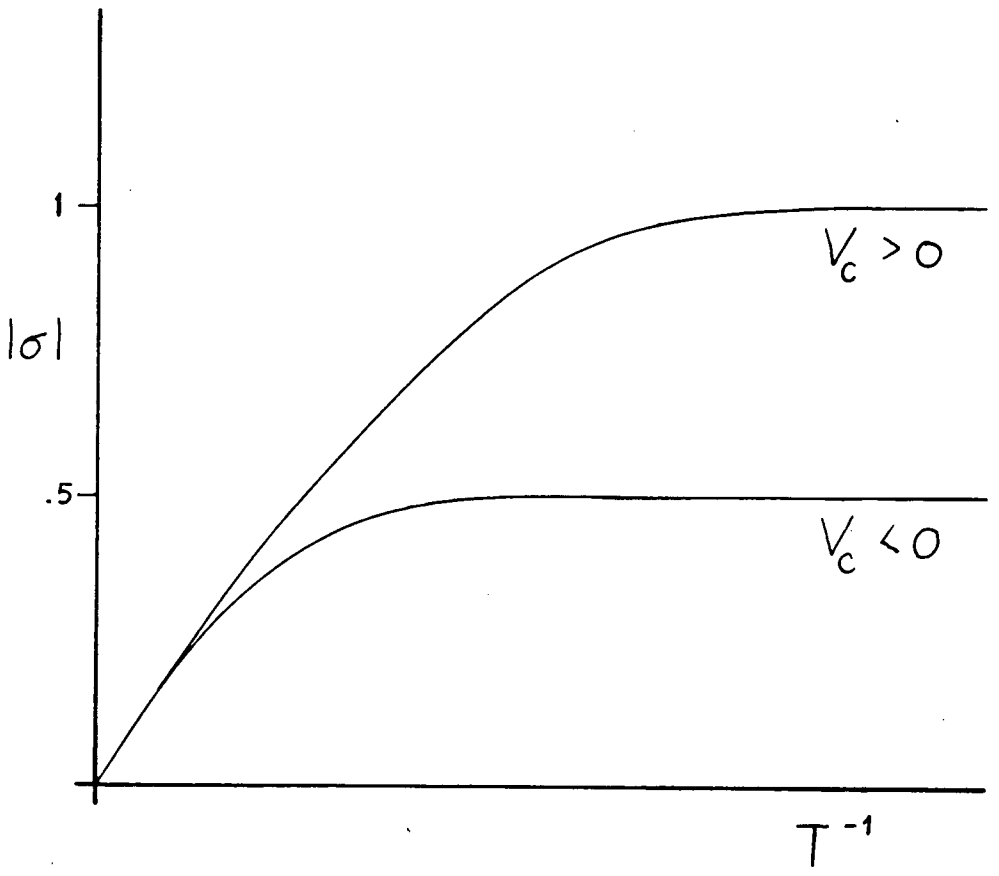

Fig. 5 $|\sigma|$ versus 1/T for the disordered state. σ and V_c have the same sign.

$$E_{\pm 1} = (V_c/3) \langle Y_1^{\pm 1} | 3J_z^2 - 2 | Y_1^{\pm 1} \rangle$$

$$= (1/3)V_c \qquad \text{(II-12b)}$$

The energy gap Δ between the ground and excited states is temperature independent and equal to $|V_c|$.

The populations of the m_J states are related by the Boltzmann factor so

$$p_o = \{1 + 2\exp(\mp\Delta/kT)\}^{-1} \qquad \text{(II-13)}$$

where the upper sign is for $V_c>0$ and the lower for $V_c<0$. In the high temperature limit, putting $\Delta = |V_c|$, expanding the exponential and retaining only the first order term

$$p_o \simeq (1/3)\ [1+(2/3)\ V_c/kT] \qquad \text{(II-14)}$$

Substitution into (II-11) gives

$$\sigma = V_c/3kT \qquad \text{(11-15)}$$

In Chapter IV it is shown that the NMR spectrum gives a direct determination of $|\sigma|$. Therefore a measurement of the temperature dependence of the spectrum gives $|V_c|$.

If the EQQ interaction is included, then within the mean field approximation Δ becomes temperature dependent and is given by

$$\Delta = V_c - 27\Gamma\sigma/2 \qquad \text{(Harris and Berlinsky, 1979)} \qquad \text{(II-16)}$$

The molecular field always opposes the crystal field since σ and V_c have the same sign. The crystal field attempts to align all of the molecules in the same direction whether it be standing up or lying down. This alignment competes with the

EQQ interaction which favours a "T" configuration for each pair.

A system of J=1 hydrogen molecules is analogous to an antiferromagnetic system with spin S=1 (Harris, 1971). The J=0 molecules are analogous to non-magnetic ions. Hydrogen resembles a particularly simple magnetic alloy in which all of the constituents have the same mass and force constants.

In the magnetic case the order parameter σ is the sublattice magnetization

$$\sigma = \langle S_z \rangle \qquad \text{(II-17)}$$

This definition is not suitable for hydrogen because if one has a non-degenerate ground state and time reversal symmetry is preserved, the ground state wave function is real and the expectation value of the momentum is zero; it is said to be quenched (Van Vleck, 1932). Even in the presence of a magnetic field the assumption of time reversal symmetry is a good approximation since the magnetic interactions of a hydrogen molecule ($\sim$1mK) are much smaller than the orientational interactions ($\sim$1K). Having effective axial symmetry, the crystal field leaves the $m_J=\pm 1$ states degenerate but at sufficiently low temperatures the symmetry will be broken by the EQQ interaction so the ground state will be non-degenerate and $\langle \vec{J} \rangle = 0$. For hydrogen the order parameters are defined in terms of the second rank tensorial components of angular momentum, the quadrupole moments. There are nine of these of which five are independent since the tensor is symmetric. One of the order parameters σ was defined in (II-10); the remaining four are

introduced in Chapter III. The crystal field of hydrogen is analogous to an applied magnetic field experienced by antiferromagnets: both try to align the molecules in the same direction. Experimentally there is a crucial difference in that the crystal field is determined by the substrate and the neighbouring molecules whereas an applied magnetic field can easily be controlled. For hydrogen σ will normally be non-zero in the pararotational state (analogous to the paramagnetic state) because the crystal field cannot be "turned off". In the absence of a magnetic field, the Hamiltonian of the antiferromagnets is invariant under the transformation $S_z \rightarrow -S_z$: above the transition temperature $\langle S_z \rangle = 0$.

The EQQ and antiferromagnetic exchange interactions are also analogous but once again there are some important differences. The former favours a "T" configuration of the molecular axes but the latter attempts to align them antiparallel. Also, the quadrupole coupling constant Γ can be calculated with reasonable accuracy whereas the exchange integral is normally a phenomenological parameter. Finally, the EQQ interaction falls off as R^{-5} but the exchange interaction has a very short range. Arguments based on the Ginzburg Criterion (Pfeuty and Toulouse, 1977) show that the longer the range of forces, the narrower the critical region will be: fluctuations in the order parameter will be reduced as more neighbouring molecules are able to interact with a given molecule. For example, in a superconductor there is no hope

of seeing the critical region because Cooper pairs interact over several thousand angstroms.

CHAPTER III

ORIENTATIONAL ORDERING

3.1 Introduction

This chapter contains a discussion of the application of mean field theory (MFT) to the study of the orientationally ordered states of an hexagonal lattice of interacting quantum quadrupoles (Harris and Berlinsky, 1979). In MFT the interactions of a molecule with its neighbours are replaced by an interaction with an average molecular field; it ignores the effects of short range correlations between pairs of molecules. Consequently one expects the mean field transition temperature to be too high. In 3D it would typically be too large by a factor of two. For bulk H_2 (D_2) the experimental and mean field ordering temperatures are 2.8 K (3.8 K) and 7.3 K (9.0 K) respectively (Silvera, 1980). However, MFT does quite well at predicting the symmetry of the ordered states since once long range order has been established the major weakness of the theory is of secondary importance. For bulk hydrogen, MFT predicts the ordered structure correctly. For these reasons we will concentrate on the structure of the ordered phases rather than the temperature dependence of the order parameters.

Harris and Berlinsky tackled the problem in two ways. The first was a numerical relaxation method based on the work of James (1968), who had applied it to bulk hydrogen. The second was an analytic method which could be formulated exactly if one

assumed a structure for the ordered state, or in terms of a Landau expansion of the free energy if one did not. The relaxation method was used to elucidate the general features of the phase diagram and to study the first order transitions. The analytic approach was used to answer more detailed questions about the structure of the phases. The Landau expansion is valid in the neighbourhood of a second order phase transition, a region where the relaxation method converges slowly.

Both approaches included the crystal field and EQQ interactions in the Hamiltonian. A rigid lattice of J=1 molecules with only nearest neighbour interactions was assumed. The mean field approximation is equivalent to writing the density matrix ρ as a direct product of the single particle density matrices, ρ_i, i.e.,

$$\rho = \prod_i \rho_i \qquad \text{(III-1)}$$

The best approximation for ρ is then obtained by choosing the ρ_i's so that they minimize the free energy F, which is given by

$$F(\rho)=\mathrm{Tr}(\rho H) + T\{\mathrm{Tr}(\rho \ln \rho)\} \qquad \text{(III-2)}$$

where H is the anisotropic Hamiltonian given by (II-7). The density matrices ρ_i can be expressed in terms of the order parameters [see (III-5) below] and, in the Landau expansion, F is expanded in powers of the order parameters. Alternatively one can obtain the ρ_i self-consistently by solving the equation

$$\rho_i = \exp(-\beta H_{\mathrm{eff}}^{\,i})/\mathrm{Tr}\,[\exp(-\beta H_{\mathrm{eff}}^{\,i})] \qquad \text{(III-3)}$$

where $\beta = 1/(kT)$ and H^i_{eff} satisfies

$$H_{eff}{}^{i} = H_c{}^{i} + Tr' \left(\sum_j H_{EQQ}{}^{ij} \prod_{k \neq i} \rho_k \right) \qquad \text{(III-4)}$$

The prime indicates that the trace is over the states of all molecules k such that $k \neq i$. In the relaxation method one takes an nxn lattice with periodic boundary conditions and assigns a value to each ρ_i. The value of n must be at least large enough to contain all of the sublattices of the ordered state. The effective Hamiltonian H^i_{eff} is then found using (III-4) and new values of ρ_i are obtained from (III-3). The process is repeated and hopefully converges. In the analytic method a sublattice structure is assumed and all of the ρ_i's on each sublattice are set equal. If two sublattices are related by a symmetry operation the number of independent ρ_i's is further reduced; in fact there are at most two for this system. (III-3) and (III-4) are then solved simultaneously. The same reduction in the number of independent ρ_i's can be made for the Landau expansion if the sublattice structure is assumed.

Provided that there is time reversal invariance, the second rank spherical tensor operators $T_2{}^m(\vec{J})$ defined by (II-6) form a complete set of dynamical variables for a system of J=1 molecules. The (real) order parameters $\sigma_i, \mu_i, \eta_i, \chi_i$, and ϕ_i are defined in terms of the thermal averages of the $T_2{}^m(\vec{J}_i)$'s by

$$\sigma_i = -(4\pi/5)^{1/2} \langle T_2{}^0(\vec{J}_i) \rangle \qquad \text{(III-5a)}$$

$$\mu_i \exp(\pm i\chi_i) = \mu_i{}^{\pm} = \pm(8\pi/15) \langle T_2{}^{\pm 1}(\vec{J}_i) \rangle \qquad \text{(III-5b)}$$

$$\eta_i \exp(\pm i2\phi_i) = \eta_i^{\pm} = -(24\pi/5)\langle T_2^{\pm 2}(\vec{J}_i)\rangle \qquad \text{(III-5c)}$$

The single particle density matrix is Hermitian and its trace is one. Its most general form is

$$\rho_i = \begin{bmatrix} (1-\sigma_i)/3 & -(\mu_i/\sqrt{2})\exp(-i\chi_i) & -(\eta_i/3)\exp(-i2\phi_i) \\ -(\mu_i/\sqrt{2})\exp(i\chi_i) & (1+2\sigma_i)/3 & (\mu_i/\sqrt{2})\exp(-i\chi_i) \\ -(\eta_i/3)\exp(i2\phi_i) & (\mu_i/\sqrt{2})\exp(i\chi_i) & (1-\sigma_i)/3 \end{bmatrix} \qquad \text{(III-6)}$$

The rows and columns are labelled from left to right and top to bottom by m=1,0, and -1 respectively.

For some values of the order parameters, it is easy to picture the average orientations of the molecular wave functions. If $\mu_i=\eta_i=0$ then the $Y_1^m(\vec{\omega}_i)$'s are eigenfunctions so there is axial symmetry about the z axis, which is normal to the surface. The molecules tend to stand up if $\sigma_i>0$ and lie down if $\sigma_i<0$. If only $\mu_i=0$, the eigenfunctions are Y_1^0 and $(e^{-i\phi_i} Y_1^1 \pm e^{i\phi_i} Y_1^{-1})/\sqrt{2}$ so one of the principal axes is along z as before and one of the others makes an angle ϕ_i with respect to the x axis. If $\mu_i\neq 0$, Y_1^0 is no longer an eigenfunction and the z axis is not a principal axis.

It is not practical from a computational point of view to allow all of the ρ_i's to be different. In any event, one expects that there will be a small number of sublattices with the ρ_i's the same on each sublattice.

If we assume that the ground state for each sublattice is non-degenerate, then at T=0 all of the molecules on a sublattice

will be aligned parallel to some axis. This can be seen from the following argument. At T=0, all of the molecules on sublattice i are in their ground state ψ_i and $\rho_i = |\psi_i><\psi_i|$.

Since the Hamiltonian is real, we can take ψ_i to be real. A set of real, orthonormal basis functions Φ_α can be defined by

$$\Phi_1(\vec{\omega}_i) = -(Y_1^1(\vec{\omega}_i) - Y_1^{-1}(\vec{\omega}_i))/\sqrt{2} \qquad \text{(III-7a)}$$

$$\Phi_2(\vec{\omega}_i) = i(Y_1^1(\vec{\omega}_i) + Y_1^{-1}(\vec{\omega}_i))/\sqrt{2} \qquad \text{(III-7b)}$$

$$\Phi_3(\vec{\omega}_i) = Y_1^0(\vec{\omega}_i) \qquad \text{(III-7c)}$$

These functions all have the same form but they are oriented along the x, y, and z axes which are parallel to the unit vectors $\hat{x}_1$, $\hat{x}_2$, and $\hat{x}_3$. The $\Phi_\alpha(\vec{\omega}_i)$'s are proportional to the direction cosines $x_\alpha(\vec{\omega}_i)$ of the unit vector $\vec{\omega}_i$ along these axes:

$$\Phi_\alpha(\vec{\omega}_i) = (3/4\pi)^{1/2} x_\alpha(\vec{\omega}_i) \qquad \text{(III-8)}$$

The ground state is a linear combination of the basis functions:

$$\psi_i = \sum_\alpha \gamma_\alpha^i \Phi_\alpha(\vec{\omega}_i) \qquad \text{(III-9)}$$

If ψ_i is normalized, the γ_α^i satisfy

$$\sum_\alpha (\gamma_\alpha^i)^2 = 1 \qquad \text{(III-10)}$$

This means that the γ_α^i's can be taken to be the direction cosines of some unit vector $\hat{z}^i$ with respect to the x, y, and z axes. The component $z^i(\vec{\omega}_i)$ of $\vec{\omega}_i$ along $\hat{z}^i$ is

$$z^i(\vec{\omega}_i) = \sum_\alpha \gamma_\alpha^i x_\alpha(\vec{\omega}_i) \qquad \text{(III-11)}$$

Substituting (III-8) and (III-11) into (III-9) gives

$$\psi_i = (3/4\pi)^{1/2} z^i(\vec{\omega}_i) = Y_1^0(\theta_i) \qquad \text{(III-12)}$$

where θ_i is the angle between $\hat{z}^i$ and $\vec{\omega}_i$. Therefore at T=0, the wave functions of all molecules on sublattice i are aligned parallel to $\hat{z}^i$. This corresponds to $\mu_i=\eta_i=0$ in the principal axis frame.

In the crystal reference frame (x, y, z), the order parameters can be expressed in terms of the orientation (θ_i,ϕ_i) of $\hat{z}_i$ by

$$\sigma_i=(3\cos^2\theta_i-1)/2 \qquad \text{(III-13a)}$$

$$\mu_i=\sin\theta_i\cos\theta_i=[(2/9)(1-\sigma_i)(1+\sigma_i)]^{1/2} \qquad \text{(III-13b)}$$

$$\eta_i=\sin^2\theta_i = 1-\sigma_i \qquad \text{(III-13c)}$$

$$\chi_i = \phi_i \qquad \text{(III-13d)}$$

Only two independent variables σ_i and ϕ_i are needed.

3.2 Orientationally Ordered States

The orientational phase diagram obtained by Harris and Berlinsky as a function of V_c/Γ and T/Γ is shown in Fig. 6.

The high temperature pararotational phase has a single sublattice characterized by

$$\sigma_i= \sigma_o \qquad \text{(III-14a)}$$

$$\mu_i= \eta_i = 0 \qquad \text{(III-14b)}$$

Unlike the other phases, it has no long range orientational order except for that induced by the substrate.

If $V_c<<-kT$, then all of the molecular axes are constrained to lie parallel to the surface. The EQQ interaction determines their azimuthal orientations. The result is the two sublattice herringbone phase shown in Fig. 3(a) with order

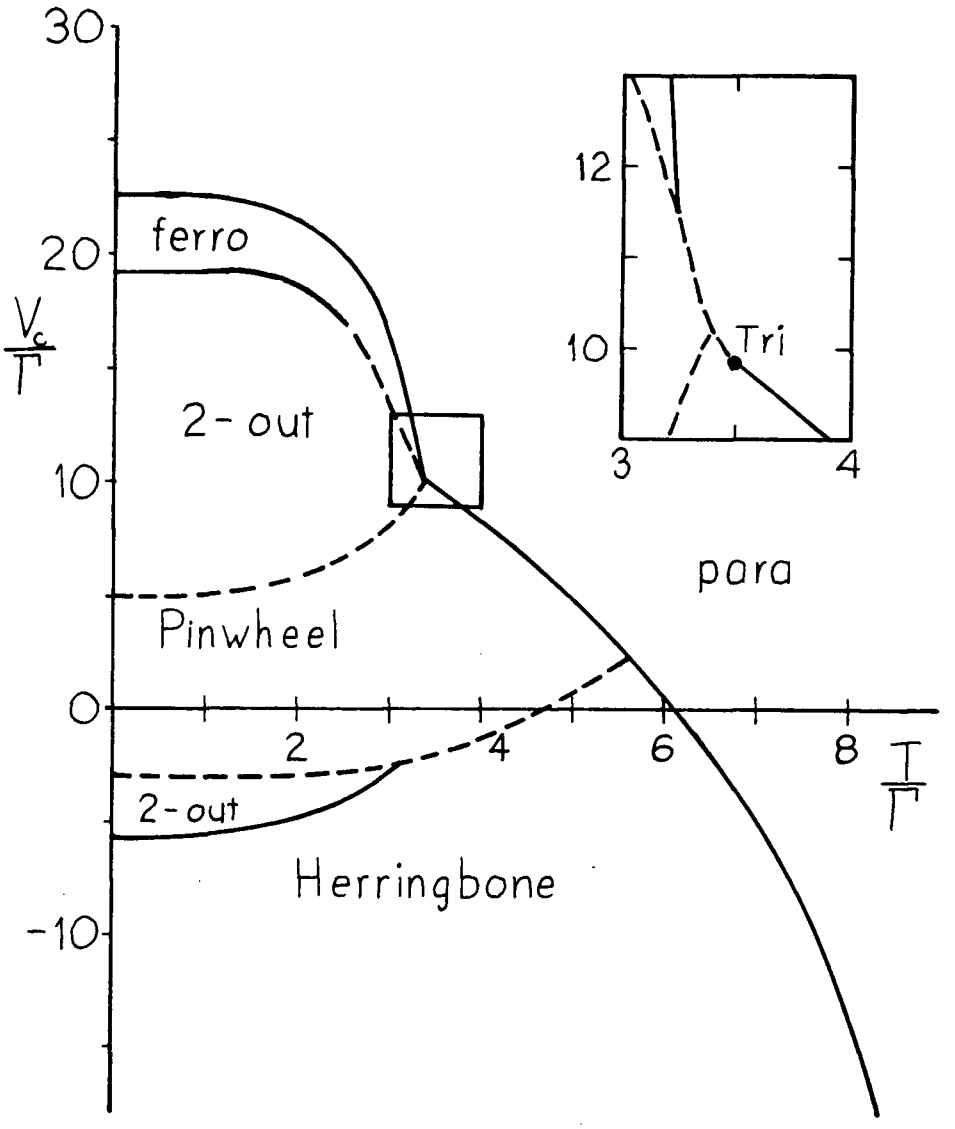

Fig. 6 Orientational phase diagram, V_c/T versus T/T, for quantum quadrupoles on a hexagonal lattice, deduced by MFT. The dashed lines are first order phase boundaries and the solid lines are continuous. The region near the tricritical point is shown with an expanded scale at the upper right.

parameters

$$\sigma_1=\sigma_2=\sigma_o \qquad \text{(III-15a)}$$

$$\mu_i=0 \qquad \text{(III-15b)}$$

$$\eta_1=\eta_2=\eta_o \qquad \text{(III-15c)}$$

$$\phi_1=180^o-\phi_2=45^o \qquad \text{(III-15d)}$$

As V_c increases there is a second order phase transition to the 2-out phase. This is a two sublattice phase similar to the herringbone phase except that μ is no longer zero so the molecular axes tilt out of the plane. The order parameters are

$$\sigma_1=\sigma_1=\sigma_o \qquad \text{(III-16a)}$$

$$\mu_1=\mu_2=\mu_o \qquad \text{(III-16b)}$$

$$\eta_1=\eta_2=\eta_o \qquad \text{(III-16c)}$$

$$\chi_1=180^o-\chi_2=\chi_o \qquad \text{(III-16d)}$$

$$\phi_1=180^o-\phi_2=\phi_o \qquad \text{(III-16e)}$$

If V_c increases further, there is a first order transition to the four sublattice pinwheel phase in which a molecule on sublattice 1 stands up and all of its neighbours lie down [Fig.3(b)]. The order parameters are

$$\sigma_1>0,\ \sigma_2=\sigma_3=\sigma_4<0 \qquad \text{(III-17a)}$$

$$\mu_i=0 \qquad \text{(III-17b)}$$

$$\eta_1=0,\ \eta_2=\eta_3=\eta_4 \qquad \text{(III-17c)}$$

$$\phi_2=\phi_3-60^o=\phi_4-120^o \qquad \text{(III-17d)}$$

As V_c increases again, there is a first order phase transition back into the 2-out phase. Next there is a second order transition to the single sublattice ferrorotational phase, which is characterized by

$$\sigma_i=\sigma_o \qquad \text{(III-18a)}$$

$$\mu_i=\mu_o \qquad \text{(III-18b)}$$

$$\eta_i=\eta_o \qquad \text{(III-18c)}$$

$$\chi_i=\phi_i=\phi_o \qquad \text{(III-18d)}$$

All of the molecules are oriented in the same direction but their azimuthal angle is arbitrary. Clearly the entropy does not depend on ϕ_o and it can be shown that for a single sublattice phase the energy cannot depend on it either. This phase is analogous to the planar XY model for spins which has a Hamiltonian of the form

$$H=-\sum_{ij} J_{ij}\vec{S}_i\cdot\vec{S}_j \qquad \text{(III-19)}$$

where $J_{ij}^z=0$ and $J_{ij}^x = J_{ij}^y \neq 0$. Unlike the other ordered states, the libron[1] spectrum for this state has no gap because of the continuous symmetry.

For further increases in V_c, there is a second order transition to the pararotational phase. Here $\sigma_i>0$ and all of the molecules are essentially standing up.

In the pinwheel and herringbone phases, at T=0 the order parameters are independent of V_c/Γ. This is not the case for the 2-out and ferrorotational phases. In the 2-out phase at T=0, MFT gives

$$\sigma_o=(164V_c/\Gamma-555)/2955 \qquad \text{(III-20)}$$

$$\cos(\phi_1-\phi_2)=2(1+2\sigma_o)/[41(1-\sigma_o)] \qquad \text{(III-21)}$$

and in the ferrorotational phase

$$\sigma_o=1/7 + 4V_c/(105\Gamma) \qquad \text{(III-22)}$$

3.3 The Landau Expansion

The ordered phases will now be explored in more detail by making a Landau expansion of the free energy F. We define the deviations $u_{\alpha i}$ of the order parameters from their equilibrium values in the pararotational state by

$$u_{1i}=\eta_i \cos 2\phi_i \tag{III-23a}$$

$$u_{2i}=\eta_i \sin 2\phi_i \tag{III-23b}$$

$$u_{3i}=\sigma_i-\sigma_{eq} \tag{III-23c}$$

$$u_{4i}=\mu_i \cos\chi_i \tag{III-23d}$$

$$u_{5i}=\mu_i \sin\chi_i \tag{III-23e}$$

where σ_{eq} is the equilibrium value of σ_i in the absence of long range cooperative ordering. It is given by (II-11), (II-13), and (II-16). To second order in the $u_{\alpha i}$'s the free energy expansion for N molecules is

$$F/(N\Gamma)=F_{eq}/(N\Gamma) + (1/2)\sum_{\alpha=1}^{5}\sum_{\beta=1}^{5}\sum_{\vec{q}}\{\chi^{-1}(\vec{q})\}_{\alpha\beta}u_\alpha^*(\vec{q})u_\beta(\vec{q}) \tag{III-24}$$

where $u_\alpha(\vec{q})=u_\alpha^*(-\vec{q})=N^{-1}\sum_i u_{\alpha i}\exp(i\vec{q}\cdot\vec{r}_i)$ (III-25)

F_{eq} = equilibrium free energy in the absence of cooperative ordering

$$= N\Gamma\{(9/2)\sigma_{eq}^2 - (2/3)(V_c/\Gamma)\sigma_{eq} + (kT/3\Gamma) \times\{3\ln 3 + (1+2\sigma_{eq})\ln(1+2\sigma_{eq}) - 2(1-\sigma_{eq})\ln(1-\sigma_{eq})\}\} \tag{III-26}$$

and $\chi^{-1}(\vec{q})$ is the inverse susceptibility. It does not couple σ_i and η_i on one hand and μ_i on the other. The normal modes of the system $Y_k(\vec{q})$ (k = 1,2,...,5) are found by diagonalizing $\chi^{-1}(\vec{q})$ for each $\vec{q}$ to get the eigenvectors

$x_\alpha{}^k(\vec{q})$ and the corresponding eigenvalues $\Lambda^k(\vec{q})$ since

$$Y_k(\vec{q}) = \sum_\alpha x_\alpha^k(\vec{q})\, u_\alpha(\vec{q}) \qquad \text{(III-27)}$$

In terms of the normal modes the free energy is

$$F/(N\Gamma) = F_{eq}/(N\Gamma) + (1/2)\sum_{k=1}^{5} \sum_{\vec{q}} \Lambda^k(\vec{q}) |Y_k(\vec{q})|^2 \qquad \text{(III-28)}$$

The entropy terms in (III-24) are all positive and contribute only to the diagonal elements. At high temperatures the entropy terms will dominate so the $\Lambda_k(\vec{q})$'s will be all positive. A second order phase transition will occur if one of the $\Lambda^k(\vec{q})$'s goes to zero for some $\vec{q}$ at a temperature T_c. If that eigenvalue is labelled k=1, then the critical order parameter is determined by $x^1_\alpha(\vec{q})$. The sublattices of the ordered state are determined by $\vec{q}$ and the orientations of the molecular axes by $x_\alpha{}^1(\vec{q})$. We will only consider $\vec{q}$ vectors that are points of high symmetry in the first Brillouin zone.[2] This means that the superlattice will be commensurate so the periodicities of interest will be temperature independent. Domany et al (1978) have found that for a triangular lattice (space group P6mm) the only temperature independent $\vec{q}$ vectors for which $\Lambda_k(\vec{q})$ can go to zero are 0, $\vec{Q}_{Ai}$ and $\vec{Q}_{Bi}$, which are shown in Fig. 7 and defined by

$$\vec{Q}_{A1}=q_o\,\hat{j},\ \vec{Q}_{A2}=q_o(\sqrt{3}\hat{i}-\hat{j})/2,\ \vec{Q}_{A3}=(-\sqrt{3}\hat{i}-\hat{j})/2 \qquad \text{(III-29)}$$

$$\vec{Q}_{B1}=-\vec{Q}_{B2}=(4\pi/3a)\hat{i} \qquad \text{(III-30)}$$

where a = lattice parameter = 4.26 $\mathring{A}$ and $q_o = (2\pi/a\sqrt{3})$.

For modes which couple η_i and $\sigma_i - \sigma_{eq}$, the eigenvalues which go to zero first as T decreases have $\vec{q} = \vec{Q}_{Ai}$. The corresponding eigenvectors are

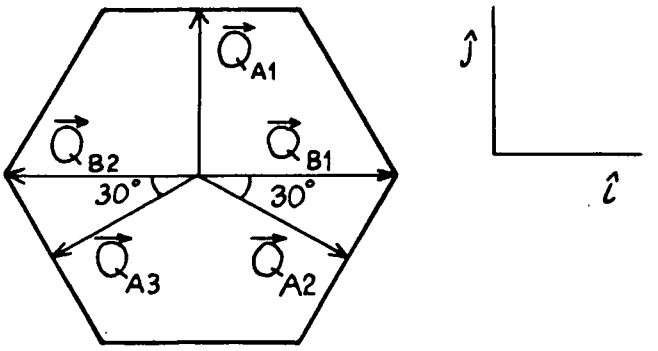

Fig. 7 The first Brillouin zone for a hexagonal lattice and the only temperature independent wave vectors that can produce soft modes.

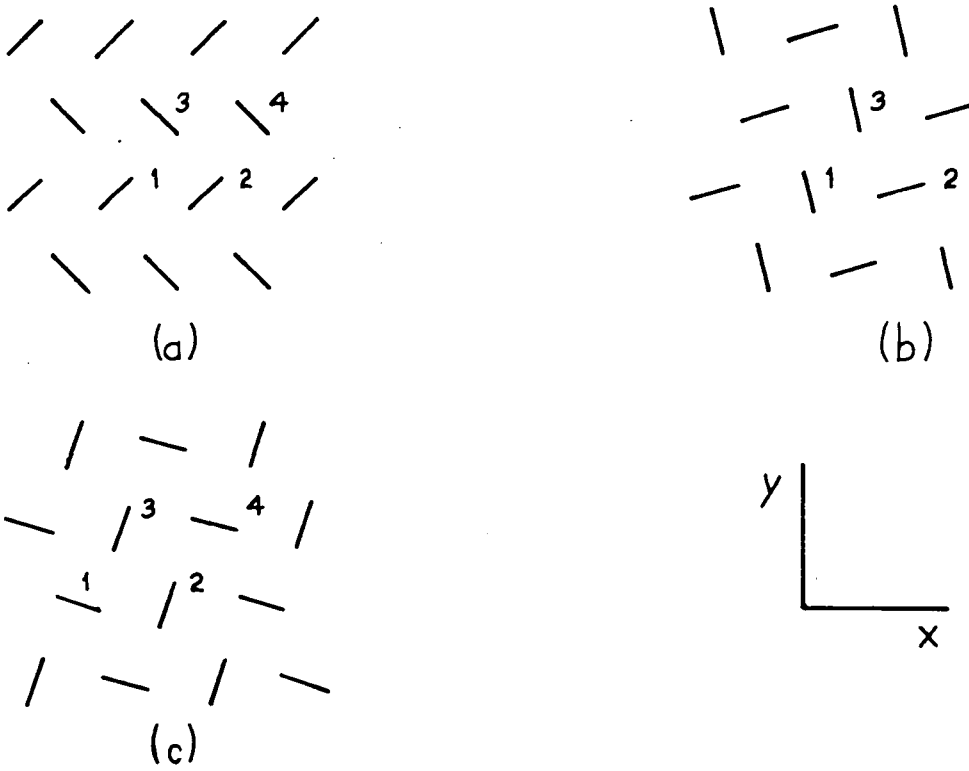

Fig. 8 The structure of the ordered states that arise when the eigenvalues for the modes corresponding to the $\vec{Q}_{Ai}$ go soft. (a) $\vec{Q}_{A1}$. (b) $\vec{Q}_{A2}$. (c) $\vec{Q}_{A3}$. They transform into each other by 120° rotations.

$$\vec{x}^1(\vec{Q}_{A1})=(0,1,0,0,0) \qquad \text{(III-31a)}$$

$$\vec{x}^1(\vec{Q}_{A2})=(-\sqrt{3},-1,0,0,0)/2 \qquad \text{(III-31b)}$$

$$\vec{x}^1(\vec{Q}_{A3})=(\sqrt{3},-1,0,0,0)/2 \qquad \text{(III-31c)}$$

The normal modes will be denoted by $y_i = Y_1(\vec{Q}_{Ai})$.

The superlattices corresponding to the $\vec{Q}_{Ai}$'s are shown in Fig. 8. In the $\vec{Q}_{A1}$ mode, $x^1(\vec{Q}_{A1})$ has no component along η_x so $\phi_i=\pm 45°$. The phases of the eigenvectors of sublattices 2, 3, and, 4 relative to that of 1 are

$$\exp\{i\vec{Q}_{A1}\cdot(\vec{r}_2-\vec{r}_1)\}=1 \qquad \text{(III-32a)}$$

$$\exp\{i\vec{Q}_{A1}\cdot(\vec{r}_3-\vec{r}_1)\}=\exp\{i\vec{Q}_{A1}\cdot(\vec{r}_4-\vec{r}_1)\} =-1 \qquad \text{(III-32b)}$$

Molecules on sublattices 1 and 2 have the same orientations and those on 3 and 4 are rotated 90° with respect to them since

$$\eta_1 \sin 2\phi_1=\eta_2 \sin 2\phi_2=-\eta_3 \sin 2\phi_3=-\eta_4 \sin 2\phi_4 \qquad \text{(III-33)}$$

The superlattices for $\vec{Q}_{A2}$ and $\vec{Q}_{A3}$ are identical to that of $\vec{Q}_{A1}$ except that they are rotated by 120° and -120° respectively.

The eigenvalues $\Lambda^1(\vec{Q}_{Ai})$ (i=1,2,3) are all degenerate so any linear combination of their eigenvectors will give the same free energy. A particularly interesting normal mode that can be formed in this manner is

$$y_4= -(y_1+y_2+y_3)/\sqrt{3} \qquad \text{(III-34)}$$

There are seven other equivalent modes corresponding to all combinations of signs in front of y_1, y_2, and y_3. The order parameters, η_x and η_y, for various normal modes are tabulated in Table II.

Table II. Normal Modes

Order parameter	y_1	y_2	y_3	y_4
η_{1x}	0	$-\sqrt{3}/2$	$\sqrt{3}/2$	0
η_{1y}	1	$-1/2$	$-1/2$	0
η_{2x}	0	$\sqrt{3}/2$	$-\sqrt{3}/2$	0
η_{2y}	1	$1/2$	$1/2$	$-2/\sqrt{3}$
η_{3x}	0	$-\sqrt{3}/2$	$-\sqrt{3}/2$	1
η_{3y}	-1	$-1/2$	$1/2$	$1/\sqrt{3}$
η_{4x}	0	$\sqrt{3}/2$	$\sqrt{3}/2$	-1
η_{4y}	-1	$1/2$	$-1/2$	$1/\sqrt{3}$

For the y_4 mode, ϕ_1 is arbitrary and

$$\phi_2=-45^\circ, \quad \phi_3=-165^\circ, \quad \phi_4=-105^\circ. \tag{III-35}$$

This is the pinwheel structure of Fig. 3(b).

In order to see which mode is favoured, it is necessary to calculate the fourth order terms of F. There are no odd order terms since

$$F(u_{i1},\ldots,-u_{i\alpha},\ldots,u_{i5})=F(u_{i1},\ldots,u_{i\alpha},\ldots,u_{i5}) \tag{III-36}$$

for all α. To fourth order F has the form

$$F/(N\Gamma)=F_{eq}/(N\Gamma) + (1/2)\Lambda^1(\vec{Q}_{A1})(y_1^2+y_2^2+y_3^2) + A_4(y_1^2+y_2^2+y_3^2)^2 + B_4(y_1^2y_2^2+y_1^2y_3^2+y_2^2y_3^2) \tag{III-37}$$

Λ^1, A_4, and B_4 are all functions of temperature. The A_4 term is isotropic in the space of (y_1, y_2, y_3). If $B_4>0$ fluctuations along the six (1,0,0) directions (the faces of a

cube) are favoured. These correspond to the herringbone phase. If $B_4<0$, fluctuations along the eight (1,1,1) directions (the body diagonals of a cube) are favoured and ordering into the pinwheel phase occurs. The free energy given by (III-37) is said to have cubic anistropy.

If the fourth order term were always greater than zero, i.e., $3A_4 + B_4 > 0$, then there would be a continuous phase transition at a temperature T_η at which $\Lambda^1(\vec{Q}_{A1}) = 0$. The second order term would be zero at T_η. However if the fourth order term is negative at T_η, the transition will be first order and will occur at a temperature $T_\eta' > T_\eta$. This is shown in Fig. 9 where, for simplicity, we write F as a function of a single order parameter y

$$F = F_o(T) + a(T)y^2 + b(T)y^4 \qquad \text{(III-38)}$$

and $a(T_\eta)=0$. If $b(T_\eta) > 0$, the second and fourth order terms are both positive for $T>T_\eta$. Below T_η, a(T) becomes negative. Since the second order term is dominant near y=0, the value of $|y|$ which minimizes F increases continuously from y=0. If $b(T_\eta)<0$, F is a minimum at y=0 only down to T_η' defined by $b(T_\eta')=0$. Below T_η', the fourth order term becomes negative and F is minimized for $|y| \to \infty$. This is characteristic of a first order transition. In reality, F would contain higher order terms which would produce a minimum at a finite value of y.

It is also possible to have ordering when a mode involving μ_i rather than η_i and $\sigma_i - \sigma_{eq}$ goes soft. The softest mode has $\vec{q}=0$ and the eigenvalue is doubly degenerate with

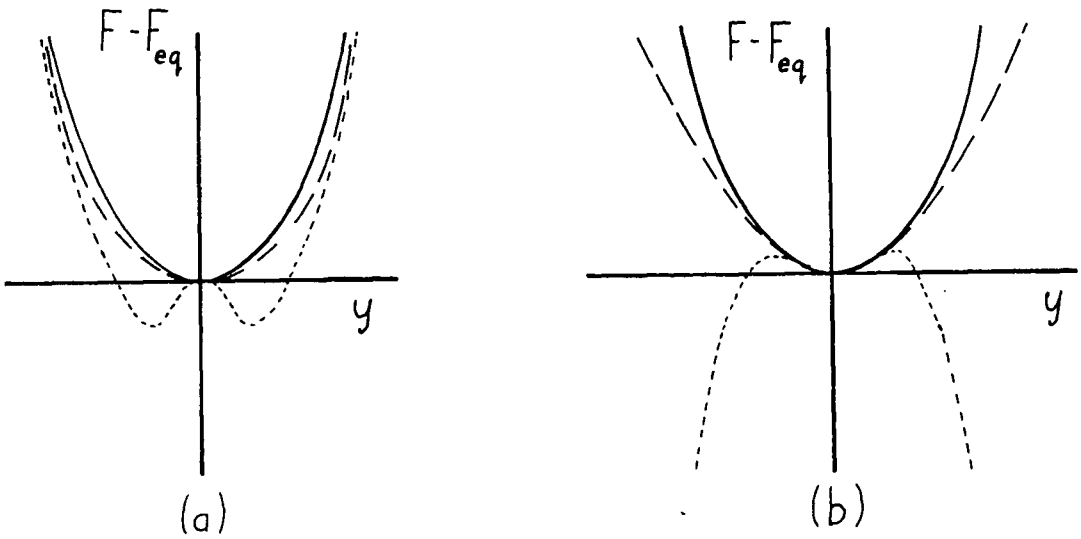

Fig. 9 The free energy $F-F_{eq}$ as a function of the order parameter y given by (III-38) near the transition temperature T_c. Here, $T>T_c$ for the solid line, $T=T_c$ for the dashed line, and $T<T_c$ for the dotted line. At T_η, a=o. In (a), $b(T_\eta)>0$, $T_c=T_\eta$, and the transition is continuous. In (b), $b(T_\eta)<0$ and $b(T_\eta')=0$. In this case, $T_c=T_\eta'$ and the transition is first order.

eigenvectors

$$x^1(0) = (0,0,0,1,0) \qquad \text{(III-39a)}$$

$$x^2(0) = (0,0,0,0,1) \qquad \text{(III-39b)}$$

The degeneracy implies that F is independent of χ. This is the ferrorotational phase. The continuous symmetry in χ is valid to any order in χ as mentioned in section 3.2.

3.4 Improvements to Mean Field Theory

The fact that MFT neglects fluctuations, which become very important near the critical point, might be expected to invalidate some of the results discussed above. Some of the problems that may arise will be considered in this section.

Monte Carlo Calculations

It has been stressed that the mean field transition temperature is expected to be too high so the temperature scale of Fig. 6 cannot be taken too seriously. In fact the transition temperature may go to zero for some or all of the ordered phases either because of quantum zero point motion or 2D fluctuations. The only other prediction of the transition temperature is based on the classical Monte Carlo calculations of O'Shea and Klein (1979). For a rigid cubic lattice of quadrupoles, they found a transition temperature of T_c (3D) = 11.5 Γ_o(3D). They then defined a constant γ_3 by $\gamma_3 = T_c(3D)/11.5$, using the experimentally observed transition temperature of bulk solid hydrogen.[3] The constant γ_3 was scaled with R_o^{-5} to

give the 2D constant γ_2, which was .13 K (.14 K) for H_2 (D_2) in the $\sqrt{3}$ x $\sqrt{3}$ solid phase on graphite. For $V_c/\Gamma_o=0$, O'Shea and Klein found ordering into the pinwheel state at T_c (2D)$\simeq 8\gamma_2$ = 1.0 K (1.1 K). For $V_c/\Gamma_o=-\infty$, they found ordering into the herringbone state at $T_c(2D)\simeq 12\gamma_2$ = 1.5 K (1.6 K). In contrast, MFT predicts that for $V_c/\Gamma_o=0$, initial ordering is into the herringbone phase at $T_c(2D)$ = 6.1 $\Gamma_o(2D)$ = 3.2 K (3.1 K). As T decreases, there is a second transition into the pinwheel state. For $V_c/\Gamma_o=-\infty$, ordering is also into the herringbone state at a somewhat higher temperature. The Monte Carlo transition temperatures are a factor of three below the mean field values. However, even the Monte Carlo results are likely to be too high since renormalization of Γ is expected to be even greater in 2D than in 3D. When making comparisons with experiment one must also bear in mind that the inevitable presence of J=0 impurities will further reduce T_c.

The temperature dependence of the critical order parameters have been obtained in another Monte Carlo study (Mouritsen and Berlinsky, 1982). A 2D hexagonal lattice of classical quadrupoles, which were constrained to lie in the plane of the lattice (i.e., $V_c/\Gamma_o=-\infty$), was found to undergo a fluctuation induced first order transition into the herringbone phase.

Second Order Perturbation Correction to the MFT Ground State

The ordered phase predicted at T=0 by MFT will not be the

true ground states because of zero point libration. In accordance with (III-12), within the mean field approximation, the ground state wave function Ψ_o of a system of N particles can be written as

$$\Psi_o = \prod_{i=1}^{N} Y_1^o(\theta_i) \qquad \text{(III-40)}$$

All of the molecules on each sublattice are aligned in the same direction. By analogy to a system of antiferromagnetic spins, this is known as the Néel state. It cannot be the true ground state because H_{EQQ} has non-zero matrix elements between Ψ_o and states Ψ_2 in which a pair of molecules is excited. Matrix elements involving Ψ_o and states Ψ_1 in which a single molecule is excited give zero when one does the sum over all neighbours of a molecule. This sum is contained in H_{EQQ}. In a system of antiferromagnetic spins, the ground state is also formed by mixing states containing excited pairs into the Néel state.

The energy shift ΔE arising from the admixture can be estimated from second order perturbation theory (Harris and Berlinsky, 1979):

$$\Delta E = \sum_{\Psi_2} |\langle \Psi_2 | H_{EQQ} | \Psi_o \rangle|^2 / E_2 \qquad \text{(III-41)}$$

where E_2 is the energy of the two excitations. The result is $\Delta E/E_o = .06$ where $E_o = -30N\Gamma/7$ is the energy of the pinwheel phase at $V_c = T = 0$. By comparison $\Delta E/E_o = .04$ for bulk solid H_2 (Van Kranendonk, 1983) and $\Delta E/E_o = .14$ for a bcc spin 1/2 antiferromagnet where E_o is the Néel state energy. For

hydrogen the effect is small enough to be neglected.

Renormalization Group Analysis

In recent years the renormalization group (RG) approach has allowed major advances in the study of critical phenomena. As yet there is very little RG work that can be applied to the orientational ordering of adsorbed hydrogen. Quadrupoles on a hexagonal lattice can be approximated by a planar Heisenberg model with cubic anisotropy since both are described by (III-37) to fourth order. In the planar Heisenberg model the spatial dimension d is 2 and the dimension of the order parameter n is 3.

The RG method is intended to be applied to systems near their critical point. Its basic premise is that long range correlations of the fluctuations near the critical point are solely responsible for the singular behaviour of certain observables such as the specific heat and susceptibility.[4] As the critical point is approached the correlation length $\xi \to \infty$. Under a RG transformation the system is mapped to one in which ξ is shorter in order to make the correlations less important.

The free energy equation (III-37) contains four parameters F_{eq}, Λ^1, A_4, and B_4. The RG transformation is carried out in the space of these parameters. Successive infinitessimal RG transformations will cause the system to describe a path in parameter space. There are certain points in parameter space, fixed points, such that if the RG transformation is applied to

them the system is carried to the same point. At a fixed point, ξ must be either zero or infinity. If it is zero, there is no long range order and the system is equivalent to one at $T=\infty$. These points will be ignored in the following discussion. The set of all points corresponding to $\xi = \infty$ form the critical surface.

Consider a small region around a fixed point. If successive RG transformations starting in this region always carry the system into the fixed point, i.e., the "flow" is into the fixed point, then the fixed point can be thought of as a valley. If one is always carried away, except at the fixed point itself, it is a peak. If one is carried in along some directions, but away along others it is a saddle point.

As the temperature is varied the system follows a path in parameter space called the physical line. If the system has a critical point, the physical line will intersect the critical surface. Applying successive RG transformations to the point of intersection, the system will flow downhill and eventually either settle into a valley or saddle point or go out to infinity. Any point on the critical surface always remains on that surface when one applies an RG transformation because all points on the surface have $\xi = \infty$. The fixed point to which the system flows governs its critical behaviour.

Normally there are only a few fixed points that appear in the parameter spaces of many different types of systems. This is the basis of the concept of universality, according to which

the critical exponents of a system depend only upon such general properties as the spatial dimension and the dimension of the order parameter but not on the detailed nature of the interactions. Systems in the same universality class flow to the same fixed point.

Cubic anisotropy is discussed in Chapter 9 of Pfeuty and Toulouse (1977). There is only one valley fixed point. If the number of components of the order parameter n, is less than a critical value $n_c(d)$, then the valley fixed point is the isotropic fixed point. This is a fixed point that would also occur if $B_4=0$ in (III-37) so that the free energy depended symmetrically on the order parameters y_1, y_2, and y_3. When $n=n_c$ the isotropic fixed point coincides with the cubic fixed point, which was a saddle point for $n<n_c$. For $n>n_c$, the two fixed points exchange stability: the cubic fixed point becomes a valley and the isotropic fixed point becomes a saddle. Unfortunately the dependence of n_c on d is not known except at d=4 where $n_c=4$. However Ketley and Wallace (1973) have expanded $n_c(d)$ about d=4. Their expansion suggests that $n_c(d=2)\simeq 2$. For the planar Heisenberg model d=2 and n=3 so one expects $n>n_c$. The cubic fixed point should govern the critical behaviour except for regions of parameter space where there are first order transitions so that (III-37) is not valid.

The results of the RG analysis are that if diagonal anisotropy is favoured ($B_4<0$) there will be a continuous transition into the pinwheel phase and the critical exponents will be those

of the cubic fixed point, which are Ising-like if d=2. If face anisotropy is favoured ($B_4>0$), there will be a first order transition into the herringbone phase. The first result is in agreement with MFT but the latter is not: the transition to the herringbone phase was also predicted to be continuous. However, the transition into the herringbone phase was found to be first order by classical Monte Carlo calculations (Mouritsen and Berlinsky, 1982) in agreement with the RG result. This is a case of a transition that is driven to be first order by fluctuations. If $B_4=0$, there is a tricritical point, a point at which the system changes from a first order to a continuous transition. In this case the critical exponents are governed by the isotropic critical point, which is a saddle point.

High Temperature Expansions

Two main pieces of information have been extracted from the NMR measurements described in this thesis. The first is the structure of the low temperature ordered state of H_2. This was derived from the shape of the .3K NMR spectrum. The second is the temperature dependence of σ in the pararotational state which allows one to determine V_c and Γ. This was obtained from the splittings of the H_2 and D_2 spectra for $T>1$ K. The way in which these two pieces of information can be obtained is described in Chapter IV.

Within MFT the temperature dependence of σ is given by

(II-11), (II-13), and (II-16). As one approaches the phase transition, MFT will break down so one might achieve better results using a high temperature expansion of σ. Initially Harris and Berlinsky (1979) expanded σ to second order in βV_c and $\beta\Gamma$. In (II-10) σ_i (T) was defined to be proportional to $\langle 3J_{iz}^2-2\rangle_T$ where $\langle\rangle_T$ indicates a thermal average at temperature T. At high temperatures $\langle 3J_{iz}^2-2\rangle_T$ can be expanded as

$$\langle 3J_{iz}^2-2\rangle_T = \frac{Tr\{(3J_{iz}^2-2)\exp(-\beta H)\}}{Tr\exp(-\beta H)} \qquad \text{(III-42a)}$$

$$= \frac{Tr\{(3J_{iz}^2-2)(1-\beta H+(1/2)\beta^2H^2+\ldots)\}}{Tr\{1-\beta H+(1/2)\beta^2H^2+\ldots\}} \qquad \text{(III-42b)}$$

$$= -\beta\langle(3J_{iz}^2-2)H\rangle_\infty + (1/2)\beta^2\langle(3J_{iz}^2-2)H^2\rangle_\infty + \ldots \qquad \text{(III-42c)}$$

since $Tr\,(3J_{iz}^2-2) = Tr^H = 0$. If one assumes a random concentration c of J=1 molecules then the EQQ interaction with a single J=1 neighbour is weighted by c. To second order in β with nearest neighbour interactions one finds

$$\sigma = \beta V_c/3 + \beta^2\{V_c^2/18 - (3/2)cV_c\Gamma - (25/6)c\Gamma^2\} \qquad \text{(III-43)}$$

MFT gives the same result except that the Γ^2 term is omitted.

More recently Harris and Berlinsky (1983) have presented a high temperature expansion that is exact in βV_c and third order in $\beta\Gamma$. It has the form

$$\sigma = A + B\beta\Gamma + C\beta^2\Gamma^2 + D\beta^3\Gamma^3 \qquad \text{(III-44)}$$

The coefficients, which are defined in Appendix A, are functions of the concentration c and βV_c.

Notes to Chapter III

1. A libron is a torsional excitation of the molecular axes.

2. This condition means that the system will satisfy the "Landau rules" for a 2D system. These rules give the conditions under which a phase transition can be continuous. They are discussed in Domany et al (1978) and Mukamel and Krinsky (1976).

3. Note that γ_3 is not an effective quadrupole coupling constant. For a system of interacting quadrupoles, the ratio of the orientational ordering temperature of a classical system to that of a quantum (J=1) system is 5/2 (Harris and Berlinsky, 1979). Thus, one cannot simply combine the classical Monte Carlo result that $T_c(3D)/\Gamma_0(3D)=11.5$ with the experimental T_c for a quantum system to get an effective quadrupole coupling constant.

4. Good introductions to the RG method are given by Pfeuty and Toulouse (1977) and Ma (1976).

CHAPTER IV

NMR AS A PROBE OF ORIENTATIONAL BEHAVIOUR

4.1 Unbroadened NMR Spectra

The magnetic interactions of hydrogen molecules will now be discussed, mainly following the treatment given in Reif and Purcell (1953), Harris (1970b), and Hardy and Berlinsky (1973). The nuclear spin degrees of freedom constitute a negligible perturbation on the molecular orientational degrees of freedom since the interaction energies differ by a factor of 10^3. For an isolated hydrogen molecule containing nuclei with spins $\vec{i}^1$ and $\vec{i}^2$ in a magnetic field H_o along the z axis, the magnetic Hamiltonian is

$$h^{-1}H_M = -aI_z - bJ_z - c\vec{I}\cdot\vec{J} + (5/2i)d_M\{\vec{i}^1\cdot\vec{i}^2 - 3(\vec{i}^1\cdot\hat{r})(\vec{i}^2\cdot\hat{r})\} + (5/2)d_Q\{3(\vec{i}^1\cdot\hat{r})^2 + 3(\vec{i}^2\cdot\hat{r})^2 - 2i(i+1)\}, \qquad \text{(IV-1)}$$

where $\vec{I} = \vec{i}^1 + \vec{i}^2$

$i = |\vec{i}^1| = |\vec{i}^2| = 1/2\ (1)$ for H_2 (D_2)

$\hat{r}$ = unit vector along the internuclear axis

The first and second terms are the nuclear and rotational Zeeman interactions. The third term is the spin-rotation interaction. The fourth term is the intramolecular dipole-dipole interaction. The fifth term is the interaction between the nuclear quadrupole moment and the local electric field gradient. It is zero for H_2 but not D_2. For a free molecule the constants are defined and evaluated (with H_o in tesla) in Table III.

Table III Hyperfine Constants for H_2 and D_2

(Hardy and Berlinsky, 1973)

Constant	Definition		Value (kHz)	
			H_2	D_2
a	$(2\mu_i/h)H_o$		42576 H_o	6535.7 H_o
b	$(\mu_J/hJ)H_o$		6717 H_o	3368 H_o
c	$(2\mu_i/h)H'$		113.8	8.773
d_M	$(2\mu_i^2/5ih)\ \langle r^{-3}\rangle_o$	(for J=1)	57.68	2.74
d_Q	$(2/5)eQ_N(\partial^2 V/\partial r^2)$	(for J=1)	0	22.50

Here μ_i is the magnetic moment of each nucleus; μ_J is the molecular rotational magnetic moment; H' is the magnetic field at the nucleus arising from molecular rotation; r is the internuclear distance and $\langle\rangle_o$ represents an average over the vibrational and electronic ground state; eQ_N is the nuclear quadrupole moment; V is the electric potential at the nucleus.

In section 2.2 we argued that the orbital angular momentum will be quenched for orientationally ordered hydrogen. However at high temperatures that argument may not be valid because the $m_J = \pm 1$ states are degenerate. Even if the ground state has $m_J=0$, there will be significant population of the $m_J=\pm 1$ states if the crystal field splitting is of the order of kT. It is not clear that $\langle\vec{J}\rangle$ would be zero and if that is not the case the spin-rotation interaction would split the NMR spectrum. When one considers the dynamics however, it is found that the spin-rotation term does in fact average to zero. The transition

rate f_m between the m_J states will be of the order of the libron bandwidth which is $\sim\Gamma/h$. Thus the NMR frequency will be modulated by an amount $f_D \sim c$, d_M, and d_Q at the rate $f_m >> f_D$. One can see, for example from the theory of frequency modulation, that if $fm >> f_D$, no side bands are produced. Therefore $\mathcal{H}_M$ should be averaged over the m_J states and the spin-rotation interaction can be neglected. The averaged Hamiltonian $\bar{\mathcal{H}}_M$ can be rewritten using a spherical basis as

$$h^{-1}\bar{\mathcal{H}}_M = -aI_z + (5/2)(4\pi/5)^{1/2} \sum_{\mu,\nu} C(112;\mu\nu)\, Y_2^{\mu+\nu*}(\vec{\omega}') \times\{d_M i_\mu^1 i_\nu^2 - d_Q(i_\mu^1 i_\nu^1 + i_\mu^2 i_\nu^2)\} \qquad \text{(IV-2)}$$

where $\vec{\omega}' = (\theta', \rho')$ = the orientation of $\hat{r}$

$\mu, \nu = 0, \pm 1$

Since $a >> d_M$ and d_Q in an NMR experiment, we only need the secular components of the second and third terms i.e., those that commute with $I_z = i_o^1 + i_o^2$ (Abragam, 1961). Only these components will affect the NMR spectrum in the region near the Larmor frequency $\nu_o = a$. The secular part of the Hamiltonian is

$$h^{-1}\bar{\mathcal{H}}_M^S = -aI_z + (5/2)(4\pi/5)^{1/2} \langle Y_2^o(\vec{\omega}')\rangle \sum_\mu C(112;\mu,-\mu) \times\{d_M i_\mu^1 i_\mu^2 - d_Q(i_\mu^1 i_{-\mu}^1 + i_\mu^2 i_{-\mu}^2)\} \qquad \text{(IV-3)}$$

$$= -aI_z + (5/4)\langle 3\cos^2\theta' - 1\rangle (-d_M\{3i_z^1 i_z^2 - \vec{i}^1 \cdot \vec{i}^2\} + d_Q\{3(i_z^1)^2 + 3(i_z^2)^2 - 2i(i+1)\}) \qquad \text{(IV-4)}$$

Quantities of the form

$$3i_z^\alpha i_z^\beta - \vec{i}^\alpha \cdot \vec{i}^\beta \quad \text{where } \alpha, \beta = 1,2$$

are the 0th components of second rank spherical tensor operators

so, according to the Wigner-Eckart Theorem (Rose, 1957), they are proportional to $3I_z^2-I(I+1)$. Evaluating the matrix elements for I=1, one finds

$$3i_z^{\alpha}i_z^{\beta} - \vec{i}^{\alpha}\cdot\vec{i}^{\beta} = \begin{cases} 3I_z^2-2 & \text{if } \alpha\neq\beta \\ -(3I_z^2-2) & \text{if } \alpha=\beta \end{cases} \qquad \text{(IV-5)}$$

Thus for I=1 the dipolar and quadrupolar terms have the same form and the secular Hamiltonian becomes

$$h^{-1}\bar{H}_M^S = -aI_z - (5/4)d\langle 3\cos^2\theta'-1\rangle\{3I_z^2-2\} \qquad \text{(IV-6)}$$

where $d=d_M+d_Q$. The resulting splitting of the NMR spectrum is depicted in Fig. 10.

For the subset of molecules whose internuclear axes make an angle θ' with respect to $\vec{H}_o$, there will be a pair of NMR frequencies

$$\nu=\nu_o \pm (15/4)d\langle 3\cos^2\theta'-1\rangle \qquad \text{(IV-7)}$$

Now, given that the order parameters describe the orientations of the molecules with respect to the substrate and not the direction of $\vec{H}_o$, it is convenient to transform to a reference frame in which the z axis is normal to the substrate (Fig. 11). Taking $\vec{\omega}_a$ and $\vec{\omega} = (\beta,\delta)$ to be the orientations of the internuclear axis and H_o in the substrate frame, the Spherical Harmonic Addition Theorem (Rose, 1957) gives

$$\langle 3\cos^2\theta'-1\rangle = (8\pi/5) \sum_m Y_2^m(\vec{\omega}) \langle Y_2^{m*}(\vec{\omega}_a)\rangle \qquad \text{(IV-8)}$$

First consider the pararotational state. Each molecule is in a site which has six-fold symmetry about the z axis. Only terms that have this symmetry (those with m=0) will be non-zero

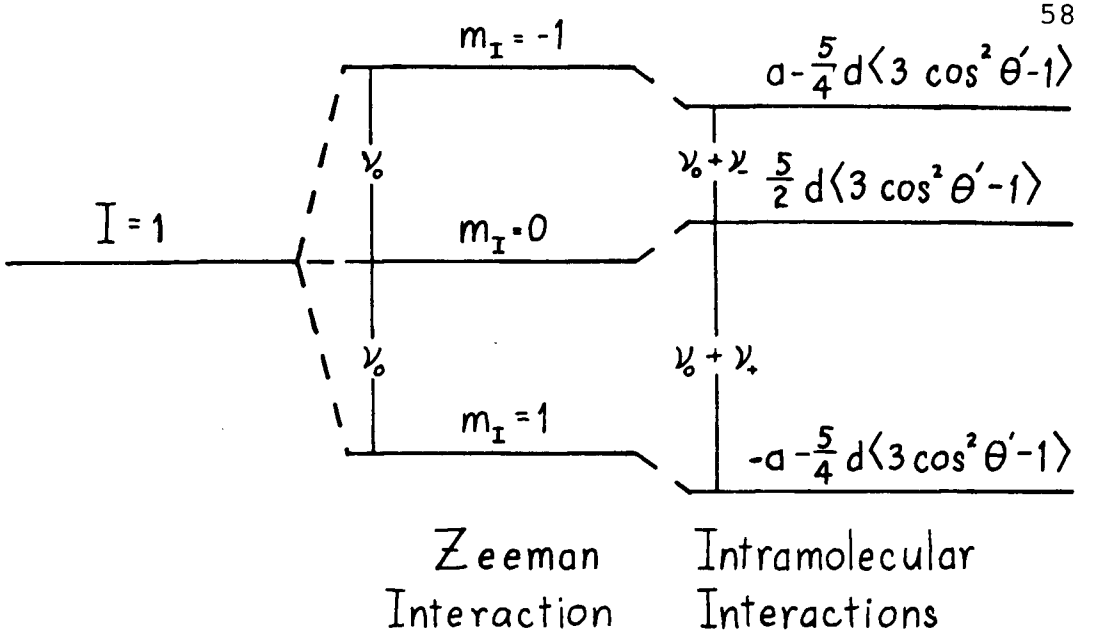

Fig. 10 Magnetic energy of a J=1 hydrogen molecule in a magnetic field. The intramolecular interactions are dipolar for H_2 and dipolar plus quadrupolar for D_2. The NMR frequencies are $\nu_o+\nu_+$ and $\nu_o+\nu_-$.

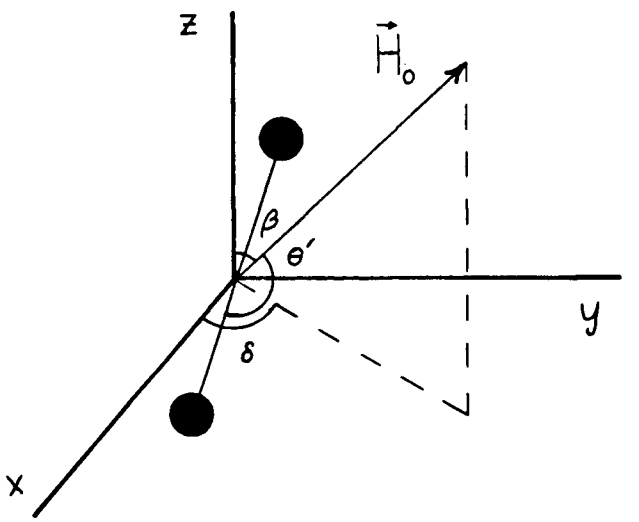

Fig. 11 Orientations of $\vec{H}_o$ and the internuclear axis with respect to the crystal reference frame. z is normal to the surface.

in (IV-8). The shifts in the NMR frequencies relative to ν_o are then

$$\nu_{\pm} = \pm (3/2) d\sigma (3\cos^2\beta - 1) \qquad \text{(IV-9)}$$

where σ is the orientational order parameter defined in (II-10). The NMR spectrum consists of a doublet which has a splitting directly proportional to $|\sigma|$. From the temperature dependence of the splitting one can obtain V_c and Γ within the mean field approximation using (II-11), (II-13), and (II-16).

In the ordered states the six-fold symmetry will in general be broken by the EQQ interaction. Using the order parameters defined in (III-5), the shifts of the NMR frequencies normalized to their maximum values are

$$\nu_{\pm}/3d = \pm (4/5\pi)^{1/2} [\sigma Y_2^{\,0}(\beta,\delta) - (3/2)^{1/2} \{\mu^- Y_2^{\,1}(\beta,\delta) - \mu^+ Y_2^{\,-1}(\beta,\delta)\} + (1/6)^{1/2} \{\eta^- Y_2^{\,2}(\beta,\delta) + \eta^+ Y_2^{\,-2}(\beta,\delta)\}] \qquad \text{(IV-10a)}$$

$$= \pm (1/2) \{\sigma(3\cos^2\beta - 1) + 6\mu \sin\beta\cos\beta\cos(\delta - \chi) + \eta \sin^2\beta \cos 2(\delta - \phi)\} \qquad \text{(IV-10b)}$$

On a single crystal substrate, each sublattice of an orientationally ordered state would produce a pair of delta function NMR lines in the absence of broadening. For Grafoil the adsorbing surfaces are primarily basal planes. The crystal x axes are oriented uniformly through the range $(0, 2\pi)$. Typically about 30% of the crystals have their z axes in an angular distribution with a full width at half maximum of 30° with respect to the normal to the foil and the remaining 70% are uniformly oriented through the range $(0, 2\pi)$ (Birgeneau et al, 1982).

In Chapter VIII the .3 K experimental spectra of H_2 are compared with the T=0 synthetic spectra expected for various ordered states. The misorientation of the Grafoil has been taken into account. The important features of the spectra can be seen by assuming that all of the z axes are parallel but that the x axes have a uniform angular distribution over the range $(0,2\pi)$. This distribution of crystallites will be called a "2D powder."

At T=0 all of the molecules on each sublattice will be aligned along some axis. The order parameters are expressed in terms of the orientation of that axis by (III-13). Substituting $\theta_i = 0^o$, 90° for molecules that are standing up or lying down gives the T=0 order parameters σ_i, μ_i, and η_i for the pinwheel and herringbone phases. These are tabulated in Table IV. For the 2-out and ferrorotational phases, θ_i depends on V_c/Γ but σ_o, μ_o, and η_o will all be non-zero. The expected T=0 NMR spectra for the 2D powder are shown in Fig. 12 for the cases with $\vec{H}_o$ normal to the substrate ($\beta = 0^\circ$) and parallel to the substrate (β=90°).

Table IV Order Parameters for the Herringbone and Pinwheel Phases at T=0

Phase	Sublattice	θ	σ_o	μ_o	η_o	ϕ
Herringbone	1,2	90°	-1/2	0	3/2	$\pm$45°
Pinwheel	1	0°	1	0	0	-
Pinwheel	2,3,4	90°	-1/2	0	3/2	-45°, -165°, -105°

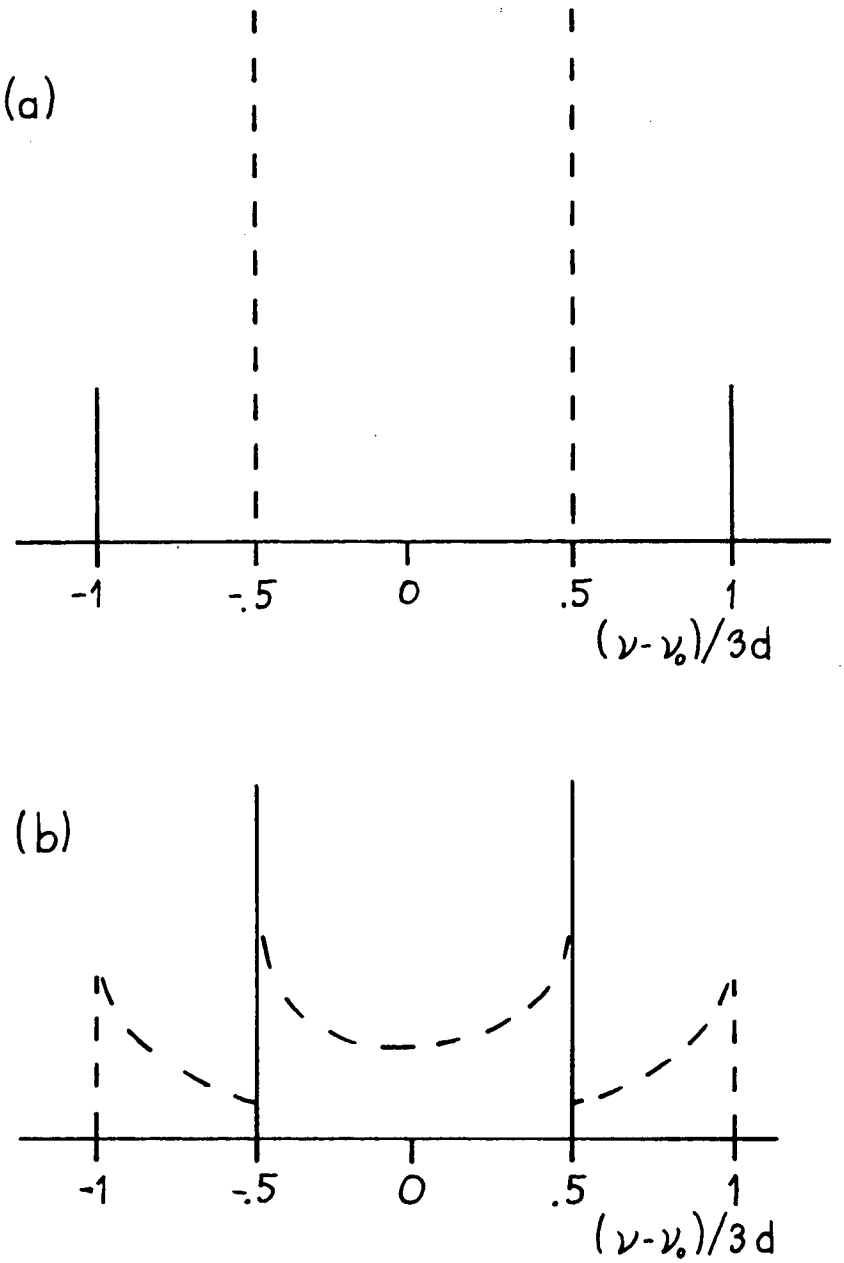

Fig. 12 Unbroadened T=0 NMR spectra for a 2D powder. The solid lines are produced by molecules with their axes normal to the surface and the dashed lines by those parallel to the surface. The herringbone phase would have only the dashed spectra. The pinwheel phase would have the dashed and solid spectra in a 3:1 intensity ratio. In (a) $\vec{H}_o$ is perpendicular to the surface and in (b) it is parallel.

For $\beta = 0°$ only the first term of (IV-10b) is non-zero so the up molecules and the down molecules each give a pair of lines with a splitting that is proportional to $|\sigma|$. The expression for ν is the same as in the pararotational state. Thus for $\beta=0°$ the distinction between the spectra of the herringbone and the pinwheel phases is very clear. The former contains only two lines with a splitting of $\Delta\nu/3d=1$. The latter contains two pairs of lines with splittings of $\Delta\nu/3d=1$ and $\Delta\nu/3d=2$. The inner lines have three times the intensity of the outer ones.

Now consider the case of $\beta=90°$ ($\vec{H}_o$ is in the plane of the substrate). The molecules standing up have $\mu=\eta=0$ so for $\beta=90°$ the first term of (IV-10b) is still the only non-zero one. For the molecules lying down, η is also non-zero so the third term also contributes. It contains the azimuthal angle δ which must be averaged over all x axis orientations. The spectrum is thus spread over the entire range of $(\nu-\nu_o)/3d$ from -1 to 1. The only difference between the herringbone and pinwheel spectra is that the inner peaks would be stronger for the latter.

In the 2-out and ferrorotational phases μ is non-zero but it is multiplied by $\sin\beta\ \cos\beta$, which is zero for $\beta=0$ or 90°. The magnitude of the splitting will depend upon V_c/Γ but otherwise the $\beta=0$ and 90° NMR spectra will be very similar to those of the herringbone phase.

The major source of broadening of the NMR spectra is the orientational distribution of the basal planes. If $\vec{H}_0$ is parallel or normal to the Grafoil, only the inside edges of the

peaks are broadened because in these two cases ν_+ and ν_- have either their maximum or minimum values if there is no misalignment of the z axes. NMR spectra for a single crystal, a 3D powder and Grafoil are compared in Fig. 13. Next are the intermolecular dipole-dipole interactions which cause each molecule to experience a local magnetic field of the order of 10^{-4}T. Finally, the substrate itself produced local magnetic fields due to its anisotropic diamagnetism. These mechanisms will be discussed in the next three sections.

4.2 Crystallite Orientational Distribution

Synthetic NMR spectra which include the misorientation of the graphite crystals have been generated. In (IV-10a) the NMR frequencies are expressed in terms of the spherical harmonics $Y_2^m(\vec{\omega})$ where $\vec{\omega}=(\beta,\delta)$ is the orientation of $\vec{H}_o$ in the crystal (xyz) reference frame. Define (α,ζ,γ) to be the Euler rotation which carries the XYZ axes fixed in the foil into the xyz axes. The Z axis is parallel to the normal of the foil and the orientation of the X axis is arbitrary for the time being. Using the convention of Rose (1957), the Euler rotation is defined by the following operations.

1) Rotation by α about Z, XYZ $\rightarrow$X'Y'Z'

2) Rotation by ζ about Y', X'Y'Z' $\rightarrow$X"Y"Z"

3) Rotation by γ about Z", X"Y"Z" $\rightarrow$x y z

The orientations of $\vec{H}_o$ and z in the XYZ frame are $\vec{\Omega}=(\overline{\beta},\overline{\delta})$ and $\vec{\Omega}'=(\beta',\delta')$ as shown in Figure 14.

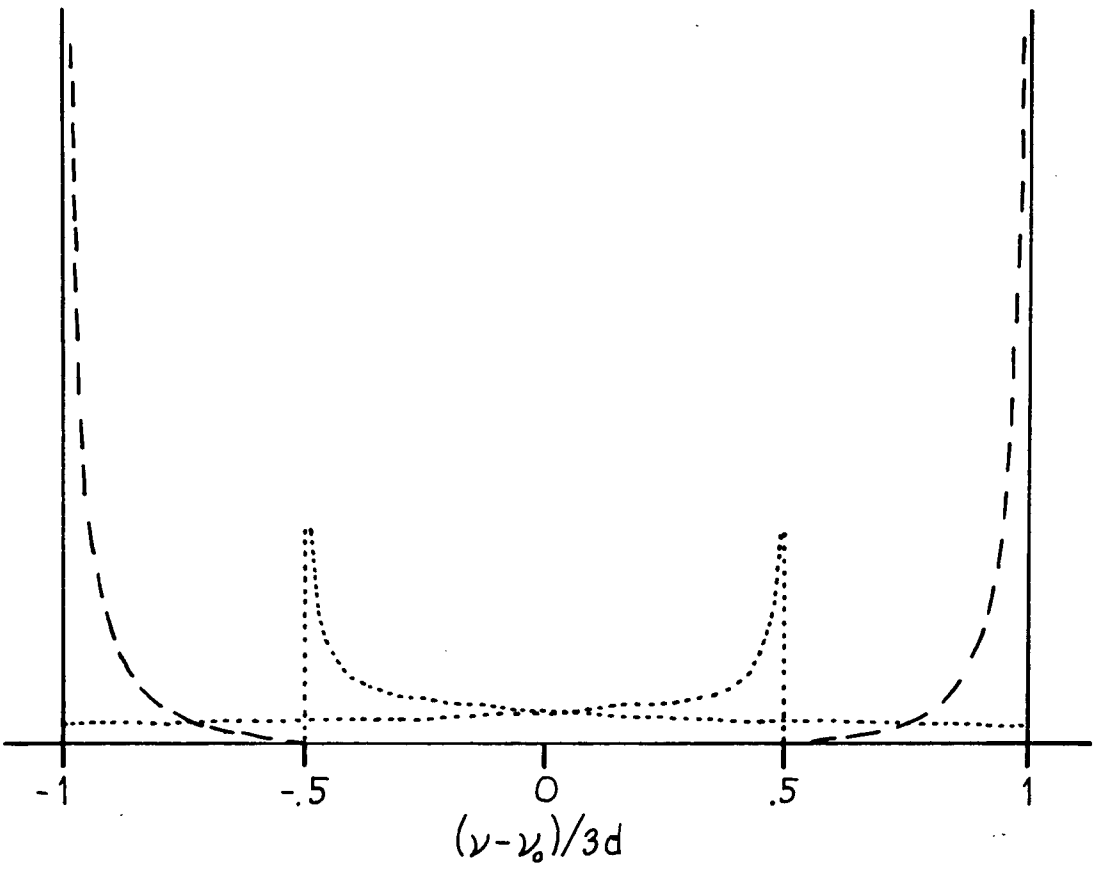

Fig. 13 Broadening of the NMR spectra due to the orientational distribution of the adsorbing surfaces. The hydrogen molecules are taken to be standing up on the surface. The solid line is for a single crystal substrate with $\vec{H}_o$ normal to the surface. The dashed line is for Grafoil with $\vec{H}_o$ normal to the foil. The dotted line is for a powder substrate. The dashed and dotted curves are normalized to the same area.

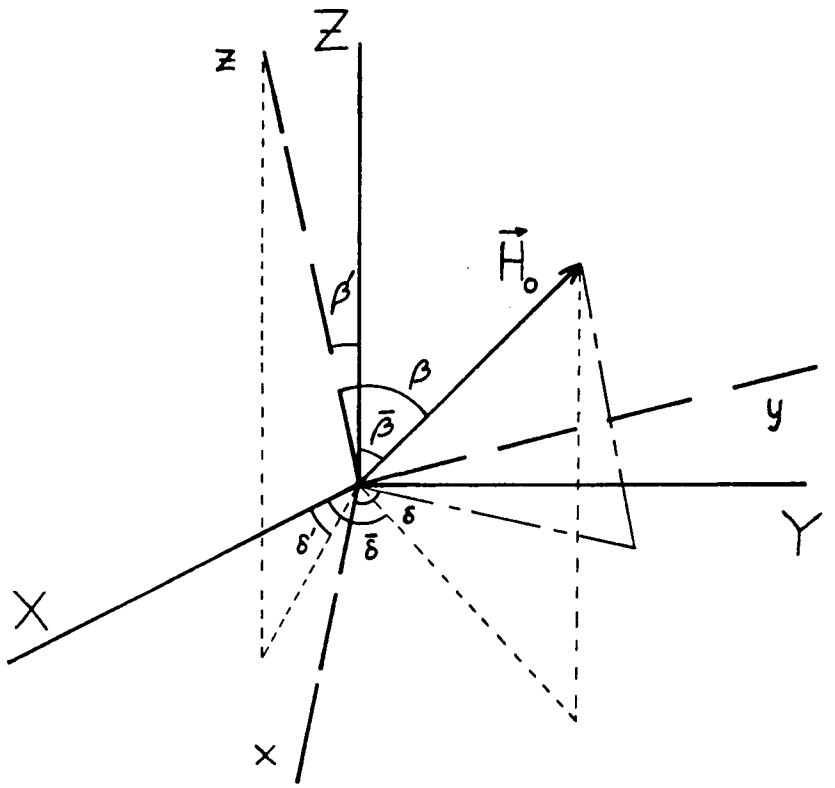

Fig. 14 Orientation of $\vec{H}_o$ with respect to the crystal axes (xyz) and the foil axes (XYZ). The z and Z axes are normal to the crystal basal plane and the Grafoil sheet respectively.

In order to take into account the orientational distribution of the adsorbing surfaces, we will first transform the expression for the NMR frequencies from the xyz frame to the XYZ frame using the rotational transformation properties of the spherical harmonics. The probability distribution $P'(\alpha,\zeta,\gamma)$ of the Euler rotations depends upon the Grafoil orientational distribution. The next step is to obtain the probability distribution of the NMR frequencies $p(\nu)$. This was done numerically using an Amdahl 470 V/8 computer. The ranges of the Euler angles were divided into intervals and for each set of intervals $P'(\alpha,\zeta,\gamma)$ and ν were determined. The range of ν was divided into intervals and after going through all of the Euler angles $p(\nu)$ was determined by weighting each value $\nu(\alpha,\zeta,\gamma)$ by $P'(\alpha,\zeta,\gamma)$. This is the NMR spectrum.

The spherical harmonics in (IV-10a) transform under the Euler rotations by

$$Y_2^m(\vec{\omega}) = \sum_n Y_2^m(\vec{\Omega})\, D^2_{nm}(\alpha,\zeta,\gamma) \qquad \text{(IV-11)}$$

where $D^2(\alpha,\zeta,\gamma)$ is a rotation matrix (Appendix A of Van Kranendonk, 1983). Inspection of Fig. 14 shows that the transformation can be made by making $\alpha=\delta'$, $\zeta=\beta'$, and γ arbitrary. Applying (IV-11) to (IV-10a) gives

$$\begin{aligned} Y_2^2(\vec{\omega}) = (1/2)e^{-i2\gamma}\{ & 2\cos^4(\zeta/2)e^{-i2\alpha}Y_2^2(\vec{\Omega}) + \sin\zeta(1+\cos\zeta)e^{-i\alpha}Y_2^1(\vec{\Omega}) \\ & + (3/2)^{1/2}\sin^2\zeta Y_2^0(\vec{\Omega}) + \sin\zeta(1-\cos\zeta)e^{i\alpha}Y_2^{-1}(\vec{\Omega}) \\ & + 2\sin^4(\zeta/2)e^{i2\alpha}Y_2^{-2}(\vec{\Omega})\} \end{aligned} \qquad \text{(IV-12a)}$$

$$Y_2^1(\vec{\omega})=(1/2)e^{-i\gamma}\{-\sin\zeta(1+\cos\zeta)e^{-i2\alpha}Y_2^2(\vec{\Omega}) + (1+\cos\zeta)(2\cos\zeta-1)e^{-i\alpha}Y_2^1(\vec{\Omega}) + 6^{1/2}\sin\zeta\cos\zeta Y_2^0(\vec{\Omega}) + (1-\cos\zeta)(2\cos\zeta+1)e^{i\alpha}Y_2^{-1}(\vec{\Omega}) + \sin\zeta(1-\cos\zeta)e^{i2\alpha}Y_2^{-2}(\vec{\Omega})\} \quad \text{(IV-12b)}$$

$$Y_2^0(\vec{\omega})=(1/2)\{(3/2)^{1/2}\sin^2\zeta e^{-i2\alpha}Y_2^2(\vec{\Omega}) - 6^{1/2}\sin\zeta\cos\zeta e^{-i\alpha}Y_2^1(\vec{\Omega}) + (3\cos^2\zeta-1)Y_2^0(\vec{\Omega}) + 6^{1/2}\sin\zeta\cos\zeta e^{i\alpha}Y_2^{-1}(\vec{\Omega}) + (3/2)^{1/2}\sin^2\zeta e^{i2\alpha}Y_2^{-2}(\vec{\Omega})\} \quad \text{(IV-12c)}$$

$$Y_2^{-1}(\vec{\omega}) = -Y_2^{1*}(\vec{\omega}) \quad \text{(IV-12d)}$$

$$Y_2^{-2}(\vec{\omega}) = Y_2^{2*}(\vec{\omega}) \quad \text{(IV-12e)}$$

The orientation of the X axis can be chosen such that the projection of $\vec{H}_o$ onto the XY plane is along X ie, $\bar{\delta}=0°$. With this choice, substitution of (IV-12) into (IV-10a) gives

$$\nu_{\pm}/3d=\pm(1/2)\{(\sigma/2)((3\cos^2\bar{\beta}-1)(3\cos^2\zeta-1) + 3\sin2\bar{\beta}\sin2\zeta\cos\alpha + 3\sin^2\bar{\beta}\sin^2\zeta\cos2\alpha) - 3\mu((1/2)(3\cos^2\bar{\beta}-1)\sin2\zeta\cos(\chi+\gamma) - \sin2\bar{\beta}\{\cos2\zeta\cos(\chi+\gamma)\cos\alpha - \cos\zeta\sin(\chi+\gamma)\sin\alpha\} - \sin^2\bar{\beta}\sin\zeta\{\cos\zeta\cos(\chi+\gamma)\cos2\alpha - \sin(\chi+\gamma)\sin2\alpha\}) + \eta((1/2)(3\cos^2\bar{\beta}-1)\sin^2\zeta\cos2(\phi+\gamma) - \sin2\bar{\beta}\sin\zeta \times \{\cos\zeta\cos2(\phi+\gamma)\cos\alpha - \sin2(\phi+\gamma)\sin\alpha\} + \sin^2\bar{\beta}\{(1/2)(\cos^2\zeta+1)\cos2(\phi+\gamma)\cos2\alpha - \cos\zeta\sin2(\phi+\gamma) \times \sin2\alpha\})\} \quad \text{(IV-13)}$$

All of the NMR measurements were made with $\bar{\beta}=0°$ or $\bar{\beta}=90°$. The results for these cases are given below.

1) $\bar{\beta}=0°$:

$$\nu_{\pm}/3d=\pm(1/2)\{\sigma(3\cos^2\zeta-1) - 3\mu\sin2\zeta\cos(\chi+\gamma) + \eta\sin^2\zeta\cos2(\phi+\gamma)\} \quad \text{(IV-14)}$$

2) $\bar{\beta}=90°$:

$$\nu_{\pm}/3d=\pm(1/2)\{(\sigma/2)(-(3\cos^2\zeta-1) + 3\sin^2\zeta\cos2\alpha) + 3\mu(\sin2\zeta\cos(\chi+\gamma)$$

$$\times\cos^2\alpha - \sin\zeta\sin(\chi+\gamma)\sin 2\alpha) + \eta(-(1/2)\sin^2\zeta\cos(\phi+\gamma)$$
$$+ (1/2)(\cos^2\zeta+1)\cos 2(\phi+\gamma)\cos 2\alpha - \cos\zeta\sin 2(\phi+\gamma)\sin 2\alpha)\} \qquad \text{(IV-15)}$$

Having transformed the expression for $\nu_{\pm}$ to the foil reference frame, we note that $P'(\alpha,\zeta,\gamma)$ actually depends only on ζ: the orientational distribution of the Grafoil adsorbing planes is characterized by the angle $\beta' = \zeta$ between the z and Z axes. Define $P(\zeta)d\vec{\Omega}$ to be the probability that z lies in the solid angle $d\vec{\Omega} = \sin\zeta d\zeta d\alpha$. The Euler angle γ does not affect the orientation of the z axis so $P(\zeta)$ involves an integration over all angles γ, giving

$$P(\zeta)d\vec{\Omega} = d\vec{\Omega}\int_0^{2\pi} P'(\alpha,\zeta,\gamma)\, d\gamma \qquad \text{(IV-16)}$$

$$P'(\alpha,\zeta,\gamma) = P(\zeta)/2\pi \qquad \text{(IV-17)}$$

If $\bar{\beta}=0°$, then most crystals would have $\beta \simeq 0°$ and the first term of (IV=10b) would dominate; the pinwheel and herringbone spectra would resemble Fig. 12(a) so they would easily be distinguished. In the pararotational state, the first term of (IV-10b) is the only non-zero term regardless of the orientation of $\vec{H}_o$. The spectrum would always consist of a doublet but its splitting would be twice as great for $\bar{\beta}=0°$ as for $\bar{\beta}=90°$. However, it is not obvious from (IV-14) and (IV-15) whether the broadening in the former case would be more or less than twice as great as in the latter case. If $\bar{\beta}=0°$, then any misalignment of the z axes will change β. On the other hand if $\bar{\beta}=90°$, rotations of the z axis about $\vec{H}_o$, ie. $\alpha=\pm 90°$ and $\zeta \neq 0°$, would not change β so they would not shift the NMR frequencies. This might lead one to think that the broadening for $\bar{\beta}=90°$ would be

less than twice that for $\bar{\beta}=0°$. However for $\bar{\beta}=90°$, it is also necessary to average over all angles α as (IV-15) shows. Experimentally we have found the spectra for $\bar{\beta}=0°$ to be better resolved than those for $\bar{\beta}=90°$ in the pararotational state so for our Grafoil sample the second misorientational effect dominates.[1]

4.3 Intermolecular Dipolar Broadening

The dipole-dipole interaction between the nuclear spins of neighbouring molecules results in broadening of the NMR line. In this section the broadening will be calculated assuming that the lattice is rigid. The interaction can have two effects. In the presence of a large magnetic field $\vec{H}_o$, an isolated magnetic moment $\vec{\mu}_1$ will precess about $\vec{H}_o$ at the Larmor frequency ω_o given by

$$\omega_o = \gamma_1 H_o \qquad \text{(IV-18)}$$

where γ_1 is the gyromagnetic ratio. If we introduce a second moment $\vec{\mu}_2$, then at the site of $\vec{\mu}_1$ it induces a static field h_s parallel to H_o and a field h_r transverse to H_o, which is rotating at a frequency ω_2 determined by its own local field. To first order the Zeeman levels of $\vec{\mu}_1$ are shifted only by h_s. This is the first effect. If the two moments are of the same type, i.e. $\gamma_1=\gamma_2=\gamma$, then h_r will be rotating near the resonance frequency ω_1 of the first moment. This produces transitions between the Zeeman levels which cause $\vec{\mu}_1$ to tip away from $\vec{H}_o$, the same effect as the applied transverse

RF field used in NMR. In order for the second mechanism to be effective it is necessary that (p.21 of Abragam, 1961)

$$h_r \gtrsim |\omega_2 - \omega_1| \qquad \text{(IV-19)}$$

The width of the resonance is h_r which is of the same order of magnitude as the static shift h_s.

Normally for a 3D solid, the NMR lineshape produced by intermolecular dipolar broadening can be approximated fairly well by a Gaussian function with a standard deviation σ_G which is equal to the second moment M_2, which is defined by

$$M_2 = \int_o^\infty (\nu - \nu_o)^2 f(\nu)\, d\nu \qquad \text{(IV-20)}$$

where $f(\nu)$ is the normalized NMR lineshape. In the rigid lattice approximation, the calculation of M_2 is straightforward if the lattice structure is known. In order to fit the experimental lineshape we have assumed that the intermolecular broadening produces a Gaussian lineshape. This source of broadening is small so this assumption is acceptable.

The expression for M_2 is obtained following the treatment in Chapter IV of Abragam (1961). The Hamiltonian H_d for the intermolecular dipole-dipole interaction is

$$H_d = \sum_{j<k} (\hbar^2 \gamma^2 / r_{jk}^3)\{\vec{I}^j \cdot \vec{I}^k - 3(\vec{I}^j \cdot \hat{r}_{jk})(\vec{I}^k \cdot \hat{r}_{jk})\} \qquad \text{(IV-21)}$$

where $\vec{r}_{jk}$ = vector between the jth and kth molecules

$\hat{r}_{jk} = \vec{r}_{jk}/r_{jk}$

As in the case of the intramolecular dipole-dipole interaction discussed in section 4.1, we will only keep the secular terms. Assuming that H_o is along the z axis, these are

$$H_d^s = \sum_{j<k} (\gamma^2 \hbar^2 / r_{jk}^3)(1 - 3\cos^2\theta_{jk})[I_z^j I_z^k - (1/4)(I_+^j I_-^k + I_-^j I_+^k)]$$

(IV-22)

$$= \sum_{j<k} (\gamma^2\hbar^2/r_{jk}^3)(1-3\cos^2\theta_{jk})(1/2)[3I_z^j I_z^k - \vec{I}_j\cdot\vec{I}_k] \qquad \text{(IV-23)}$$

where θ_{jk} = angle between $\vec{r}_{jk}$ and $\vec{H}_o$. The first term of (IV-22) in the square brackets arises from the static parallel field h_s. The second term is due to the rotating transverse field h_r.

If the RF field used to produce the NMR transitions is applied along the x axis, then the expression for the second moment given by Abragam is

$$M_2 = \frac{-\mathrm{Tr}\,([\mathcal{H}_d^s, I_x]^2)}{h^2\mathrm{Tr}(I_x^2)} \qquad \text{(IV-24)}$$

The expression for $\mathcal{H}_d^s$ given in (IV-23) was obtained assuming that all lattice sites were occupied by spins of the same type with resonant frequencies ω_i such that for any pair of spins

$$|\omega_i - \omega_j| \lesssim \gamma h_r \qquad \text{(IV-25)}$$

However for hydrogen, the intramolecular dipole-dipole interaction can be much larger than the intermolecular interaction at low temperatures so that (IV-25) would not be satisfied for all pairs of spins. In that case h_r is not resonant and the second term in the square brackets of (IV-22) should be deleted. It has been found for bulk solid H_2 that M_2 of one peak of the fully split doublet is 5/6 that of the unsplit line (Ishiguro et al, 1951). Since it was not possible to obtain a very precise measurement of M_2 in the experiments described in this thesis, we will simply use (IV-23) in (IV-24) giving

$$M_2 \simeq (3/4)(\gamma/2\pi)^4 h^2 I(I+1) \sum_k (1-3\cos^2\theta_{jk})^2 r_{jk}^{-6} \qquad \text{(IV-26)}$$

If the J=1 concentration is denoted by c and I=1, then we get [2]

$$M_2 \simeq (3/2)c(\gamma/2\pi)^4 h^2 \sum_k (1-3\cos^2\theta_{jk})^2 r_{jk}^{-6} \qquad \text{(IV-27)}$$

For D_2, 5/6 of the J=0 spins have I=2 so these contribute to the broadening of the J=1 spectra. At low temperatures most pairs consisting of an I=1 and an I'=2 spin will not satisfy (IV-25) so it is more appropriate to delete the second term of (IV-22). If this is done, the contribution of the I'=2 spins to the second moment of the I=1 spins is

$$M_2 \simeq (1/3)(\gamma/2\pi)^4 h^2 I'(I'+1)(1-c)(5/6) \sum_k (1-3\cos^2\theta_{jk})^2 r_{jk}^{-6} \qquad \text{(IV-28)}$$

where the sum is over all molecules. The total second moment for the I=1 spins of D_2 is

$$M_2 \simeq (3/2)\{c+(10/9)(1-c)\}(\gamma/2\pi)^4 h^2 \sum_k (1-3\cos^2\theta_{jk})^2 r_{jk}^{-6} \qquad \text{(IV-29)}$$

In view of the S:N it is sufficient to approximate the Grafoil by a 2D powder when calculating M_2. Two cases will be considered. If $\vec{H}_o$ is normal to the foil ($\bar{\beta}=0°$), then $\theta_{jk}=90°$ for all j and k so $(1-3\cos^2\theta_{jk})^2=1$. If $\vec{H}_o$ lies in the foil plane ($\bar{\beta}=90°$) then all angles θ_{jk} in the range $(0,2\pi)$ have equal probability. Averaging over these gives

$$\langle(1-3\cos^2\theta_{jk})^2\rangle = (1/2\pi)\int_o^{2\pi}(1-3\cos^2\theta)^2 d\theta \qquad \text{(IV-30a)}$$

$$= 11/8 \qquad \text{(IV-30b)}$$

The fact that M_2 depends upon the orientation of H_o is a well known result for NMR of 2D systems (Cowan, 1980).

Now the sum of r_{jk}^{-6} will be calculated for the $\sqrt{3} \times \sqrt{3}$ solid. The neighbours of the jth molecule lie on a

series of concentric hexagons. Let S_i be the contribution from the ith hexagon to the sum and let a=1.420Å be the intraplaner C-C separation. Then for the first three hexagons

$$S_1 = 8.231 \times 10^{-3} a^{-6} \qquad \text{(IV-31a)}$$

$$S_2 = .434 \times 10^{-3} a^{-6} \qquad \text{(IV-31b)}$$

$$S_3 = .059 \times 10^{-3} a^{-6} \qquad \text{(IV-31c)}$$

(IV-32)

The square roots of the second moments are

$$H_2: \quad M_2^{1/2}/3d = \begin{cases} .0277c^{1/2} & \text{if } \bar{\beta}=0^\circ \\ .0325c^{1/2} & \text{if } \bar{\beta}=90^\circ \end{cases} \qquad \text{(IV-33)}$$

$$D_2: \quad M_2^{1/2}/3d = \begin{cases} .00149\{c+(10/9)(1-c)\}^{1/2} & \text{if } \bar{\beta}=0^\circ \\ .00173\{c+(10/9)(1-c)\}^{1/2} & \text{if } \bar{\beta}=90^\circ \end{cases} \qquad \text{(IV-34)}$$

4.4 Graphite Diamagnetism

Graphite has a large anisotropic diamagnetism. Consequently the magnetic field at the surface of the crystal in the Grafoil will depend upon the direction of the applied field with respect to the normal to the crystal. The distribution of crystal orientations will lead to broadening of the NMR spectra. Hickernell et al (1974) measured the room temperature frequency shift of ethyl alcohol adsorbed on Grafoil with the magnetic field parallel and perpendicular to the foil. They used a cylindrical sample in which the normal to the Grafoil sheets was perpendicular to the axis of the cylinder.[3] At 30 MHz the

shift was 2.4 kHz. If one assumes that the shift is the same at liquid helium temperatures, then for the 8 MHz experiments described in this thesis one would expect the contribution to $M_2^{1/2}/3d$ to be of the order of 3.7×10^{-3} (9.3×10^{-3}) for H_2 (D_2). Comparing with (IV-33) and (IV-34) one can see that for H_2 the intermolecular dipolar broadening is likely to be much larger than the effect of the graphite diamagnetism but for D_2 the reverse is true.

Notes to Chapter IV

1. This corrects a misconception in the paper of Kubik and Hardy (1978). At that time we believed that the first effect would dominate.

2. In general we will define c to be the odd J concentration. At liquid helium temperatures this is the same as the J=1 concentration.

3. This is the same sample geometry as used in the work described in this thesis.

CHAPTER V

SAMPLE PREPARATION AND CONVERSION MEASUREMENTS

5.1 Introduction

For bulk solid H_2 and D_2 the temperature of the orientational ordering transition decreases linearly with the J=1 concentration c down to $c \simeq .6$. It then drops rapidly to zero at $c \simeq .55$. For adsorbed hydrogen the depression of the transition temperature is likely to be even more rapid so it was desireable to limit the J=0 concentration to a few percent. In this chapter we will consider the preparation of enriched samples of J=1 hydrogen and measurements of the conversion rate.

In thermodynamic equilibrium the odd J concentration c_{eq} is given by

$$c_{eq} = g_J Z^{-1} \sum_{\text{odd } J} (2J+1) \exp(-E_J/kT) \qquad \text{(V-1)}$$

where E_J = energy of the Jth rotational level

g_J = nuclear degeneracy factor which is different for odd J and even J (see Table I)

$$Z = \sum_{\text{all } J} g_J (2J+1) \exp(-E_J/kT)$$

A graph of c_{eq} versus T is shown in Fig. 15. Room temperature is essentially the high temperature limit and c_{eq} = .749 (.333) for H_2 (D_2). These are referred to as normal-H_2 and normal-D_2 (n-H_2 and n-D_2). At temperatures below 10 K, $c_{eq} \simeq 0$ for H_2 and D_2.

Transitions from odd J states to even J states require a simultaneous change of parity of the orbital and nuclear

spin wave functions. For an H_2 molecule, conversion necessitates the presence of a magnetic field gradient. For D_2 either an electric or magnetic field gradient is sufficient because deuterons have a quadrupole moment. If the magnetic field gradient is provided by the nuclear and rotational magnetic moments of neighbouring molecules, the conversion is called "intrinsic". Paramagnetic ions have electronic magnetic moments that are one thousand times greater than nuclear moments so their presence can strongly catalyze conversion.

As a practical matter, non-equilibrium hydrogen samples can be stored at room temperature in clean glass bulbs. At 1 atmosphere pressure, H_2 will convert 1% in a week whereas for D_2 it may take a year for a similar change. Conversion of the gas is believed to be due primarily to the presence of O_2 impurities.

A glance at Fig. 15 suggests that the creation of hydrogen samples in which the J=1 concentration is higher than in normal hydrogen (enriched samples) might be a hopeless task. However at low temperatures, J=1 molecules are preferentially adsorbed on some substrates such as alumina. Silvera and Nielsen (1976) used inelastic neutron scattering to measure the separation coefficient S which is defined as

$$S = \{c_s(1-c_s)\}/\{c_g(1-c_g)\} \qquad (V-2)$$

where c_s and c_g are the concentrations of odd J molecules on the surface and in the gas. They found $S=39^{+2}_{-8}$ ($5.0\pm.3$) for H_2 (D_2) on Alcoa activated alumina.[1]

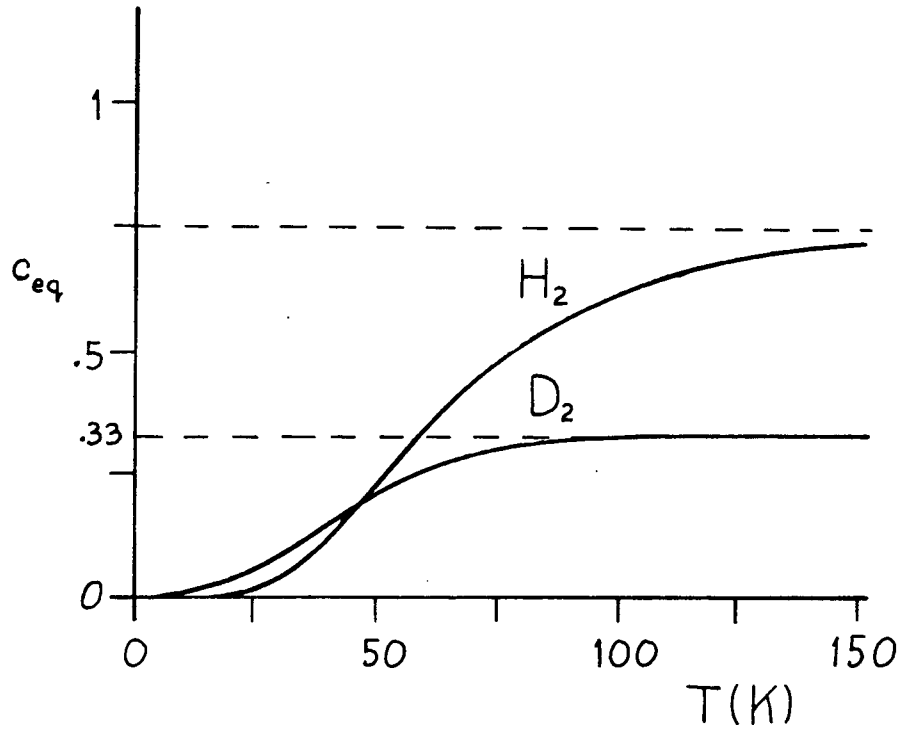

Fig. 15 Graph of the equilibrium J=1 concentration c_{eq} versus T for H_2 and D_2.

5.2 Preparation of Enriched Hydrogen Samples

Enriched hydrogen samples were prepared in an apparatus (Fig. 16) largely constructed by W.N. Hardy, based on the method of Depatie and Mills (1968). The n-H_2 had a purity of 99.999% (Matheson Ultra-high Purity) and the n-D_2 was 99.65% (Bio-Rad Laboratories). The hydrogen was adsorbed onto Alcoa activated alumina contained in a 1.23 m long, 1.27 cm diameter stainless steel tube held at 20 K. The alumina had initially been washed in concentrated HCl in order to remove paramagnetic impurities, mainly Fe^{3+}. How effectively this reduced conversion on the surface (back conversion) is not known. After being placed in the wand, the alumina was baked at 120 C under vacuum for a day and flushed several times with hydrogen. The alumina can withstand far higher baking temperatures but it has been found by Hardy that baking at a temperature of 200 C caused an increase in back conversion. This process may have broken some bonds of the surface molecules, creating paramagnetic ions. Before each enrichment run the wand was pumped out and flushed with hydrogen at room temperature.

Ideally the temperature of the wand would be controlled by placing it in liquid H_2 at its boiling point of 20.4 K. At that temperature the vapour pressure above a sub-monolayer would be very low and there would be no danger of pockets of bulk solid hydrogen forming since the triple point temperature is 13.8 K (18.7 K) for H_2 (D_2). Unfortunately the use of a liquid hydrogen bath had to be rejected for safety

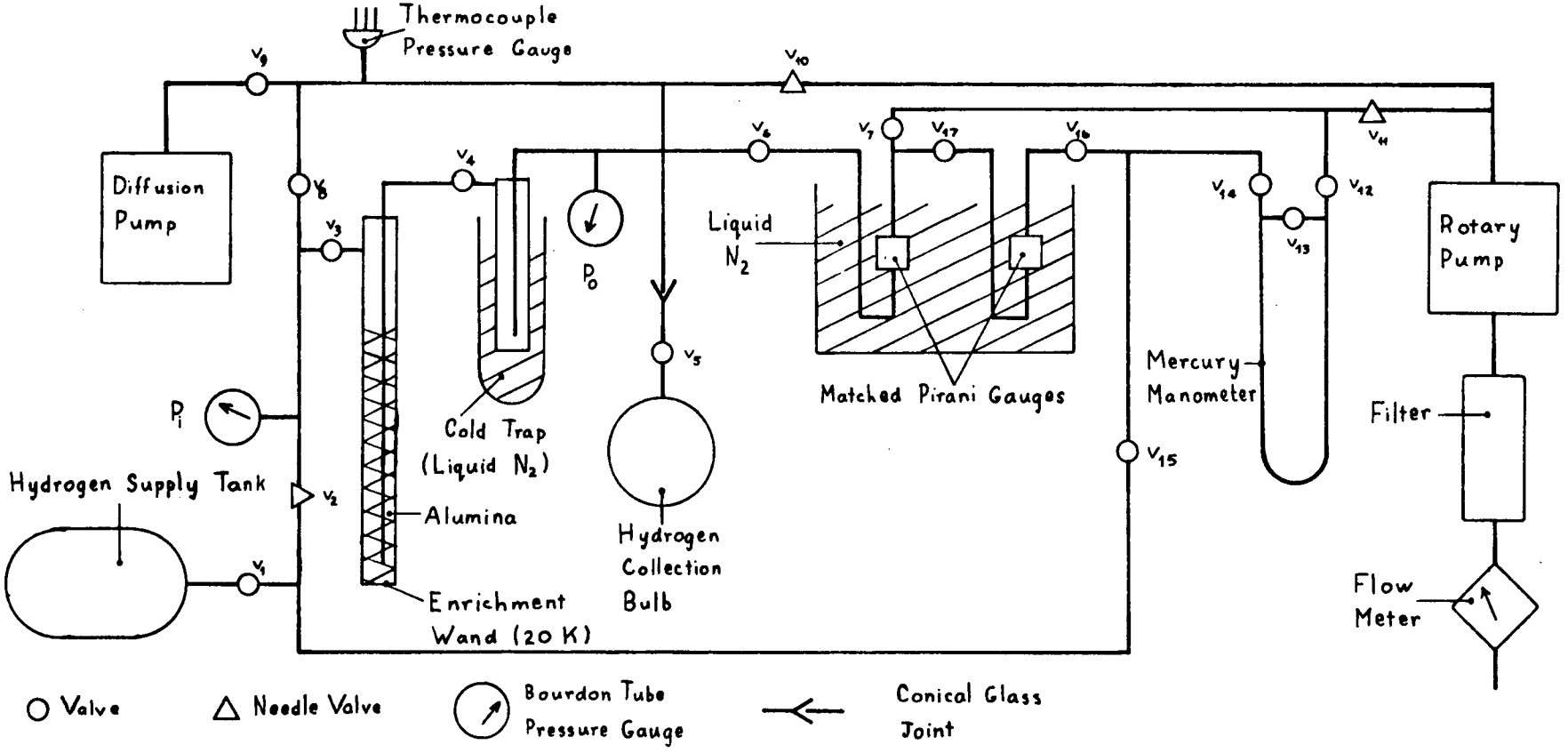

Fig. 16 Hydrogen enrichment apparatus.

considerations. Instead the wand was placed inside a copper cylinder which was cooled by pumping liquid ^4He from a storage dewar at about .5 l(liquid)/h through copper tubes soldered onto the cylinder. Better stability was obtained by pumping the ^4He through rather than pressurizing the storage dewar. Typically, for H_2 the bottom of the cylinder was held at about 19 K and the top at 23 K. Temperatures were measured using an Au (.07% Fe)/Chromel-P thermocouple (Rosenbaum, 1969) with a liquid N_2 reference temperature.

After cooling the wand to 20 K, n-H_2 was pumped through it by a rotary pump at a rate of .30 l(STP)/min and an input pressure $P_i \simeq 150$ torr. Initially the effluent gas had a low J=1 concentration but after a few minutes it stabilized at $\simeq .65$. Since the incoming n-H_2 has c = .75, there must have been some back conversion on the alumina. These conditions were maintained for half an hour to ensure that the adsorbed hydrogen was in equilibrium with the flowing gas. The valve v_3 at the input of the wand was then closed and the wand was raised 2 cm every 15 s. Enriched H_2 desorbed from the top end of the wand, flowed down through the alumina, further enriching the adsorbed H_2, and then up the centre. When the wand had been raised .76 m the concentration of the effluent gas had risen to $c \simeq .97$. The valves v_6 and v_{10} to the rotary pump were closed, the stopcock v_5 on the 2 l Pyrex collection bulb was opened and the wand was rapidly pulled out. Immediately afterwards v_5 was closed to prevent impurities on the alumina from desorbing

into the bulb. In this manner about 2 l(STP) of H_2 with c>.98 could be collected. The results for D_2 were similar though there were minor modifications to the procedure.

It is important to be able to monitor the J=1 concentration of the effluent gas. This was done using a matched pair of Pirani gauges. Each Pirani gauge consists of a cell containing 40 torr of hydrogen and a filament. The filament was heated by passing a 650 mA (500 mA for D_2) current through it. The temperature of the filament as measured by its resistance depends upon the thermal conductivity of the gas. At this pressure the mean free path of the hydrogen was much less than the dimensions of the gauge and convection was insignificant so the thermal conductivity was independent of the pressure. The ortho and para species have different thermal conductivities because the rotational energies are different; the difference is maximized near the boiling point of N_2 so the gauges were immersed in a flask of liquid N_2. The filaments of the two gauges were connected to a resistance bridge which had been balanced with n-H_2 in each of the gauges. The n-H_2 in the left arm was then replaced with slowly flowing effluent gas from the wand. Valves v_{10} and v_{11} were adjusted to maintain 40 torr pressure and to replace the gas in the gauge approximately every 15 s. The bridge imbalance is approximately linearly dependent on c and would be accurate to about 1% if it was calibrated using samples of known concentration. In practice the bridge was only used to monitor the production

process; absolute measurements of c were made using Raman scattering as described in Section 5.3.

5.3 Measurement of the J=1 Concentration by Raman Scattering

It is important that c be measured both before and after an NMR experiment. During the course of NMR measurements, the relative concentration was monitored by the intensity of the NMR signal. An absolute calibration of the NMR intensity would have been difficult. It was found that during the processes of adsorption and desorption conversion was much faster than when the hydrogen was in the $\sqrt{3}$ x $\sqrt{3}$ solid. We suspect that when the hydrogen is fluid on the surface many molecules can come close to paramagnetic surface impurities and are converted quickly but in the solid phase only those molecules at sites close to the impurities will be converted rapidly. In order to get a uniform film the hydrogen must be adsorbed at temperatures high enough ($\gtrsim$40 K) that there will be a significant 3D vapour pressure ($\gtrsim$1 torr) to allow exchange between the film and vapour. At these temperatures the adsorbate is fluid. We could not measure c during adsorption or desorption but by measuring it before adsorption and after desorption the conversion was estimated.

About 3 cm^3(STP) of hydrogen was used in the NMR experiments. This is too small a quantity to be analyzed with our Pirani gauges. Consequently the sample was transferred to a

square optical cell and c was determined from the intensity ratio of a pair of Raman lines. If J is a good quantum number, the selection rules for Raman scattering between states J and J' are $J'-J=0,\pm 2$. We will only be concerned with the case $J'-J=2$. For unpolarized light the differential scattering cross-section per unit solid angle and per unit frequency is

$$d\sigma_{JJ'}/d\Omega d\omega' = A\omega(\omega')^3 P_J s_J \delta(E_J - E_{J'} + \hbar\omega - \hbar\omega') \qquad (V-3)$$

where A is independent of J and J' but depends on the anisotropic polarizability

ω = frequency of the incident light

ω' = frequency of the scattered light

$s_J = (J+2)(J+1)/(2J+3)$ for $J'>J$ (Stokes lines)

E_J = energy of the J^{th} rotational state

$= BJ(J+1)$ in the harmonic approximation

P_J = probability that the J^{th} state is occupied

$= \exp(-E_J/kT) \sum'_{J''} (2J''+1)\exp(-E_{J''}/kT)$

The prime on the summation symbol indicates that the sum is over all even (odd) J" if J is even (odd).

For the 19,435 cm^{-1} Ar laser line, the intensity ratios $d\sigma_{J,J+2}/d\sigma_{1,3}$ are given in Table V. P_J and $\omega-\omega'$ have been evaluated in the harmonic approximation.

Raman spectra were obtained using a Spex Ramalog spectrometer with 400 mW unpolarized light from an Ar laser. The slit width of 150 μm corresponded to a bandwidth of 2.8 cm^{-1},

which is much greater than the intrinsic linewidth. For a pure o-H_2 NMR sample (3 cm^3(STP)) with a pressure $\approx$350 torr in the optical cell, the S:N with a 2 s time constant was $\approx$40. Concentrations could be measured with an accuracy of 2%.

Table V. Raman Frequencies and Intensity Ratios

	H_2		D_2	
J	$\frac{\omega-\omega'}{2\pi c}$ (cm^{-1})	$\frac{d\sigma_{J,J+2}}{d\sigma_{1,3}}$	$\frac{\omega-\omega'}{2\pi c}$ (cm^{-1})	$\frac{d\sigma_{J,J+2}}{d\sigma_{1,3}}$
0	356.0	1.025	178.3	.757
1	593.4	1	296.8	1
2	830.8	.434	413.9	.785
3	1068	.099	529.4	.420
4	1306	-	642.2	.160

5.4 The Substrate

The substrate employed in these experiments was GTA grade Grafoil, a form of exfoliated graphite. It is prepared by intercalating graphite crystals with a strong oxidizing agent such as sulfuric acid, rinsing, and rapid heating. Then it is rolled into sheets with a density $\approx$1 g/cm^3, about half that of graphite. The main impurities are Fe, Si, Al, Mg, and Mn with levels $\sim$10-100 ppm. These levels can be reduced to

<10 ppm by baking at 1700 C under vacuum (Hegde and Daunt, 1978) although this was not done with our sample.

The exfoliation process results in an enormous increase in the area of the exposed basal planes but little change in that of the edge planes (Dash, 1978). Broadening of x-ray diffraction peaks indicates that the crystals are ∿100 planes thick. The surface area is typically 20-30 m^2/g.

Grafoil has quite homogeneous surfaces. A common criterion for determining the homogeneity of an adsorbent is to measure the sharpness of the steps in the 3D vapour pressure isotherms of an inert gas such as Kr. The steps result from the coexistence of two surface phases in addition to the 3D vapour. For such a system we can take the thermodynamic variables to be the 3D vapour pressure P, the 2D spreading pressure ϕ, T, and N. When there is coexistence of two surface phases on a uniform surface, the chemical potentials of the two phases $\mu_1(\phi,T)$ and $\mu_2(\phi,T)$ and that of the 3D vapour $\mu_v(P,T)$ must all be equal independent of N. Therefore P will be independent of N also. At low temperatures, the two surface phases are usually a solid and a gas and the steps can cover almost the entire range of N for each layer. For Kr adsorbed on Grafoil, five steps can be observed in addition to sub-steps caused by phase transitions between other 2D phases during formation of the first layer. Exfoliated graphite exhibits better homogeneity than graphitized carbon black which was popular in earlier surface studies (Thomy and Duval, 1969). The uniformity and specific surface areas of

several forms of exfoliated graphite are compared in Table VI (Birgenau et al, 1981; Rosenbaum et al, 1983; R. Clarke, P.M. Horn, S.E. Nagler, and T.F. Rosenbaum, to be published).

Table VI. Properties of Exfoliated Graphite

Substrate	Surface Coherence Length (A)	Specific area (m^2/g)	z Axis Distribution
Grafoil*	100-200	20-30	70%: isotropic 30%: FWHM = 30°
Papyex†	200-300	20	70%: isotropic 30%: FWHM = 30°
UCAR Foam*	900	27	isotropic
UCAR ZYX*	2000	2.8	FWHM = 20-30°
Exfoliated single crystal	4000	.3	FWHM = 17°

* Union Carbide Corp., Carbon Products Div., 270 Park Ave., New York, USA

† Carbone Lorraine, 37-41 rue Jean-Jaures, 92231, Gennevilliers, France

Another property of Grafoil that is important for NMR measurements is that the normals to the adsorbing planes, the crystal z axes, are preferentially aligned parallel to the foil normal, the Z axis (see Table VI). The distribution was obtained from an analysis of the shape of the diffraction peaks of adsorbed gases: one cannot use the graphite peaks because one wants only the contributions from the surface planes. Fig. 13 shows that the intensity of the peaks in the NMR spectrum can

be enhanced considerably if the adsorbing surfaces are preferentially aligned.

Among the various forms of exfoliated graphite, Grafoil was chosen as the substrate because it makes a good compromise among the properties listed in Table VI. Paramount among these for this work is the specific surface area because the NMR S:N ratio is quite poor. Apparently the surface coherence length of Grafoil is sufficient to allow orientational ordering of H_2. Other substrates will be discussed in Chapter X.

5.5 Adsorption

A typical procedure for adsorbing a gas onto Grafoil begins by pumping out the cell at room temperature and then filling it with a measured quantity of gas. The cell would then be cooled over a period of several hours to adsorb the gas. Afterwards it would be slowly heated until the vapour pressure had risen to about 1 torr to anneal the sample. Finally it would be slowly cooled again. This procedure was found to be unsuitable for hydrogen because during the adsorption process the conversion rate was very rapid. In order to keep the conversion to <5% it was necessary to adsorb the sample in less than 15 min. In early experiments the samples were held at temperatures of 30 - 40 K corresponding to vapour pressures of several hundred microns for about 40 min. Pure o-H_2 samples converted to about 25% o-H_2. Fig. 15 shows that this is close to c_{eq} at those temperatures.

The sample cells were quite different for the ^4He and ^3He cryostats so the adsorption procedures will be described separately. In the ^4He cryostat the Grafoil was at the bottom of a long glass wand shown schematically in Fig. 17. The volume V_o contained the hydrogen gas, V_2 was a calibrated volume, and V_3 contained the Grafoil. V_3 was always evacuated except when filled with hydrogen. Prior to an experiment V_1, V_2, and V_3 would be pumped out at room temperature by a diffusion pump with a liquid N_2 trap for at least one day and flushed a few times with hydrogen. Occasionally the bottom of the wand was baked at 180 C during the pumping and flushing. The temperature was limited by the presence of Teflon sheets in the cell as described in Chapter VI. Stopcock v_{23} was then closed and V_2 was filled to a pressure P_2 measured by a Bourdon tube pressure gauge. Valve v_{12} was closed, v_{23} was opened and the wand was lowered fairly rapidly into the liquid ^4He bath. As soon as the pressure P_3 measured by the Veeco DV-1M thermocouple pressure gauge (1-2000 μ) began to drop below the 1 atmosphere mark the wand was raised a couple of centimeters to bring P_3 back up. The wand was then lowered over a period of 12 - 15 min until P_3 was down to 100 μ whereupon it was lowered rapidly into the ^4He bath. The object of this procedure was to adsorb most of the gas fairly quickly but then to hold the pressure near 1 torr for several minutes to allow it to anneal. Once essentially all of the gas was adsorbed it was cooled rapidly to minimize conversion.

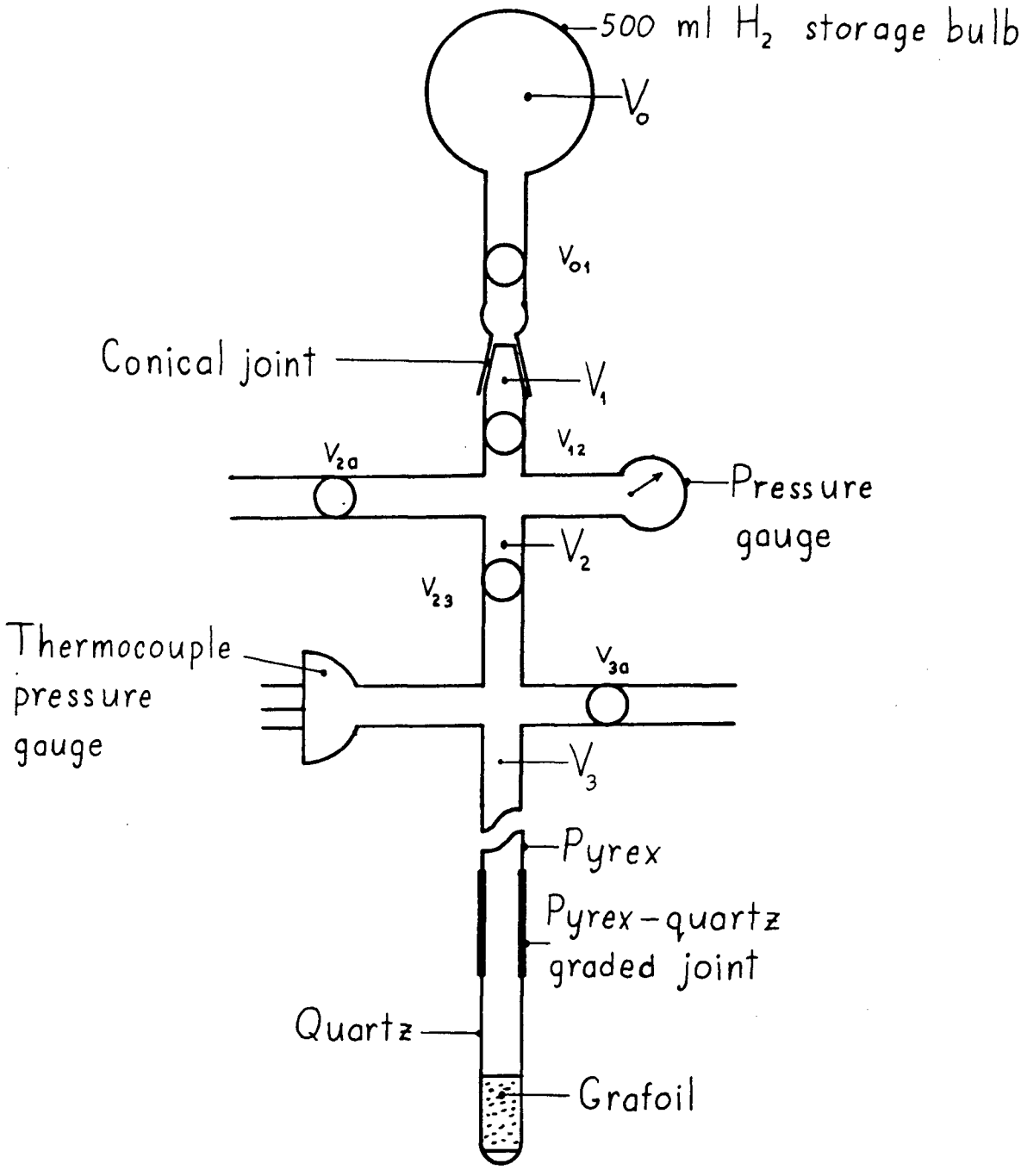

Fig. 17 Sketch of the wand containing the Grafoil sample used in the ^{4}He cryostat (not to scale).

In the ^{3}He cryostat the sample cell was mounted on the ^{3}He pot so the hydrogen was introduced via an insulated, heated stainless steel tube. The system is shown in Fig. 18. It was pumped out and flushed at room temperature as described for the ^{4}He cryostat. On the occasions that the Grafoil cell was baked, it was only heated to 120 C to avoid damaging the copper-quartz joint described in Appendix B. The liquid ^{4}He bath was filled to a few cm above the 4 K plate so that by the time that the hydrogen entered the cell the level was just below the plate. This prevented the formation of cold spots where the hydrogen might condense. The H_2 fill line and ^{4}He pot heaters were used to heat the ^{4}He pot to T_4=52 K and the ^{3}He pot to T_3=40 K. Throughout the process of adsorption $T_4 > T_3$ so that the Grafoil should have been in the coldest region of the fill line. The hydrogen was gradually allowed to enter the Grafoil cell V_4 from the 16.96 cm^3 calibrated volume V_2. After about two minutes, less than 1% of the hydrogen remained in V_2 and the pressure P_4 above the Grafoil was about 1 torr. This pressure was maintained for 6 min at which time 30μ of ^{4}He was allowed into the vacuum can. Five minutes later P_4 had dropped to 100μ, T_4=40 K and T_3=30 K. The vacuum can pressure was increased to 200μ of ^{4}He and 2 min later $P_4 < 1\mu$, T_4=27 K, and T_3=20 K. The heaters were then turned off and within a minute T_4 went to 10 K and T_3 to 4 K. The total time elapsed since the start of adsorption was 16 min.

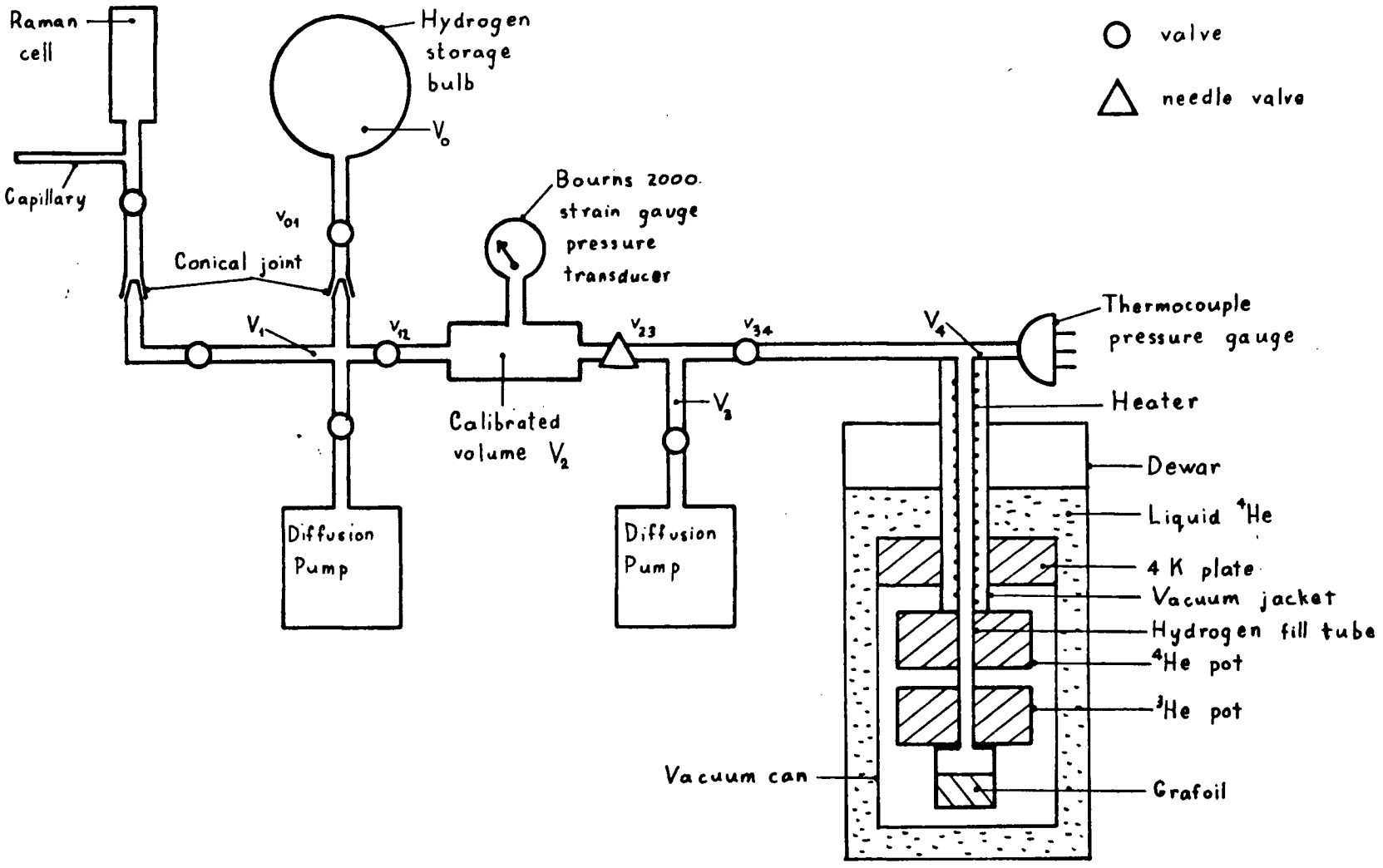

Fig. 18 ^{3}Sketch of the adsorption and desorption apparatus used with the ^{3}He cryostat.

For a few runs a different procedure was tried. T_3 was raised to only about 25 K using the fill line and ^{4}He pot heaters. Hydrogen was then leaked into V_4 through the needle valve V_{23} at such a rate that P_4 was maintained at about 500μ. This was well above the equilibrium vapour pressure but well below the bulk hydrogen vapour pressure. After 10-15 min virtually all of the hydrogen was in V_4 and P_4 began to drop. The heaters were turned off and 50μ of ^{4}He was added to the vacuum can. In about 3 min T_3 dropped to 4 K. This procedure was abandoned because it apparently resulted in non-uniform films: the NMR signals were very weak and broad.

Since the coverage ρ is an important experimental parameter, it was necessary to determine the surface area of the Grafoil substrate. The amount of gas N_3 that will give full coverage in the $\sqrt{3}$ x $\sqrt{3}$ solid, ie. ρ=1, can be determined from the heat capacity, neutron scattering, or adsorption isotherms. The latter was by far the simplest for us.

In principle, it should be possible to determine N_3 by identifying the transition from the $\sqrt{3}$ x $\sqrt{3}$ solid to the incommensurate solid in the low temperature adsorption isotherms as has been done, for example, for Kr adsorbed on graphite. However, this has not been done for light gases such as hydrogen and helium because the pressures involved are quite low, $\lesssim$10μ, and thermomolecular pressure effect corrections would be large. There is controversy concerning the effect of the walls of the container on these corrections (McConville, 1969;

Bernat and Cohen, 1974) (see p. 97).

The approach that we adopted was to use the adsorption isotherms to determine the monolayer coverage N_m of ^4He; this only involves the measurement of pressures greater than a few tens of microns. The heat capacity of ^4He on Grafoil exhibits a sharp peak at $N=N_3$ and a minimum in the heat capacity has been interpreted as monolayer completion (Bretz et al, 1973; Huff and Dash, 1976). These measurements gave $N_3/N_m=.556$ at 1.0 K. Also, the lattice parameters of ^4He on graphite at $N=N_3$ and $N=N_m$ have been measured by elastic neutron scattering (Carneiro et al, 1976). Assuming a uniform surface, these results imply $N_3/N_m = .561$ at 4.2 K in good agreement with the heat capacity measurements.

We determined N_m for ^4He by the "Point B" method (Young and Crowell, 1962). This is an empirical procedure that has been used extensively for determining monolayer coverages although it is not as precise as the heat capacity method. For each layer of adsorbed molecules, interactions between molecules can be neglected at low coverages so that Henry's Law (Young and Crowell, 1962) should be valid. It states that for a uniform surface the pressure is proportional to the coverage. In practice, there will always be some rounding of the isotherms due to surface heterogeneity and thermal promotion to the next layer. The point at which the isotherm becomes linear is "Point B"; this has been interpreted as layer completion. Applying the Point B method to their ^4He on Grafoil adsorption isotherms at

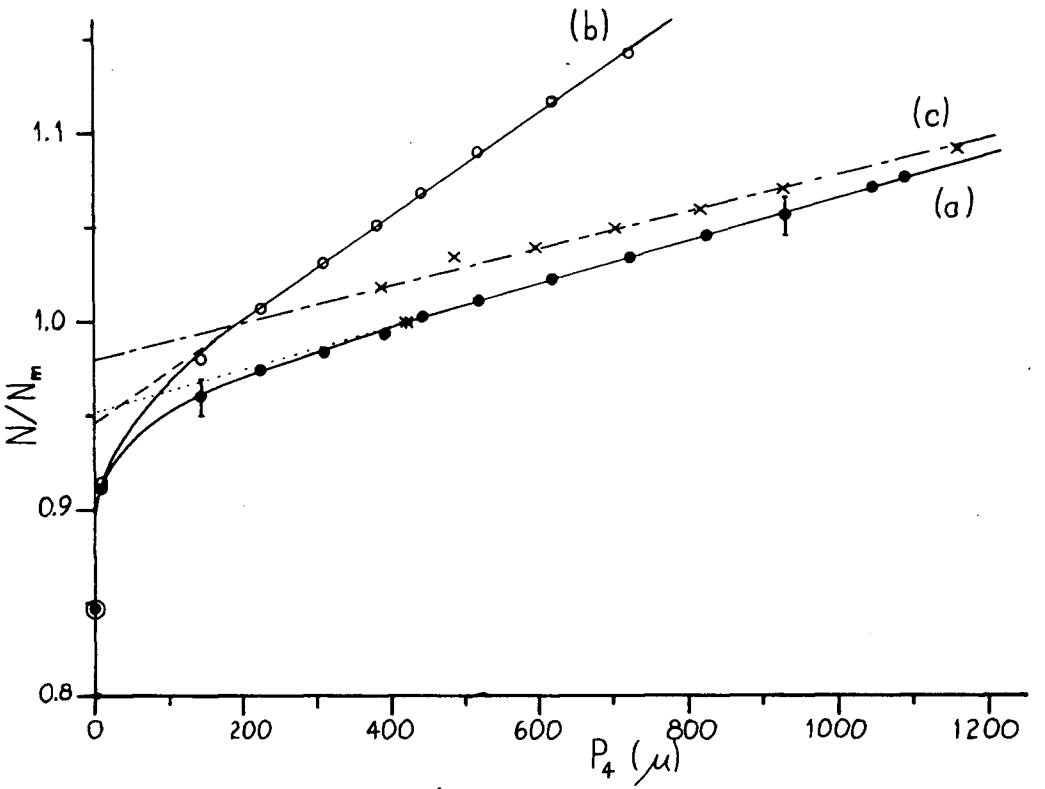

Fig. 19 Adsorption isotherm for ^{4}He on Grafoil: P_4 versus N/N_m. Monolayer coverage N_m was determined by the Point B method. Dashed lines are extrapolations of the Henry's Law region. Point B is denoted by an asterisk. The solid circles [curve (a)] were obtained from our Grafoil substrate in cell B after correcting for the vapour in the dead volume. The error bars are primarily due to the error in measuring the calibrated volume V_2. The open circles [curve (b)] show the total amount N of helium removed from the calibrated volume. In this case, N/N_m was calculated using N_m from curve (a). The crosses [curve (c)] are the data of Goellner et al (1975).

4.2 K, Goellner et al (1975) found a monolayer density of $.115\mathring{A}^{-2}$, which agreed with the heat capacity result.

Fig. 19(a) shows our 4.23 K isotherm of ^4He on the Grafoil sample in cell B, which is described in section 6.3. The number of adsorbed molecules is normalized to monolayer coverage N/N_m. Note that there is clearly a region where Henry's Law is valid. The pressure above the Grafoil, P_4, was measured by an MKS Baratron model 170 capacitance manometer with a 1 torr sensor. Corrections for the thermomolecular pressure difference between 4.2 K and 300 K have been made using the data of Roberts and Sydoriak (1956); they found good agreement with the Weber-Schmidt equation (Weber and Schmidt, 1936). The corrections were significant at the lower pressures, being -14% at 145 μ but only -3% at 520μ.

The adsorption isotherm was measured by metering a quantity N_T of gas from the calibrated volume V_2 into V_3 and V_4 (see Fig. 18). For pressures P_4 near 100μ, it was necessary to wait up to two hours for P_4 to approach equilibrium but this time was reduced to a few minutes for $P_4>200\mu$. To determine the quantity N of hydrogen adsorbed on the Grafoil, it was necessary to correct for the 3D vapour in V_3 and V_4; this is called the dead volume correction. Of this volume, 12 cm^3 was at room temperature, 8 cm^3 was at 4.2 K, and 12 cm^3 was in a vacuum jacketed tube between 4.2 K and room temperature. Since the temperature gradient down the tube was not known, it was difficult to predict the amount of gas in it.

However, there was a similar tube connected to a vapour pressure cell in the ^{3}He pot which could be filled with ^{4}He and sealed off. By monitoring the pressure in that tube as a function of the level of the liquid helium bath, the amount of gas in the fill line for the Grafoil cell could be estimated. In fact the pressure in the vapour pressure line was almost insensitive to the liquid helium level. Although the dead volume correction was quite large for $P_4 > 100\mu$, it only changed the position of Point B by 2% [compare Fig. 19(a) and (b)].

For comparison purposes, the 4.24 K ^{4}He on Grafoil adsorption isotherm obtained by Goellner et al[2] is also shown in Fig. 19(c). The data has been normalized using the monolayer coverage of 6.56 cm^3(STP) determined by Goellner et al using the Point B method. The slopes of Fig. 19(a) and (c) are slightly different; this is probably due to an error in our dead volume correction. The shift in the curves is probably the result of an error in the Point B determination: Goellner et al chose Point B to be at $P_4 = 200\mu$, whereas we have taken it to be at 430μ. There are several possible explanations. According to McConville (1969), the thermomolecular pressure effect correction for stainless steel tubes (which were used in our ^{3}He cryostat) is larger than that predicted by the Weber-Schmidt equation. This would mean that our values of P_4 are too high especially at pressures below about 200μ. However, this point is controversial. Goellner et al used a capacitance manometer operating at 4.2 K so they had no thermomolecular

pressure difference. For pressures near 100 μ, equilibration times for the adsorption of hydrogen were greater than an hour so our pressures in this range could be too high.

Using Point B, we have estimated monolayer coverage to be 6.63 cm^3(STP)/g ±3% for ^{4}He. For a monolayer density of .115 $Å^{-2}$, this corresponds to a specific surface area of 15.6 m^2/g for the Grafoil in cell B - somewhat less than the usual range of 20-30 m^2/g for Grafoil but quite close to Goellner et al.

Upon completion of an NMR experiment, the hydrogen was quickly desorbed and transferred to the Raman cell for measurement of the J=1 concentration. The procedure for doing this is as follows. First the liquid ^{4}He was boiled off until its level was below the 4 K plate. The hydrogen fill line was then heated at a rate of 2.3 W until T_3 = 10 K. Then the ^{3}He pot was also heated at 2.3 W. Meanwhile, one arm of the evacuated Raman cell was exposed to a stream of cold ^{4}He gas from a liquid ^{4}He storage dewar. After the ^{3}He pot had been heated for 5-8 min, the pressure P_4 approached a maximum and the hydrogen was allowed to enter the Raman cell. It liquified in the cell so that within a minute virtually all of it was removed from the cryostat. The cell was then sealed and taken to the Raman spectrometer.

5.6 Conversion Rate Measurements

H_2 molecules with I=1 produce a dipolar magnetic field,

which results in a field gradient at neighbouring molecules. This is the source of the intrinsic conversion of H_2. It leads to a second order rate equation

$$dc/dt = -kc^2 \qquad (V-4)$$

which is obeyed in bulk solid H_2 with k = 1.90(5)%/h (Silvera, 1980).

The same process occurs in D_2. In addition, I=1 molecules interact with the dipolar fields produced by the I=2 molecules and, since deuterons have a nuclear spin i=1, they also interact with the electric field gradient produced by those D_2 molecules which have an electric quadrupole moment (I=1 or 2). Thus, the rate equation contains both first and second order terms

$$dc/dt = -kc^2 - k'c(1-c) \qquad (V-5)$$

For bulk solid D_2, it has been found that $k \simeq k' = .060(3)\%/h$. Consequently, the rate equation is approximately first order.

For hydrogen adsorbed on graphite, one might expect interactions with the surface to catalyze conversion, particularly if there were paramagnetic impurities or dangling bonds with associated unpaired electrons. Conversion would then be a first order process

$$dc/dt = -kc \qquad (V-6)$$

We have determined the conversion rate of o-H_2 and p-D_2 in the $\sqrt{3}$ x $\sqrt{3}$ solid phase on Grafoil by measuring the time dependence of the integral of the NMR adsorption spectrum S. It is proportional to the static magnetization M_o produced

by the magnetic field H_o in the absence of the RF excitation field H_1. In the high temperature limit, which pertains in our case, M_o obeys the Curie Law

$$M_o = C/T \qquad (V-7)$$

For N nuclei with spin I and gyromagnetic ratio γ, the Curie constant C is given by (Abragam, 1961)

$$C = N\gamma^2\hbar^2 I(I+1)H_o/3k \qquad (V-8)$$

For sufficiently low values of H_1, S is proportional to H_1 and the shape of the spectrum is independent of H_1. However, if the saturation parameter $\gamma^2 H_1^2 T_1 T_2$, where T_1 and T_2 are the longitudinal and transverse relaxation times, becomes comparable to 1, S increases more slowly than H_1 and the shape of the spectrum will depend on H_1. Usually for solids, T_1 increases as T decreases so saturation becomes more likely.

In order that we be able to plot data obtained under different conditions on the same graph, S has been normalized. The normalized amplitude s is defined by

$$s = a\, S/(mNGQV_i) \qquad (V-9)$$

where a = arbitrary constant

m = number of sweeps through the resonance

N = number of hydrogen molecules

G = total gain of the measuring system

Q = quality factor of the NMR tuned circuit

V_i = RF input voltage to the tuned circuit

QV_i is the RF voltage across the coil which contains the

Grafoil. In the absence of saturation, s should be proportional to the fraction of hydrogen molecules with I=1 and to T^{-1} but independent of all other parameters.

Our final H_2 spectra were obtained from three samples labelled G19, G20, and G21. All of these were contained in cell B. The first two samples were used to study the temperature dependence of the spectra at high J=1 concentrations and were removed after the hydrogen had been adsorbed for a total time t of less than 80 h. Sample G21 was studied until c had dropped to .2 after nearly 400 h.

Fig. 20 is a plot of sT_3 versus t for this sample at 1.81, .575, and .333 K. At each temperature the data were fitted to the equation

$$\ln (sT_3) = -kt + \ln (s_i T_3) \qquad \text{(V-10)}$$

with k and s_i as parameters. (V-10) is derived from the first order rate equation (V-6).

The 1.81 K data has the least scatter because it is near the temperature at which the S:N ratio was the highest. At higher temperatures, the absorption signal was a little narrower but its amplitude had dropped because of the Curie Law. At temperatures below 1 K, the signal broadened considerably so that the amplitude dropped despite the net increase in area due to the Curie Law. In addition, there was coherent noise (discussed in Chapter VII) which became more severe at low temperatures. The scatter in the data increased with time because of the decrease in J=1 concentration c.

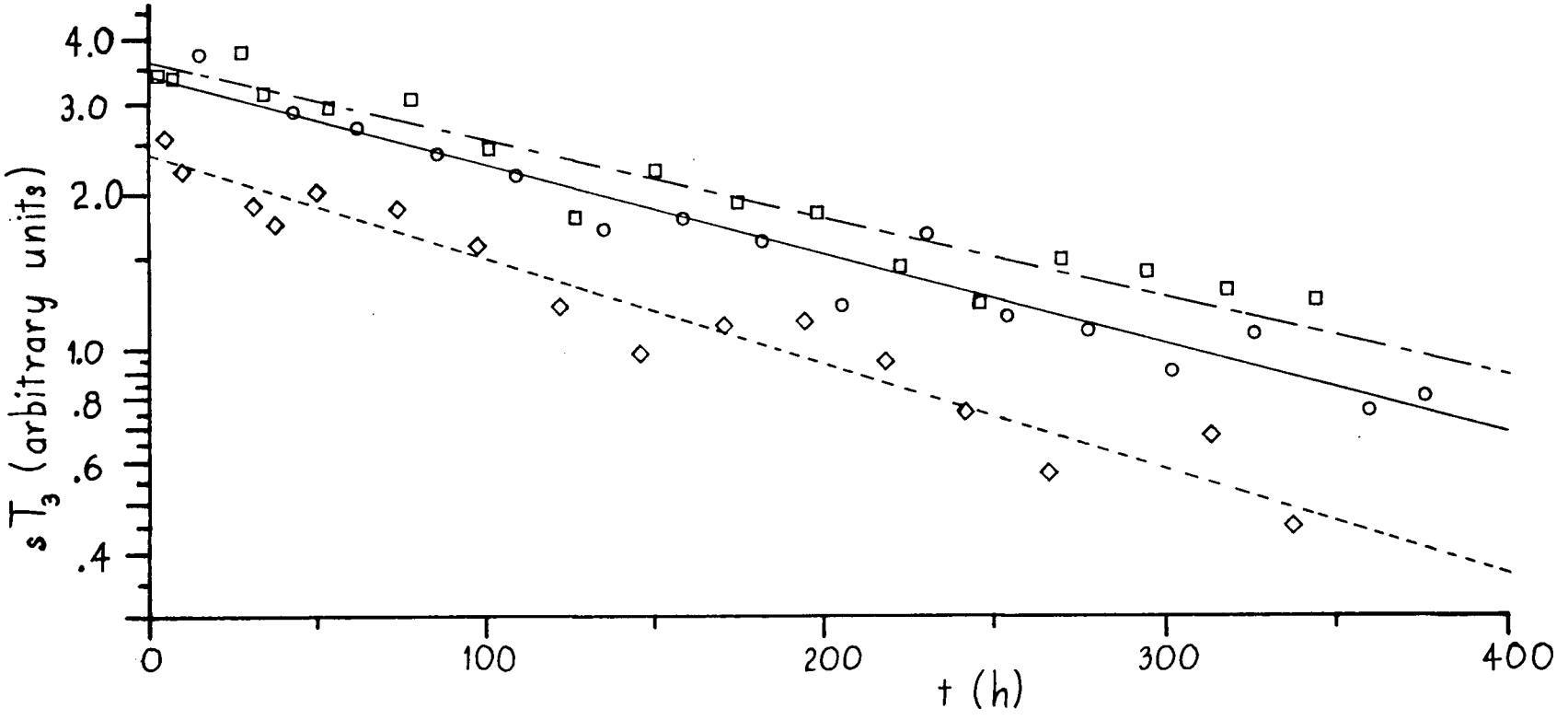

Fig. 20 Graph of sT_3 versus the time since adsorption, t, for H_2 sample G21 at: (a) T_3=1.81 K (circles, solid line), (b) T_3=.575 K (squares, dot-dashed line), and (c) T_3=.333 K (diamonds, dotted line). All of the data have the same RF input attenuation, A=13 dB. The lines are two parameter least squares fits to the data at each temperature. The slopes k and intercepts s_iT_3 are given in Table VII.

The results of the two parameter least squares fit to (V-10) are shown in Table VII. The data were weighted by the square of the S:N ratio. The values of s_iT_3 at 1.81 K and .575 K are about the same but s_iT_3 is decidedly lower at .333 K. The reason is discussed in section 7.3. On the other hand, there is moderately good agreement between the three values of k. Consequently the weighted mean of the three values, k = .40(2)%/h, was used and one parameter least squares fit were made to the data at each temperature to find the new y-intercepts $s_i'T_3$ (see Table VII). A graph of $1/sT_3$ was also plotted; it would be linear if the rate equation were second order. The fit to a straight line was much poorer than in Fig. 20.

Table VII $\underline{O\text{-}H_2}$ Conversion Rate Constants

T_3(K)	k(%/h)	s_iT_3	$s_i'T_3$
1.81	.402 (27)	3.43 (15)	3.40
.575	.355 (28)	3.67 (14)	3.82
.333	.457 (36)	2.40 (10)	2.27

Having measured the conversion rate, it was necessary to determine the absolute concentrations of the H_2 samples. An absolute calibration of the NMR spectrometer would have been difficult because it would have entailed a calibration of the spectrometer gain. This might have been done by measuring S for a known quantity of $o\text{-}D_2$ or HD. It would have been necessary

to ensure that there was no saturation or RF heating by checking the signal at lower RF levels, reducing the already marginal S:N ratios. In section 7.4, we present evidence that the o-D_2 signal was saturating at the normal RF levels used for o-H_2 and p-D_2 samples.

We were able to avoid the calibration by measuring the J=1 concentration before adsorption and after desorption using the rotational Raman spectra. The amount of conversion during adsorption and desorption was unknown but it was possible to make estimates based on the time for adsorption and desorption, the initial and final concentrations, and the relative change of concentration obtained from the NMR measurements. In addition, the NMR spectra of H_2 sample G21 provided information about the shape of the NMR spectra at a fixed temperature as a function of time. For example, using that information, it was clear that for a G21 spectrum taken at t=3.55 h and T_3=.573 K, c must have been lower than for two G20 spectra taken at t=10.19 h and T_3 = .382 K and at t = 7.88 h and T_3 = .563 K.

Table VIII contains the data used to estimate the concentration c_i at the completion of adsorption (t=0). The concentrations before adsorption and after desorption as measured by Raman spectroscopy are c_a and c_d. The times elapsed during adsorption and desorption are t_a and t_d. The time between adsorption and desorption is t_f.

Using these values of c_i, a graph of c/c_i versus t has been plotted in Fig. 21. The data for G21 and G19 fit the

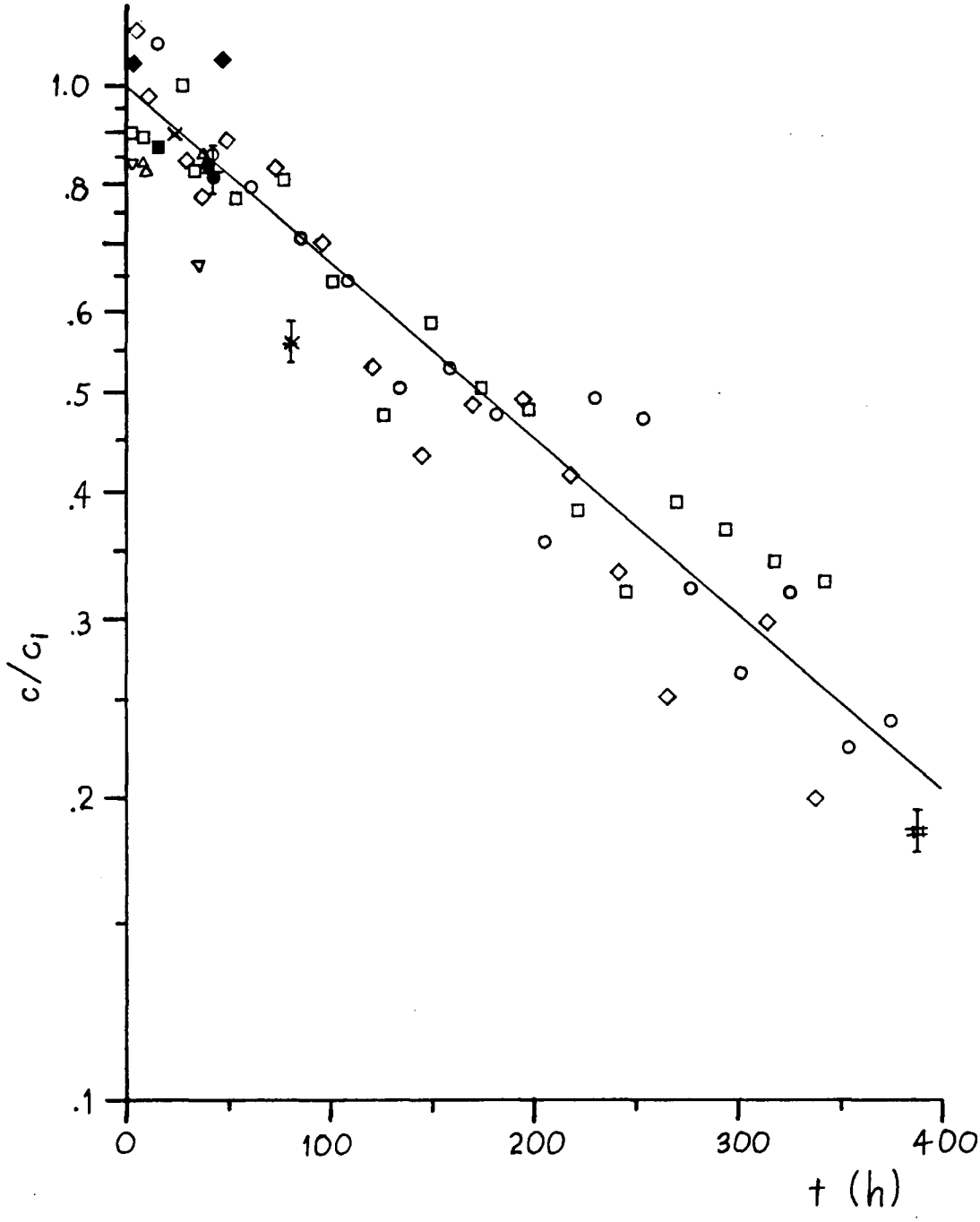

Fig. 21 Graph of c/c_i versus t for three H_2 samples, all in cell B, at three temperatures T_3: (a) G21, 1.81 K (open circles); (b) G21, .575 K (open squares); (c) G21, .333 K (open diamonds); (d) G21, Raman (#); (e) G19, 1.8 K (solid circles); (f) G19, .57 K (solid squares); (g) G19, .31 K (solid diamonds); (h) G19, Raman (*); (i) G20, 1.8 K (x); (j) G20, .57 K (open triangles); (k) G20, .33 K (inverted open triangles); and (l) G20, Raman (+). In every case, A=13 dB. The straight line has a slope k=.40%/h, which was obtained from the G21 data.

straight line fairly well. All of the data for G20 fall on or below the line. Nevertheless, the value of c_i taken in that case is supported by the comparison of the shapes of some of the spectra as described above and by the Raman results. For G19 and G20, c_d was above the equilibrium concentration at all temperatures during desorption so it is a lower limit for $c(t=t_f)$. For G21, c_d was equal to c_{eq} at T≈40 K, a temperature at which the hydrogen would have been partially desorbed. Therefore c_d could be either smaller or greater than $c(t=t_f)$.

Table VIII. Initial J=1 Concentrations of the H_2 Samples

Sample	c_a	c_d ±.02	t_a(min)	t_d(min)	t_f(h)	c_i ±.03	$c_i e^{-kt_f}$
G21	>.96	.17	8	13.5	388.10	.93	.20
G20	>.98	.79	5	14	43.00	.96	.81
G19	>.98	.56	12	16	76.38	.95	.70

For D_2, conversion rate measurements were less precise than for H_2 because the S:N ratio was much poorer and the rate constant was smaller. Coherent noise made the determination of the baseline of the spectra very difficult in many cases. Data concerning the effects of the temperature and the RF level on the magnitude of the integral of the absorption spectrum were minimal (see section 7.4).

Those J=0 molecules that have I=2 give a narrow line at the centre of the spectrum. At high temperatures, the J=1 molecules produce a doublet with a splitting that increases as T decreases: the same as for H_2. Near 1 K, the broadening begins to increase much more rapidly than the splitting so that at low tempratures the doublet transforms into a weak, broad hump. Consequently, the conversion rate measurements were restricted to $T_3 \geq$ 1.6 K. Above 4 K the splitting becomes small and it is difficult to separate the J=0 and J=1 components: those spectra were not used either. For 1.6 K $\leq T_3 \leq$ 4.2 K, the normalized integrals s_o and s_1 of the J=0 and J=1 components of the adsorption spectra obeyed the Curie Law (see section 7.4).

Had it been necessary to rely on s_1 alone to determine the conversion rate, it would not have been possible to get a reliable estimate because the scatter was so large. However, the absolute J=1 concentration can be obtained from the ratio s_1/s_o since

$$s_1/s_o = \{I_1(I_1+1)/I_2(I_2+1)\}\, c/\{(5/6)(1-c)\} \qquad \text{(V-11a)}$$

$$= (2/5)\, c/(1-c) \qquad \text{(V-11b)}$$

where I_1=1 and I_2=2. The factor of 5/6 is the fraction of J=0 molecules that have I=2.

The D_2 conversion rate data is not extensive enough to ascertain whether the rate equation is first or second order. However, for H_2 conversion was found by experiment to follow a first order rate equation so that in this case conversion must

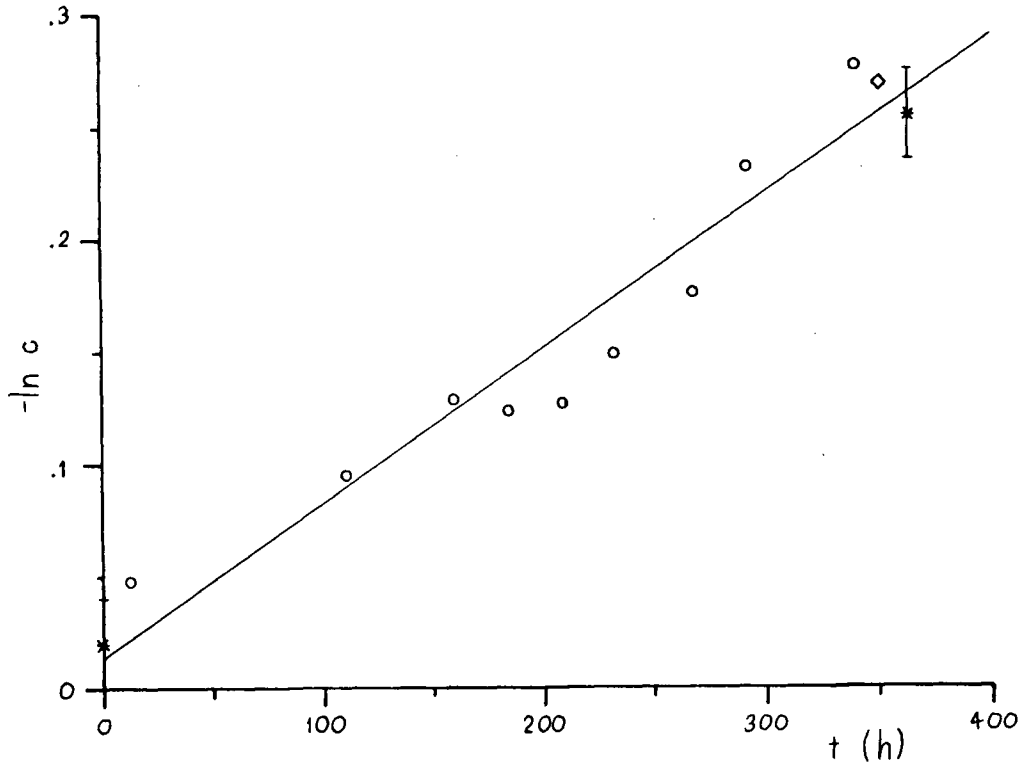

Fig. 22 Graph of -ln c versus t for D_2 sample G18 in cell B. 1.6 K $\leq T_3 \leq$ 4.2 K. The RF input attenuation was A=13 dB (circles) or A=19 dB (diamond). The concentrations before adsorption c_a and after desorption c_d, determined by Raman scattering, are also shown (*). The line is a least squares fit to the NMR data. It gives c_i=.99(2) and k=.069(15)%/h.

be catalyzed by the surface. Presumably the same is also true fo D_2 given that its intrinsic conbersion rate is less than that of H_2.

A graph of -ln c versus t for D_2 sample G18 in cell B is shown in Fig. 22. The Raman measurements before adsorption and after desorption are also shown. The former is a lower limit on -ln c and the latter is an upper limit. A least squares fit to the NMR data gives c_i=.99(2) and k=.069(15)%/h.

Some D_2conversion rate measurements were also made for cell A which contained a different type of Grafoil from cell B (see section 6.3). Fig. 23 is a plot of -ln c versus t obtained from p-D_2 sample G7 in cell A. The data covers a very limited concentration range from .94 to .97. A least squares fit to a first order rate equation gives c_i=.976(4) and k=.026(7)%/h. The rate constant is only .38 of that measured for cell B; it is not surprising that different types of Grafoil give different conversion rates.

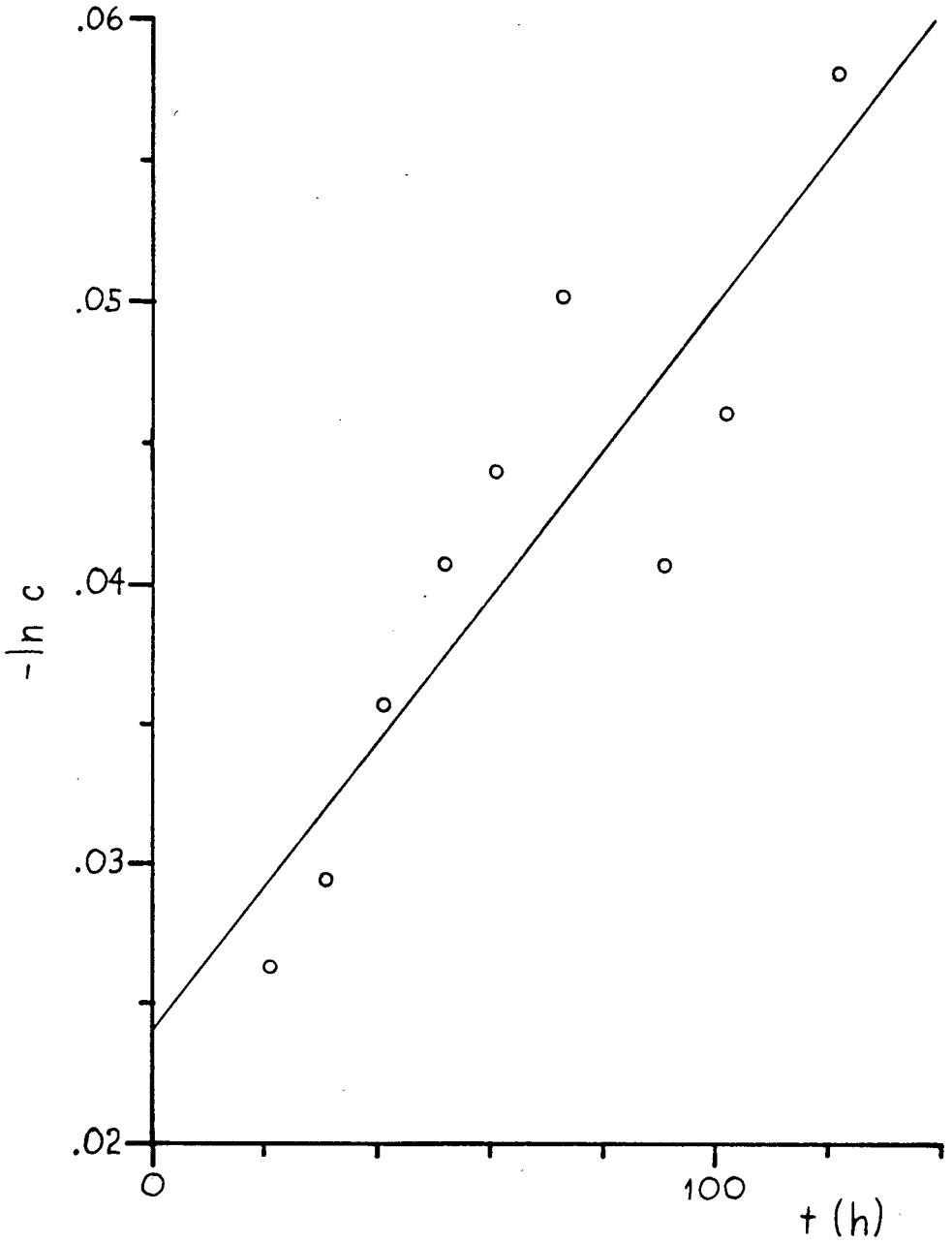

Fig. 23 Graph of -ln c versus t for D_2 sample G7 in cell A. .3 K $\leq T_3 \leq$ 1.4 K. A=14 dB. The line is a least squares fit. It gives c_i=.976(4) and k=.026(7)%/h.

Notes to Chapter V

1. Alcoa Chemicals, activated alumina grade F-1, mesh 8-14.

2. The data were actually taken from Novaco (1975). The data of Goellner et al for $P_4 < 388\mu$ were not tabulated.

CHAPTER VI

THE NMR CRYOSTATS

6.1 The ^{4}He Cryostat

Our first NMR measurements for hydrogen adsorbed on Grafoil were made in the temperature range 1.3-4.2 K using a cryostat which was immersed in liquid ^{4}He. The primary purposes of the measurements were to determine the crystal field and to search for evidence of orientational ordering. In these experiments, the Grafoil was at the bottom of a long Pyrex wand with a quartz tip (Fig. 17), which could be lowered into the liquid ^{4}He. The temperature was controlled by pumping on the bath using either a rotary pump throttled by a Walker regulator (Walker, 1959) or a diffusion ejector pump. The ^{4}He vapour pressure was measured by a mercury manometer, an oil manometer, or a McLeod gauge depending upon the pressure. Corrections for the thermomolecular pressure effect were made at the lowest pressures. The pressure was converted to the temperature of the ^{4}He bath using the 1958 ^{4}He temperature scale (van Dijk et al, 1960).

The tip of the 9 mm outside diameter (OD) wand fit snugly inside a coil holder containing a 10 mm long, 10 turn, 1.1 μH copper coil which produced the oscillating magnetic field to excite the spins in the sample. The coil, composed of 26 AWG wire, was wrapped on a thin, threaded Teflon cylinder which was placed inside a more rigid outer cylinder of Teflon. The

thermal contraction of Teflon exceeds that of both copper and quartz so the whole assembly fit tightly together at low temperatures, reducing the possibility of microphonics.

Most of the NMR measurements were made using a sample consisting of 39 g of .25 mm thick, rectangular Grafoil sheets[1] with a density of 1.12 g/cm^3. These were interleaved with .01 mm Teflon sheets in order to reduce RF shielding since Grafoil is an electrical conductor (Hedge et al, 1973). Copper plates were inserted against the outer Grafoil sheets to squeeze the sample tightly inside the quartz tube. This improved the thermal contact between the Grafoil and the quartz tube and helped to prevent microphonics. Prior to assembly of the sample, the Grafoil sheets had been baked under vacuum at 1000 C for 12 h and purged several times with pure H_2 gas. The Grafoil was exposed to air while the sandwich was being assembled and was then baked under vacuum at 220 C for 15 h and purged with H_2. We were concerned that Teflon vapour might contaminate the Grafoil so a second sample was constructed in which the Teflon was replaced by .1 mm thick sapphire plates. After assembly this sample was baked at 900 C. It gave identical NMR signals to the Grafoil and Teflon sample.

We employed an 8.5 MHz continuous wave, single coil NMR spectrometer. The absorption signal (the imaginary part of the susceptibility) was observed by sweeping the magnetic field through the resonance, which was at .2 T for H_2 and 1.3 T for D_2. Simultaneously, the field was modulated at 280 Hz by

.17 mT peak to peak. The AC component of the amplified voltage across the coil was then demodulated using a lock-in detector and fed into a signal averager. This yielded the derivative of the absorption, which could be integrated using the "integrate" facility of the signal averager.

In order to prevent spurious NMR signals from being detected when we observed the resonance of the H_2 molecules, fairly exacting measures were necessary to keep the number of ^1H nuclei near the coil at an acceptably low level. The modulation coils, composed of enamelled copper wire, were covered by aluminum foil to shield them from the RF field. Initially the Grafoil had been placed inside a Pyrex tube but it was found that at 4 K the Pyrex produced an absorption peak with a full width at half maximum (FWHM) of .16 mT. Its amplitude was comparable to that of the o-H_2 signal which had a FWHM of .56 mT at 4 K. No ^1H signal could be detected in quartz so the Pyrex was replaced by quartz. Despite these measures, a triangular ^1H signal with a FWHM of 1.1 mT persisted. Teflon gave an ^1H signal of the same shape. It could be reduced by baking the Teflon under vacuum at 220 C for two days so the Teflon coil holder and Teflon sheets in the wand were also baked under vacuum. Afterwards, the background signal had an amplitude of about one third that of o-H_2 at 4.2 K; the background was still significant. Consequently, it was necessary to measure the background signal before the H_2 was adsorbed on the Grafoil and later subtract it from the signal obtained with

o-H_2 adsorbed. Presumably the background signal was from the Teflon, although we could not rule out the possibility that some other material produced an ^1H signal of the same shape.

In order to maintain the homogeneity of the magnetic field, no superconducting metals could be allowed near the NMR coil. For type I superconductors below their critical temperature T_c, magnetic flux penetration is zero (apart from a very thin region at the surface) in a magnetic field H less than a critical value H_c and it is complete for $H>H_c$. For type II superconductors, it is zero for $H<H_{c1}$ and complete for $H>H_{c2}$ where

$$H_{c1} H_{c2} = H_c^2 \qquad \text{(VI-1)}$$

Typically $H_{c2}-H_{c1} \sim .1-.5\ H_c$. H_o was above H_c for any type I superconductor but did not exceed H_{c2} of many type II superconductors, in particular some solders. Many of these also have $T_c>4$ K. Solder joints near the NMR coil were made using the following materials: In (type I, T_c = 3.4 K, H_c = .0293 T), Pb (type I, T_c = 7.2 K, H_c = .080 T), and 60 Sn/40 Pb [type II, T_c = 7.0 K, H_c = .083 T, $(H_{c2}-H_{c1})/H_c$ = .18].[2]

6.2 The ^{3}He Cryostat

The NMR measurements made using the ^{4}He cryostat allowed us to determine $|V_c|$ and Γ for H_2 and D_2 but did not show any evidence of cooperative orientational ordering (Kubik and Hardy, 1978). However, they did show that EQQ interactions were

important, at least for D_2. This motivated us to build a ^3He cryostat that would allow us to extend the measurements down to .3 K. The cryostat was also built with a view to extending the measurements up to 25 K in order to study the solid-fluid transition. Due to lack of time, no measurements have been made above 12 K: the S:N ratio deteriorates rapidly above 8 K. We could have attained even lower temperatures using a dilution refrigerator but this would have been more difficult to construct. It also seemed very likely that the interesting orientational behaviour would occur above .3 K.

The principle of ^3He cryostats is simple and good discussions of their design are contained in Rose-Innes (1973) and Lounasmaa (1974). The tail of our cryostat is depicted in Fig. 24. The cryostat was immersed in a bath of liquid ^4He. The first cooling stage below 4 K was a continuously operating ^4He refrigerator which served to condense the ^3He gas from a tank at room temperature and to thermally shield the ^3He pot. Liquid ^4He was pumped from the bath through a flow impedance into the ^4He pot where it boiled at 1.3 K. When the valve on the ^3He supply tank was opened, 1.6 l(STP) of ^3He gas was adsorbed by a charcoal adsorption pump at sub-monolayer coverage. The ^3He valve at the top of the cryostat was closed and the pump was heated at .5 W to desorb the ^3He, which would then condense as it passed through the ^4He pot and dribble into the ^3He pot. After 20 min the pump temperature reached 35 K and nearly all of the ^3He was desorbed. It was then

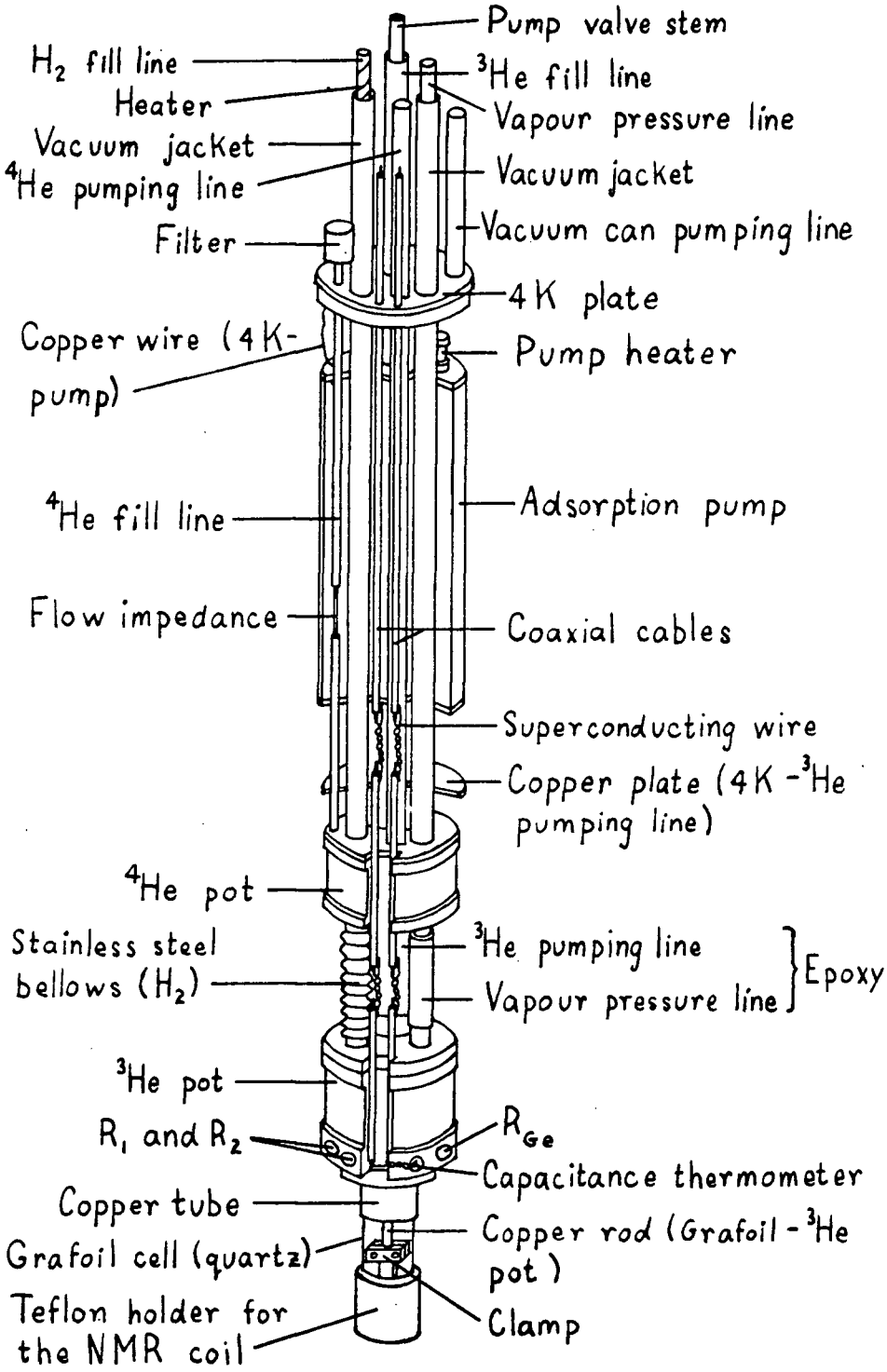

Fig. 24 The tail of the ^{3}He cryostat, drawn approximately to scale. The section below the 4 K plate was enclosed in a vacuum can, which was soldered to the 4 K plate.

necessary to turn off the pump heater or the ^{4}He pot would be drained and warm up to 4 K. As the charcoal cooled, it would begin to adsorb ^{3}He producing a minimum temperature of T_3 = .295 K after about 30 min. Operation at .3 K could be sustained for 18 h before the ^{3}He had to be recondensed, implying a heat leak of 30μW into the ^{3}He pot. For operation at higher temperatures, it was often necessary to heat the ^{3}He pot; at a temperature of 1.2 K, the ^{3}He only lasted about 3 h.

Up to .6 K, the temperature could be controlled by means of a throttle valve at the base of the adsorption pump. This consisted of an 8 mm long, tapered brass plug in a 12.7 mm OD, stainless steel tube. As the charcoal surface became covered with ^{3}He the pumping speed decreased. However, temperature stability of <1 mK could be maintained by opening the throttle valve slightly every 15 min or so. Alternatively, the temperature could be controlled using a Lakeshore Cryotronics CS-400 GR $SrTiO_3$ capacitance sensor on the ^{3}He pot, a detector consisting of a General Radio 1615A capacitance bridge with a Princeton Applied Research 122 lock-in amplifier, an A-05 temperature controller constructed by the departmental electronics shop, and a heater on the ^{3}He pot. Typically, 5 μW of heater power was used. The capacitance sensor exhibited considerably more drift than the carbon and germanium resistors used for temperature measurements. The rate of drift increased as T decreased, since below 1 K the sensitivity of the capacitance sensor dropped. Even at .3 K, this was not a problem

because the drift rate was only -.3 pF/h,[3] corresponding to about -2 mK/h. At .6 K the drift rate was -.05 pF/h, corresponding to -.3 mK/h.

Above .6 K the throttle valve was kept closed. In order to avoid putting large amounts of heat directly into the ^{3}He pot and boiling off ^{3}He, the ^{3}He pressure in the pump was regulated by heating the pump in order to lower its pumping speed. The pressure was controlled using an MKS Baratron model 170 capacitance manometer with a 1000 torr sensor and another A-05 temperature controller. It was found to be best to control the ^{3}He pot temperature directly as well because the pump had a long thermal time constant. Once the pressure had stabilized, regulation by the pump pressure alone was as good as with the capacitance sensor on the ^{3}He pot.

At T_3 = 1.3 K, the pump heater power was .2 W. If the heating was increased much more the ^{4}He pot would begin to drain causing the ^{3}He to boil off rapidly. It was impossible to operate in the range 1.3 K $< T_3 <$ 1.6 K for more than a few minutes so no NMR measurements were made there.

Between 1.6 K and 4.2 K, the ^{3}He pot was empty and its temperature was maintained by throttling the ^{4}He pot pump and using the capacitance sensor to regulate T_3. The ^{4}He pot could operate as low as 1.3 K but the minimum ^{3}He pot temperature during NMR measurements was 1.6 K due to eddy current heating by the magnetic field modulation and to a lesser extent by the RF field. Above 4.2 K only the capacitance sensor was

used to regulate the temperature.

Some of the components of the ^3He cryostat will now be discussed in more detail. The adsorption pump was a 9.0 cm long, 3.5 cm diameter semi-circular copper cylinder which contained 16.3 g of Fisher activated coconut charcoal (6-14 mesh). Coconut charcoal was chosen over zeolite, another common adsorbent, because per unit volume of bulk material charcoal has a monolayer capacity of 170 $cm^3(STP)/cm^3$ at 4.2 K (Rose-Innes, 1973) compared to 130 $cm^3(STP)/cm^3$ for zeolite (Daunt and Rosen, 1970). Above 4 K the monolayer capacity of charcoal for helium drops rapidly from its low temperature value of 390 $cm^3(STP)/g$ so for effective pump operation at low temperatures, it is crucial that the charcoal be well anchored thermally to the ^4He bath. Consequently parallel copper plates were placed inside the pump 6 mm apart to aid in cooling the charcoal. The plates contained holes to facilitate gas flow.

The pump was cooled via a .1 mm diameter, 18 mm length of copper wire attached to the 4 K plate. Ideally the thermal link should have very high thermal conductance at 4 K and very low thermal conductance between about 20 K and 40 K. Thus, when the pump is adsorbing ^3He, it will not be heated much above 4 K but when it is heated to 30-40 K to desorb the ^3He, it will not provide a large thermal load for the ^4He bath. Some high purity metals satisfy this criterion fairly well because they have a peak in their thermal conductivity near 10 K. The

greater is the purity, the higher the peak and the lower the peak temperature. We used commercial copper wire but its thermal conductivity was increased by annealing for 24 h at 970 C under a pressure of 1.0×10^{-4} torr of dry air (Rosenblum et al, 1977). Assuming a 30 μW heat leak into the ^{3}He pot, the heat of adsorption would generate 1.7 mW in the pump. The temperature rise of the pump was found to be <1 K. The pump could be maintained at 45 K by .5 W of heater power.

The continuously operating ^{4}He refrigerator shown schematically in Fig. 25 was based on the design of De Long et al (1971). When pumping on the ^{4}He pot commenced, liquid ^{4}He was drawn from the main bath at 4.2 K, through the filter and flow impedance, into the ^{4}He pot. There was a pressure differential across the flow impedance causing the ^{4}He to be cooled to 1.3 K. About half of the latent heat of evaporation of the ^{4}He was required to cool the incoming ^{4}He. The remainder was used to balance the heat flux into the ^{4}He pot. If there were no external load, the liquid ^{4}He rose up the pumping tube until the heat flux down the tube equalled the refrigeration capacity. As the load increased, the liquid level dropped until, at the critical power $\dot{Q}_c$, the ^{4}He pot itself began to be depleted. Eventually it was emptied and the temperature rose rapidly. $\dot{Q}_c$ is the long term power input that the ^{4}He pot can sustain. During the ^{3}He condensation, we found that $\dot{Q}_c$ was exceeded; the length of time for which T_4 could be maintained at 1.3 K under overload

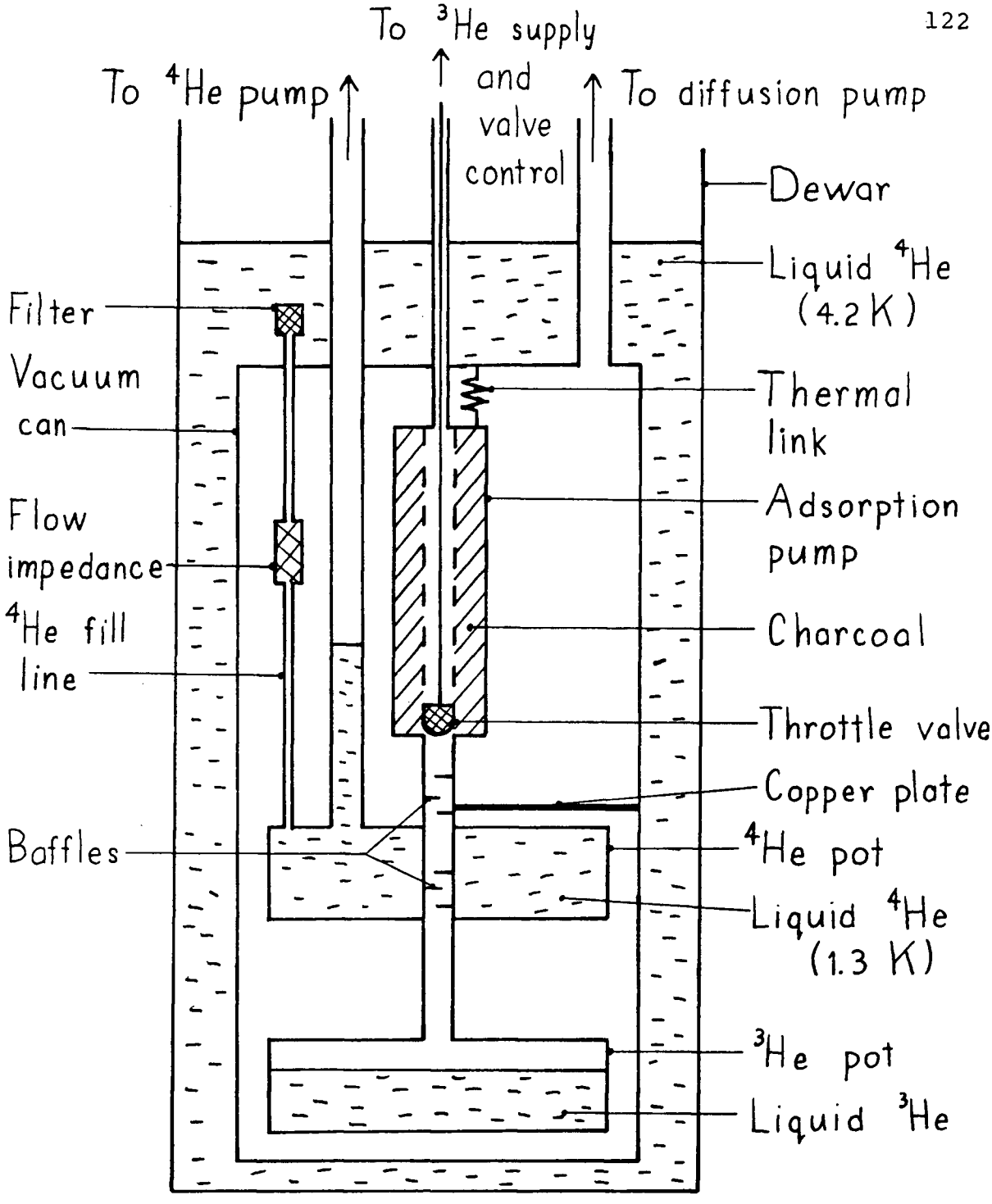

Fig. 25 Schematic diagram of the ^{4}He refrigerator. The Grafoil cell and hydrogen fill line have been omitted. The thermal link at the top of the adsorption pump is a copper wire. The copper plate between the ^{3}He pumping line and the vacuum can provides a thermal link from 4 K to the baffles, which cool the ^{3}He gas desorbed from the pump.

conditions depended on the capacity of the ^{4}He pot. In order to reduce the heat load on the ^{4}He pot during ^{3}He condensation a 5 mm section of the stainless steel ^{3}He pumping line, starting at a point 5 mm above the ^{4}He pot, was thermally anchored to 4 K by a copper plate soldered to the vacuum can. Semi-circular copper baffles were also placed inside the pumping line to cool the incoming ^{3}He gas. It would have been desireable to cool the incoming ^{3}He more effectively by increasing the length of the heat exchanger or to have increasd the 5.2 cm^3 internal volume of the ^{4}He pot. Space limitations precluded this.

De Long et al found that the critical power per unit flow rate for their refrigerator was 4.5 mW/(10^{-4} moles/s). Using this result, we determined the required flow rate $\dot{n}$ from the expected heat leak into our ^{4}He pot. The flow rate is fixed by the value of the flow impedance z. Given the flow rate, T_4 is fixed by the speed S of the ^{4}He pump. For laminar, incompressible flow through a porous medium, the volume flow rate $\dot{V}$ is given by Darcy's Law[4] (Collins, 1961)

$$\dot{V} = (P_B - P_4)/(\eta z) \qquad \text{(VI-2)}$$

where P_B = pressure above the ^{4}He bath = 760 torr

P_4 = pressure in the ^{4}He pot

η = fluid viscosity

We expect $P_4 \sim 1$ torr so it can be dropped. (VI-2) implies that $\dot{n}z$ should be independent of z. De Long et al found that this is actually not quite true. This is hardly surprising

because there will be a turbulent mixture of liquid and gas in the flow impedance so the assumptions of (VI-2) would not be fulfilled. Nevertheless, (VI-2) is useful as a guide.

Gauthier and Varoquaux (1973) found that they could predict the flow impedance of a tube of length L and cross-sectional area A containing a powder of particles of diameter d using

$$z = L/AB \qquad \text{(VI-3a)}$$

where $B = 8 \times 10^{-4}\ d^2$ (VI-3b)

For our powders, this value of B was not reliable, probably because of the distribution of grain sizes and differences in packing, so z had to be measured. This was done by flowing N_2 gas through the flow impedance at room temperature. The input pressure was 1500 torr and the output pressure was 760 torr. A flow impedance was constructed from industrial grade 3 μm Al_2O_3 powder in a 16 mm long, 1.1 mm inside diameter stainless steel tube. The measured value of z was 4.1×10^{12} cm^{-3} compared to a value of 2.3×10^{12} cm^{-3} obtained from (VI-3). Extrapolating the values of $\dot{n}z$ given by De Long et al, we expected $\dot{n}z \simeq 1.5 \times 10^{8}$ (moles/s)/cm^3 so our measured value of z implies $\dot{n} \simeq 4.5 \times 10^{-4}$ moles/s. Therefore we anticipated a critical power $\dot{Q}_c$ of 20 mW.

The expected ^{4}He pot temperature was determined from $\dot{n}$ and the pumping speed S of the ^{4}He pot pump, a Sargent-Welch model 1397. At 1 torr, it had a pumping speed of 7 l/s which was not limited by the pumping line. The ^{4}He pot pressure P_4 was obtained from the ideal gas equation

$$P_4 = \dot{n}RT/S \qquad \text{(VI-4)}$$

where R is the gas constant. This gave P_4 = 1.2 torr implying T_4 = 1.30 K. The thermal boundary resistance between the liquid ^{4}He and the copper ^{4}He pot (Lounasmaa, 1974) at 1.3 K is 10 mK-cm^2/mW. If the 25 cm^2 interior surface of the ^{4}He pot had been smooth, a 20 mW heat flux into the ^{4}He pot would have produced an insignificant 8 mK difference between the temperatures of the ^{4}He and the copper. In fact, the interior of the ^{4}He pot was sandblasted so the difference would be even less.

The operation of the ^{4}He pot was tested by filling it with liquid ^{4}He and applying enough heater power $\dot{Q}_h$ to empty it. Then $\dot{Q}_h$ was reduced in steps and T_4 was measured when equilibrium was reached. The resulting graph of T_4 versus $\dot{Q}_h$ is shown in Fig. 26. For heater power inputs up to 9.1 mW, a constant temperature of T_4 = 1.28 K was maintained. For higher powers, T_4 rose rapidly. Since we expect $\dot{Q}_c \simeq$ 20 mW, this implied a heat leak into the ^{4}He pot of 11 mW. This would come primarily through the copper plate soldered to the vacuum can at 4.2 K and the ^{4}He pumping line.

Filling the ^{4}He pot required 40 min so it was desireable to ensure that it was not emptied by an overload such as condensation of the ^{3}He. It was possible to tell that the ^{4}He pot was draining by measuring T_4. When the pot was full, T_4 was 1.28 K but as the pot emptied T_4 dropped to 1.23 K before

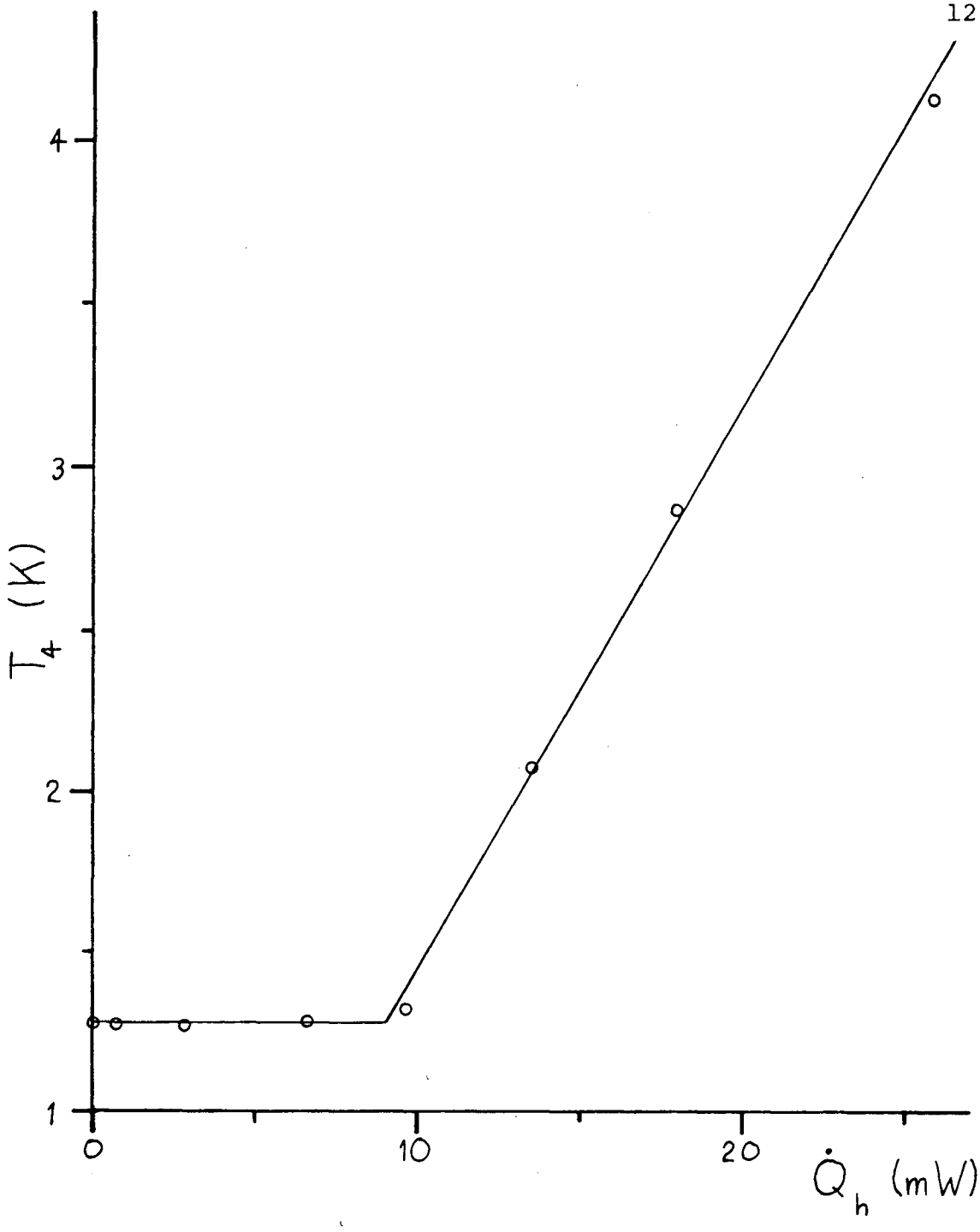

Fig. 26 ^{4}He pot temperature versus heater power. The critical heater power, obtained from the intersection of the two straight lines, is 9.1 mW.

rising rapidly when the pot was completely empty.

The ^{3}He pot, shown in Fig. 27, was constructed from electrolytic tough pitch copper. The lid was brazed with Easy-flo 45 solder[5] (.45 Ag/.15 Cu/.24 Cd/.16 Zn), which is not superconducting above 64 mK. Originally a layer of copper powder had been sintered into the bottom of the ^{3}He pot in order to increase the surface area and lower the thermal boundary resistance: for a smooth surface, we expected a temperature gradient of 13 mK for a 30 μW heat leak into the pot. The sintering was done at 870 C in an H_2 atmosphere. Later, we discovered that after thermal cycling to liquid helium temperatures very small holes were produced in the 3 mm thick walls of the ^{3}He pot. The H_2 had diffused into the copper during sintering and reacted explosively with oxygen impurities to form water. Consequently, the ^{3}He pot had to be removed from the cryostat and replaced. The second version was sand-blasted inside to lower the boundary resistance and filled with copper foam. The foam not only increased the surface area of the copper but, more importantly, equalized the temperature of the liquid ^{3}He, which is a poor thermal conductor.

Within the ^{3}He pot, there was a separate cell enclosing (after being filled with copper foam) a volume of .43 cm^3. It could be used to calibrate the temperature sensors against the vapour pressure of helium or hydrogen. The hydrogen fill line went through two 90° bends in the ^{3}He pot in order to trap radiation.

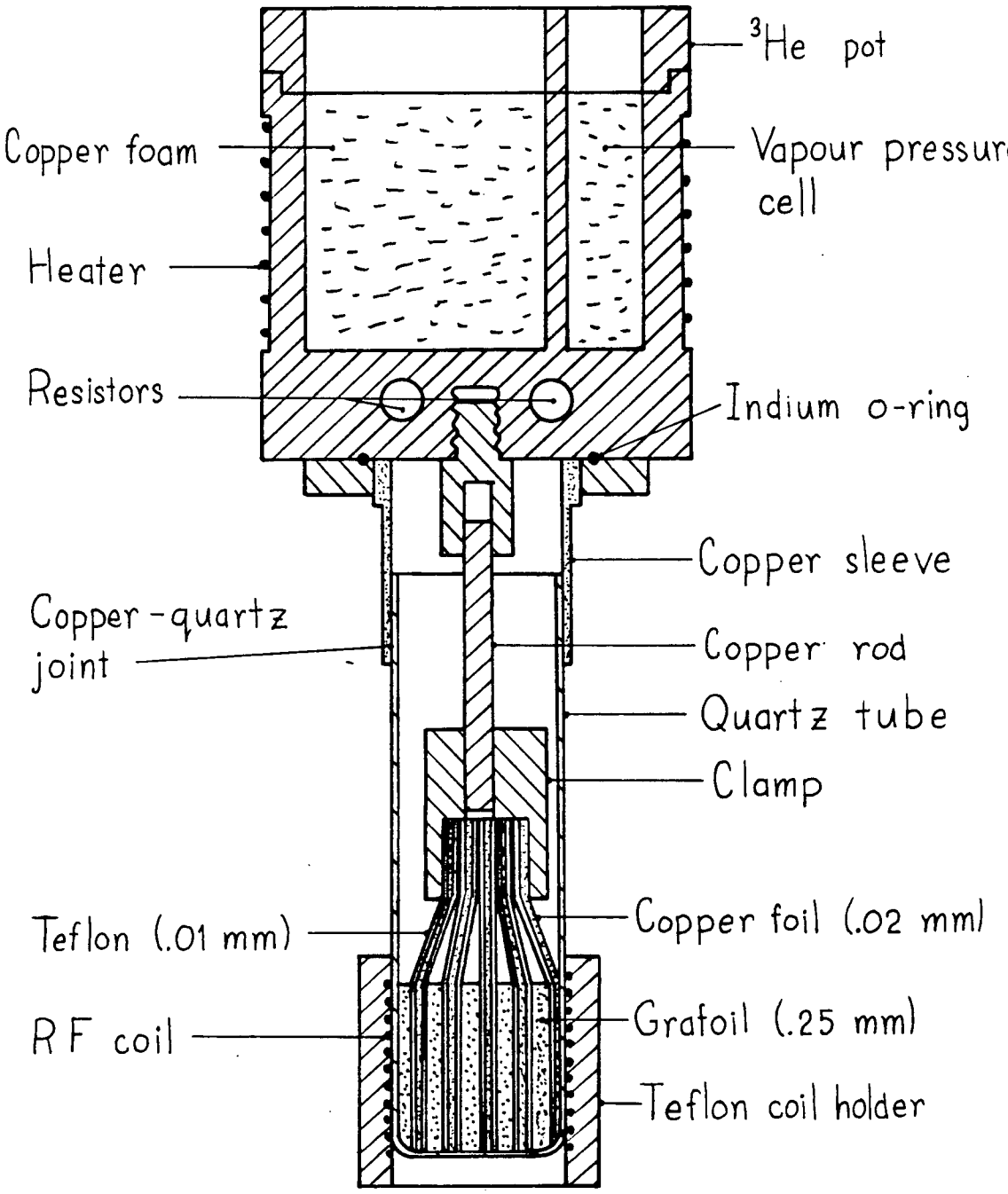

Fig. 27 Cross-section of the ^{3}He pot and the Grafoil cell, drawn to scale.

The main heat leaks into the ^{3}He pot were due to conduction down the hydrogen fill line and the ^{3}He pumping line. The former was a 35 mm long, 10 mm diameter, .15 mm thick stainless steel bellows which produced a heat leak of 11 μW between 1.3 K and .3 K. The latter was a 13 mm long, 13 mm diameter, .6 mm thick tube constructed from fibreglass mat and Stycast 2850 FT[6] epoxy which was epoxied to two .25 mm thick brass tubes. It produced a heat leak of 12 μW between 1.3 K and .3 K. These expected heat leaks compare quite well with the total measured heat leak of 30 μW.

6.3 Grafoil Cell

The Grafoil cell shown in Fig. 27 was attached to the ^{3}He pot using an indium O-ring seal between the ^{3}He pot and the brass flange at the top of the cell. The simplest way to join the quartz cell to the brass flange would have been to use a quartz-Pyrex graded joint and a Pyrex-copper Housekeeper seal. Given our space limitations, this would have been much too long so a soldered quartz-copper joint was fabricated as described in Appendix B. It was desireable to avoid using epoxy in the joint in order to prevent possible contamination of the Grafoil by vapour from the epoxy. The joint has survived cycling from 4 K to 300 K over twenty times.

Heating of the Grafoil had been a problem in the ^{4}He cryostat so we wished to avoid such heating in the ^{3}He cryostat. Grafoil is a very poor thermal conductor at low

temperatures because the thermal contact between the crystallites is poor. Measurements between 1.5 K and 4.2 K have shown that the thermal conductivity in the plane of the foil κ_l is proportional to T and between 1.5 K and 20 K the conductivity normal to the foil κ_t is proportional to T^2 (Hedge et al, 1973). Extrapolating these measurements to .3 K, we estimate $\kappa_l \simeq 2.0 \times 10^{-5}$ W/cm/K and $\kappa_t \simeq 3.2 \times 10^{-9}$ W/cm/K. Using our measured conversion rates for cell B, the conversion heating for pure J=1 hydrogen with a coverage $\rho = .85$ would be 200 (20) nW for H_2 (D_2). The RF heating at our normal power level (input attenuation A=13dB) would have been 24 nW corresponding to a magnetic field of 160 nT RMS. Heating by 4.2 K radiation would have been about 8 nW. The transverse thermal conductance of the Grafoil limits the rate at which heat is carried away. For .25 mm thick Grafoil sheets covered with pure o-H_2 and both sides at .3 K, the temperature rise at the centre of the each sheet would be of the order of .6 mK so heating of the Grafoil should not be a problem if the sides of each sheet are adequately thermally anchored. Although the extrapolation of the thermal conductivity data may not be very precise, it is not likely to be too far from the truth.

Two Grafoil cells were constructed for the ^{3}He cryostat. Cell A contained 1.15 g of .13 mm thick, 13 mm long sheets of GTA grade Grafoil which were covered on one side by a 200 Å evaporated film of copper. The Grafoil had previously been activated at 900 C for 71 h. Pairs of sheets were then sintered

to .05 mm copper foil at 900 C in an H_2 atmosphere. After sintering, the sample was baked under vacuum at 850 C for 13 h. Each piece of foil had a tab which was clamped to one end of a 37 mm long piece of 12 AWG copper wire. The other end of the wire was clamped to the ^{3}He pot. Each pair of Grafoil sheets was wrapped in .01 mm Teflon to reduce RF shielding. The Teflon contained numerous slits to aid gas flow.

The thinnest Grafoil available, with a thickness of .13 mm, was chosen so that gas flow into the sample, RF field homogeneity, and thermal conductance normal to the sheets would be maximized. After measuring the ^{4}He adsorption isotherm, we found this Grafoil had the added advantage of a specific surface area of 27.7 m^2/g compared to only 15.6 m^2/g for the .25 mm Grafoil used in the ^{4}He cryostat. This enhanced the S:N ratio considerably. Also, the J=1 to J=0 conversion was a factor of .38 times smaller on the .13 mm Grafoil, at least for D_2.

On the other hand, X-ray measurements had shown that the isotropic powder component of the graphite crystals in our .25 mm Grafoil was smaller than usual (J.G. Dash, private communication). However, X-rays are sensitive to all of the basal planes, not just the ones on the surface, so there was no information about the orientational distribution of the surface planes. It was not clear whether the broadening due to mis-orientation of the surface would be signficantly less in the .25 mm Grafoil than in the .13 mm Grafoil.

Spectra obtained with cell A were not as clearly resolved

as those obtained with the ^{4}He cryostat. This was particularly evident for D_2. In the ^{4}He cryostat, the J=1 peaks of D_2 had been clearly resolved over the entire temperature range of 1.2 K - 4.2 K but in cell A the peaks were barely resolved at the low temperature end of that range. Four possible explanations occurred to us: 1) The Grafoil in cell A was less well oriented. 2) It may have been contaminated by copper during evaporation or sintering. 3) It may have been contaminated by Teflon during the bake-out of the sample. 4) The hydrogen may not have plated the Grafoil uniformly. The adsorption procedure was different from that used in the ^{4}He cryostat. Teflon contamination seemed unlikely because the same bake-out procedure was used in the ^{4}He cryostat. Copper contamination was also doubtful because similar procedures have been used in specific heat measurements of ^{3}He and ^{4}He on Grafoil (Bretz et al, 1973) with no apparent deleterious effects. Some caution must be exercised with regard to this last conclusion because although a film may be uniform with respect to some properties, it may not be for others.

Since there was reason to suspect that the poor spectra were due to the misorientation of the Grafoil, a new sample, called cell B, was constructed using .911 g of the original .25 mm Grafoil obtained from J.G. Dash. As an additional precaution, copper was not evaporated or sintered onto the Grafoil. Between each pair of 13 mm long Grafoil sheets was a sheet of .01 mm Teflon film, a sheet of .03 mm copper and a

second sheet of Teflon. The Teflon sheets contained slits as in cell A and they had been baked for one week at 200 C to reduce the ^{1}H background NMR signal. The copper sheets contained 10 mm long, 1.6 mm wide slits, spaced 1.6 mm apart, to improve gas flow and penetration of the oscillating magnetic fields. They were anchored to the ^{3}He pot in the same manner as in cell A. The whole assembly was tightly wrapped with Teflon film. The intensities of the NMR absorption spectra obtained with cells A and B were about the same as the temperature and RF level were varied, so the thermal contact to the Grafoil sheets must have been comparable.

Spectra obtained with cell B were still poor so the adsorption procedure became the prime suspect. All of the samples up to this point had been adsorbed at temperatures of 30 K or less so that the hydrogen vapour pressure above the Grafoil would have been at most 100 μ. Subsequently, we were able to consistently obtain spectra of the same quality as in the ^{4}He cryostat by adsorbing the hydrogen at 40 K, where the vapour pressure was about 1 torr, as described in section 5.5. Since the uniformity of all of the films in cell A is suspect, it was never determined whether the better alignment of the graphite crystals in cell B had a significant effect.

6.4 Temperature Measurement in the ^{3}He Cryostat

The temperature measurement and control system of the ^{3}He cryostat is shown in Fig. 28. The 1/8 W Ohmite carbon

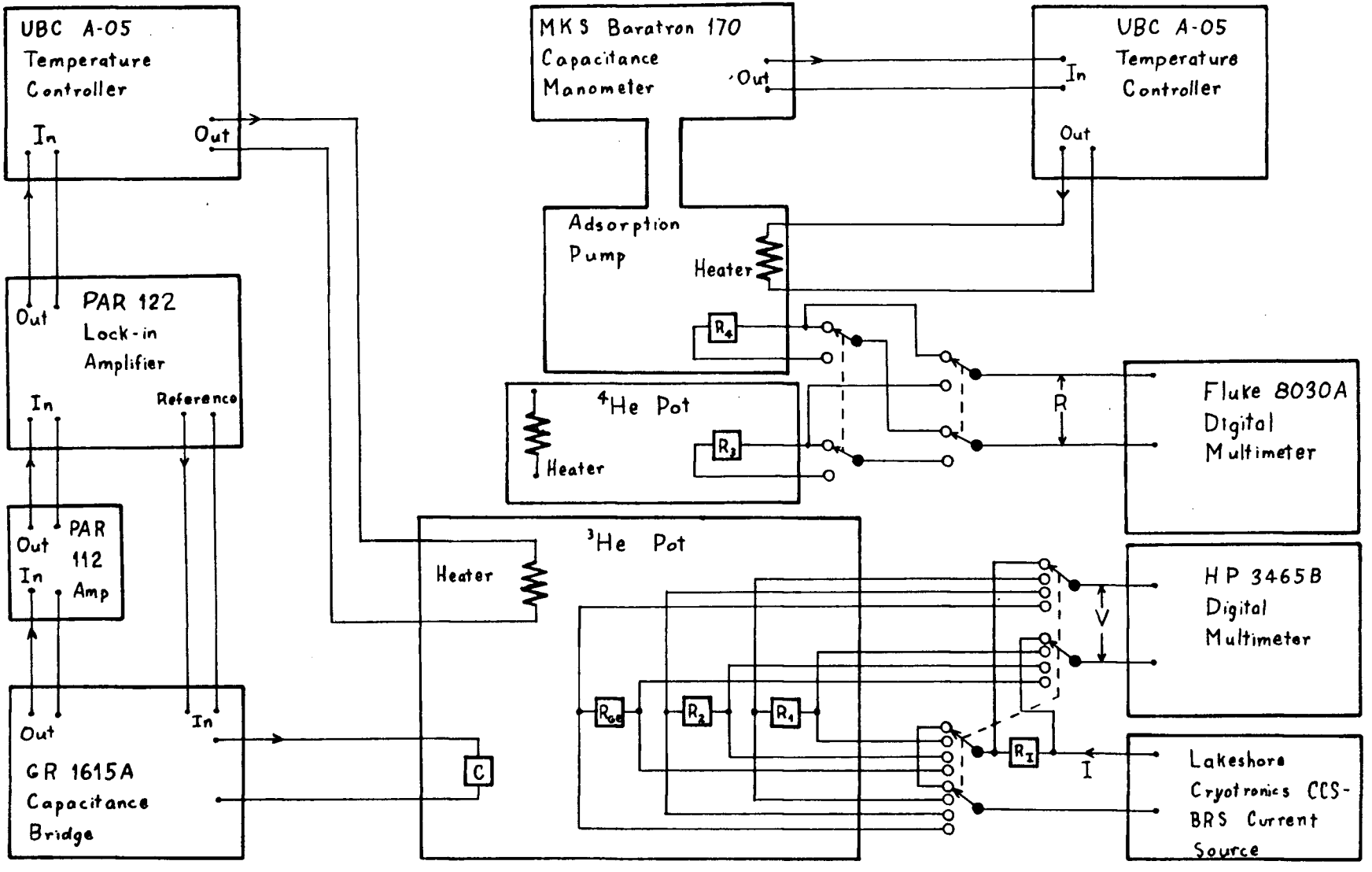

Fig. 28 Temperature measurement and control system for the ^{3}He cryostat.

resistors R_1, R_2, R_3, and R_4 were 10Ω, 680Ω , 220 Ω, and 680 Ω respectively. Most of the epoxy coating was removed by sandblasting. The 100 Ω germanium resistor R_{Ge} was a Lakeshore Cryotronics model GR-200A, which was filled with ^3He gas. The SrT_iO_3 capacitance sensor C was a Lakeshore Cryotronics model CS-400GR. The current sense resistor R_I could be selected to be either a 1 kΩ or a 100 kΩ wire wound resistor each of which had a temperature coefficient of 50 ppm/C. Sensors R_1, R_2, R_{Ge}, and C were all coated with Apiezon M grease and placed in holes in the base of the ^3He pot. R_1 was used between .3 K and 2 K, whereas R_2 was used above 2 K. R_3 and R_4 were varnished to the ^4He pot and the adsorption pump respectively with GE 7031 varnish.

R_3 and R_4 were measured using the resistance setting of a Fluke 8030A digital multimeter. Three leads were used. Assuming that they were identical, this allowed one to compensate for the lead resistance. The ^3He pot resistors were measured using a four lead configuration. A Lakeshore Cryotronics CCS-BRS DC current source drove a current through the selected resistor via two of the leads and the voltage across the resistor was measured by a Hewlett-Packard (HP) 3465B digital multimeter connected to the other two leads. Since the HP 3465B has a high input impedance, the voltage drop down the voltage leads was insignificant. The current was determined by using the HP 3465B to measure the voltage across the sense resistor R_I in series with the temperature sensors. An

average of the absolute value of the voltage obtained with the current in opposite directions was used in order to compensate for thermoelectric voltages in the leads. The power dissipation and temperature errors resulting from the measurement system, at several temperatures, are shown in Table IX. The voltages across R_1 and R_{Ge} were always 1-4 mV. It was necessary to disconnect the HP 3465B from the carbon resistors during NMR measurements because it increased the noise slightly.

A General Radio 1615A capacitance bridge was used to measure the two components of the impedance of the capacitance thermometer. The output of the bridge was detected by a Princeton Applied Research (PAR) model 122 lock-in amplifier with a model 112 preamplifier. The 5 kHz, 1 V reference signal from the lock-in amplifier was used to excite the sensor. It was necessary to ensure that the bridge was not greatly unbalanced or the voltage applied across the sensor would change. Changes in the amplitude or frequency of this voltage would cause the sensor to drift. Coaxial leads to the capacitance sensor were used to reduce interlead capacitance. Power dissipation was less than 1 nW.

R_3 and R_4 were only used to monitor the operation of the cryostat so they did not require accurate calibration. A two point calibration was made between 4.2 K and 77 K using the equation

$$T = \frac{A \log R}{(\log R - B)^2} \qquad \text{(VI-5)}$$

where A and B are constants determined by the resistance at 4.2 K and 77 K. R_3 was also calibrated against the ^4He vapour pressure between 1.2 K and 4.2 K.

Table IX Power Dissipation and Temperature Errors in the ^3He Pot Resistors

T(K)	Power Dissipation (nW)			Temperature Error (mK)		
	R_1	R_2	R_{Ge}	T_1	T_2	T_{Ge}
4	400	14	15	4	1	3
1	3	-	1.5	1	-	1
.6	1	-	.5	.5	-	.4
.3	.2	-	.5	.04	-	.1

The capacitance sensor was the only sensor that had no observable magnetic field dependence for the range of fields that we used ($H \leq 1.3$ T). However, it had poor reproducibility on thermal cycling and it was subject to considerable drift, particularly during the first couple of hours after cooling from 77 K to 4.2 K. The germanium resistor R_{Ge} had the best reproducibility and stability but exhibited the greatest sensitivity to magnetic fields, especially if they were greater than .3 T. Its resistance depended on both the magnitude and orientation of the field. Although the carbon resistors were not as stable and reproducible as the Ge resistor, they were

adequate for these experiments. After the initial calibration, the resistors were checked at 4.2 K in zero magnetic field against the ^{4}He vapour pressure at the beginning of each NMR experiment (see Fig. 29). The 1958 ^{4}He temperature scale was used to determine T_{He}. A DC calibration from .3 K to 6 K by Lakeshore Cryotronics Inc. gave T_{Ge}. The carbon resistors were calibrated against T_{He} at 318 days and at other times their temperatures were determined using the temperature dependence of their resistances. For the carbon resistors, the three measurements up to 263 days have much more scatter than later measurements. In those three cases R_1, R_2, and R_{Ge} were measured using an SHE model ARB automatic resistance bridge operating at 27.5 Hz with 20 μV excitation. A three terminal connection was used to compensate for lead resistance. Otherwise the system described above was used. The Ge resistor shows a change of about 10 mK in its calibration between 117 and 263 days. This may have been caused by inadvertent heating of the ^{3}He pot to 50 C during that period. Even with this shift, the calibration was satisfactory for our work.

The magnetoresistance of the carbon resistors, $\Delta R=R(H)-R(0)$ is a complicated function of H and T. At 1.35 K, $\Delta R_1/R_1$ was found to be positive and proportional to H^2 but at .3 K, it had a positive peak of a few percent below .1 T and then decreased, appearing to level out at -5.6% near 1.3 T (measurements were only made up to 1.4 T). At .2 T, the field

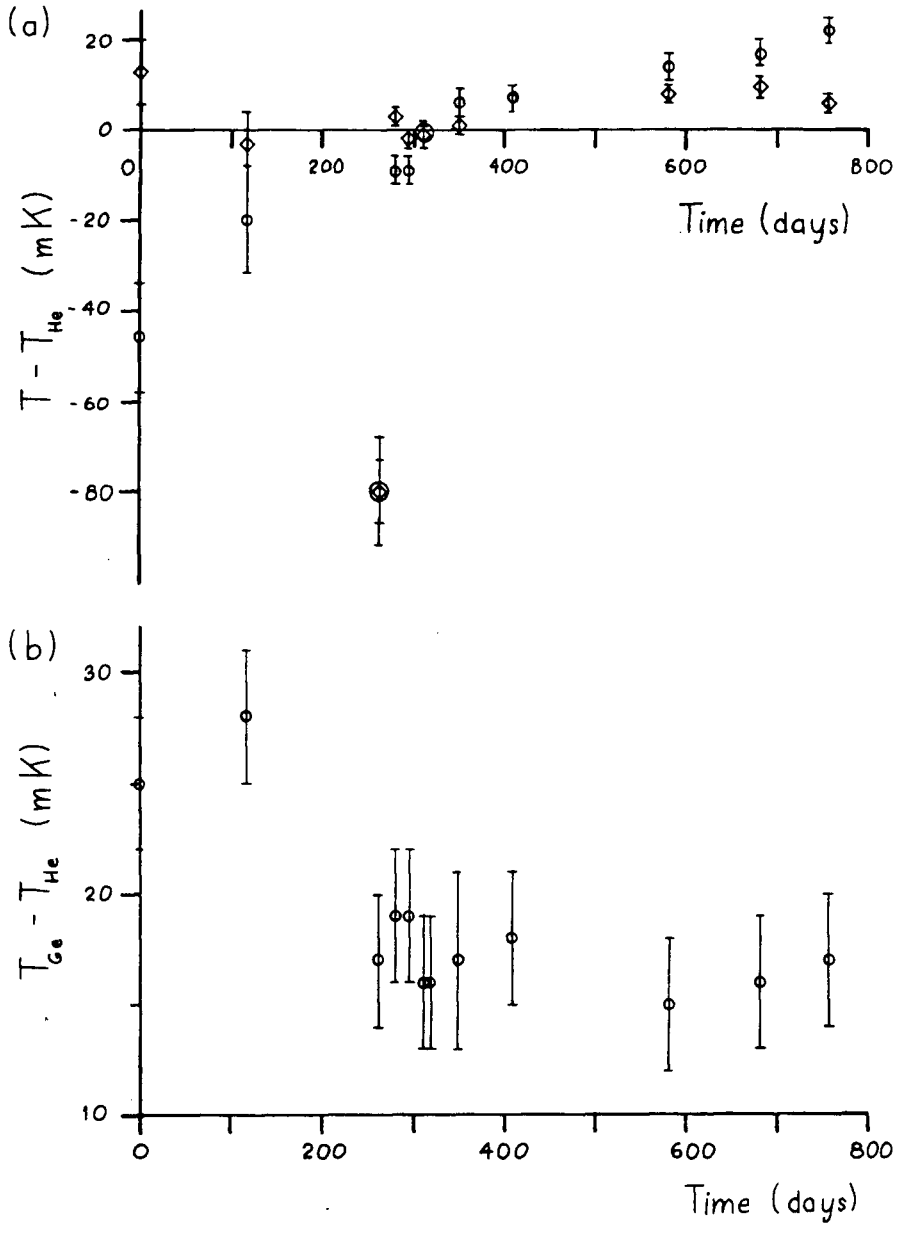

Fig. 29 Stability of the resistance thermometers on the ^{3}He pot at 4.2 K in zero magnetic field. The temperatures obtained from the carbon and Ge resistors are T_1, T_2, and T_{Ge}; that obtained from the vapour pressure of the ^{4}He in the main dewar is T_{He}. The vacuum can contained ^{4}He gas at pressures between .1 and 1 torr. In (a), we show T_1 (circles) and T_2 (diamonds) and in (b), T_{Ge} is shown. Note the difference in the vertical scales.

used for H_2 NMR, the equivalent temperature shift ΔT of R_1 and R_2 was never more than .2% throughout the temperature range in which each was used. Since ΔT was either comparable to or less than the uncertainty with which the ^3He pot temperature could be measured and less than the temperature drift during an NMR measurement, it was ignored. At 1.3 T, the field used for D_2 NMR, the magnetoresistance was small but significant so the carbon resistors were calibrated at that field. Table X contains a few typical results. σ_{T1} and σ_{T2} are the errors in T_1 and T_2, taking into account the accuracy of the measuring instruments and the stability of the resistors.

Table X Typical Magnetoresistance Measurements

T(K)	H(T)	$\frac{\Delta R_{Ge}}{R_{Ge}}$(%)	$\frac{\Delta R_1}{R_1}$(%)	$\frac{\Delta R_2}{R_2}$(%)	$\frac{\Delta T_1}{T_1}$(%)	$\frac{\sigma_{T_1}}{T_1}$(%)	$\frac{\Delta T_2}{T_2}$(%)	$\frac{\sigma_{T_2}}{T_2}$(%)
4.22	.19	.05(4)	- .23(6)	- .08(5)	.3 (1)	.3	.04(3)	.2
1.35	.19	.1(1)	.02(3)	-	- .01(2)	.2	-	-
.32	.19	3.0(6)	.9 (4)	-	- .2 (1)	.06	-	-
4.22	1.3	4	0.0 (3)	.21(7)	0.0 (3)	.3	- .10(3)	.2
2.0	1.3	-	.5 (4)	1.0 (7)	- .3 (3)	.2	- .22(2)	.1
1.35	1.3	11	1.4 (4)	-	- .7 (2)	.2	-	-
.33	1.3	80	-5.6 (3)	-	1.07 (6)	.06	-	-

Notes to Chapter VI

1. This Grafoil was kindly supplied to us by J.G. Dash, Physics Dept., University of Washington, U.S.A.

2. Values of H_c are for T=1.3 K (Warren and Bader, 1969).

3. The drift rate was measured several hours after cooling to liquid helium temperatures. Immediately after cooling, it was much greater.

4. (VI-2) can also be used for an ideal gas, in which $P\dot{V}$ rather than $\dot{V}$ is constant, provided that one interprets $\dot{V}$ as the average volume flow rate.

5. Easy-flo 45 is a product of Handy and Harman Co. It is very similar in compositon to Castolin 1802 (Castolin S.A., Lausanne St-Sulpice, Switzerland) so the transition temperature of the latter has been quoted (Landau and Rosenbaum, 1972).

6. Emerson and Cuming Inc., Canton, Mass., U.S.A.

CHAPTER VII

THE NMR SPECTROMETER

3.1 Introduction

At the present time, most NMR work is conducted using pulsed, rather than continuous wave, spectrometers. In a continuous wave spectrometer, low level RF excitation is applied in order to tip the nuclear spins by a small angle. One measures the power absorbed as one sweeps either the field or the frequency through resonance. In a pulsed spectrometer, one or more short, high power RF pulses are applied at the resonance frequency. These tip the spins by a large angle (usually 90° or 180°) and one observes the recovery of the magnetization after the pulses. Pulse techniques dominate the scene because in most cases they produce better S:N ratios and because sophisticated pulse sequences will often allow one to isolate the effects of specific interactions. In our case, they were rejected because large angle pulses would lead to intolerable heating of the Grafoil: nearly all of the losses in the tuned circuit are due to the Grafoil. Since thermal time constants become long at low temperatures, the time required for the thermal recovery of the sample would greatly exceed the recovery time of the magnetization. We found in the ^{4}He cryostat that the heating of the sample was about .1 K at 1 K using our normal RF field of about 8×10^{-7} T. In the ^{3}He cryostat, thermal sinking of the Grafoil was much better but the transverse thermal

conductivity κ_t of the Grafoil was insufficient to allow the use of large angle pulses.

The simplest single coil nuclear resonance circuit, a Q-meter, is shown in Fig. 30. A current generator drives a current i into a parallel resonant circuit. At resonance the voltage v across the coil, detected by the amplifier, is maximized and is given by

$$v = iQ\omega_o L \qquad \text{(VII-1)}$$

where Q = quality factor of the tuned circuit

ω_o = resonance frequency of the tuned circuit

L = inductance of the coil

If the NMR sample is placed inside the coil, then, as one sweeps the magnetic field through resonance, power is absorbed by the sample, which lowers the Q. This results in a drop in v. The change in the Q is proportional to the imaginary part of the magnetic susceptibility, which is called the absorption (Abragam, 1961).

The Q-meter has the disadvantage that it is fairly sensitive to microphonics. Vibrations of the cryostat result in small changes ΔC in the tuned circuit capacitance C. These shift ω_o, adding noise to v. At resonance, the change in 1/Q is second order in ΔC:

$$\Delta(1/Q) = Q(\Delta C/C)^2 \qquad \text{(VII-2)}$$

In practice, the circuit will actually be mistuned by an amount ΔC_o so that

$$\Delta(1/Q) = Q(\Delta C_o \Delta C/C^2) \qquad \text{(VII-3)}$$

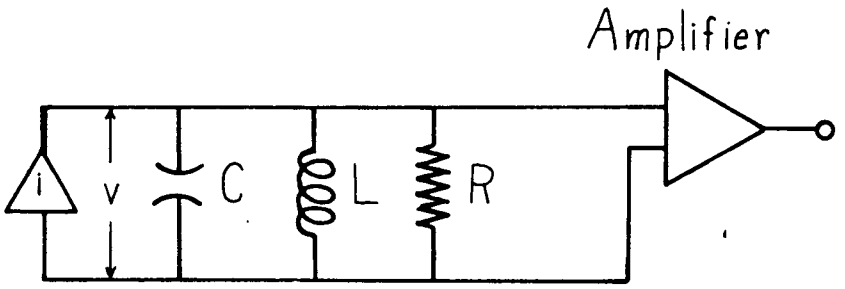

Fig. 30 Q-meter circuit.

Typically, one might expect to maximize the circuit response to within 1%, in which case the mistuning would be

$$\Delta C_o/C = .1/Q \qquad \text{(VII-4)}$$

Therefore the sensitivity to noise would be

$$\Delta(1/Q) = .1\,\Delta C/C \qquad \text{(VII-5)}$$

Instead of a Q-meter, we chose to use a Robinson oscillator circuit (Robinson, 1959) because it is less sensitive to microphonics. A Robinson oscillator consists of a closed loop containing a tuned circuit, an amplifier, a phase shifter, a limiter, and an attenuator. Our limiter was a high gain amplifier with diode clipping so that its output was relatively insensitive to wide variations in the input amplitude. The level of the RF excitation was set by the attenuator. The oscillator frequency ω was determined by the requirement that, in order for oscillations to occur, the total phase shift around the loop must be an integral multiple of 360°. The phase shifter was adjusted so that $\omega=\omega_o$. Near ω_o, the phase shift produced by the tuned circuit is a strong function of frequency. If the tuned circuit capacitance changes, ω must follow ω_o in order to maintain the same phase shift. The sensitivity to small changes in capacitance becomes

$$\Delta(1/Q) = (1/2Q)(\Delta C/C) \qquad \text{(VII-6)}$$

This is a factor of $Q/5 \sim 20$ times less than for the Q-meter for a typical NMR circuit.

Significant improvement in the S:N ratio can be achieved by cooling the tuned circuit to a low temperature T (Alderman,

1970). For a sample at a temperature T_S with magnetization $M(T_S)$, the S:N ratio at the output of an amplifier with noise figure F is proportional to $M(T_S)(Q/FT)^{1/2}$, assuming that the noise is Johnson noise from the tuned circuit (Abragam, 1961). As T decreases, Q will usually increase to a limiting value. In our case, it changed from 30 at room temperature to 70 at liquid helium temperatures. (This applies when the coil contains the Grafoil; the intrinsic Q is much higher). It is possible to reduce F by cooling the amplifier as well. However, even if F remained unchanged, cooling might still be desireable. Say that a cooled tuned circuit was connected to a room temperature amplifier via a coaxial cable. The cable forms part of the tuned circuit. The cable must have low thermal conductance which generally means that it will have poor electrical conductance. Therefore it will lower the Q and add high temperature Johnson noise. In fact a long lossy cable may make the S:N ratio worse than if the entire tuned circuit was at room temperature. Our solution was to employ a liquid ^{4}He cooled amplifier which allowed us to keep the cable short and entirely at liquid helium temperatures. The amplifier had a noise temperature of 8 K.

There are some disadvantages to using a cooled amplifier. The three p-Ge junction field-effect transistors (JFETs) in our amplifier dissipated 9 mW each when operated at 6 V so that the amplifier was responsible for about half of the total liquid ^{4}He consumption of the cryostat. The electronic components

of the amplifier had to be able to withstand repeated thermal cycling. Also, it is convenient if all of the passive components are independent of temperature. Our spectrometer operated at a fixed frequency but if one wished to have a tunable spectrometer, it would be necessary to tune it from room temperature. Finally, adjustment and repair of a cooled amplifier can be tedious.

In general, the S:N ratio can be improved by increasing the total measuring time. There are two main approaches that can be adopted. The first is to use a short detector time constant, sweep through the resonance relatively rapidly (typically $\sim$ 10 ms), and average many spectra. The second is to sweep slowly (typically $\sim$ 100 s) only a few times, using a long time constant. If the noise spectrum is flat and the resonance is not saturated, then in principle the two methods are equally effective. In practice, fast sweeps often have several advantages over slow ones. Normally, if the resonance signal is weak, one operates near saturation in order to get as large a signal as possible without distorting it. If saturation occurs, a fast sweep is less likely to distort the signal because the spins are saturated more uniformly than with a slow sweep. In the latter case, there may be a transfer of polarization among the spins during the sweep. Another consideration is that the noise tends to increase at low frequencies with an approximate 1/f spectrum. For example, drift in the spectrometer gain will cause fluctuation of the baseline during a slow sweep. During

a fast sweep, the gain will be approximately constant producing unimportant shifts in the baseline from one sweep to the next. Finally, a strong but brief disturbance will affect only one scan so its influence will be diminished if many fast scans are accumulated rather than a few slow ones.

If the NMR spectrum is quite wide and the spectrometer operates at low temperatures, fast sweeps can produce serious side effects. A changing magnetic field will induce eddy currents in the electrically conducting sections of the cryostat, creating oscillating magnetic moments. In the presence of a large static field H_o, there will be oscillating torques which cause vibration coherent with the sweep. The vibrations modulate the tuned circuit capacitance, which in turn modulates the resonance frequency. In addition the eddy currents will cause heating. We chose our sweep rate of .3 mT/s to be as fast as possible without producing significant eddy current heating of the ^{3}He pot.

It is possible to escape from the effects of the low frequency noise inherent with slow sweeps by shifting the detection frequency away from zero. We did this by modulating H_o sinusoidally at 280 Hz using a small pair of coils mounted on the inside of the vacuum can. With this technique, in the limit of small modulation, the derivative of the absorption is observed. The modulation field H_m induced coherent vibration but it was much less severe than the vibration produced by a fast sweep for two reasons. First, the modulation field was

only .17 mT peak to peak compared to 10 -20 mT for the sweep field. Secondly, since the modulation field is so small it need not be very homogeneous so the coils can be made quite small. On the other hand, the sweep coils had to be quite large and homogeneous so eddy currents were induced in a much larger section of the cryostat. Nevertheless, coherent interference arising from the modulation field was a serious problem (see section 7.3).

Even with slow sweeps, we found it necessary to accumulate spectra with a signal averager. Typically, about 100 scans were added in the signal averager and then transferred to an Amdahl 470 V/8 computer for comparison with the synthetic spectra. The H_2 spectra required 2-4 h of signal averaging whereas the low temperature D_2 spectra needed up to 20 h because D_2 has a smaller magnetic moment and a broader spectrum.

7.2 Description of the Spectrometer

Fig. 31 is a block diagram of the spectrometer, showing the Robinson oscillator, the detection system, and the driving system for the modulation coils. The supports for the cryostat and dewars were embedded in sand to dampen vibrations. The pumping lines for the rotary pumps contained ballast volumes that were also embedded in sand.

The tuned circuit is shown in Fig. 32. The 1.2 μH inductance of the NMR coil is denoted by L and R is the equivalent parallel resistance of the tuned circuit. All of

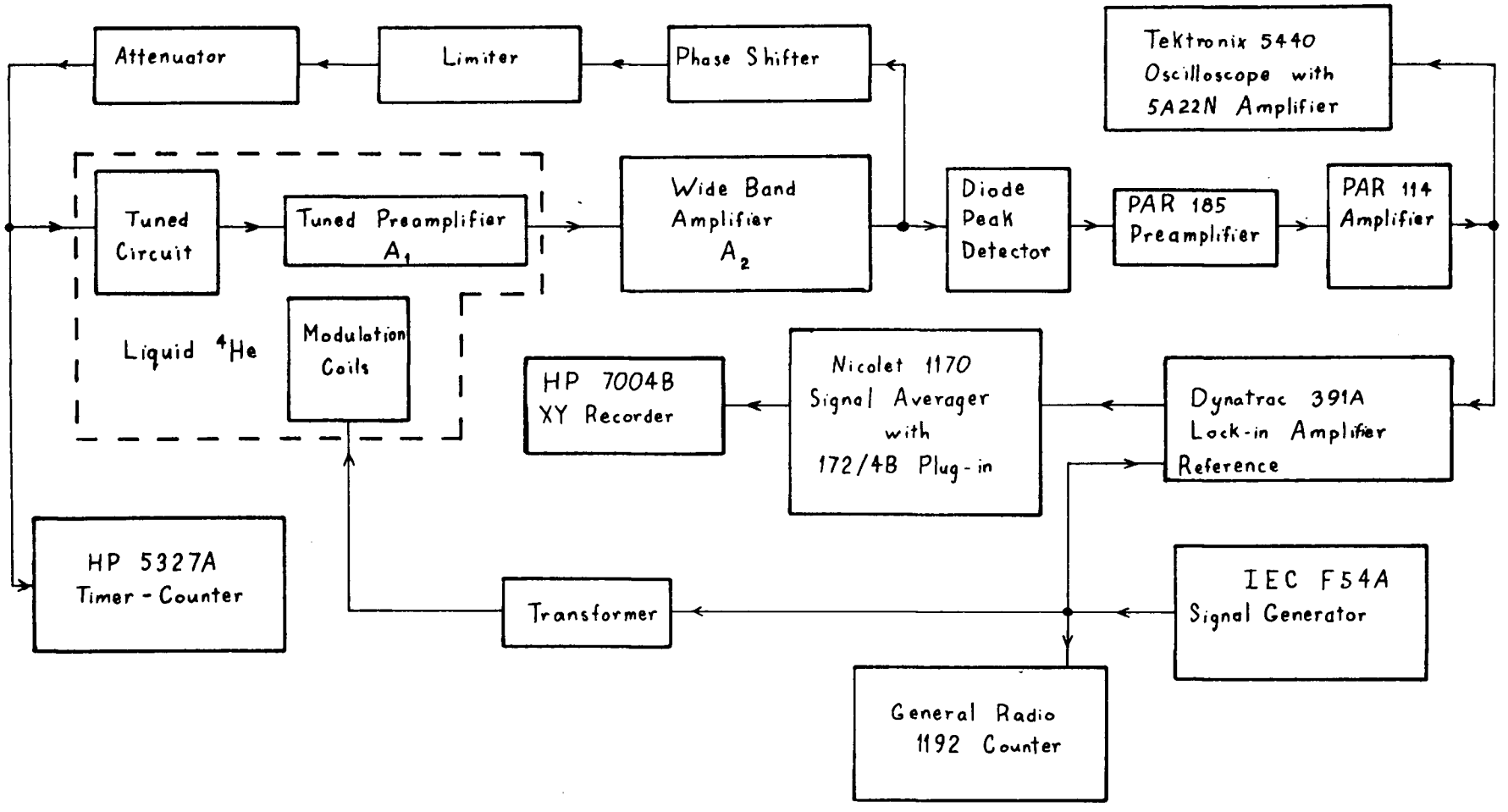

Fig. 31 Block diagram of the NMR spectrometer.

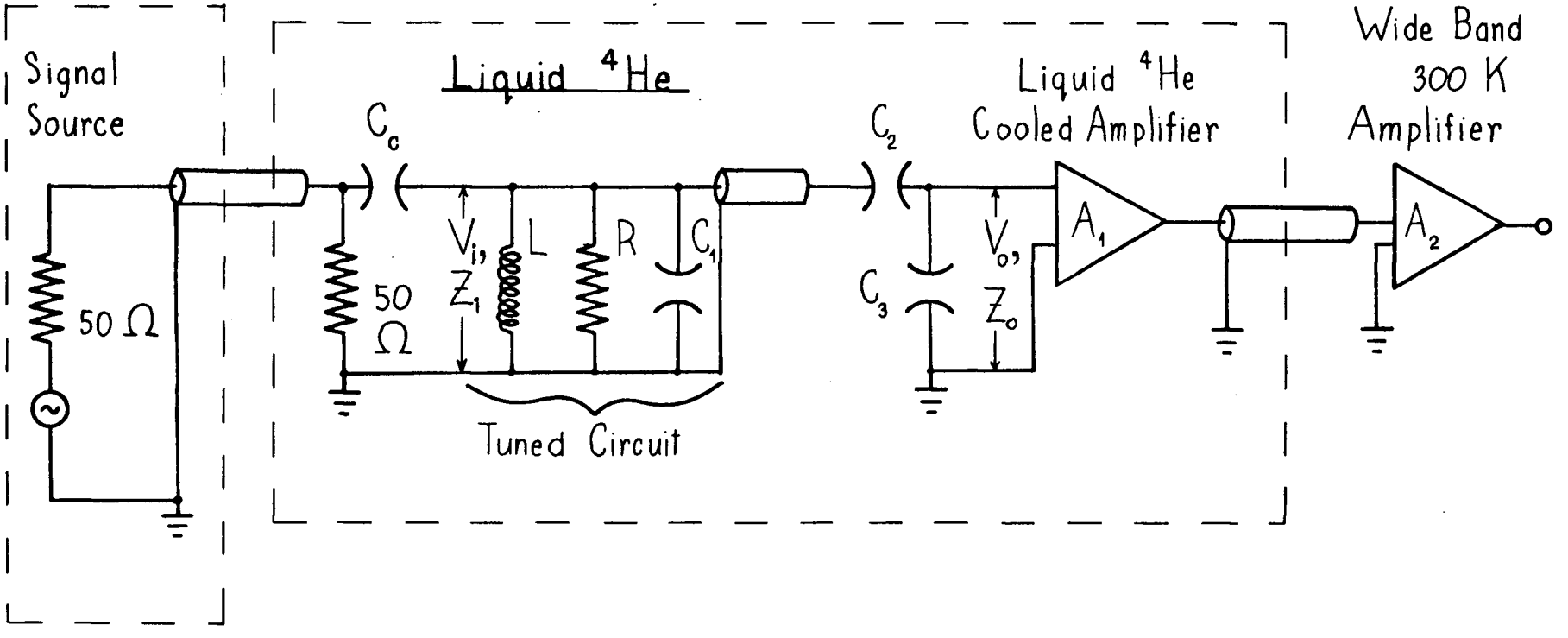

Fig. 32 The tuned circuit.

the capacitors were silver-mica and the 50Ω resistors were metal glaze. These components show little temperature dependence between 300 K and 4 K. A 2 pF coupling capacitor C_c made the RF power source look like a current generator. Two capacitors, C_3 and C_2, were used to match R = 4.3 kΩ to the optimum source resistance of the liquid helium cooled amplifier A_1, which was 2.9 kΩ at 4 K. This was necessary in order to minimize the noise figure of the amplifier. The 7 pF input capacitance of A_1 is included in C_3.

The values of C_2 and C_3 were chosen as follows. Define Z_i to be the impedance across the coil and Z_o to be the impedance seen by A_1 across its input. One can easily show that

$$Z_i = Q/[\omega L + iQ(\omega L - 1/\omega C)] \qquad \text{(VII-7)}$$

where $C = C_1 + C_2C_3/(C_2+C_3)$

At resonance $\omega^2 LC = 1$ so

$$Z_i = Q/\omega L \qquad \text{(VII-8a)}$$

$$= R \qquad \text{(VII-8b)}$$

Since the matching impedances are both capacitors, V_o is in phase with V_i and is a maximum at resonance. It is straightforward to show that the output impedance of the matching network is

$$Z_o = \frac{1 + iQ(\omega^2 LC_a - 1)}{i\omega C_b[1 + iQ(\omega^2 LC - 1)]} \qquad \text{(VII-9)}$$

where $C_a = C_1+C_2$ and $C_b = C_2+C_3$

Although Z_i is real at resonance, Z_o is in general

complex. This is undesireable because the source impedance of A_1 should be real in order to obtain the best noise figure. Z_o will be approximately real if

$$R>>(C_2+C_3)/(\omega C_2^2) \qquad \text{(VII-10)}$$

We satisfied (VII-10) and obtained Z_o = 2.9 kΩ by making C_1 = 300 pF, C_2 = 180 pF, and C_3 = 40 pF.

The coaxial cable between the tuned circuit and A_1 was thermally anchored to the ^{3}He pot, the ^{4}He pot, and the 4 K plate. In those sections, it was constructed from copper conductors with Stycast 2850 FT epoxy[1] as the dielectric. Between these sections, it was necessary to have low thermal conductance but high electrical conductance or the Q would be degraded. These conditions were met by using short sections of superconducting Nb-Ti wire. Although the wire has non-zero resistance at RF frequencies, it is small.

The liquid helium cooled amplifier A_1 consisted of a cascode stage (designed by Walter Hardy) and a source follower. The transistors in it were TIXM12 and TIXM301 p-Ge JFETs[2]. For our purposes, a FET amplifier can be treated as a noiseless amplifier with both a current noise generator and a voltage noise generator at its input. The voltage noise generator can be represented by a fictitious resistor R_n, which generates Johnson noise as shown in Fig. 33. V_s is the signal voltage and R_s is the source resistance.

The noise added by the liquid helium cooled amplifier came primarily from the input FET. Since the noise properties of

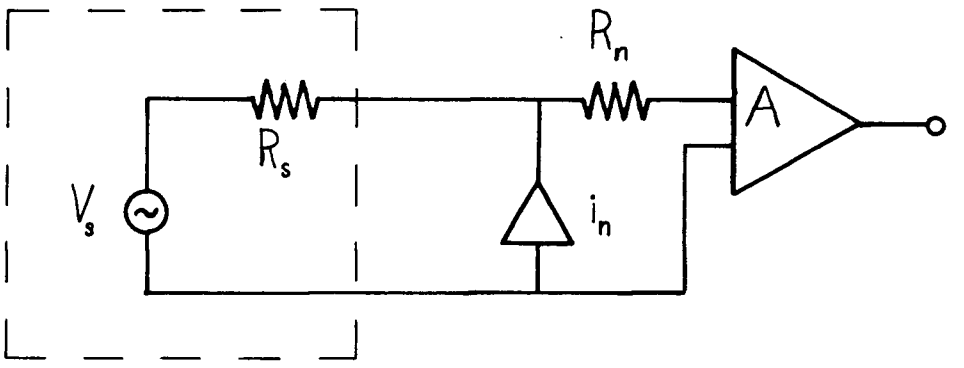

Fig. 33 Equivalent circuit of a FET amplifier. The amplifier A is noiseless. The current noise is i_n. The noise resistor R_n at the amplifier temperature T generates voltage noise, $v_n=(4kTR_n\Delta f)^{1/2}$, in bandwidth Δf.

Table XI: Characteristics of TIXM301 #13

v_{DS}=-3.40 V, I_{DS}=-4.0 mA, V_{GG}=.69 V

T(K)	g_m(mmho)	R_n(ohms)	I_{GS}(nA)
4.2	21	52	-4
77	16	48	-3
298	8	190	-800

the TIXM12 and TIXM301 JFET's vary considerably from one device to the next, it was necessary to measure these properties at 4 K for several devices in order to be able to select a good one.

The original input FET TIXM301 #502 provided reliable operation for nearly ten years. All of the measurements in the ^{4}He cryostat and some preliminary mesurements in the ^{3}He cryostat were made with it. Eventually, the bond between a wire and the silicon chip inside the transistor can broke during cooling to 77 K. Apparently, the thermal contraction of the lacquer covering the chip pulled off the wire. The FET was replaced several times but the replacements all failed in a similar manner after one or two cool downs. One of these, TIXM301 #13, was repaired by removing the lacquer with acetone and bonding the wire with silver paint[3]. It has survived more than a dozen thermal cycles and spectra obtained with it are as good as those for TIXM301 #502.

The properties of the FET's that we measured were the transconductance g_m which determines the gain, the noise resistance R_n, and the gate-source leakage current I_{GS}. The current noise i_n is the shot noise produced by I_{GS}. The noise properties of TIXM301 #13 are shown in Table XI. Another FET with $R_n(4.2\ K) = 89\Omega$ and $|I_{GS}| \leq 1nA$ gave distinctly noisier spectra.

After amplification by the tuned, liquid helium cooled amplifier, the amplitude modulated RF signal went through a low noise, wide band amplifier A_2 at room temperature. The RF

carrier was then removed by a diode peak detector. The resulting 280 Hz signal was amplified by a Princeton Applied Research (PAR) model 185 single ended amplifier with ground isolation and a PAR 114 signal conditioning amplifier. The signal then went to an Ithaco Dynatrac 391A lock-in amplifier and finally to a Nicolet 1170 signal averager with a model 172/4B input module. The output of the PAR 114 amplifier was monitored on a Tektronix 5440 oscilloscope with a 5A22N differential input amplifier. This was important for checking for coherent interference and intermittent microphonic noise.

Power for all of the non-commerical amplifiers was provided by Hewlett-Packard (HP) 6215A power supplies filtered by NiCd solid gel batteries. The batteries alone were not suitable because their voltage dropped as the batteries discharged, causing the amplifier gain to drift. The 60 Hz ripple on the power supplies was 200 μV peak to peak; it was reduced to 40 μV when filtered by the batteries. With filtering, there was no noticeable change in the noise observed on the oscilloscope when each power supply was switched on and off. Signal lines had to be routed carefully to prevent magnetic coupling to sources of 60 Hz interference.

Two pairs of coils clamped to the inside of the vacuum can were used to produce the modulation fields parallel and perpendicular to the Grafoil. The rectangular parallel coils (for $\bar{\beta}=90°$) were each 180 turns of 32 AWG copper wire bonded with GE 7031 varnish. Each coil had mean dimensions of

22 mm x 25 mm; they were 3.0 mm square in cross-section. Their 20 mm separation was 30% greater than the value that minimizes d^2H/dz^2 halfway between the coils, where the z axis is the axis of the coils. An effort was made to wind the coils very evenly and to align them accurately. If the modulation field was not parallel to $\vec{H}_o$, there would be an oscillating torque on the coils. The perpendicular coils had to fit between the parallel coils so the former were considerably less homogeneous. Each was made from 189 turns of 32 AWG wire. The mean coil dimensions were 24 mm x 12 mm and they were 2.5 mm wide by 4.1 mm thick. The mean separation was 24 mm. The modulation field of .17 mT peak to peak, used in both cases, was large enough to broaden some of the spectra slightly (see Section 8.5) but smaller fields would have decreased the signal amplitude.

The static magnetic field was provided by a Magnion electromagnet with a 6.4 cm gap and 23 cm pole caps. It was controlled by an FFC-4 Field Regulator which used a Rawson Lush 920 MCM rotating coil probe. The peak to peak separation of the derivative of the room temperature D_2O absorption signal was $2x10^{-5}$ T: the linewidth was entirely due to the magnetic field inhomogeneity. The sweep field H_s was provided by a pair of disc shaped coils mounted on the pole faces of the magnet. They were driven by an Interstate Electronics Corp. model F54A function generator and a Kepco model 36-5M bipolar operational amplifier, which was in the current sense mode. The function generator also triggered the signal averager. The

rotating coil probe was positioned such that the sweep field was primarily perpendicular to the coil axis so as to minimize cancellation of the sweep field by the magnet; the probe detected about 1% of the sweep field.

7.3 Coherent Interference

In the remaining sections of this chapter, various procedures necessary for obtaining good spectra will be discussed. The first topic is the choice of the modulation frequency and the nature of the coherent noise associated with it. Next, the dependence of the signal amplitude on the temperature and on the amplitude of the RF excitation will be considered. Finally, the ^1H background signal that had to be subtracted from the H_2 spectra will be mentioned.

The modulation frequency f_m had to be chosen judiciously in order to avoid compromising the S:N ratio. The best frequency was found to be 280 Hz. Ideally, f_m should be above the threshold value where excess low frequency noise becomes significant. The noise in a 1 Hz bandwidth was measured as a function of f_m at H_o=1.3 T. The noise was found to decrease as f_m increased from 100 Hz to 700 Hz.[4] At 280 Hz it was 40% higher than at 700 Hz. An upper limit to f_m is set by the condition that it be small compared to the linewidth or the spectrum will be distorted. Over the temperature range covered in these experiments, this limit was a few kHz for both H_2 and D_2.

Near the harmonics of 60 Hz, there was strong coherent interference so the difference between f_m and these harmonics had to be several times the lock-in detector bandwidth, which was at most 3 Hz. Also, the mechanical resonances of the cryostat had to be avoided. These could be readily observed by sweeping the frequency of a large sinusoidal current running through the sweep coils. In the range of 200-700 Hz, there were only five regions ranging from about 5-20 Hz in width where cryostat vibrations were not excited.

At first, a modulation frequency of 570 Hz was tried but at H_o=1.3 T coherent oscillations in the baselines of the derivative spectra were observed. The oscillations had a period of 1.1 mT and at 1.7 K their amplitude was about one third that of the p-D_2. This made their study quite difficult because the p-D_2 signal itself could only be discerned after several minutes of signal averaging. The amplitude of the oscillations was proportional to the modulation amplitude and independent of the sweep rate; the amplitude decreased as H_o decreased causing the oscillations to become unobservable at .6 T. These results suggested that the oscillations might have arisen from the magnetoresistance of some material near the NMR coil. The de Haas-van Alphen effect was suspected at first but this seemed unlikely because it is normally only seen in very pure metals. De Haas-van Alphen oscillations should have a period that is proportional to H^2 but the oscillations that we observed had about the same period at .85 T and 1.3 T. Fortunately, it was

not necessary to establish the source of the oscillations: at f_m=385 Hz they were quite weak and at 280 Hz, our ultimate choice for f_m, they had conveniently disappeared.

At this juncture, another form of interference was revealed. The modulation pick-up had a relatively large constant component v_o plus a small component Δv whose sign depended on the direction of the sweep. For the triangular sweep field H_s shown in Fig. 34(a), the modulation pick-up is shown in Fig. 34(b). In the following discussion, v_o will be ignored because it could easily be removed by an offset on the lock-in amplifier. The sweep dependent component Δv was independent of the modulation amplitude ΔH_m, the sweep amplitude ΔH_s, and the magnitude of the sweep rate $|\dot{H}_s|$ except when these parameters were very close to zero. If any of the parameters were equal to zero, then Δv was zero. The pick-up was observed at .2 T and 1.3 T but was larger at the higher field. The rise time of the pick-up was independent of ΔH_s but increased inversely with $|\dot{H}_s|$. Study of the pick-up was quite tedious because its amplitude was somewhat less than that of the p-D_2 signal and because it fluctuated. It source was not determined but its behaviour suggests the following scenario. The torques created by the interaction of $\vec{H}_o$ with eddy currents induced by H_s causes some part of the cryostat to move between two positions, x_1 and x_2. The force required to move it between these positions is very small but a very

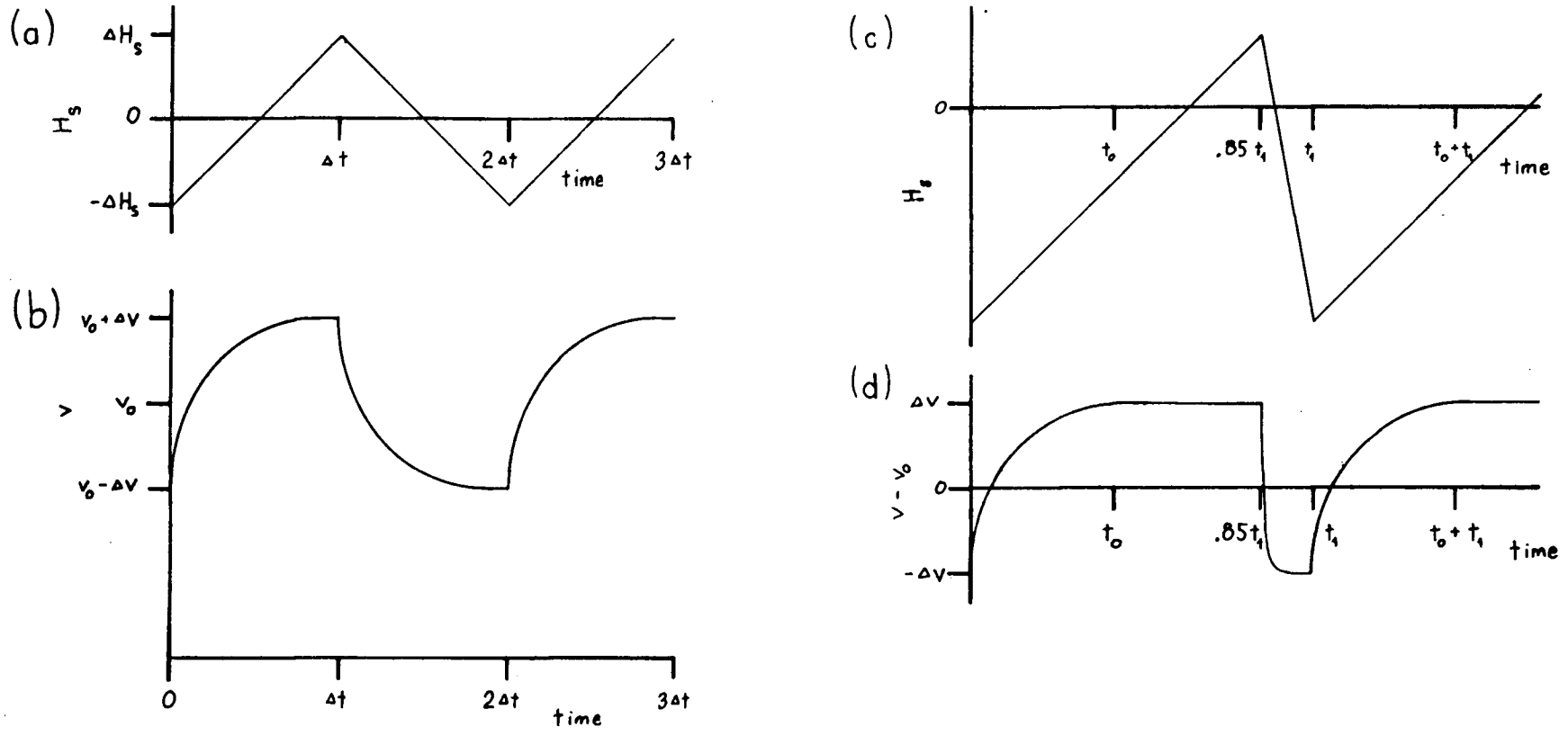

Fig. 34 (a) Triangular sweep field. (b) Modulation pick-up produced by the triangular sweep field. In reality $v_o >> \Delta v$. (c) The sweep field actually used. The signal averager starts collecting data at t_o, stops at .85 t_1 and restarts at $t_o + t_1$. (d) The modulation pick-up produced by the sweep of (c). The constant component has been subtracted.

large force is needed to move it outside that range. Provided that $|\dot{H}_s|$ exceeds some very small value, the cryostat would move to x_1, if $\dot{H}_s>0$ and to x_2 if $\dot{H}_s<0$. The interaction of $\vec{H}_m$ with $\vec{H}_o$ creates oscillating torques, causing coherent vibration. One could imagine that the amplitude of the vibration would be different at x_1 and x_2. Also, it might be restricted in such a way that it does not depend on $|\dot{H}_m|$, provided that $|\dot{H}_m|$ exceeds some very small value. Which part of the cryostat might be vibrating in this manner is an open question: it is even possible that it is the crystallites in the Grafoil. The pick-up was considerably larger when $\vec{H}_o$ (and $\vec{H}_m$) were perpendicular to the Grafoil ($\bar{\beta}=0°$) than when they were parallel ($\bar{\beta}=90°$).

We were unable to eliminate the pick-up. Its fluctuation also precluded observing it off resonance and subsequently subtracting it from the spectra. The pick-up could be avoided to a large extent by triggering the signal averager after the pick-up had become relatively constant [see Fig. 34(c) and (d)]. At the end of each sweep, H_s could not be returned to its initial value too quickly or there would be excessive eddy current heating of the ^{3}He pot. Consequently an 85%/15% ramp was used as shown in Fig. 34(c). Data was collected for 40% of the time for D_2 and 60% of the time for H_2.

7.4 Signal Intensity

For hydrogen molecules in state J, the normalized

absorption integral s_J was defined in (V-9). It should be proportional to 1/T and to the concentration of the nuclear spins being observed but independent of factors such as the size of the sample, the gain of the measuring system, and properties of the tuned circuit other than its frequency. Provided that the RF level is low enough to avoid RF heating and saturation, one can take the sample temperature T to be equal to the ^3He pot temperature T_3 and s_J to be independent of the RF level. It is important to avoid saturation because it may cause distortion that depends on measuring conditions such as the sweep rate. On the other hand, the RF level should not be too low because, in the absence of saturation and heating, the (unnormalized) signal is proportional to the RF level.

The simplest way to check for RF heating was to observe the J=0 signal from a sample of pure o-D_2[5] as a function of temperature and RF amplitude. 0-D_2 gave a single, narrow peak with a shape that was independent of temperature for our entire range. Although the amplitude of the o-D_2 absorption signal is less than that of o-H_2 at 4K, it is greater at .3K because the latter broadens considerably. The narrower o-D_2 signal also allowed a shorter time for each scan. The peak to peak height s_o^d of the derivative signal has been plotted in Fig. 35. At high temperatures and low RF levels, the Curie Law is obeyed but as T_3 decreases below 1K deviations occur, particularly at the higher RF levels. No distortion of the signal was seen so the deviations could be due to either RF

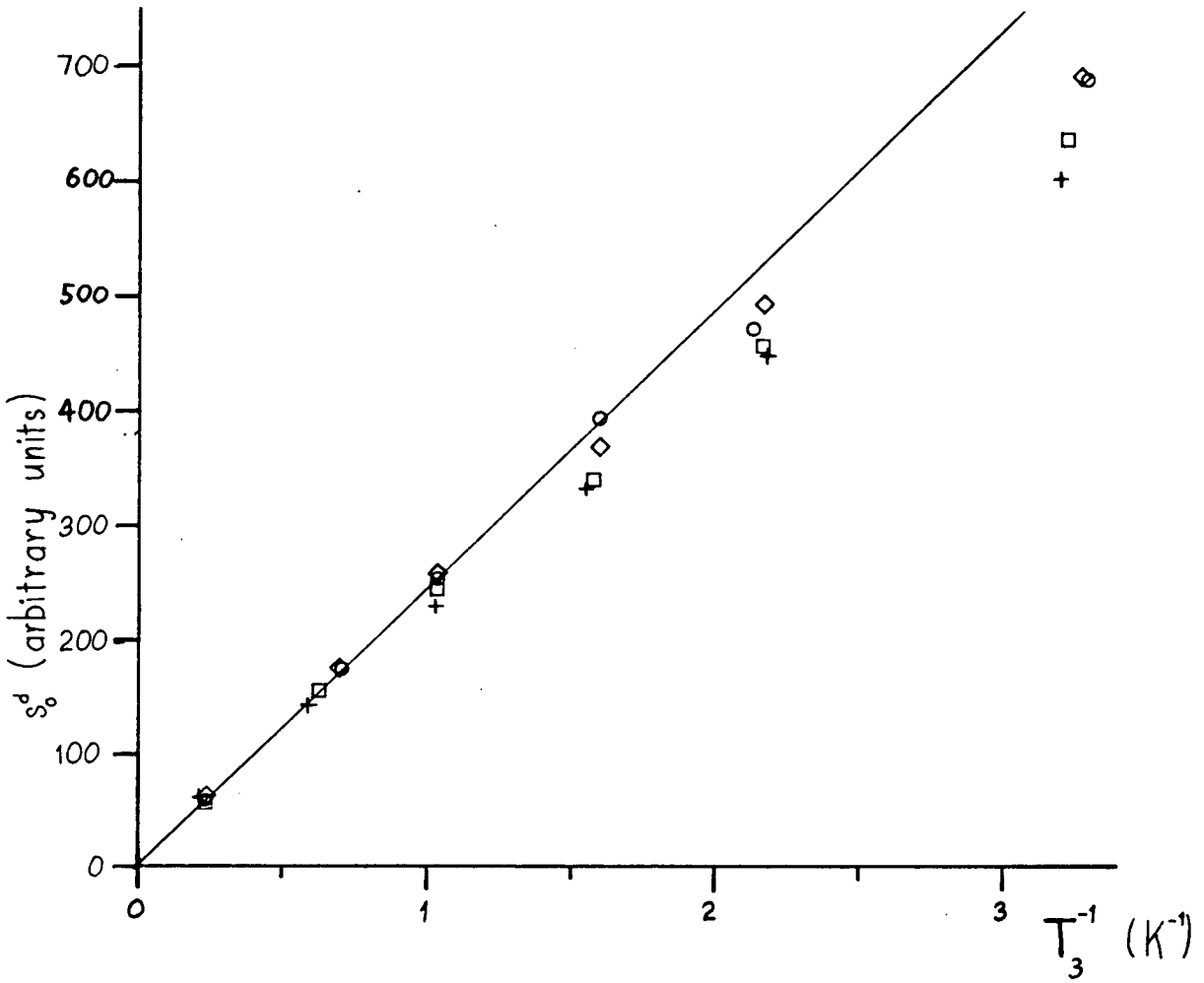

Fig. 35 Peak to peak height of the derivative of the absorption s_o^d versus $1/T_3$ for o-D_2 sample G14 in cell B. The RF input attenuation A was 10 dB (crosses), 13 dB (squares), 19 dB (diamonds), and 28 dB (circles). The straight line is the best fit to the high temperature and low RF level data. The J=1 concentration was $0.00^{+.02}_{-.00}$

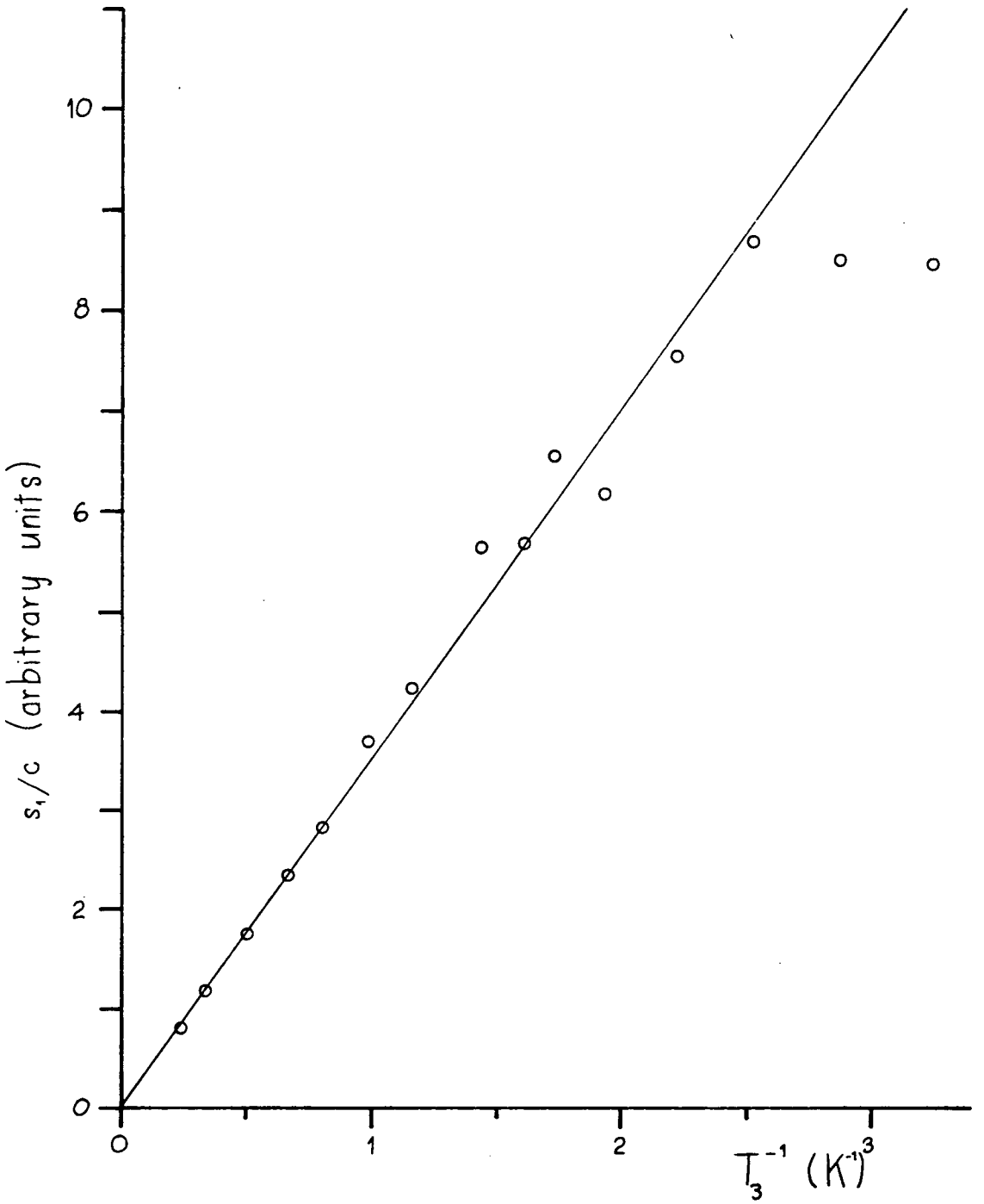

Fig. 36 Graph of s_1/c versus $1/T_3$ for o-H_2 sample G19 in cell B. $\bar{\beta}=90°$, A=13 dB, and $.78 \leq c \leq .94$. The straight line is a least squares fit to the Curie Law for the data with $T_3 \geq .4$ K.

heating or saturation. Heating is expected to increase in severity as the temperature drops because both the specific heat and thermal conductivity drop.

The absorption integral of o-H_2 normalized to c=1 has been plotted against T_3^{-1} in Fig. 36. The RF level was the same as that used in the measurements discussed in Chapters VIII and IX, i.e., RF attenuation A=13 dB. At higher levels, extra noise, apparently from the oscillator, became evident. The Curie Law was obeyed down to .4 K, much lower than for o-D_2. But in pure o-H_2 the conversion heating is ten times the RF heating at A=13dB. Therefore, the deviation of the o-D_2 data from the Curie Law should be attributed to saturation. For o-H_2, the deviation from the Curie Law appears to be much more sudden than one would expect for heating, although the data is rather limited. The temperature rise should be inversely proportional to κ_t for the Grafoil, which goes as T^2, at least between 1.5 K and 20 K (Hegde et al, 1973). The signal may be saturating at low temperatures but it is also possible that there are weak wings on the low temperature spectra that were not integrated because they were buried in the noise. A least squares fit to the Curie Law using the data at $T_3 > .4$ K gives

$$s_1/c = 3.52/T_3 \qquad \text{(VII-11)}$$

The absolute magnitude of the slope has no significance because s_1 contains an arbitrary normalization constant. However, this normalization constant is the same for all of the

absorption integrals discussed in this thesis so the results for different types of spins can be compared.

A plot of $s_o/(1-c)$ versus T_3^{-1} for the small J=0 component of two D_2 samples is given in Fig. 37. Sample G7 in cell A was absorbed at 23-27 K and the J=1 peaks were not resolved below 1.4 K, implying a non-uniform film. Sample G18 in cell B was adsorbed at 40 K and is believed to have been uniform: the J=1 peaks were clearly resolved down to .85 K. Data from the two samples agree well and the Curie Law is obeyed over the entire temperature range. This is rather surprising considering that the J=0 component of pure o-D_2 showed evidence of saturation below 1 K. The I=2 nuclei are apparently relaxed more effectively by I=1 neighbours than by I=2 neighbours. However, this conclusion should not be overemphasized because the scatter in the p-D_2 data is fairly large, particularly for G18 at low temperature. A least squares fit to the Curie Law yields

$$s_o/(1-c) = 1.71/T_3 \qquad \text{(VII-12)}$$

Fig. 38 is a graph of s_1/c versus T_3^{-1} for the same two samples of D_2. Above .9 K, both follow the Curie Law although the G7 data is fairly limited in that region. A least squares fit to the high temperature data gives

$$s_1/c = .705/T_3 \qquad \text{(VII-13)}$$

In accordance with (V-8), one expects the ratio of the slopes given in (VII-12) and (VII-13) to be equal to (5/6)(6/2)=5/2. The factor 5/6 is the fraction of J=0 molecules that have I=2

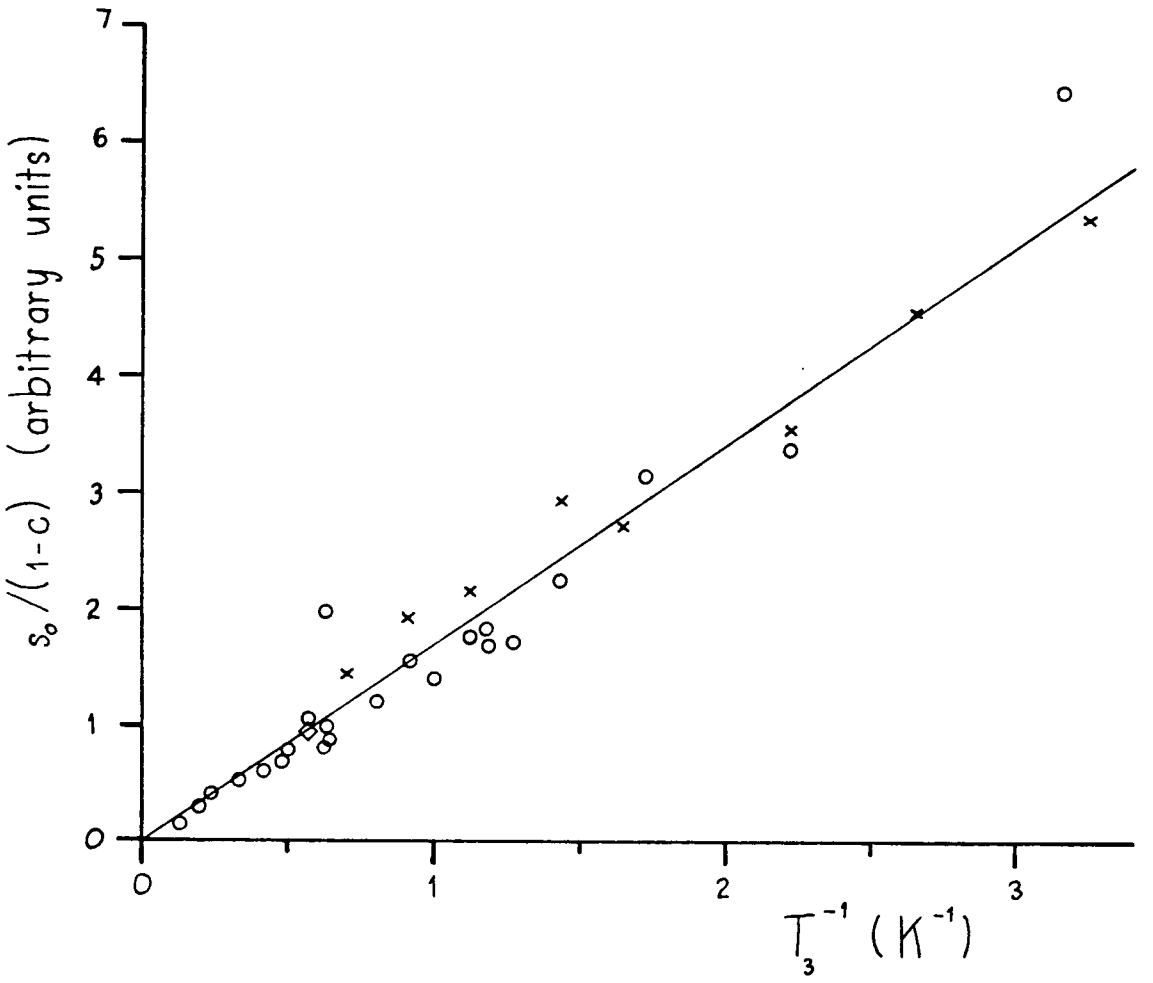

Fig. 37 Graph of $s_o/(1-c)$ versus $1/T_3$ for the J=0 component of D_2. $\bar{\beta}=90°$. The data is from D_2 sample G18 in cell B ($.77 \leq c \leq .98$) with A=13 dB (circles) and A=19 dB (diamond), and from D_2 sample G7 in cell A ($.94 \leq c \leq .97$) with A=14 dB (crosses). The line is a least squares fit to the Curie Law.

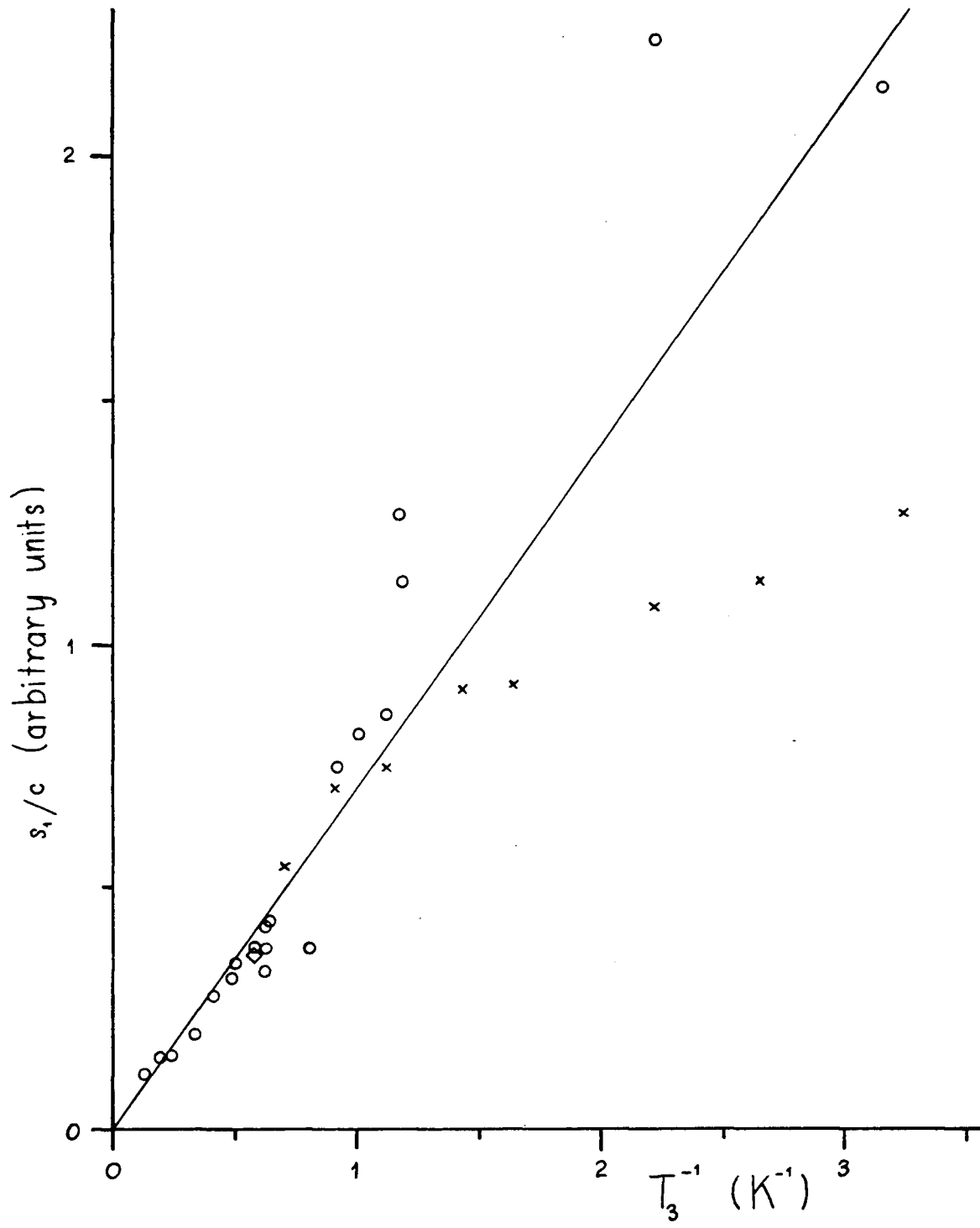

Fig. 38 Graph of s_1/c versus $1/T_3$ for the J=1 component of D_2. $\bar{\beta}=90°$. The data is from D_2 sample G18 in cell B ($.77 \leq c \leq .98$) with A=13 dB (circles) and A=19 dB (diamond), and from D_2 sample G7 in cell A ($.94 \leq c \leq .97$) with A=14 dB (crosses). The line is a least squares fit to the Curie Law, using only the data with $T_3 \geq .9$ K.

and 6/2 is the ratio of I(I+1) for I=2 and I=1. The measured slopes agree well with this result since

$$(2/5)(J=0 \text{ slope}/J=1 \text{ slope}) = .97 \qquad \text{(VII-14)}$$

(V-8) also implies that the ratio of the slopes of s_1/c versus T_3^{-1} for o-H_2 and p-D_2 should be equal to the ratio of $\gamma^2 H_0 = \gamma\omega_0$; ω_0 was the same in each case. One finds

$$[\gamma(D_2)/\gamma(H_2)](H_2 \text{ slope}/D_2 \text{ slope}) = .77 \qquad \text{(VII-15)}$$

which is significantly less than the expected value of one. The reason is not clear.

Below .9 K, s_1/c is quite different for G18 and for G7. Sample G18 appears to continue to obey the Curie Law but the scatter in the data is very large because the modulation pick-up made it very difficult to determine the baseline. In fact, between .5 K and .7 K it was impossible so s_1 could not be determined for the spectra in that range. For G7 the task was somewhat easier; the surface area of the Grafoil in cell A was twice as great as that in cell B so the relative effect of the coherent interference was much less. Even so, data near .6 K should be treated cautiously. The difference in the low temperature behaviour of G7 and G18 can only be attributed to the nature of the two samples. It is known that G7 was not uniform so perhaps some molecules experienced different crystal fields from most of the others and produced a broad and weak component of the absorption spectrum that was not included in theintegral giving s_1. We found, using the ^{4}He cryostat, that when the coverage was increased above $\rho = 1$ ($\sqrt{3} \times \sqrt{3}$

coverage), the NMR spectrum at 4 K rapidly broadened and disappeared. The adsorbate went out of registry with the substrate so that the contribution to the crystal field arising from interactions with the surface began to vary from one molecule to the next.

When the J=1 concentration of G7 was calculated from s_1/s_0, this hypothetical missing component was included by assuming that s_1 obeyed the Curie Law all the way down to .3 K. The correction to s_1/c was insignificant because $c \tilde{=} 1$ for all of the G7 data. However, for $s_0/(1-c)$ the correction was large. The fact that the corrected values of $s_0/(1-c)$ fit the Curie Law quite well supports the hypothesis of the missing component.

7.5 ^1H Background

The ^1H background signal contained three components. The peak to peak widths of the absorption derivatives of the two narrow components were 1.3 mT and about .1 mT. The broad component, which extended beyond our maximum o-H_2 sweep width of 12 mT, was very weak and could only be discerned near .3 K. When observing the o-H_2 spectra, we used a peak to peak magnetic field modulation of .17 mT so the narrowest component of the ^1H background signal was not resolved. Its width was about the same as that of the ^1H signal previously seen by us in Pyrex. The fact that it is so narrow suggests that it is due to isolated impurities in some material. The medium width

component was similar to the signal that we had previously seen in Teflon so it probably arose from the Teflon coil holder and Teflon film inside the Grafoil cell.

Fig. 39 shows the temperature dependence of the combined absorption integrals of the two narrow components. For each RF level, s versus T_3^{-1} is linear but the y-intercept is positive. This could occur if part of the signal were from spins at $T=T_3$ and part were from spins at some fixed temperature. The latter might, for example, be in the enamel on the modulation coil leads, which were not completely covered by aluminum foil. The straight line is a least squares fit to the 13 dB data. It gives.

$$s = 2.27/T_3 + .56 \qquad \text{(VII-16)}$$

At low temperatures, s increases as the RF level decreases, as one would expect if there were saturation. Examination of the absorption signal shown in Fig. 40 provides further evidence of saturation. The response of the spins that first come into resonance, i.e, at the left side of the scan, is stronger that that from those that come into resonance later. At lower RF levels this distortion did not occur. This effect can be explained by the following argument. As the field sweeps up from its initial value H_i, the first spins to come into resonance are slightly depolarized. They interact with the other spins, depolarizing them slightly. If these spins come into resonance in a time shorter than the longitudinal relaxation time T_1, they will produce a weaker signal. This

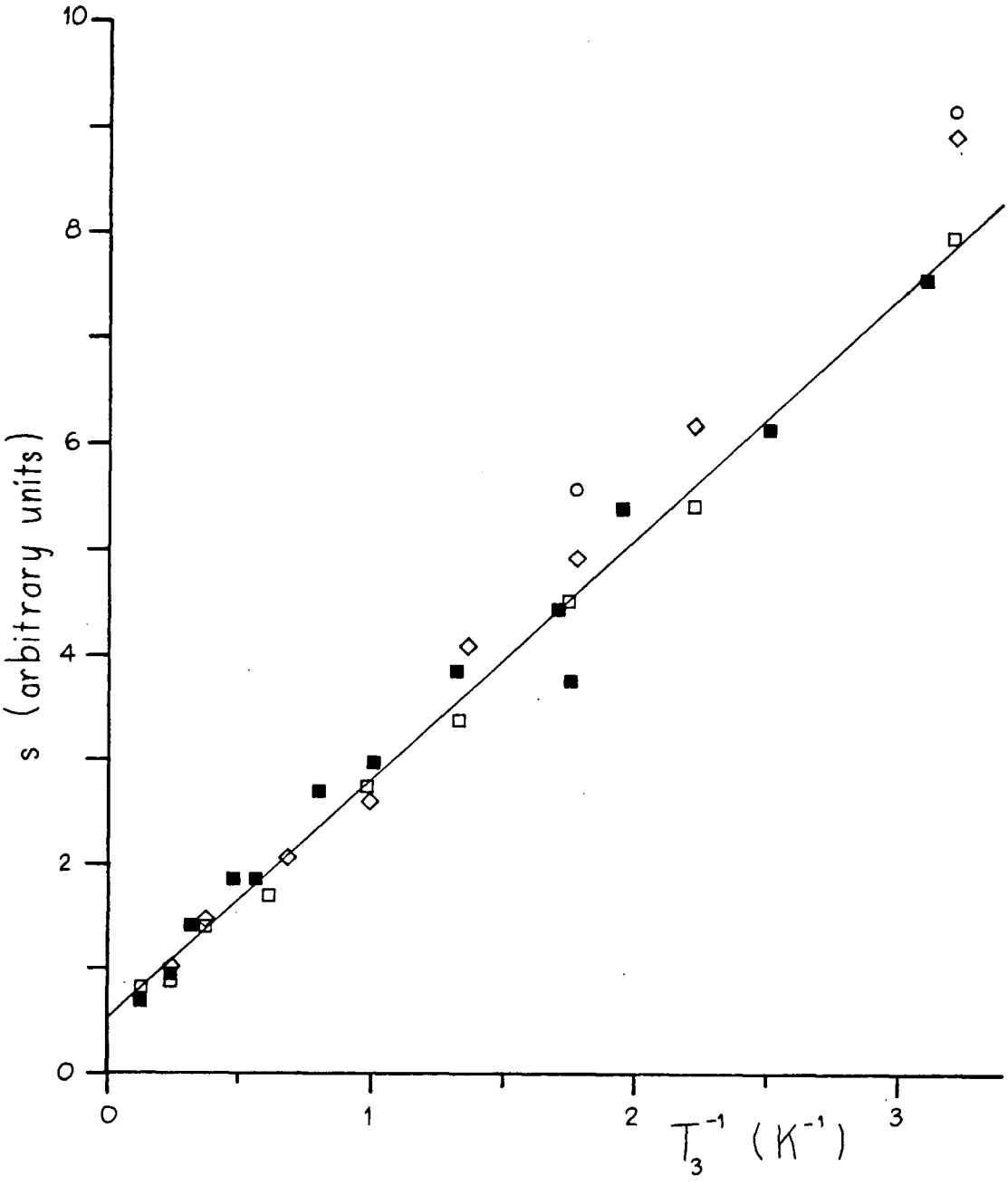

Fig. 39 Graph of s versus $1/T_3$ for the ^1H background signal. The solid squares are for $\bar{\beta}=0°$ and all of the other symbols are for $\bar{\beta}=90°$. The RF attenuation A was 13 dB (squares), 19 dB (diamonds), and 25 dB (circles). The straight line is a least squares fit to the 13 dB data.

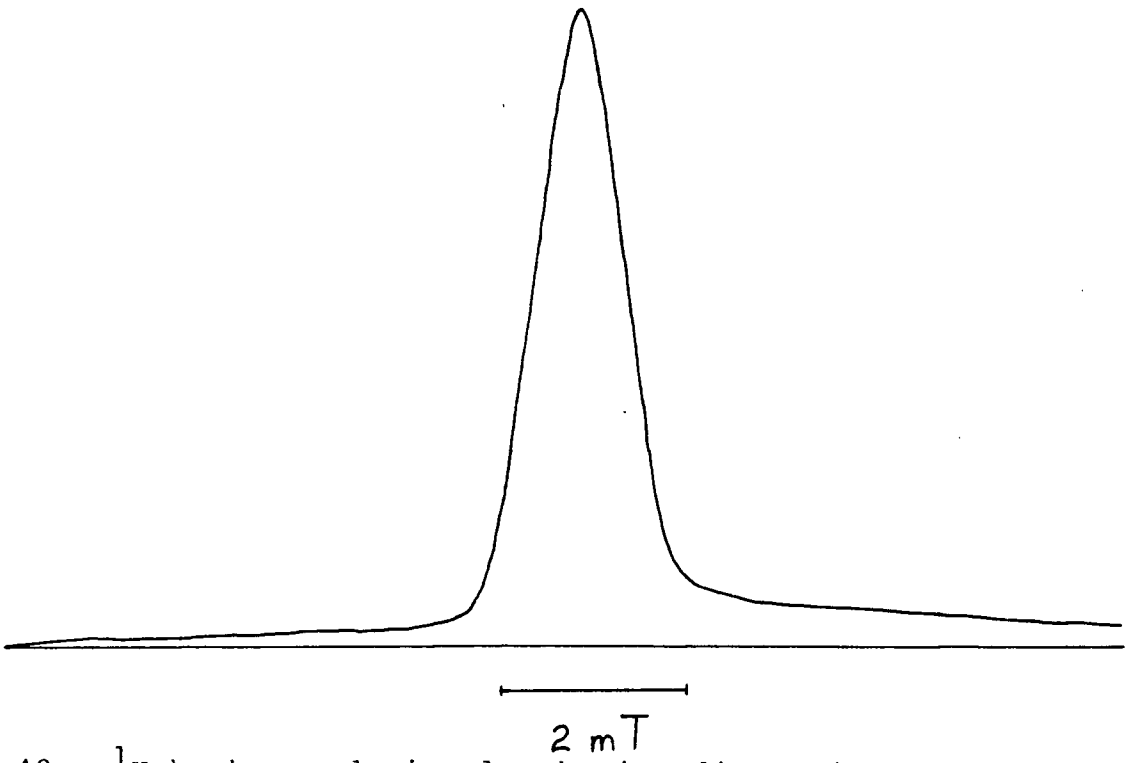

Fig. 40 ^{1}H background signal, showing distortion due to saturation. The broad component extends beyond the width of the scan. The .1 mT component of the signal cannot be seen because it is overmodulated. The total measuring time t_m was 9.1 h, A=13 dB, T_3=.314 K, and $\bar{\beta}$=90°.

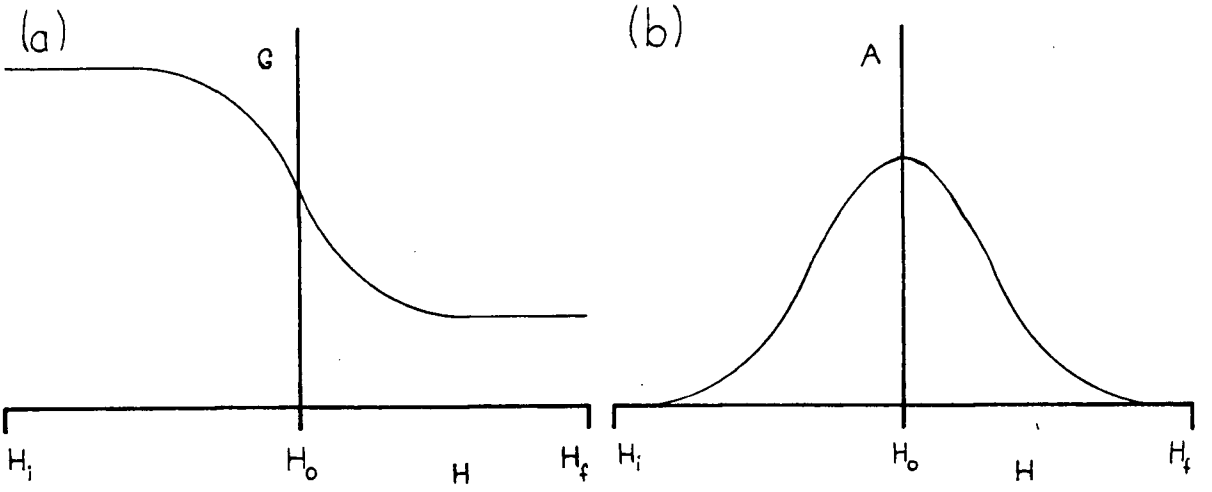

Fig. 41 (a) The effective gain G of the NMR system when sweeping from H_i to H_f and saturating the spins. (b) The unsaturated absorption signal A(H).

effect can be modelled by saying that the effective gain G decreases as the sweep proceeds as shown in Fig. 41(a). In the limit of small modulation, we observe a signal G(H)A'(H) where A'(H) is the derivative of the unsaturated absorption signal A(H). If H_i and H_f are respectively well below and well above the resonance region, then $A(H_i)=A(H_f)=0$. Integrating by parts, we find that the integral of the product G(H)A'(H) is greater than zero:

$$\int_{H_i}^{H_f} G(H)A'(H)\,dH = A(H_f)G(H_f) - A(H_i)G(H_i) - \int_{H_i}^{H_f} G'(H)A(H)\,dH \quad \text{(VII-17a)}$$

$$= -\int_{H_i}^{H_f} G'(H)A(H)\,dH \quad \text{(VII-17b)}$$

A(H) is a positive, even function of $H-H_0$ and G'(H) is a negative function so the right hand side of (VII-17b) is positive, producing the offset seen at the right side of Fig. 40.

The absorption integrals of the ^1H background and pure $o\text{-}H_2$ were quite similar in size so it was important that the background be subtracted accurately. In particular, if the background signal was not centered correctly a spurious, narrow central component would be generated. Consequently, background spectra were obtained at least every .2 K for temperatures below 1 K. Above 1.5 K, ^1H background spectra were measured at the same temperatures as the $o\text{-}H_2$ spectra. The background spectra and $o\text{-}H_2$ spectra were recorded under identical conditions. Some typical derivative spectra with and without the background are shown in Fig. 42.

Fig. 42 Derivatives of the absorption signal with [(a), (c), and (e)] and without [(b), (d), and (f)] the ^{1}H background signal. A=13 dB and $\tilde{\beta}=0°$. The horizontal bars are 2 mT. The total measuring time is t_m. (a) and (b): .318 K, t_m=1.2 h, c=.95. (c) and (d): .664 K, t_m=2.4 h, c=.91. (e) and (f): .860 K, t_m=1.2 h, c=.89.

Notes to Chapter VII

1. Emerson and Cuming Inc., Canton, Mass., U.S.A.

2. Manufactured by Texas Instruments but no longer available.

3. This delicate operation was performed by J.F. Carolan.

4. This statement disregards various peaks in the noise at certain values of f_m, which are discussed below.

5. We also tried using the ^{13}C resonance of Grafoil but that signal saturated at all RF amplitudes that were large enough to give a useful signal.

CHAPTER VIII

NMR SPECTRA OF o-H_2

8.1 Evidence for Orientational Ordering

Some NMR absorption spectra obtained from a high concentration sample of o-H_2 (G20) with $\bar{\beta}=0°$ and $\rho=.85$ are shown in Fig. 43 and 44. The ^1H background has been subtracted. At high temperatures, there is a doublet with a splitting $\Delta\nu$ that increases slowly as T decreases. This is what one would expect for the pararotational state, which is characterized by a single order parameter σ. A feature that is not expected is that below 1.2 K the centre of the spectrum begins to fill in. Near .6 K, the splitting increases very rapidly and a central peak emerges. Below .6 K, the central peak disappears, the splitting slowly approaches a maximum, and two small, outer peaks appear. At low temperature, the spectra are strong functions of the concentration; there are many similarities in the changes in the spectra caused by lowering c or raising T. Due to the concentration dependence, there was insufficient time to obtain good S:N ratios. In any event, even with extensive signal averaging, the baselines of the spectra would not have been flat because of fluctuating modulation pick-up. The shape of the baselines that it produced changed with temperature.

The spectra shown in Fig. 45 and 46 were obtained from another high concentration sample of o-H_2 (G19) but this time with $\bar{\beta}=90°$ and $\rho=.85$. The behaviour of these spectra is

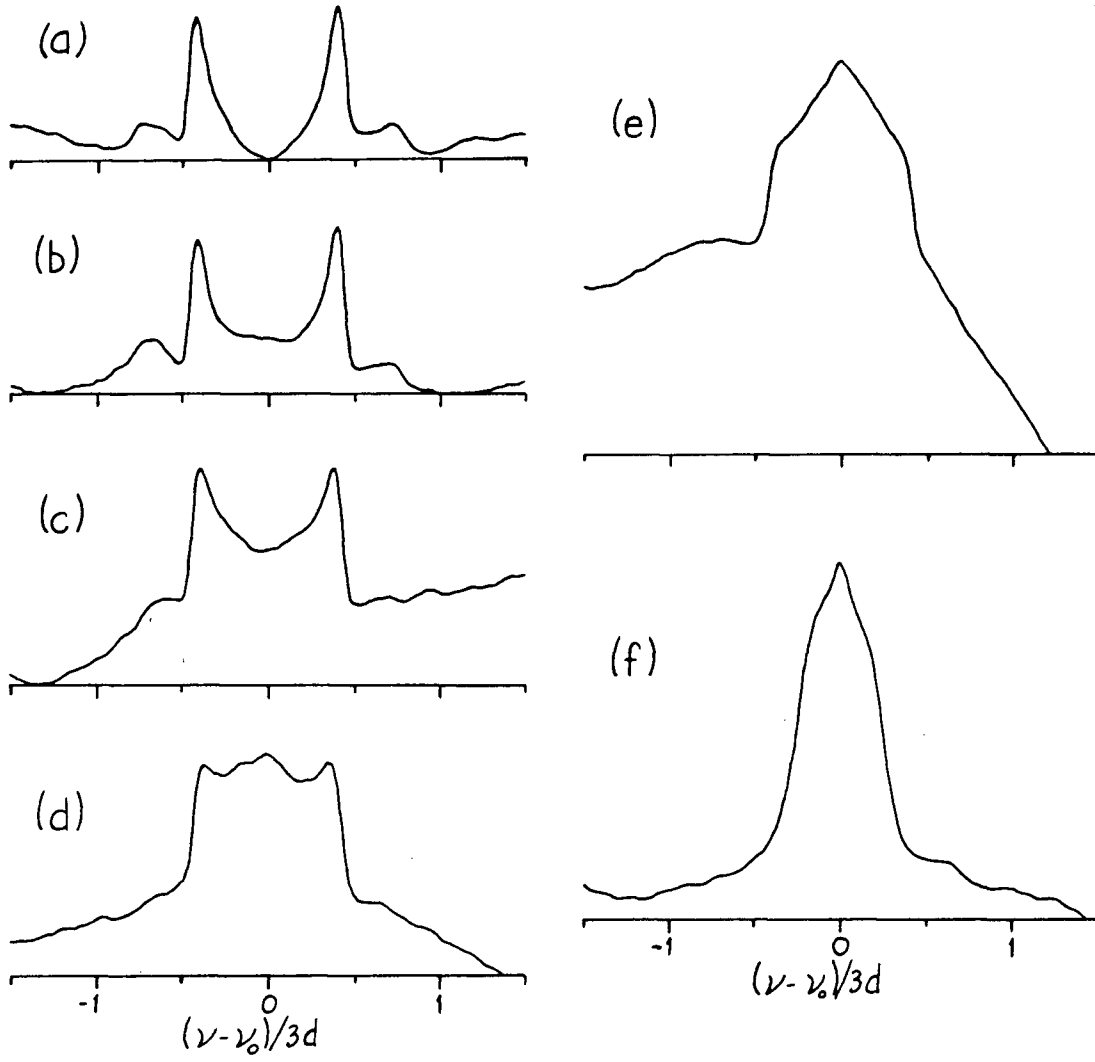

Fig. 43 Absorption spectra of o-H_2 sample G20 with $\bar{\beta}$ =0°. A=13 dB. ρ =.85.

Spectrum	(a)	(b)	(c)	(d)	(e)	(f)
T(K)	.318	.400	.508	.563	.582	.664
c	.95	.94	.94	.93	.92	.91
t_m(h)	1.2	1.2	1.2	1.2	2.4	2.4

The vertical scale is the same for all of the spectra. The amplitudes of the signals have been multiplied by T so that if the Curie Law were obeyed and if c were constant, the area under each of the spectra would be expected to be the same.

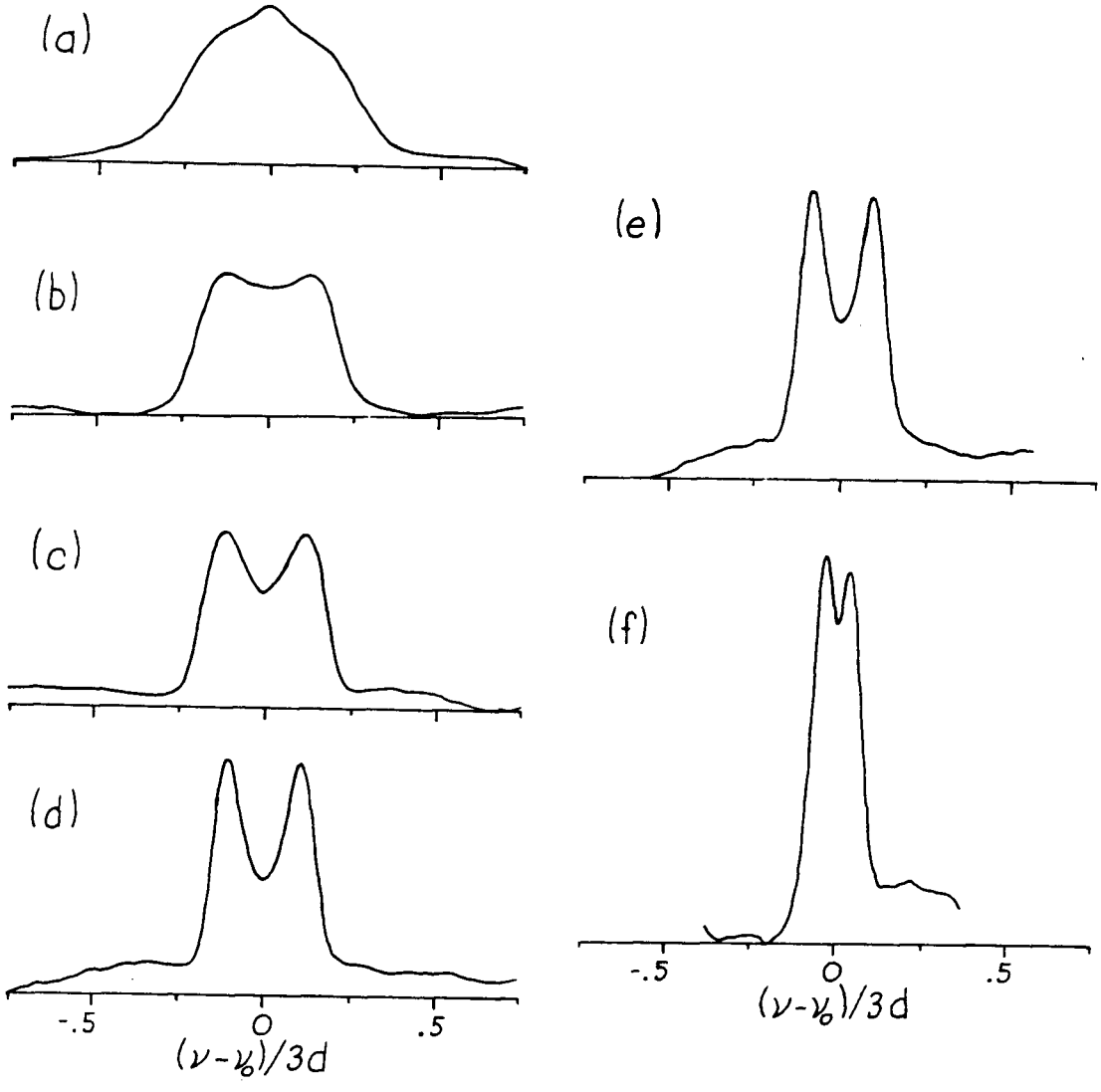

Fig. 44 Absorption spectra of o-H_2 sample G20 with $\bar{\beta}=0°$. A=13 db. $\rho=.85$.

Spectrum	(a)	(b)	(c)	(d)	(e)	(f)
T(K)	.664	.752	.860	1.19	1.76	4.24
c	.91	.90	.89	.88	.87	.85
t_m(h)	2.4	1.2	1.2	1.2	.90	1.2

The vertical scale is twice as great as in Fig. 43 and the horizontal scale is half as great. The spectra have been normalized in the same manner as those in Fig. 43. Note that (a) is the same as Fig. 43(f).

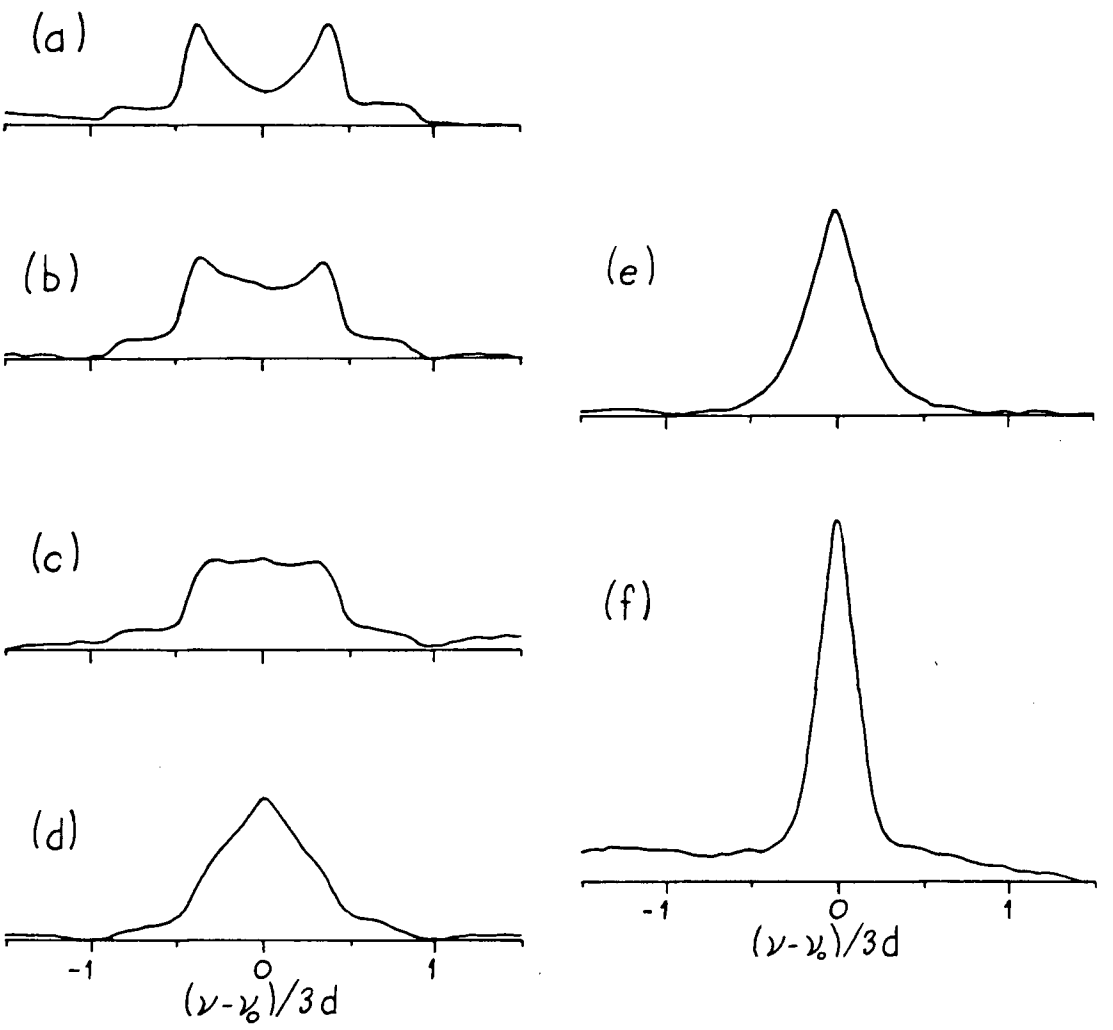

Fig. 45 Absorption spectra of o-H_2 sample G19 with $\bar{\beta}=90°$. A=13 dB. $\rho=.85$.

Spectrum	(a)	(b)	(c)	(d)	(e)	(f)
T(K)	.309	.450	.519	.577	.620	.693
c	.94	.92	.91	.90	.87	.86
t_m(h)	1.2	2.1	2.4	3.7	2.4	3.9

The spectra have been normalized in the same manner as those in Fig. 43. The vertical scale is the same for all of the spectra here.

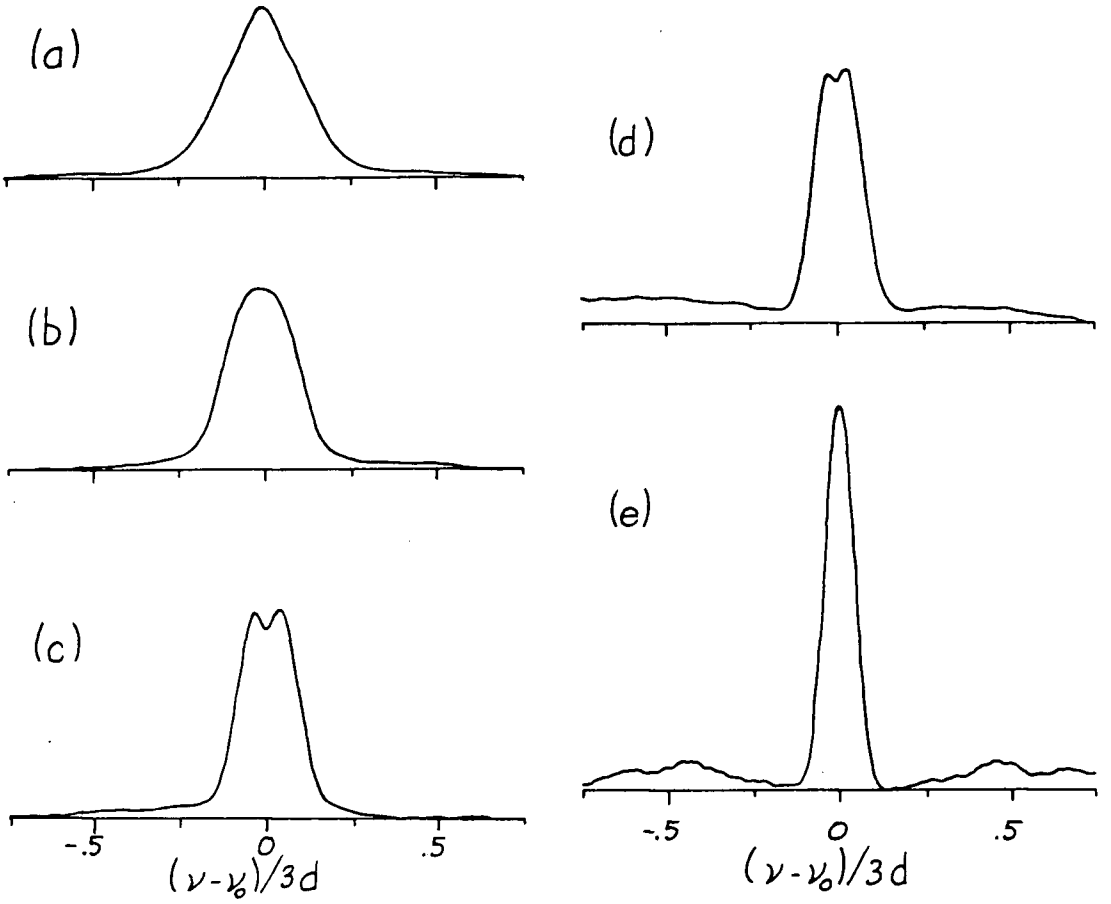

Fig. 46 Absorption spectra for o-H_2 sample G19 with $\bar{\beta}=90°$. A=13 dB. $\rho=.85$.

Spectrum	(a)	(b)	(c)	(d)	(e)
T(K)	.693	.863	1.25	1.98	4.22
c	.86	.84	.82	.80	.79
t_m(h)	3.9	2.4	2.4	2.8	2.4

The spectra have been normalized in the same manner as those in Fig. 43. The vertical scale is twice as great as in Fig. 45 and the horizontal scale is half as great. Note that (a) is the same as Fig. 45(f).

similar to that of the $\bar{\beta}=0°$ spectra but the features are not as clearly resolved. As (IV-14) and (IV-15) show, this is because in the case of $\bar{\beta}=90°$ it is necessary to average over the azimuthal angle α of the graphite crystal axes but for $\bar{\beta}=0°$ it is not.

In Fig. 47, the temperature dependences of the main peaks of the absorption spectra of G19 and G20 have been plotted. Note that in the disordered state $\Delta\nu/3d=|b|$ for G19 but $\Delta\nu/3d=2|b|$ for G20 because $\bar{\beta}=90°$ and 0° respectively. For G20, the peaks at $T^{-1}=1.51$ and 1.72 K^{-1} were not resolved but their positions could be estimated. The same applies to $T^{-1}=1.73$ K^{-1} for G19. However, for the G19 spectra in the ranges $1.16\ K^{-1}<T^{-1}<1.61\ K^{-1}$ and $T^{-1}<.331\ K^{-1}$, the peak positions could not even be estimated. The peak splittings have been corrected for the effect of broadening which was assumed to be Gaussian.[1] If two delta function peaks, which have a splitting $\Delta\nu$, are subject to Gaussian broadening with a standard deviation σ_G, then the broadened peaks will be pulled together. Their splitting $\Delta\nu'$ is given by

$$x = (\Delta\nu'/2\sigma_G)^2 \coth x \qquad \text{(VIII-1)}$$

where $x = \Delta\nu\Delta\nu'/4\sigma_G^2$

The broadening was determined from the width of the outer edges of the main peaks: these edges are not affected by the orientational distribution of the graphite crystals. For G20, the correction was insignificant unless $T^{-1}<.31\ K^{-1}$. For G19, the correction was insignificant for $T^{-1}>1.7\ K^{-1}$ but was about a factor of two for $.5\ K^{-1}<T^{-1}<1.0\ K^{-1}$. For

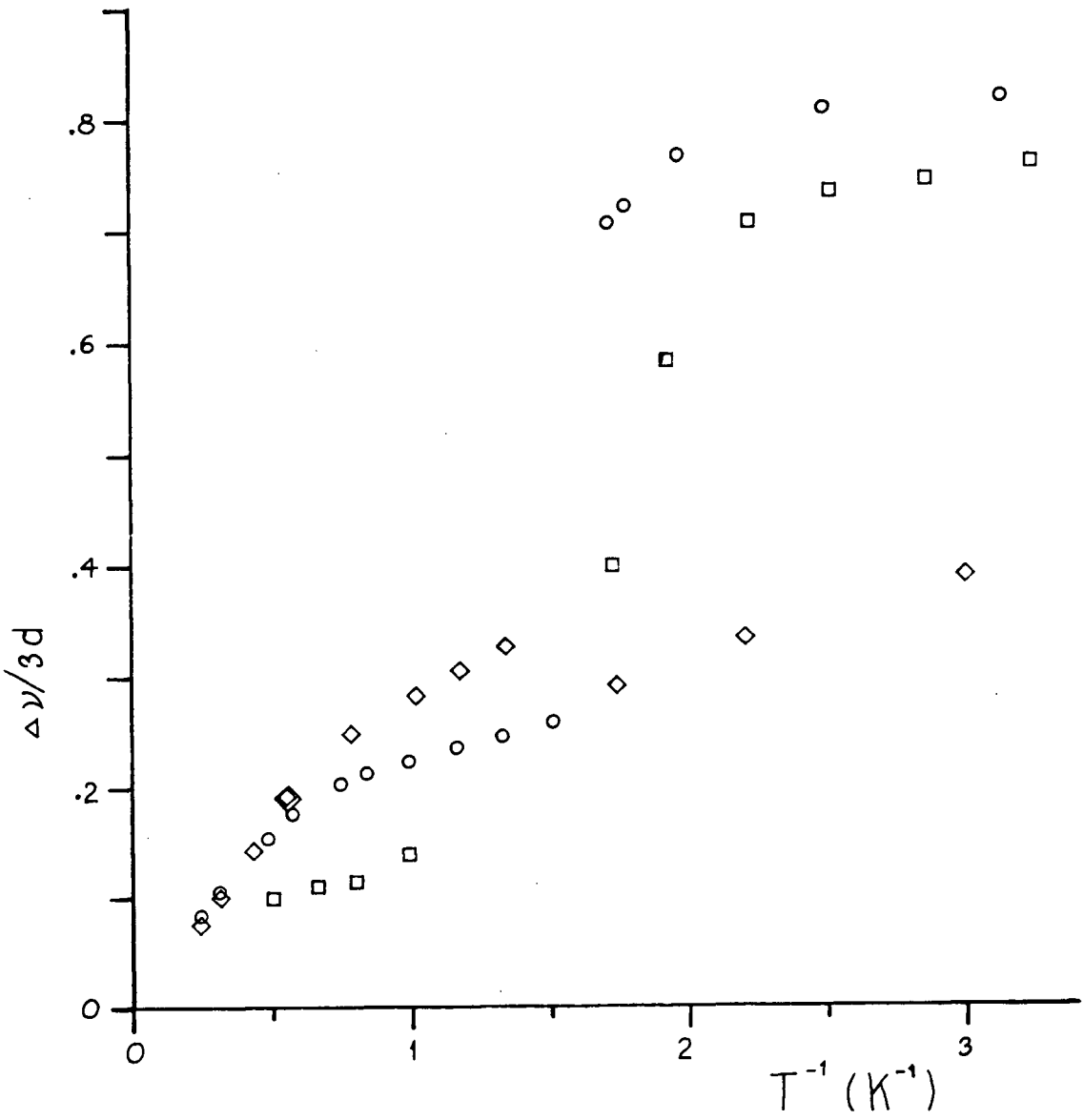

Fig. 47 Splitting of the absorption peaks $\Delta\nu/3d$ versus 1/T for three o-H_2 samples: G20 with $.83 \leq c \leq .95$ (circles), G21 with $.21 \leq c \leq .26$ (diamonds), and G19 with $.78 \leq c \leq .94$ (squares). Samples G20 and G21 had $\beta = 0°$ whereas G19 had $\beta = 90°$.

the latter points the correction is so large that it cannot be considered to be very reliable since the broadening is not exactly Gaussian and the unbroadened spectra are not delta function lines.

For both samples measurements were initiated at .3 K and T was increased successively for subsequent measurements. The temperature was not increased monotonically because it was necessary to warm the sample to 4 K when the ^{3}He was re-condensed. For G20, this first occurred after the measurement at .5 K and for G19, during the measurement at .58 K and again after the measurement at .69 K. The G19 spectra at .58 K obtained before and after warming to 4 K appeared to be identical so they were added together. The spectra are very sensitive to temperature in this region so if there were any hysteresis it must have been very small.

We have interpreted the rapid, factor of three increase in $\Delta\nu$ near .6 K as a transition to an orientationally ordered state. The two data points of G20 bracketing the sharp rise have c=.91 and c=.92. Note that the transition temperature T_c will drop as c decreases, so that on Fig. 47 the transition will appear to be a little sharper than it actually is. At .3 K, $\Delta\nu$ appears to be close to its maximum value so the spectrum would be unlikely to change much if T were lowered any further. Consequently, we have fit the .3 K spectra to the T=0 spectra expected for the various orientationally ordered states predicted by MFT. This is discussed in the next section. The results show

conclusively that the pinwheel phase is the only one of these states that is consistent with the .3 K spectra.

No attempt has been made to analyze the shapes of the spectra intermediate between the high temperature doublet and the .3 K spectrum. A particularly interesting feature of these spectra is the emergence of the central peak and its subsequent disappearance as T decreases. Spectra in the intermediate temperature regime exhibit many of the characteristics seen in the NMR spectra of bulk o-H_2 for .2<c<.55 and .2 K<T<.7 K (Estève et al, 1982; Washburn et al, 1982). Bulk o-H_2 is known not to have long range orientational order at such low concentrations but, as mentioned in Section 1.3, it has been proposed that it undergoes a transition to a quadrupolar glass (Sullivan, 1976). Regardless of whether the symmetry of the low temperature state is actually any different from that of the pararotational phase, it is well established that the NMR lineshapes can be explained by changes in the probability distribution $P(|\sigma|)$ of the magnitude of the order parameter σ. Some bulk o-H_2 spectra and the corresponding $P(|\sigma|)$'s deduced from them are depicted in Fig. 48. Note that in the intermediate temperature range, where $P(|\sigma|)$ is very broad, a central component is observed in the spectra. Even at the lowest temperatures, the centre of the spectrum is nearly filled in because of the long tail of $P(|\sigma|)$.

Some success in predicting the temperature dependence of $P(|\sigma|)$ has been achieved by using a mean field model in which

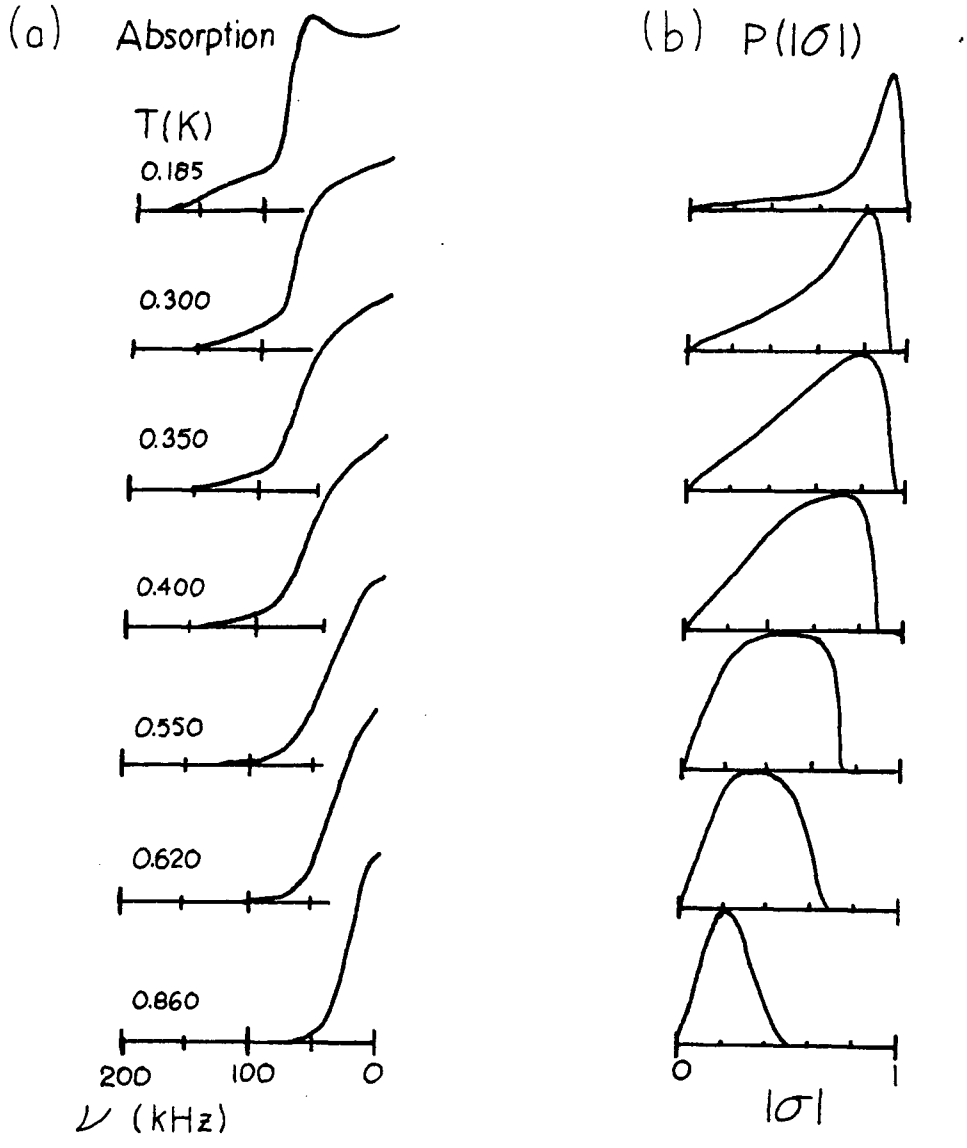

Fig. 48 Temperature dependence of (a) the NMR absorption spectrum (only half is shown) and (b) the order parameter distribution $P(|\sigma|)$ of bulk o-H_2 in the disordered state for c=.55 (Washburn et al, 1982). At each temperature, the experimental spectrum is virtually identical to the synthetic spectrum derived from $P(|\sigma|)$.

molecules are assumed to interact with a random distribution of axially symmetric quadrupolar fields (Estève et al, 1982). These fields would depend on the local distribution of J=1 molecules. The energy levels of a J=1 molecule would be split into an $m_J=0$ level and a pair of degenerate $m_J=\pm 1$ levels as in the case of an adsorbed J=1 molecule which experiences an axially symmetric crystal field. The magnitude of the energy gap would vary randomly from site to site. The peak of $P(|\sigma|)$ becomes narrow at low temperatures because the energy gap is large compared to kT; virtually all of the molecules are in the ground state regardless of the width of the gap.

In light of the low concentration, bulk o-H_2 measurements, it appears that our intermediate temperature, high concentration adsorbed o-H_2 spectra might well be explained in terms of a distribution of the order parameters. For $\bar{\beta}=0°$, probably only σ would be needed but for $\bar{\beta}=90°$, it might also be necessary to include η. It would be necessary to improve the S:N ratios of the spectra in order to be able to pursue this approach.

There are some other alternatives for explaining the central peaks of the adsorbed o-H_2 spectra but they are less appealing. Such a peak might arise if some of the molecules were undergoing motion that was fast compared to the intramolecular dipolar interaction. An example would be molecular reorientation such as that occurring at high temperatures. Critical fluctuations might produce such motion but they are

normally seen only in very pure systems. Another example would be the 2D translational motion of adsorbed molecules in a fluid phase. It would only be fully effective for crystallites for which the polar angle β of $\vec{H}_o$ in the crystal reference frame was equal to the so-called magic angle of 55° (Aleksandrov, 1966). One can see this by examining the equation for the NMR frequencies (IV-10b). The second and third terms of the right hand side will always be zero because the motion makes it necessary to average over all azimuthal angles δ. The first term will only be zero if $3\cos^2\beta - 1 = 0$, i.e., $\beta = 55°$. For crystallites at other angles, the reduction in the splitting would be less. This hypothesis is considered further in Section 8.3.

In the 2-out phase, it is possible to get a spectrum consisting of a single peak without requiring any motion. For V_c/Γ in the range 3-4, (III-20) shows that $|\sigma| < .03$. With such a small value of $|\sigma|$, if $\bar{\beta} = 0°$, the splitting of the absorption peaks would be less than the broadening so only one peak would be resolved. These values of V_c/Γ are quite close to the values deduced from the high temperature NMR data discussed in Section 7.4. Therefore, one might suppose that the central peak observed near .6 K arises from formation of domains of the 2-out phase in the transition region. However, there is also a central peak in the $\bar{\beta} = 90°$ spectra. In that case (IV-10b) shows that for $\sigma \simeq 0$, one expects peaks at $\nu/3d = \pm\eta/2$. At T=0, (III-13c) gives $\eta = 1 - \sigma \simeq 1$ so there would be a pair of peaks at $\nu/3d = \pm 1/2$ contrary to the experiment.

With our final o-H_2 sample, G21, we obtained some limited data concerning the temperature dependence of T_c on the J=1 concentration. In that experiment, NMR spectra with $\bar{\beta}=0°$ at three temperatures .333, .575, and 1.81 K were measured as functions of c over the range $.2 \leq c \leq .92$ with $\rho=.85$, as usual. Fig. 49 is a graph of the splitting $\delta\nu/3d$ of the peaks of the derivative of the absorption signal against c for G20 and G21. The derivative peaks rather than the absorption peaks were plotted because for several spectra in the transition region, the derivative peaks could be seen clearly but the absorption peaks were obscured by the central component of the signal. For G21, the critical concentration was arbitrarily defined to be the one at which $\delta\nu/3d$ was halfway between its maximum value and the constant value it took when c was low. At .3 K, $\delta\nu/3d$ appears to be approaching a maximum near c=.9. For .58 K, $\delta\nu/3d$ is apparently somewhat below its maximum even at our highest J=1 concentration. Nevertheless, $\delta\nu/3d$ is a strong function of c so the error in determining the critical concentration would be small. For G19 and G20, T_c was determined from the absorption peak splitting shown in Fig. 47. Fig. 50 shows T_c as a function of c for the three o-H_2 samples.

8.2 The Ordered State

The .3 K o-H_2 spectra of G19 and G20 have been compared to the T=0 spectra calculated for the various ordered states. The NMR transition frequencies as a function of crystallite

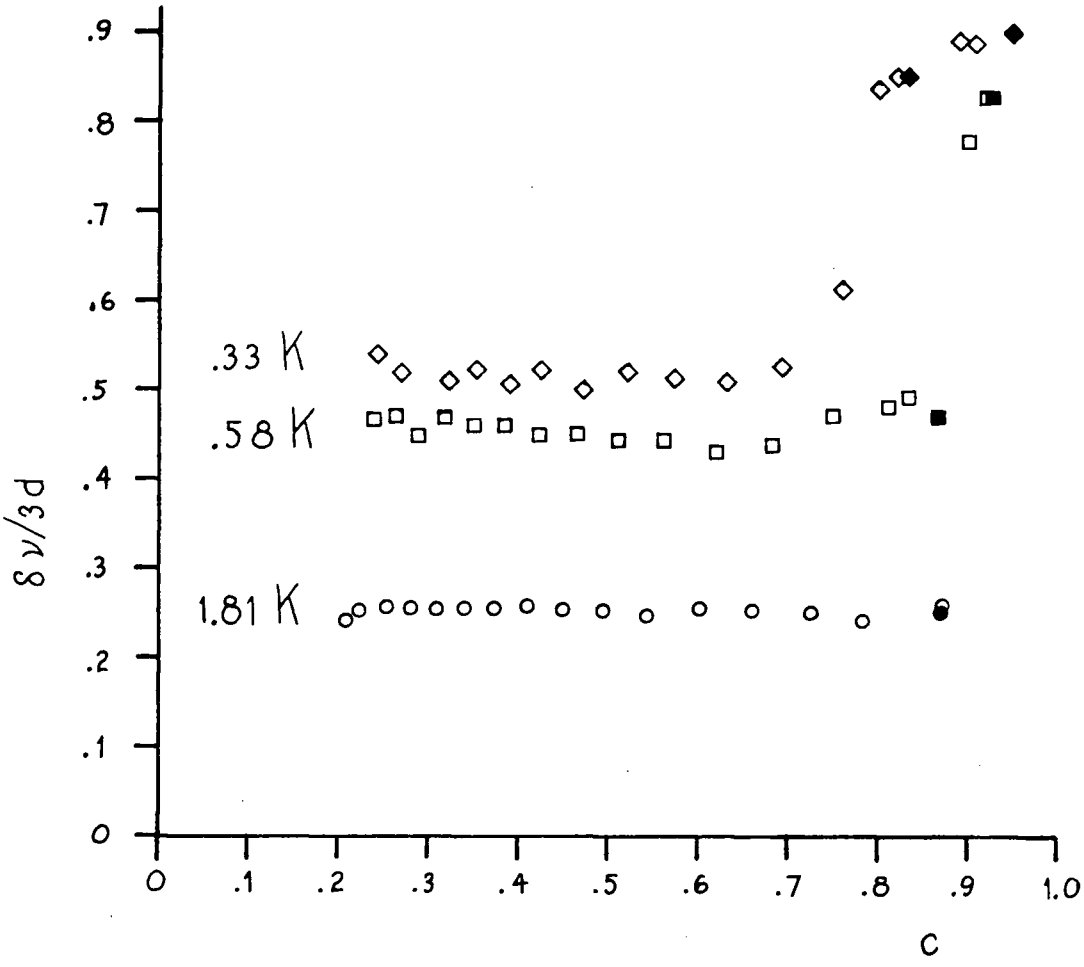

Fig. 49 The splitting of the peaks of the absorption derivative $\delta\nu/3d$ versus c for o-H_2 samples G21 (open symbols) and G20 (solid symbols). All measurements were with $\bar{\beta}=0°$ and A=13 dB. The temperatures were .33 K (diamonds), .58 K (squares), and 1.81 K (circles).

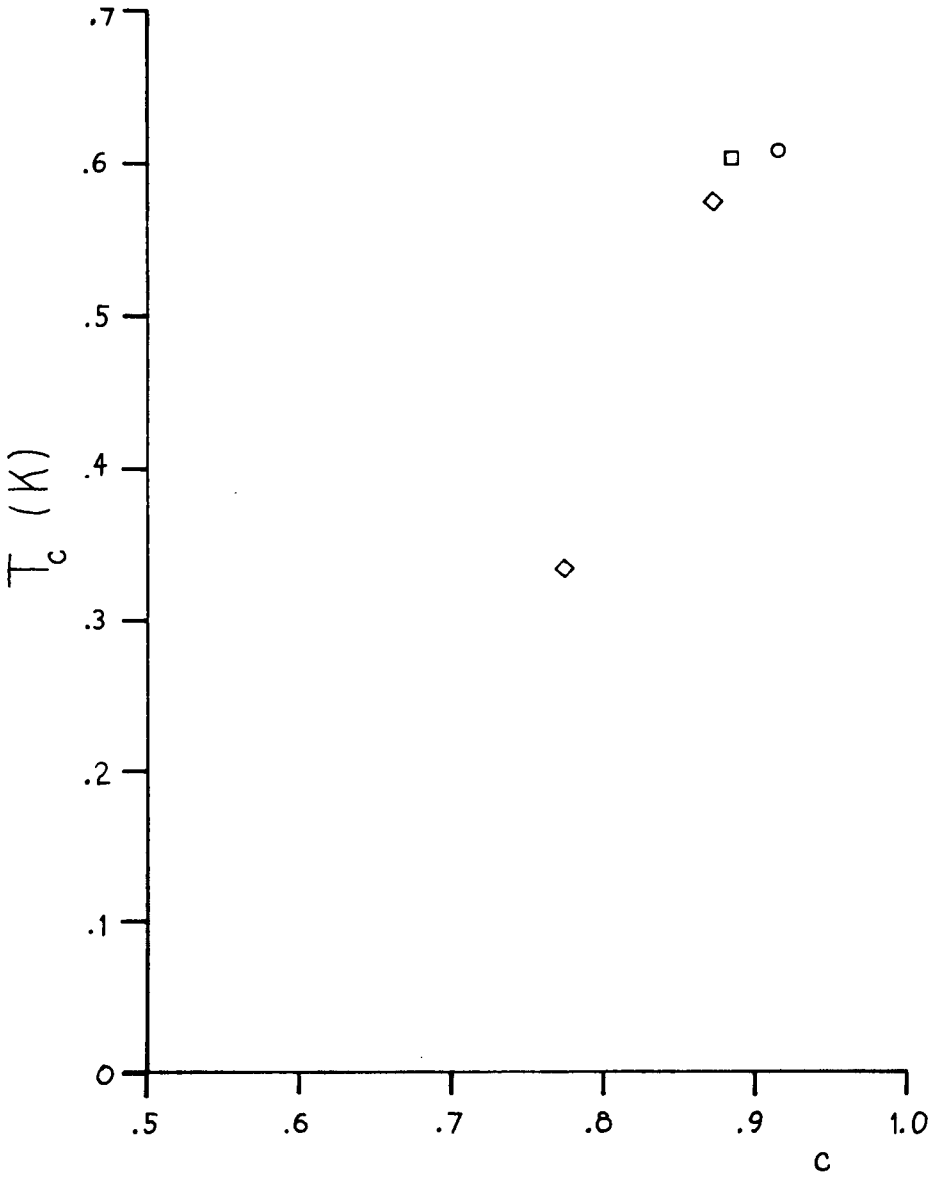

Fig. 50 The transition temperature T_c versus c for three o-H_2 samples: G19 (square), G20 (circle), and G21 (diamonds).

orientation are given by (IV-14) and (IV-15) for $\bar{\beta}=0°$ and 90°. The probability of each frequency $p(\nu)$ was calculated numerically as described in Section 4.2 using the orientational distribution function for the adsorbing surfaces $P(\zeta)d\vec{\Omega}$. It is the probability that the c-axis of a graphite crystal lies in the solid angle $d\vec{\Omega}$, which makes an angle ζ with the normal to the Grafoil. The frequency probability function $p(\nu)$ was then convoluted with a Gaussian function with standard deviation σ_G.

Initially, we took $P(\zeta)$ to be a Poisson kernel defined by

$$P(\zeta) = \frac{q^{1/2}(1+q)}{2\pi \tanh^{-1}(q^{1/2})\{(1+q^2)-4q\cos\zeta\}} \qquad \text{(VIII-2)}$$

This orientational distribution function has been used to fit the neutron scattering peaks of CH_4 adsorbed on Papyex (Coulomb et al, 1981). The best fit was obtained using q=.6. If ζ is less than the half width at half maximum (HWHM) of $P(\zeta)$, then $P(\zeta)$ is almost identical to a Lorentzian. However, $P(\zeta)$ has a shorter tail at large values of ζ. We tried to fit the resulting lineshape to our .3 K spectra using the order parameters, q, and σ_G as adjustable parameters. For $\bar{\beta}=0°$ and q=.6, the fits were very poor, primarily because the small outer peaks of the experimental spectra were not reproduced in the synethetic spectra. These peaks come from molecules that are standing up on crystals that have $\zeta \simeq 0$. However, in the synthetic spectra, the contributions from these molecules were suppressed because $P(\zeta)$ was multiplied by the factor sin ζ

contained in $d\vec{\Omega}$. As a consequence, the contribution from the tail of $P(\zeta)$ was relatively large. The tail could be reduced by increasing q but this also reduced the width of the peak: it was still not possible to obtain a good fit.

In order to fit the neutron scattering lineshape of N_2 adsorbed on Grafoil, Kjems et al (1976) used an orientational distribution function which was the sum of a Gaussian and isotropic components

$$P(\zeta) = A_0 + A_1 \exp(-\zeta^2/2\delta^2) \qquad \text{(VIII-3)}$$

Their best fits were obtained with $A_0/A_1=.78$ and $\delta=12.7°$. This function has the advantage that the width of the peak and the size of the tail can be adjusted independently provided that δ is not too large.

There is an important difference between the orientational distribution functions defined by Coulomb et al and Kjems et al. Coulomb et al used a 2D distribution function so it was multiplied by $\sin\zeta$. Kjems et al used a 1D distribution function so it was not multiplied by $\sin\zeta$. For the NMR spectra a 2D distribution function is required so $\sin\zeta$ should be included. We have defined $P(\zeta)$ to be

$$P(\zeta)=f_p + \{(1-f_p)/I(\delta)\}\exp(-\zeta^2/2\delta^2) \qquad \text{(VIII-4)}$$

and normalized it by

$$\int_0^{\pi/2} P(\zeta)\sin\zeta \, d\zeta=1/2\pi \qquad \text{(VIII-5)}$$

The upper limit of the integral is $\pi/2$ rather than π because crystallites oriented at an angle ζ are indistinguishable from ones at $\zeta+\pi$. The term f_p is the fraction of adsorbing

surfaces forming the isotropic powder component. In the second term, $I(\delta)$ is defined by

$$I(\delta) = \int_0^{\pi/2} \exp(-\zeta^2/2\delta^2)\sin\zeta \, d\zeta \qquad \text{(VIII-6a)}$$

$$\simeq \delta^2(1-\delta^2/3+\delta^4/15-\delta^6/105) \text{ if } \delta << 1 \text{ radian} \qquad \text{(VIII-6b)}$$

Synthetic spectra for the pinwheel phase generated with this form for $P(\zeta)$ compared quite well with the .3 K experimental spectra, particularly for $\bar{\beta}=0°$, as shown in Fig. 51(a) and (b). As expected on the basis of the 2D powder spectra discussed in Section 4.2, the synthetic spectra for the other ordered phases were quite different from the experimental spectra, especially if $\bar{\beta}=0°$. All of these synthetic spectra showed only two peaks for $\bar{\beta}=0°$. The experimental lineshape in Fig. 51(a) was obtained by subtracting a parabola from the .318 K spectrum shown in Fig. 43(a). The baselines of all of the spectra with $\bar{\beta}=0°$ at .3 K were found to be approximately parabolic because of modulation pick-up.

The best fits for both $\bar{\beta}=0°$ and 90° were obtained using $f_p=.2$, $\delta=15°$, $\sigma_G/3d=.042$, $\sigma/\sigma_o=.78$ for the up spins, and $\sigma/\sigma_o=\eta/\eta_o=.87$ for the down spins. σ_o and η_o are the values of σ and η for T=0 and c=1, which are given in Table IV. The fact that σ/σ_o and η/η_o are both less than one could be because $c<1$ or because of quantum fluctuations. The fits were not very sensitive to either f_p or δ. The σ's for the spins lying down and standing up were determined by the positions of the inner and outer peaks of the $\bar{\beta}=0°$ spectra, respectively. Given these values, η was determined by the positions of the

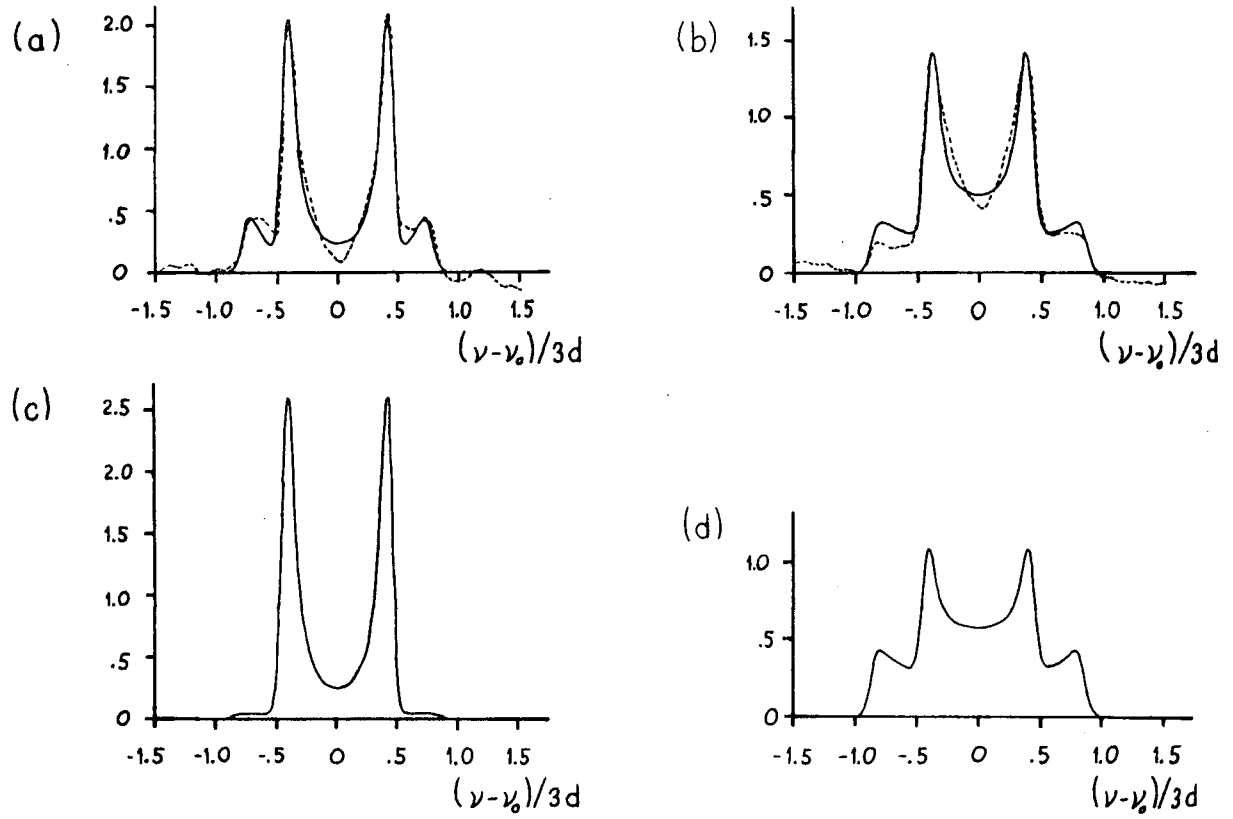

Fig. 51 Comparison of the .3 K experimental spectra (dashed lines) with the synthetic spectra (solid lines) calculated for the pinwheel [(a) and (b)] and herringbone [(c) and (d)] phases. Spectra in (a) and (c) are for $\bar{\beta}=0°$ and those in (b) and (d) are for $\bar{\beta}=90°$. The experimental parameters are (a) T=.318 K, c=.95, A=13 dB, t_m=1.2 h and (b) T=.309 K, c=.94, A=13 dB, t_m=1.2 h. The synthetic parameters are given in the text. The spectra have been normalized to the same areas.

outer peaks of the $\bar{\beta}=90°$ spectrum. Since the σ's for the spins lying down and those standing up are different, the inner peaks for $\bar{\beta}=90°$ actually consist of two unresolved peaks; that is why their outer edges are broader than for $\bar{\beta}=0°$. The position and width of the inner peaks for $\bar{\beta}=90°$ gave some redundancy in the determination of the order parameters.

It should be possible to improve the fit by modifying the Gaussian function in (VIII-4). For $\bar{\beta}=0°$, the main problem is that the central minimum of the synthetic spectrum is too shallow and the outer minima are too deep. The main contribution to the outer minima is from the spins standing up on crystals with $\zeta\simeq 25°$. The main contribution to the central minimum is from all spins with $\zeta\simeq 55°$. The peaks are produced by spins on surfaces with $\zeta=0°$. Therefore, it seems that the number of surfaces with $\zeta=0°$ should be maintained, near $\zeta=25°$ they should be increased, and near $\zeta=55°$ they should be decreased.

8.3 Is There Another Transition?

Besides observing the spectra of o-H_2 samples with $c\simeq .9$, we also studied a sample (G21) with $c\simeq .2$ and $\bar{\beta}=0°$. All of these spectra consisted of a doublet. In Fig. 47, the temperature dependence of the splitting $\Delta\nu/3d$ of this low concentration sample of o-H_2 has been plotted. The splittings of the high and low concentration samples agree well at high temperatures where the effects of the EQQ interaction are averaged out by

rapid rotation. As T decreases, the splitting of the high concentration sample increases more slowly than that of the low concentration sample: the EQQ interactions oppose the alignment that the crystal field attempts to impose. The most striking feature of the low concentration data is the small discontinuity in $\Delta\nu/3d$ which occurs at the same temperature as the orientational ordering transition of the high concentration sample. A concentration of .2 is far too low for the small discontinuity to be a cooperative effect. Perhaps there is another transition at .6 K in addition to the orientational ordering transition. A candidate for such a transition is suggested by comparing the translational phase diagrams of adsorbed hydrogen shown in Fig. 1 and adsorbed ^4He shown in Fig. 52 (Ecke and Dash, 1983). Fig. 52 contains a greater variety of phases but this is probably simply a consequence of the more intensive study that ^4He has been subjected to. In particular, the neutron scattering measurements of hydrogen would not have had sufficient S:N ratios to be able to distinguish between a $\sqrt{3}$ x $\sqrt{3}$ solid and islands of $\sqrt{3}$ x $\sqrt{3}$ solid coexisting with a 2D fluid. The peak intensities and diffuse scattering would have been slightly different in the two cases. Consequently, it is possible that for $\rho<1$, H_2 undergoes a transition from a $\sqrt{3}$ x $\sqrt{3}$ solid with vacancies to a $\sqrt{3}$ x $\sqrt{3}$ solid plus 2D vapour. If that were the case, the orientational ordering in the pure $\sqrt{3}$ x $\sqrt{3}$ solid might be suppressed by the vacancies and only occur when the temperature was low enough

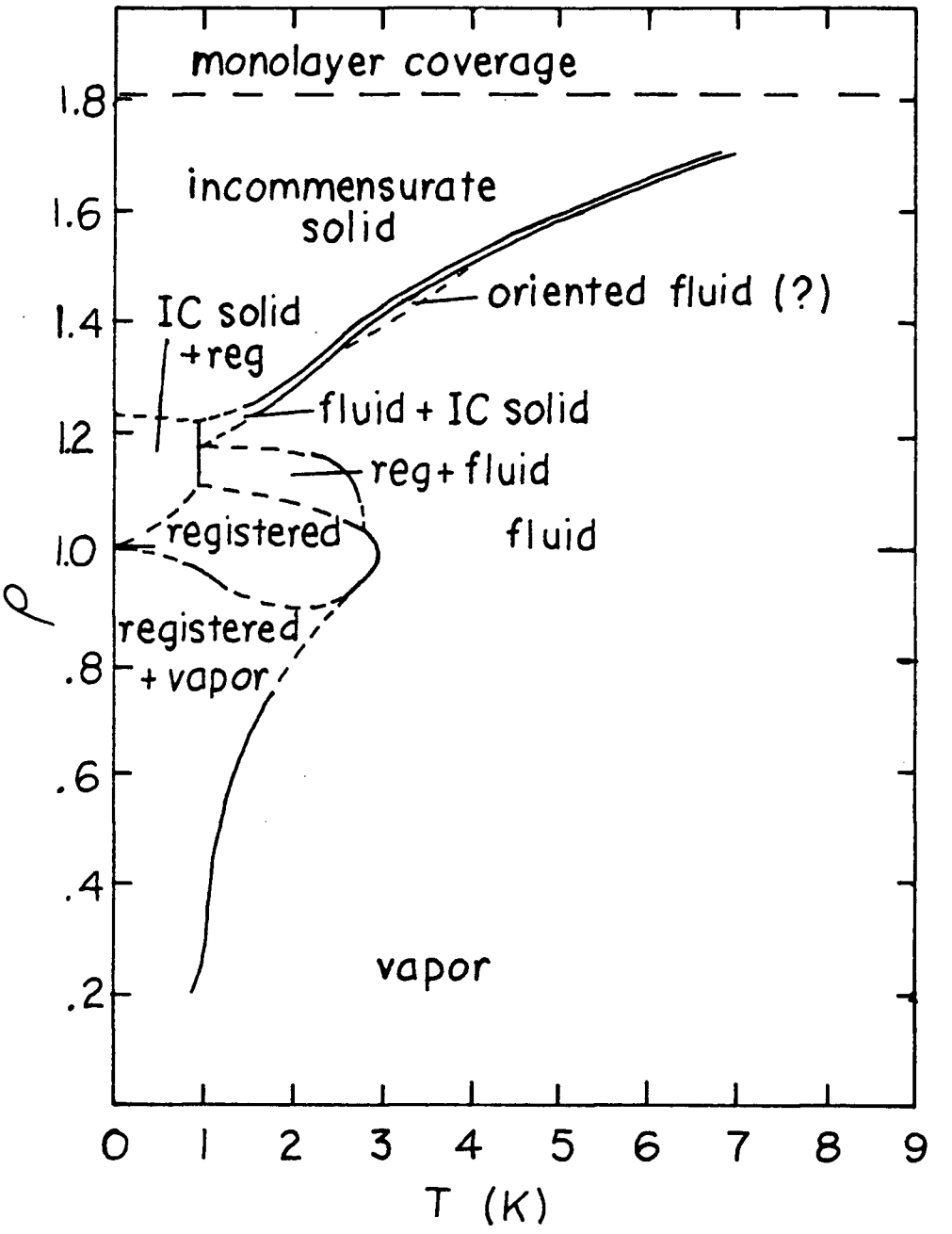

Fig. 52 Proposed phase diagram of ^{4}He on graphite (Ecke and Dash, 1983). The solid lines represent regions where the data are adequate to determine the phase boundary. The dashed lihes are conjectured phase boundaries. The registered phase is the $\sqrt{3}$x $\sqrt{3}$ solid.

for islands of the $\sqrt{3}$ x $\sqrt{3}$ solid to form.

This hypothesis might explain the central peak in the NMR spectrum seen near .6 K. There should be coupling between the translational and rotational motion of adsorbed hydrogen molecules because orientations of the molecules that minimize the interaction energy with the surface depend upon position (Riehl and Fisher, 1973; Steele, 1977). The combined rotational and translational motion of molecules in the 2D vapour phase could result in motional narrowing of the NMR spectrum regardless of crystallite orientation, producing the central peak. The peak would then disappear at lower temperatures as the 2D vapour pressure dropped. There are some problems with this interpretation. The centre of the spectrum starts to fill in above 1K, a much higher temperature than the supposed transition temperature. Also, the orientational ordering temperature is strongly dependent on concentration. If orientational ordering were triggered by a translational phase transition, the transition temperature should not depend on c. Experiments at other coverages, particularly $.85<\rho\leq 1$ should be able to settle the question of whether there is a translational phase transition.

8.4 The Disordered State

In the pararotational state, the splitting of the absorption doublet is proportional to $|b|$. Its temperature dependence allows the determination of V_c and Γ. We have done this by fitting the high temperature expansion of σ calculated by Harris

and Berlinsky (private communication, 1983) and given in (III-44) to our experimental data. Using various trial values of V_c and Γ, σ was calculated for the values of T and c used in the experiments. For G20, with .83<c<.89, the best results were obtained with V_c=.65 K and Γ=.12K. For G21, with .21<c<.26, we found V_c=.55 K and Γ=.19 K. The experimental and fitted values of $|\sigma|$ have been plotted as functions of T^{-1} in Fig. 53. The fits were not sensitive to 10% changes in V_c if Γ was readjusted. For the high concentration sample, it was necessary to change Γ by 10% and for the low concentration sample, by 25%. The differences between the parameters for the two samples is probably not significant. Poor convergence of the high temperature expansion at low temperatures makes it difficult to choose the best parameters. For G20, the $(\beta\Gamma)^3$ term contributed about 10% to σ at .75 K and .5% at 4.2 K. For G21, convergence was poorer because a larger value of Γ was needed: the $(\beta\Gamma)^3$ term contributed more than 10% below 1.3 K. Note that according to the mean field orientational phase diagram shown in Fig. 6, these results for V_c and Γ are consistent with the ordered state being the pinwheel phase.

We also tried using the mean field result for σ, given in (II-16), to fit the NMR data. This was quite successful above 1.3 K but broke down at lower temperatures. Positive and negative values of V_c gave equally good results, in contrast to the high temperature expansion. The parameters obtained from least squares fits of the mean field results to the data above

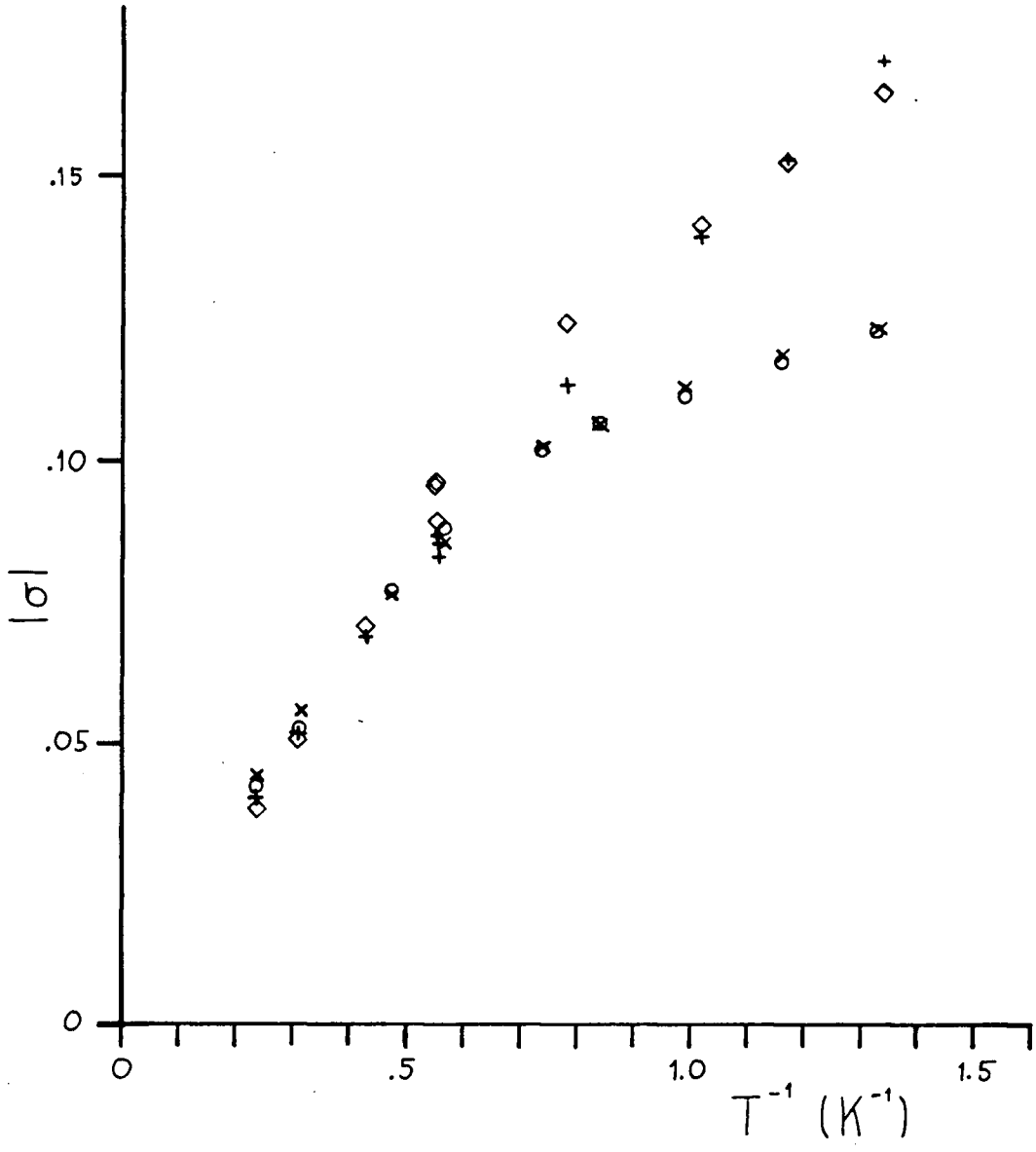

Fig. 53 $|\sigma|$ versus 1/T for o-H_2 samples G20 with $.83 \leq c \leq .89$ (circles) and G21 with $.21 \leq c \leq .26$ (diamonds). $\bar{\beta}=0°$. The results of the high temperature expansion of σ for $V_c=.65$ K and $\Gamma=.12$ K (x) and for $V_c=.55$ K and $\Gamma=.19$ K (+) are also plotted. Since $V_c>0$, $\sigma>0$. The concentration varies from point to point so a single curve cannot be drawn through each of the two sets of data.

1.3 K are included in Table XII.

Table XII Results for V_c and Γ for o-H_2

Sample	MFT		HT expansion (no vacancies)		HT expansion (with vacancies, ρ=.85)	
	V_c(K)	Γ(K)	V_c(K)	Γ(K)	V_c(K)	Γ(K)
G20	.44	.09	.65	.12	.30	.11
	-.44	.05			-.85	.13
G21	.51	.12	.55	.19	.23	.17
	-.51	.02				

If adsorbed hydrogen formed a pure $\sqrt{3}$ x $\sqrt{3}$ solid phase above .6 K, then (III-43) would no longer be correct in the disordered state, except at $\rho = 1$, because it assumes that all sites are filled by hydrogen molecules. Berlinsky (private communication, 1983) has made a high temperature expansion of σ to second order in βV_c and $\beta\Gamma$ which takes into account random vacancies with concentration x for the case $\rho < 1$. The first step was to see how the vacancies affect the anisotropic Hamiltonian of a system of hydrogen molecules given in (II-4). The Hamiltonian of the J=1 molecules can be expressed as

$$H = \sum_i H_c^i + (1/2) \sum_{i,j} H_{EQQ}^{ij} + \sum_{i,j} H_v^{ij} \qquad \text{(VIII-7)}$$

The first sum is over all J=1 molecules, the second is over all nearest neighbour J=1 pairs, and in the third sum i is a J=1 molecule and j is a vacancy. H_v^{ij} is the change in energy

of molecule i when a molecule at site j is removed. Using (II-4b), the vacancy energy is

$$H_v^{ij} = -(8\pi/5) \sum_m Y_2^m(\vec{\omega}_i) B(R_{ij}) Y_2^{m*}(\vec{\Omega}_{ij}) \qquad \text{(VIII-8)}$$

For hydrogen in the $\sqrt{3}$ x $\sqrt{3}$ phase on graphite, taking only nearest neighbour interactions, $R_{ij}=R_o=4.26$ Å so $B(R_{ij})$ $=-.65$ K (van Kranendonk, 1983).[3] Taking the z axis normal to the surface, the polar angle of $\vec{\Omega}_{ij}$ is 90° and the azimuthal angle is ϕ_{ij}. Within the J=1 manifold, the $Y_2^m(\vec{\omega}_i)$'s can be replaced by the spherical tensors defined by (II-6). The vacancy energy then becomes

$$H_v^{ij} = -\frac{4}{5}\left(\frac{\pi}{5}\right)^{1/2} B(R_o)\{T_2^0(\vec{J}_i) - (3/2)^{1/2}\{T_2^2(\vec{J}_i)e^{-i2\phi_{ij}} + T_2^{-2}(\vec{J}_i)e^{i2\phi_{ij}}\}\} \qquad \text{(VIII-9)}$$

Taking the high temperature expansion given in (III-42c) to second order, Berlinsky found that

$$\sigma \simeq \beta\{V_c/3 + (6/5)(1-x)B(R_o)\} + \beta^2\{V_c^2/18 - (6/25)(1-x)B^2(R_o) + (24/25)(1-x)^2B^2(R_o) - (2/5)(1-x)V_cB(R_o) - (3/2)cxV_c\Gamma + 3cx(1-x)\Gamma B(R_o) - (25/6)cx\Gamma^2\} \qquad \text{(VIII-10)}$$

The crystal field V_c includes a contribution from the interactions of a J=1 molecule with the surface as well as with neighbouring hydrogen molecules.

Using $x=1-p$, we compared this expansion for various values of V_c and Γ to the experimental splittings. The fits were about as good as with the previous expansion which did not include vacancies, except that divergence of the series was a more serious problem. The β^2 term was more than 20% of the β term below 1.8 K for c=.9 and below 1.1 K for c=.2. The best

values of V_c and Γ are given in Table XII. The introduction of vacancies had no significant effect on Γ because, like J=0 molecules, vacancies do not engage in the EQQ interaction. However, they did have a large effect on V_c. Within the ranges where the high temperature expansions for σ converge, V_c and Γ could be chosen so that either the pure $\sqrt{3}$ x $\sqrt{3}$ phase or $\sqrt{3}$ x $\sqrt{3}$ islands coexisting with a 2D fluid are consistent with the temperature dependence of the splitting of the NMR doublet.

The values of Γ given in Table XII are all surprisingly low compared to the nearest neighbour, rigid lattice value of .528 K.[4] There are no calculations of the renormalization of Γ for adsorbed hydrogen but it is hard to imagine such a large change.

8.5 Broadening

It was mentioned in Chapter IV that the dominant source of broadening for pure o-H_2 is expected to be the intermolecular dipole-dipole interaction, which is temperature independent. Fig. 54 shows that the measured broadening δ is a considerably more interesting function of temperature. We have defined δ to be the width at half maximum of each of the outer edges of the main absorption peaks. It does not include the effects of the misorientation of the graphite crystals. For the 90% J=1 spectra at .58 K and .66 K, where the peaks could not be resolved because of the central component, the shoulders have

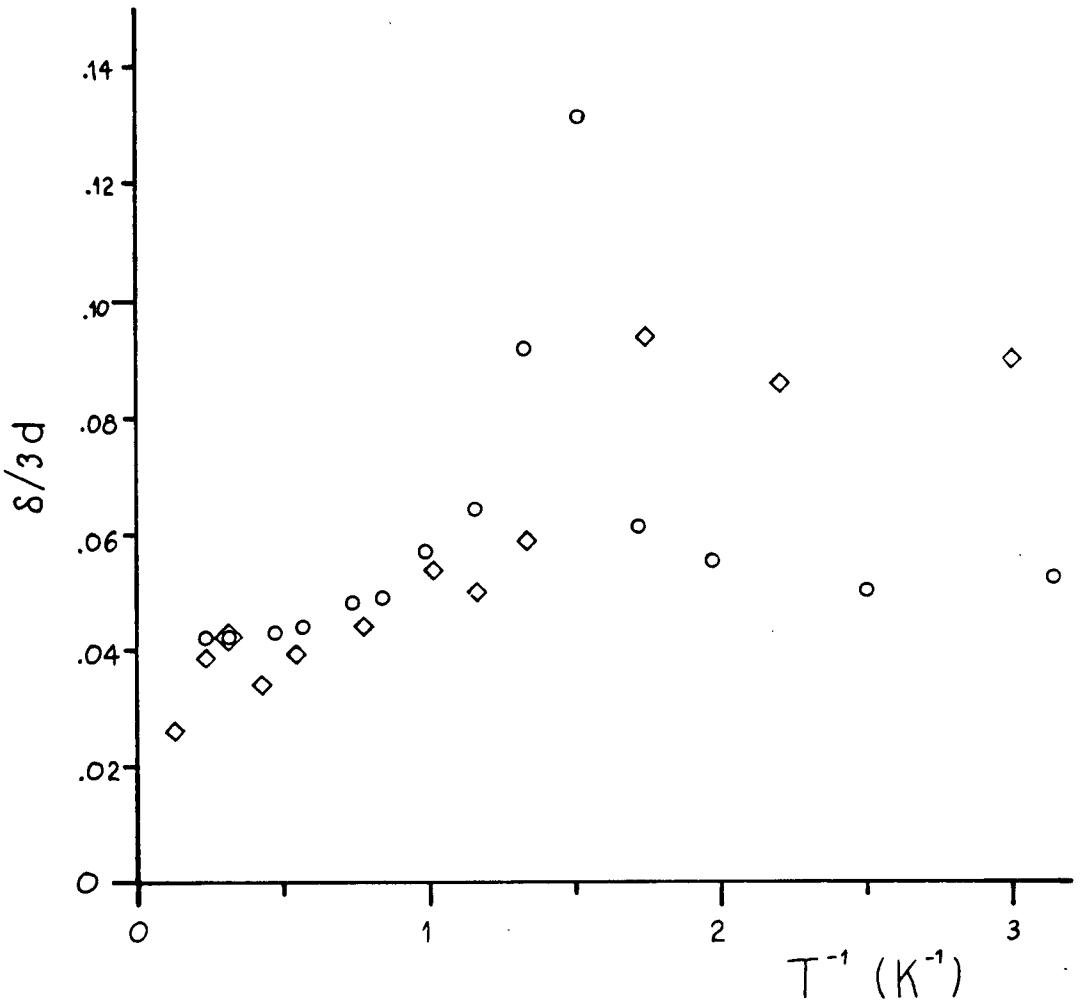

Fig. 54 Broadening $\delta/3d$ versus 1/T for o-H_2 samples G20 with $.83 \leq c \leq .95$ (circles) and G21 with $.21 \leq c \leq .26$ (diamonds). $\bar{\beta} = 0°$.

been taken instead of the peaks.

As the 90% J=1 sample was cooled, it exhibited an increase in $\delta/3d$ prior to the transition. This was followed by a sharp drop, almost down to the high temperature limit, as orientational ordering occurred. For $T>T_c$,[5] $\delta/3d$ of the 20% J=1 sample also increased slowly as T decreased. Going through T_c, $\delta/3d$ rose more rapidly and settled at a value about twice as great as that of the 90% J=1 sample. It is possible that there is also a peak at T_c in the 20% J=1 sample but the data is not extensive enough to determine this.

If it is assumed that the intermolecular dipolar broadening is Gaussian, then the standard deviation would be equal to the square root of the second moment $M_2^{1/2}$. The HWHM would be $1.17\ M_2^{1/2}/3d$, which, according to (IV-33), is .030 for c=.90 and .015 for c=.23. The magnetic field modulation would produce additional (rectangular) broadening with a HWHM equal to the amplitude of the modulation, which is $\Delta H_m/3d = .018$. These results are approximately consistent with the high temperature limits of the measured values of $\delta/3d$ for both concentrations.

A fairly convincing explanation of the broadening measurements is as follows. Consider an o-H_2 sample for which c is somewhat less than one. At high temperatures, the EQQ interaction would be averaged out by molecular reorientation and the energy gap Δ of the m_J sub-levels of the J=1 level would be equal to the crystal field. All of the molecules would

experience the same crystal field (ignoring vacancies and interstitials, if any) so they would have the same value of σ. As T decreased the EQQ interactions would begin to compete with the crystal field. Fluctuations in the molecular field, arising from different local distributions of J=1 molecules, would start to become important. A distribution of energy gaps Δ would be produced, resulting in increasing broadening of the NMR spectrum. At T_c, the molecular field would overpower the crystal field and rapidly widen the energy gap between the ground state and first excited state. Local variations in the gap would no longer be important because the gap would now be much greater than the thermal energy. This would mean that the broadening would drop rapidly at T_c, perhaps as low as the high temperature value.

This scenario is consistent with the graph of $\delta/3d$ versus T^{-1} for the c=.9 sample. It is also supported by the fact that the .3 K NMR spectra could be fit by just two values of σ, one for the spins standing up and one for those lying down. Finally, it predicts that at intermediate temperatures there would be distribution of order parameters. This was already expected from the comparison with the low concentration bulk o-H_2 spectra. If the scenario were correct, the peak in δ should diminish when c becomes very close to 1 because there would be little variation of the local molecular fields.

The situation for c=.2 is less intuitive. At high temperatures, δ should increase as T decreases and the molecular field

begins to assert itself. Near T_c, we have found that σ has a small but fairly rapid drop (see Fig. 47). In this region, inhomogeneities such as the local distribution of J=1 molecules would become more important so there might be a small peak in δ. Below T_c, σ begins to flatten as T decreases so δ should not be strongly temperature dependent.

Notes to Chapter VIII

1. In the remainder of this thesis, the term broadening does not include the distribution of splittings arising from the different crystallite orientations in the Grafoil. The dashed spectrum of Fig. 13 will be referred to as an unbroadened spectrum.

2. For G20, the derivative peak splitting gave virtually the same T_c.

3. We have used the conventional definition of $B(R_{ij})$ but Van Kranendonk's $B(R_{ij})$ is a factor of two larger.

4. The values of Γ obtained from G20 are probably more reliable than those obtained from G21. The fit to the G20 data is considerably more sensitive to Γ because c is much higher.

5. T_c refers to the orientational ordering transition temperature of the high concentration sample.

CHAPTER IX

NMR SPECTRA OF p-D_2

9.1 Temperature Dependence of the p-D_2 Spectra

NMR absorption spectra of p-D_2 have been observed by us in the temperature range of .3 K to 8 K. Some of these, from sample G18 with ρ=.85 and .77$\leq$c$\leq$.95, are shown in Fig. 55. At high temperatures, there was a doublet from the J=1 molecules and a central peak from those J=0 molecules with I=2. As T decreased, the splitting increased but below about 1.6 K the broadening of the J=1 peaks also increased. At about .8 K, the doublet could no longer be resolved, as was the case with the high concentration o-H_2. Upon further cooling, the shapes of the spectra contrasted sharply with those of o-H_2 and of the synthetic spectra calculated for the ordered phases of MFT: the p-D_2 spectra became very broad and weak. At .6 K, the J=1 spectrum had become triangular. At .3 K, it was somewhat semicircular, with a maximum width slightly greater than $\Delta\nu/3d = 1$. The spectrum could, in principle, have a maximum width of $\Delta\nu/3d = 2$. The S:N ratio was quite poor so the existence of weak wings extending beyond $\Delta\nu/3d = 1$ is not precluded. However, the data from sample G18 shown in Fig. 38 implies that such wings could not contribute very much to the total intensity. In the region near .6 K, it was impossible to determine the maximum extent of even the main component of the spectrum, because the baseline produced by the modulation

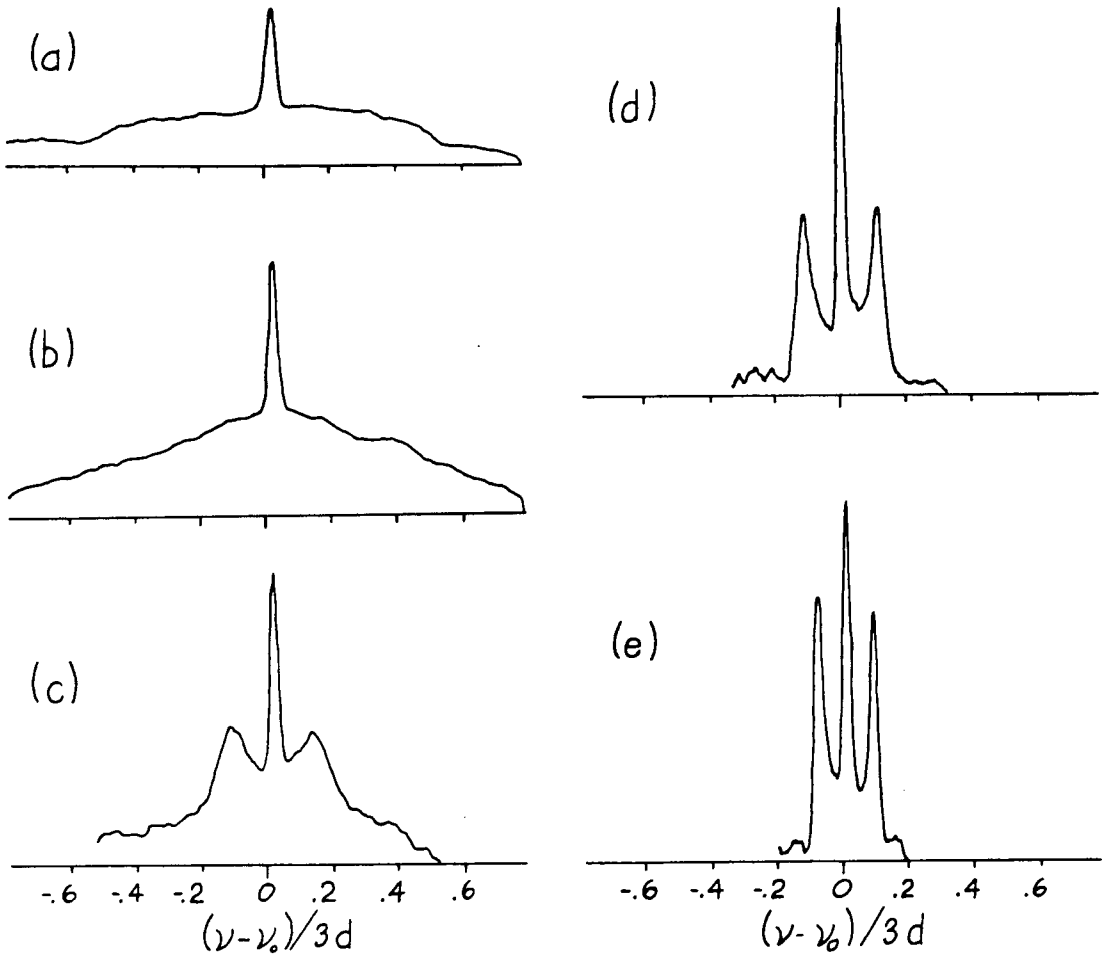

Fig. 55 Absorption spectra of D_2 sample G18 with $\bar{\beta}=90°$. A=13 dB. $\rho=.85$.

Spectrum	(a)	(b)	(c)	(d)	(e)
T(K)	.318	.580	.892	1.61	3.01
c	.93	.91	.90	.83	.86
t_m(h)	8.52	17.1	5.70	11.0	10.3

The spectra have been normalized n the same manner as those in Fig. 43. The vertical scale is the same for all of the spectra.

pick-up had the same triangular shape as the J=1 spectrum. Modulation pick-up was much more severe for D_2 than for H_2 because the magnetic field was 1.3 T instead of .2 T. Unfortunately, the pick-up was much worse for $\bar{\beta}=0°$. We have already seen that the $\bar{\beta}=90°$ spectra are expected to be much more difficult to interpret because they involve averages over the azimuthal angles α of the crystal axes whereas the $\bar{\beta}=0°$ spectra are independent of α.

The S:N ratios did not warrant any quantitative analysis of the low temperature spectra. As regards the qualitative features, one conjecture is that p-D_2 has a wider distribution of order parameters than o-H_2 at low temperatures. In section 8.5, the increase in the broadening of the o-H_2 spectra as T decreased towards T_c was interpreted as being due to the increasing importance of spatial variations of the molecular field. At T_c, the orientational ordering caused the broadening to drop rapidly. In p-D_2 there is no evidence of orientational ordering so one might suppose that as T decreases the broadening of the p-D_2 spectra would continue unabated. Further evidence of this is presented in section 9.3.

9.2 The J=1 Doublet

As in the case of o-H_2, we attempted to use the high temperature expansion given by (III-44) to fit the temperature dependence of the splitting $\Delta\nu/3d$ of the J=1 doublet. This was not successful because larger values of Γ were needed than in

the case of o-H_2 so the series diverged even at high temperatures. Consequently, we resorted to MFT. Fig. 56 is a plot of $|\sigma|$ versus T^{-1} obtained from sample G18. Since $\bar{\beta}=90°$, (IV-15) shows that $|\sigma| = \Delta\nu/3d$. As in Fig. 47, c was not constant so the data could not be fitted to a single curve. For large values of T^{-1}, the doublet was poorly resolved so the error bars of $|\sigma|$ are quite large. A two parameter least squares fit gave V_c=2.3 K and Γ=.50 K or V_c=-2.4 K and Γ=.44 K; the former values gave a slightly better fit but the difference was not significant. The values of Γ are a little smaller than the rigid lattice value, Γ_o=.510 K. This is to be expected because there is likely to be some renormalization due to zero point motion.

9.3 Broadening

The broadening δ of the J=1 doublet was extracted in the same manner as for o-H_2 in those cases where the doublet could be resolved. At low temperatures, there was only one broad J=1 peak so a different procedure was needed. Fig. 56 indicates that the splitting $\Delta\nu/3d = |\sigma|$ may be approaching a limiting value of about .25 at low temperatures. Consequently, $\Delta\nu/3d$ was taken to be equal to .25 for the purpose of calculating δ when $T^{-1} \geq 1.2\ K^{-1}$. Alternatively, we might have extrapolated the mean field behaviour of $\Delta\nu/3d$ to low temperatures. However, since a doublet is not observed there, MFT is probably not valid. Even if it were, small errors in V_c and Γ(which are

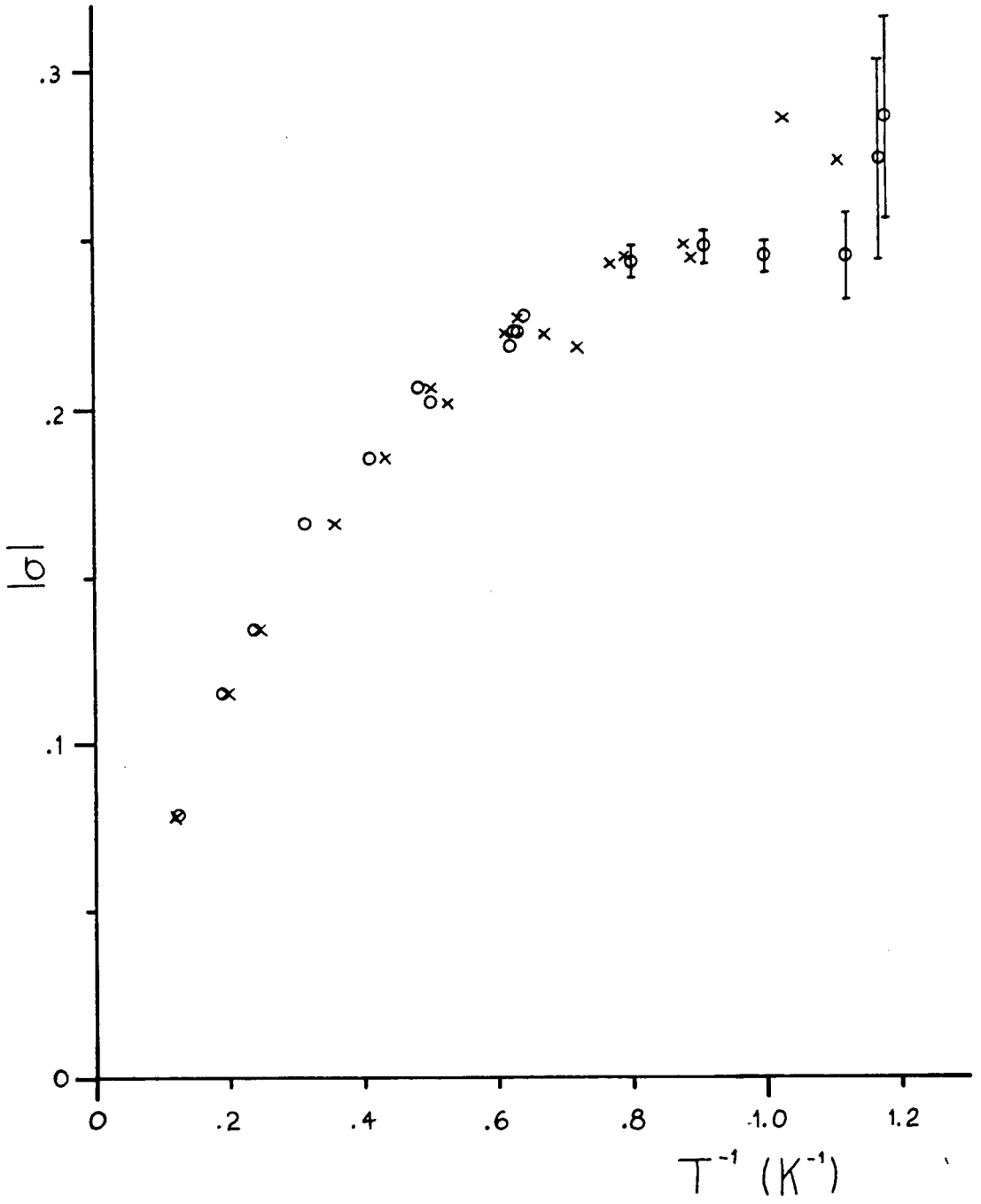

Fig. 56 $|\sigma|$ versus 1/T for p-D_2. $\bar{\beta}$=90°. Data from sample G18 with $.77 \leq c \leq .95$ (circles) and the best fit using MFT (crosses) are shown. The latter gives V_c=2.3 K and Γ=.50 K. An equally good fit was obtained for V_c=-2.4 K and Γ=.44 K.

determined from the high temperature measurements) would produce substantial errors in $|\sigma|$ as T decreased. For the low temperature spectra consisting of a single J=1 peak, δ was defined by

$$\delta/3d=(1/2)[(FWHM)/3d - .25] \qquad (IX-1)$$

Fig. 57 shows $\delta/3d$ versus T^{-1}. At high temperatures, δ increases very slowly as T decreases but near 1.1 K, the increase becomes more rapid and continues at least down to .3 K. This behaviour is consistent with the conclusions of section 9.1, according to which p-D_2 develops an increasingly wide distribution of order parameters as T decreases. The high temperature limit of $\delta/3d$ is .011. In section 4.4 it was shown that for D_2 broadening by the graphite diamagnetism was expected to be larger than intermolecular dipolar broadening. Based on the room temperature diamagnetic susceptibility of Grafoil (which is expected to be temperature independent), $M_2^{1/2}/3d$ was estimated to be .009. If the broadening is assumed to be Gaussian, for simplicity, this correspondends to a HWHM/3d of .011. The good agreement is somewhat fortuitous considering the assumptions that have been made.

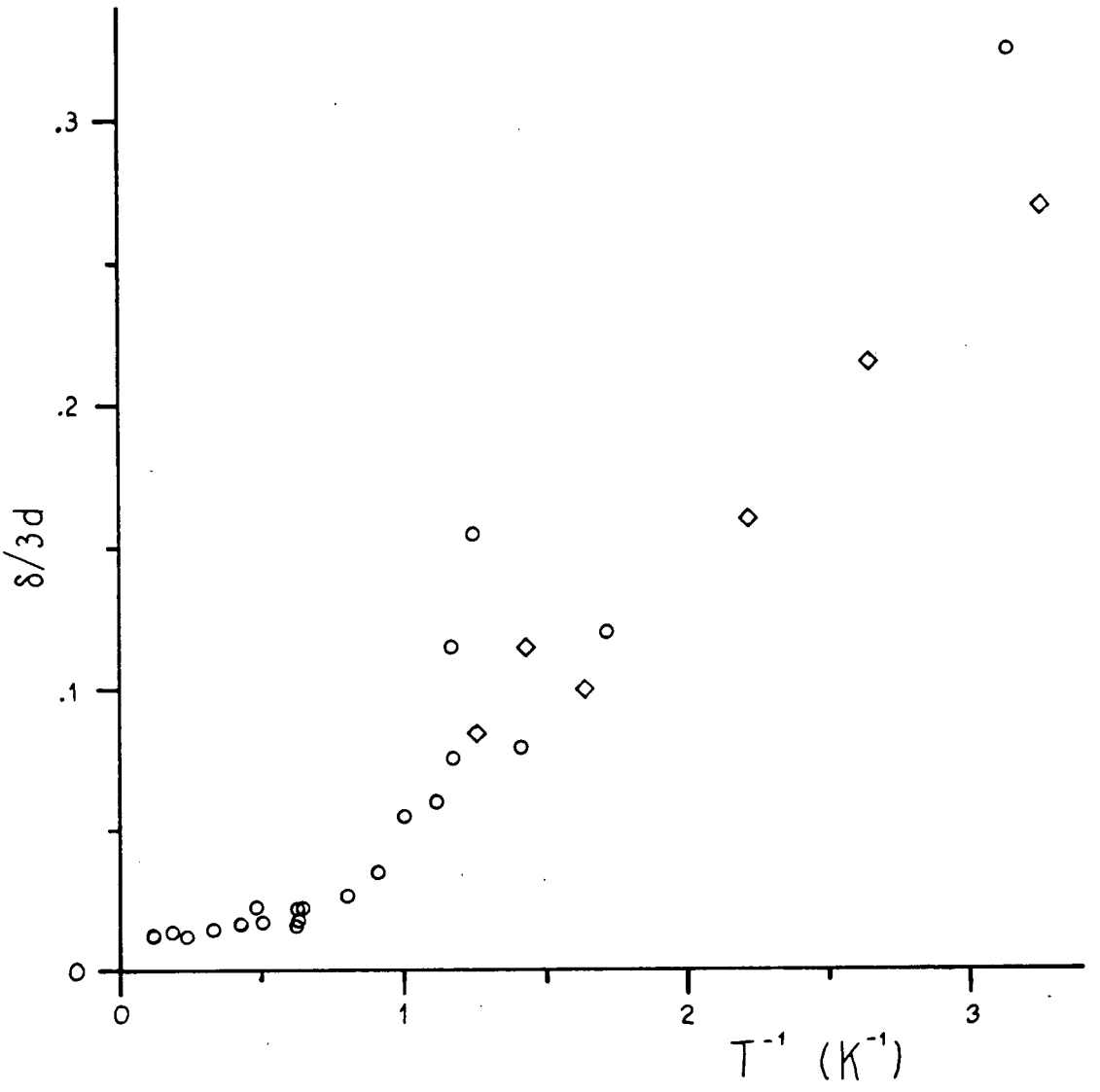

Fig. 57 Broadening $\delta/3d$ versus $1/T$ for p-D_2. $\bar{\beta}=90°$. The data is from sample G18 in cell B with $.77 \leq c \leq .95$ (circles) and G7 in cell A with $.95 \leq c \leq .97$ (diamonds).

CHAPTER X

CONCLUSIONS

10.1 Précis

Unquestionably, the most important result of our NMR studies of hydrogen adsorbed on graphite is that 90% o-H_2 at a coverage of ρ=.85 undergoes an orientational ordering transition at .6 K into the pinwheel phase. This is one of the low temperature ordered states predicted by MFT. Although there is good reason to expect MFT to correctly identify possible ordered states, it was by no means clear that ordering would in fact occur. Fluctuations due to quantum effects or the 2D nature of the system might well have prevented it. The nature of the transition is still in question. The small discontinuity in the temperature dependence of the splitting of the absorption signal of 20% o-H_2 is particularly puzzling. We have suggested that it may be due to a transition from a pure $\sqrt{3}x\sqrt{3}$ solid to a $\sqrt{3}x\sqrt{3}$ solid coexisting with a 2D fluid at .6 K. Experiments at other coverages, especially $.85<\rho\leq 1$, should settle this question. Given improved S:N ratios for the o-H_2 spectra, it would be worthwhile to fit the experimental spectra for .3 K<T<1 K to synthetic spectra generated using a distribution of order parameters. For $\bar{\beta}=0°$, it is probably necessary to use only one order parameter, σ.

P-D_2 exhibited surprisingly different low temperature behaviour from o-H_2: there was no evidence of orientational

ordering down to .3 K. In contrast, pure, bulk p-D_2 orders at 3.8 K, a higher temperature than the 2.8 K of pure bulk o-H_2. We do not understand the reason underlying the different behaviour of adsorbed p-D_2 and o-H_2. NMR spectra of p-D_2 with $\bar{\beta}=0°$ might clarify the situation; as we have seen for o-H_2, they are much easier to interpret than the $\bar{\beta}=90°$ spectra. To obtain good spectra with $\bar{\beta}=0°$, it is essential that the S:N ratios be improved. Modulation pick-up is the most serious impediment to accomplishing this task. Assuming that the spectra can be improved, the increase in the broadening at low temperatures makes it appear that it will be necessary to use a distribution of order parameters to generate the synthetic spectra below 1 K.

The temperature dependence of the splitting of the NMR doublet observed in the pararotational state gives V_c and Γ. For $\rho<1$, if hydrogen forms islands of the $\sqrt{3}x\sqrt{3}$ solid coexisting with a low density 2D fluid, there should be few vacancies in the solid. In that case, fitting a high temperature expansion of σ to the NMR data gives $V_c=.65$ K and $\Gamma=.12$ K for 90% o-H_2. The expansion is exact in βV_c and third order in $\beta\Gamma$. For a pure $\sqrt{3}x\sqrt{3}$ solid, there would be vacancies if $\rho<1$. We then found that, for $\rho=.85$, $V_c=.30$ K or $-.85$ K with Γ virtually unchanged. For 20% o-H_2, we found $V_c=.55$ K and $\Gamma=.19$ K without vacancies but $V_c=.23$ K and $\Gamma=.17$ K with vacancies for $\rho=.85$. The expansion developed convergence problems near 1 K. This may explain the difference in the

results for the two samples.

For 90% p-D_2, divergence of the high temperature expansion was more serious because a larger value of Γ was required. Consequently, MFT was used to fit the temperature dependence of the splitting. The fit was equally good using V_c=2.3 K and Γ=.50 K or V_c=-2.4 K and Γ=.44 K.

The values of Γ obtained for p-D_2 are a little smaller than the nearest neighbour, rigid lattice value, Γ_o=.510 K: translational zero point motion is expected to reduce Γ slightly. In the bulk solid, the value of Γ deduced from experiments is .87Γ_o for both H_2 and D_2 but in 2D the renormalization is expected to be greater. Although H_2 might be expected to have greater zero point motion than D_2 because H_2 is a lighter molecule, this could not account for the anomalously low measured value of Γ for adsorbed o-H_2. The rigid lattice value is Γ_0=.528 K. We have no explanation for this discrepancy.

As yet, there are no reliable calculations of the crystal fields of H_2 or D_2 adsorbed on graphite but even so it is surprising that the measured values differ so greatly. There are two contributions to the crystal field of an adsorbed J=1 hydrogen molecule. One is from interactions with neighbouring hydrogen molecules and the other is from interactions with the surface. The hydrogen contribution V_c^H is given by the first term of (II-5a). For hydrogen on a surface with its normal along the z axis, if we use (II-5b) V_c^H becomes

$$V_c^H = (3/5) \sum_j B(R_{ij}) \qquad (X\text{-}1)$$

Summing over nearest neighbours and using $B(R_o) = -.65$ K (van Kranendonk, 1983)[1], we find $V_c^H = -2.3$ K. Further neighbours make a small additional contribution that could easily be included.

The substrate contribution to the crystal field V_c^S is more difficult to estimate but the calculation would be tractable. It would involve summing the pair interactions of a J=1 hydrogen molecule with the C atoms in the substrate. Assuming the carbon atoms to be spherically symmetric, the pair interaction V would have the form

$$V(R,\vec{\Omega}) = U_1(R) + U_2(R)Y_2^o(\vec{\Omega}) \qquad (X\text{-}2)$$

where R is the vector between the hydrogen molecule and the carbon atom and $\vec{\Omega}$ is the orientation of $\vec{R}$ with respect to the hydrogen internuclear axis. A procedure for summing the pair interactions has been given by Steele (1973). The sum can be represented by a Fourier series in the position variables of a hydrogen molecule in a plane parallel to the surface. Only the uniform component is retained and the sum over all graphite planes except the first is replaced by an integral. Using Steel's procedure, an estimate of V_c^S has been made previously (Kubik and Hardy, 1978) but we now feel that it is not very realistic. The anisotropic potential $U_2(R)$ was taken to be proportional to the isotropic potential $U_1(R)$, which was represented by a Lennard-Jones potential. The potential parameters were obtained by combining those of the H_2-H_2 and C-C

Lennard-Jones potentials. The well depth of the C-H potential was set equal to the geometric mean of the well depths and the position of the well was the arithmetic mean of the positions.

A general anisotropic hydrogen-substrate interaction potential has since been derived (Wang et al, 1980). Parameters for the spherically averaged form of this potential were obtained from H_2 molecular beam scattering data (Mattera et al, 1980). They are significantly different from the results obtained by combining the H_2-H_2 and C-C Lennard-Jones potentials. It has been claimed that the primary reason is that the assumption of spherical symmetry of the C atoms in graphite is not valid since the graphite dielectric constant is anisotropic (Crowell and Brown, 1982).

The quadrupole coupling constant, the crystal field, and the ordering behaviour of H_2 and D_2 are all surprisingly different; it seems unlikely that the differences in the translational zero point motion are sufficient to account for this. In contrast, their bulk solid behaviour is very similar. Some of the further experimental work suggested above should illuminate the picture.

Using the intensities of the NMR signals, we have found conversion to be a first order process for H_2 with a rate constant of .40(2)%/h in our cell B. The D_2 data had much more scatter and covered a smaller concentration range so it was difficult to ascertain whether the process was first or second order. However, assuming it to be first order, we obtained rate

constants of .069(15)%/h in cell B and .026(7)%/h in cell A. The conversion rate was much higher during the process of adsorption but nevertheless, we were able to obtain adsorbed samples with initial J=1 concentrations of .99 for D_2 and .96 for H_2.

10.2 Future Work

The experiments described in this thesis have shown that hydrogen has some unique orientational properties and that their elucidation has only begun. To proceed further, using NMR, the most important requirement is to improve the S:N ratios. Presently, the measuring times are too long for extensive measurements. Two improvements would be relatively straightforward. The modulation coils for $\vec{H}_o$ parallel to the Grafoil are larger and considerably more homogeneous than those for $\vec{H}_o$ perpendicular to the Grafoil. For the latter, the variation of H_m over the sample causes significant loss of signal intensity. Since the clearest results can be obtained with H_o perpendicular to the Grafoil, it would be worthwhile to rotate the sample cell by 90°. Incidentally, if this were done, it would be interesting to see whether the modulation pick-up was still worst for $\bar{\beta}$=0°. If it were, it would strongly suggest that the Grafoil was the source of the pick-up. If not, the source must be outside the sample cell. Virtually all of the measurements discussed in Chapters VIII and IX employed cell B. However, the Grafoil in cell A had twice the surface area of

that in cell B even though the two cells had the same volume. In addition, the conversion rate for p-D_2 in cell A was found to be .4 times that in cell B. The disadvantage of cell A is that it is believed to have greater misorientation of the adsorbing surfaces. However, it is not clear how large this effect is because all of the hydrogen samples in cell A are now believed to have been non-uniform because the adsorbing temperature was too low. Considering the potential gains in the S:N ratio and the conversion rate, it would be useful to switch back to cell A and check the NMR signal produced by a uniform sample.

Additional measures would probably still be necessary, at least for D_2. Using an RF amplitude of 2×10^{-7} T, we did not find any evidence of saturation of the NMR signal except in the case of pure o-D_2, so it should be possible to increase the signal by increasing the excitation. We tried this but found that the noise increased faster than the signal at higher RF levels and that the first stage of the liquid helium cooled amplifier began to saturate causing distortion. The extra noise must have been from the oscillator. Usually in NMR, the problem of amplifier distortion is solved by using a bridge to reduce the voltage across the amplifier input. However, bridges tend to introduce microphonics and extra Johnson noise so this approach may create more problems than it solves. A better solution is probably to modify the amplifier itself so that it does not saturate at such a low level. Unfortunately, the modulation pick-up can be expected to increase in proportion to the

RF level so the pick-up will limit the potential improvements.

In many cases in NMR, the S:N ratio can be raised by increasing H_o because the S:N ratio is proportional to $H_o^{3/2}$ (Abragam, 1961). In our case, we might get some improvement for H_2 but perhaps not for D_2, at least at temperatures greater than about 1 K. At high temperatures, the broadening of the D_2 signal arises primarily from the graphite diamagnetism so increasing H_o would result in an increase in the broadening, reducing the increase in the amplitude of the absorption signal. At low temperatures there is additional broadening, probably from the order parameter distribution, so some extra broadening from the diamagnetism may not be significant. A more serious problem is the modulation pick-up. Experimentally, we have found it to be greater at 1.3 T than at .2 T and expect that it is proportional to H_o. If this is the case, not much improvement in the S:N ratio could be achieved by raising H_o.

Presently, only about half of the total measuring time can be utilized for recording data because it is necessary to wait for the pick-up to stabilize at the culmination of each sweep of the magnetic field. Even so, the baselines of the spectra were often quite poor. The dead time could probably be reduced somewhat if the signal averager could collect data in both sweep directions using a symmetric, triangular sweep. We have been unable to isolate the source of the pick-up but it may well come from the Grafoil itself. In that case, it might be desireable

to abandon magnetic field modulation altogether. We have considered using frequency modulation instead but it is likely to introduce new problems. Normally, the frequency is modulated by varying the tuning capacitor, which, in our case, is inside the cryostat. This would best be done using a varactor diode since mechanical tuning would introduce microphonics. The main problem with frequency modulation is that the measuring system has a frequency dependent gain so there would be a spurious background that would probably have to be subtracted.

The techniques described in this thesis could be used to study many variants of the hydrogen on graphite system. Ideally, one would like to be able to vary the crystal field in order to further explore the orientational phase diagram depicted in Fig. 6. To achieve this end, one would require a substrate on which hydrogen forms a registered, hexagonal lattice. If it were not registered, there would be a distribution of crystal fields resulting in broadening. Such a substrate may be difficult to find in view of requirements such as a high specific surface area. We have preplated the Grafoil with Kr at 95% of the $\sqrt{3}$ x $\sqrt{3}$ coverage and then adsorbed H_2 onto it. The NMR spectra of H_2 were quite broad so we suspect that the Kr was compressed out of registry. Broad spectra were also observed for H_2 on bare Grafoil if $\rho > 1$. MgO powder promises to be a good substrate (Bienfait et al, 1980; Vilches et al, 1984; Jordan et al, 1983). It has good uniformity and a high specific surface area. The crystal structure is cubic so

if there were a registered phase, it would not be $\sqrt{3}$ x $\sqrt{3}$. MgO also has better electrical and magnetic properties than Grafoil for NMR work.

We have only studied the orientational phase transition of adsorbed hydrogen. However, NMR may also prove to be useful for studying the translational phases. In particular a solid-fluid transition should be characterized by narrowing of the NMR spectrum due to the motion of the molecules.

Notes to Chapter X

1. Van Kranendonk's B(R) is a factor of two greater than ours, which is the conventional one.

BIBLIOGRAPHY

Abragam, A., The Principles of Nuclear Magnetic Resonance (Oxford University Press, London, 1961).

Alderman, D.W., Rev. Sci. Instr., 41, 192 (1970).

Aleksandrov, I.V., Theory of Nuclear Magnetic Resonance, translated by Scripta Technica, translation editor C.P. Poole, Jr. (Academic Press, New York, 1966), P. 106-113.

Berlinsky, A.J., private communication (1983).

Bernat, T.P., and H.D. Cohen, J. Low Temp. Phys., 14, 597 (1974).

Bienfait, M., J.G. Dash, and J. Stoltenberg, Phys. Rev. B, 21, 2765 (1980)

Birgenau, R.J., P.A. Heiney, and J.P. Pelz, Physica B+C, 110, 1785 (1982).

Bretz, M., and T.T. Chung, J. Low Temp. Phys., 17, 479 (1974).

Bretz, M., J.G. Dash, D.C. Hickernell, E.O. McLean, and O.E. Vilches, Phys. Rev. A, 8, 1589 (1973).

Carneiro, K., W.D. Ellenson, L. Passell, J.P. McTague, and H. Taub, Phys. Rev. Lett., 37, 1695 (1976).

Chung, T.T., and J.G. Dash, Surf. Sci., 66, 559 (1977).

Collins, R.E., Flow of Fluids Through Porous Materials (Rheinhold Publishing Corp., New York, 1961), Chapter 3.

Constabaris, G., J.R. Sams, Jr., and G.D. Halsey, Jr., J. Phys. Chem., 65, 367 (1961).

Coulomb, J.P., M. Bienfait, and P. Thorel, J. Phys. (Paris), 42, 293 (1981).

Cowan, B.P., J. Phys. C, 13 4575 (1980).

Crowell, A.D., and J.S. Brown, Surf. Sci., 123, 296 (1982).

Dash, J.G., Films on Solid Surfaces (Academic Press, New York, 1975).

Daunt, J.G., S.G. Hegde, S.P. Tsui, and E. Lerner, J. Low Temp. Phys., 44, 207 (1981).

Daunt, J.G., and C.Z. Rosen, ibid. 3, 89 (1970).

De Long, L.E., O.G. Symko, and J.C. Wheatley, Rev. Sci. Instrum, 42, 147 (1971).

Depatie, D.A., and R.L. Mills, ibid. 39, 105 (1968).

Dericbourg, J., Surf. Sci., 59, 565 (1976).

Diehl, R.D., M.F. Toney, and S.C. Fain, Jr., Phys. Rev. Lett., 48, 177 (1982).

Domany, E., M. Schick, J.S. Walker, and R.B. Griffiths, Phys. Rev. B, 18, 2209 (1978).

Ecke, R.E., and J.G. Dash, ibid. 28, 3738 (1983).

Eckert, J., W.D. Ellenson, J.B. Hastings, and L. Passell, Phys. Rev. Lett., 43, 1329 (1979).

Estève, D., M. Devoret, and N.S. Sullivan, J. Phys. C., 15, 5455 (1982).

Gauthier, M., and E.J.A. Varoquaux, Cryogenics, 13, 272 (1973).

Goellner, G.J., J.G. Daunt, and E. Lerner, J. Low Temp. Phys., 21, 347 (1975).

Goldman, V.V., Phys. Rev. B, 20, 4478 (1979).

Hardy, W.N., and A.J. Berlinsky, ibid. 8, 4996 (1973).

Harris, A.B., ibid. 1, 1881 (1970a).

Harris, A.B., ibid. 2, 3495 (1970b).

Harris, A.B., J. App. Phys., 42, 1574 (1971).

Harris, A.B., and A.J. Berlinsky, Can. J. Phys., 57, 1852 (1979).

Harris, A.B., and A.J. Berlinsky, private communication (1983).

Hegde, S.G., and J.G. Daunt, J. Low Temp. Phys., 32, 765 (1978).

Hegde, S.G., E. Lerner, and J.G. Daunt, Cryogenics, 13, 230 (1973).

Hickernell, D.C., D.L. Husa, J.G. Daunt, and J.E. Piott, J. Low Temp. Phys., 15, 29 (1974).

Huff, G.B., and J.G. Dash, ibid. 24, 155 (1976).

Ishiguro, E., K. Kambe, and T. Usui, Physica, 17, 310 (1951).

James, H.M., Phys. Rev., 167, 862 (1968).

James, H.M., and J.C. Raich, ibid. 162, 649 (1967).

Jordan, J.L., J. P. McTague, L. Passell, and J.B. Hastings, Bull. Am. Phys. Soc., 28, 874 (1983).

Ketley, I.J., and D.J. Wallace, J. Phys. A, 6, 1667 (1973).

Kjems, J.K., L. Passell, H. Taub, J.G. Dash, and A.D. Novaco, Phys. Rev. B, 13, 1446 (1976).

Kubik, P.R., and W.N. Hardy, Phys. Rev. Lett., 41, 257 (1978).

Landau, J., and R. Rosenbaum, Rev. Sci. Instrum., 43, 1540 (1972).

Lounasmaa, O.V., Experimental Principles and Methods Below 1 K (Academic Press, London, 1974).

McConville, G.T., Cryogenics, 9, 122 (1969).

Ma, S.K., Modern Theory of Critical Phenomena (W.A. Benjamin, Reading, Mass., 1976).

Mattera, L., F. Rosatelli, C. Salvo, F. Tommassini, U. Valbusa, and G. Vidali, Surf. Sci., 93, 515 (1980).

Migone, A.D., H.K. Kim, M.H.W. Chan, J. Talbot, and D.J. Tildesley, Phys. Rev. Lett., 51, 192 (1983).

Mouritsen, O.G., and A.J. Berlinsky, ibid. 48, 181 (1982).

Mukamel, D., and S. Krinsky, Phys. Rev. B., 13, 5065 (1976).

Nielsen, M., J.P. McTague, and W. Ellenson, J. Phys. (Paris), C4, C4-10 (1977).

Novaco, A.D., J. Low Temp. Phys., 21, 359 (1975).

O'Shea, S.F., and M.L. Klein, Chem. Phys. Lett, 66, 381 (1979).

Pfeuty, P., and G. Toulouse, Introduction to the Renormalization Group and Critical Phenomena, translated by G. Barton (John Wiley and Sons, New York, 1977).

Reif, F., and E.M. Purcell, Phys. Rev., 91, 631 (1953).

Riehl, J.W., and C.J. Fisher, J. Chem. Phys., 59, 4336 (1973).

Roberts, T.R., and S.G. Sydoriak, Phys. Rev., 102, 304 (1956).

Robinson, F.N.H., J. Sci. Instrum., 36, 481 (1959).

Rose, M.E., Elementary Theory of Angular Momentum (John Wiley and Sons, New York, 1957).

Rose-Innes, A.C., Low Temperature Laboratory Techniques (English Universities Press, 1973).

Rosenbaum, R.L., Rev. Sci. Instrum., 40, 577 (1969); 39, 890 (1968).

Rosenbaum, T.F., S.E. Nagler, P.M. Horn, and R. Clarke, Phys. Rev. Lett., 50, 1791 (1983).

Rosenblum, S.S., W.A. Steyert, and F.R. Fickett, Cryogenics, 17, 645 (1977).

Seguin, J.L., and J. Suzanne, Surf. Sci., 118, L241 (1982).

Silvera, I.F., Rev. Mod. Phys., 52, 393 (1980).

Silvera, I. and M. Nielsen, Phys. Rev. Lett., 37, 1275 (1976).

Steele, W.A., Surf. Sci., 36, 317 (1973).

Steele, W.A., J. Phys. (Paris), C4, C4-61 (1977).

Stockmeyer, R., H. Stortnik, and R. Wagner, Ber. Bunsenges. Phys. Chem., 82, 1314 (1978).

Sullivan, N.S., J. Phys. Lett. (Paris), 37, L-209 (1976).

Sullivan, N.S., and J.M. Vaissiere, Phys. Rev. Lett., 51, 658 (1983).

Thomy, A., and X. Duval, J. Chim. Phys. Physiochim. Biol., 66, 1966 (1969); 67, 286 (1970); 67, 1101 (1970).

van Dijk, H., M. Durieux, J.R. Clement, and J.K. Logan, J. Res. Nat. Bur. Stand., Sect. A, 64A, 1 (1960).

Van Kranendonk, J., Solid Hydrogen (Plenum Press, New York, 1983).

Van Vleck, J.H., The Theory of Electric and Magnetic Susceptibilities (Clarendon Press, Oxford, 1932).

Vilches, O.E., J.P. Coulomb, and T.S. Sullivan, Bull. Am. Phys. Soc., 29, 268 (1984).

Walker, E.J., Rev. Sci. Instrum., 30, 854 (1959).

Warren, W.H., and W.G. Bader, ibid. 40, 180 (1969).

Washburn, S., M. Calkins, H. Meyer, and A.B. Harris, J. Low Temp. Phys., 49, 101 (1982).

Weber, S., and G. Schmidt, Leiden Comm., 246C (1936).

Young, D.M., and A.D. Crowell, Physical Adsorption of Gases. (Butterworths, Washington, D.C., 1962).

APPENDIX A

HIGH TEMPERATURE EXPANSION OF σ

We will now give the coefficients for the high temperature expansion of σ obtained by Harris and Berlinsky (1983). The expansion to third order in $(\beta\Gamma)$ is

$$\sigma \simeq A+B(\beta\Gamma)+C(\beta\Gamma)^2+D(\beta\Gamma)^3 \qquad \text{(III-44)}$$

where the coefficients are exact in $V=\beta V_c$. If c is the J=1 concentration, then the coefficients are

$$A = [1-e^{-V}] / [1+2e^{-V}] \qquad \text{(A-1)}$$

$$B = -(81/2)ce^{-V}[1-e^{-V}] / [1+2e^{-V}]^3 \qquad \text{(A-2)}$$

$$\begin{aligned} C = {} & \frac{9c}{16V^2(e^V+2)^5}\,[-17e^{5V}+e^{4V} \\ & \times(-380V^2c-140V^2+68V-102) \\ & + e^{3V}(3900V^2c-6V^2+306V-187) \\ & + e^{2V}(-4680V^2c-1260V^2+408V-34) \\ & + e^{V}(1160V^2c-700V^2+136V+204)+136] \end{aligned} \qquad \text{(A-3)}$$

$$\begin{aligned} D = {} & \frac{9c}{512V^3(e^V+2)^7}\,[e^{7V}(48960Vc^2+16320Vc \\ & +1632V-9672c+1792) + e^{6V}(-533376V^3c^2 \\ & -888V^3c+864V^3-489600V^2c^2-137352V^2c \\ & -11424V^2+195840Vc^2+124980Vc+7840V-67704c \\ & +17920) + e^{5V}(-3692632V^3c^2-1127688V^3c \\ & -55328V^3-1370880V^2c^2-532800V^2c-54176V^2 \\ & +336456Vc-432V-145080c+69888) + e^{4V} \\ & \times(2692408V^3c^2+541443V^3c-28768V^3+685440V^2c^2 \end{aligned}$$

$$-385296V^2c-108640V^2-685440Vc^2+317100Vc$$
$$-72576V-9672c+125440) + e^{3V}(-18491424V^3c^2$$
$$-4521774V^3c-56064V^3+3133440V^2c^2+368544V^2c$$
$$-177408V^2-244800Vc^2-104664Vc-200816V+309504c$$
$$+71680) + e^{2V}(6604864V^3c^2+3027732V^3c$$
$$+380864V^3-391680V^2c^2+36288V^2c-225664V^2$$
$$+881280Vc^2-350064Vc-282528V+232128c-86016) + e^{V}$$
$$\times(13420160V^3c^2+3658488V^3c+409024V^3$$
$$-1566720V^2c^2-354432V^2c-109568V^2$$
$$+195840Vc^2-228768Vc-234048V-154752c-143360)$$
$$-(391680Vc^2+111360Vc+89984V+154752c+57344)] \qquad (A-4)$$

APPENDIX B

CONSTRUCTION OF A QUARTZ-COPPER SEAL

The precision bore quartz tube was 13.05 mm OD, .58 mm thick, and 47.2 mm long. It was cleaned using the following process:

1. Boiled for 15 min in a detergent solution.[1]
2. Rinsed several times in hot water.
3. Etched in 10% HF for 4 min.
4. Rinsed several times in water.
5. Boiled in a solution of 25 ml of KOH pellets in 100 ml of water.
6. Rinsed several times in hot water.
7. Rinsed in electronic grade methanol.
8. Boiled in methanol for 30 min.
9. Rinsed in methanol.

Immediately after cleaning, the tube was placed in an evaporator and coated with about 500 Å of Cr followed by 1100 Å of Cu. Pre-coating with Cr was necessary because Cu does not adhere well to quartz. Attempts to solder directly to the film were unsuccessful because the indium alloy solders used appeared to alloy with the copper and lifted off the film. Consequently the Cu film thickness was increased to .02 mm by electroplating at 50 mA/cm^2 in a .74 molar solution of $CuSO_4$. The tube was then soldered to a 13.67 mm OD, .25 mm thick, 11.1 mm long copper tube using Indalloy #5 solder[2]

(.375 Sn/.375Pb/.25In) and Kester 115[3] pure rosin flux. The soldering operation was performed using an iron in a stream of helium gas heated to 180 C. It was very important to use a mild flux in order to prevent damage to the film. The solder had to be non-superconducting in fields >.15 T and it was desireable that its melting point be greater than 150 C so that the sample cell could be baked out when it was mounted in the cryostat.

Notes to Appendix B

1. The water used throughout the cleaning procedure was distilled and demineralized.

2. Indium Corporation of America, Utica, N.Y., U.S.A.

3. Kester Solder, Chicago, Ill., U.S.A.